Interactions in a Quantum Gas of Dysprosium Atoms

Von der Fakultät Mathematik und Physik der Universität Stuttgart
zur Erlangung des akademischen Grades eines Doktors der
Naturwissenschaften (Dr. rer. nat.) genehmigte Abhandlung

vorgelegt von

Thomas Maier

aus Ulm

Hauptberichter:	Prof. Dr. Tilman Pfau
Mitberichter:	Prof. Dr. Harald Giessen
Prüfungsvorsitzender:	Prof. Dr. Günter Wunner
Tag der mündlichen Prüfung:	10.11.2015

5. Physikalisches Institut
Universität Stuttgart
2015

Abstract

The subject of this thesis is the creation of a dipolar quantum gas of dysprosium atoms as well as the investigation of its two-body interactions. For this purpose we setup a new experimental apparatus which allows us to study dipolar many-body systems with ultra-cold bosonic ^{164}Dy, ^{162}Dy as well as fermionic ^{161}Dy atoms. In this work I present our developed cooling and trapping scheme to create a cold sample of dysprosium atoms based on a magneto-optical trap operating at the 626 nm transition and forced evaporative cooling in a crossed optical dipole trap. With our methods we can create Bose-Einstein condensates with $N \approx 25 \times 10^3$ ($N \approx 30 \times 10^3$) atoms of the ^{164}Dy (^{162}Dy) isotope, respectively. In addition, degenerate Fermi gases with $N \approx 10 \times 10^3$ and $T/T_F \approx 0.5$ can be realized. By comparing the experimentally obtained data with the prediction of theoretical calculations we show that for both bosonic isotopes the dipole-dipole interaction dominates the two-body interaction energy. Furthermore, we observe the effects of the complex atomic structure of dysprosium as a dense and correlated distribution of narrow Feshbach resonances. Despite many narrow resonances we also observe broad resonances which are caused by universal s-wave halo states. These resonances offer the possibility to tune the two-body interactions in dysprosium in a controlled way.

List of Publications

- H. Kadau, M. Schmitt, M.Wenzel, C. Wink, T. Maier, I. Ferrier-Barbut and T. Pfau: *"Observing the Rosensweig instability of a quantum ferrofluid."*, arXiv:1508.05007 (submitted 2015).
- T. Maier, I. Ferrier-Barbut, H. Kadau, M. Schmitt, M. Wenzel, C. Wink, T. Pfau, K. Jachymski and P. S. Julienne, *"Broad universal Feshbach resonances in the chaotic spectrum of dysprosium atoms."*, Phys. Rev. A **92**, 060702(R) (2015).
- T. Maier, H. Kadau, M. Schmitt, M. Wenzel, I. Ferrier-Barbut, T. Pfau, A. Frisch, S. Baier, K. Aikawa, L. Chomaz, M. J. Mark, F. Ferlaino, C. Makrides, E. Tiesinga, A. Petrov and S. Kotochigova, *"Emergence of chaotic scattering in ultracold Er and Dy."*, Phys. Rev. X **5**, 041029 (2015).
- T. Maier, H. Kadau, M. Schmitt, A. Griesmaier and T. Pfau, *"Narrow-line magneto-optical trap for dysprosium atoms."* Optics Letters **39**, 3138 (2014).
- M. Schmitt, E. A. L. Henn, J. Billy, H. Kadau, T. Maier, A. Griesmaier and T. Pfau, *"Spectroscopy of a narrow-line optical pumping transition in atomic dysprosium."*, Optics Letters **38**, 637 (2013).
- J. Billy, E. A. L. Henn, S. Müller, T. Maier, H. Kadau, A. Griesmaier, M. Jona-Lasinio, L. Santos and T. Pfau, *"Deconfinement-induced collapse of a coherent array of dipolar Bose-Einstein condensates."*, Phys. Rev. A **86**, 051603(R) (2012).

Contents

Zusammenfassung

Gegenstand dieser Dissertation ist die Erzeugung eines dipolaren Quantengases aus Dysprosium Atomen und die Untersuchung seiner interatomaren Wechselwirkungen. Für diesen Zweck wurde eine neue Experimentierapparatur geplant und aufgebaut, welche die Möglichkeit bietet, dipolare Vielteilchensysteme mit ultrakalten Dysprosium Atomen zu untersuchen.

Die Entdeckung der Supraflüssigkeit und des Supraleiters zu Beginn des 20. Jahrhunderts begründete ein neues Forschungsfeld, welches sich mit den Eigenschaften von stark wechselwirkenden Vielteilchensystemen beschäftigt. Das grundlegende Verständnis dieser Systeme würde uns erlauben, neue Materialien zu entwickeln, welche unser tägliches Leben revolutionieren könnten. In den letzten zwanzig Jahren wurden Bose-Einstein-Kondensate (BEK)[1] [15] sowie entartete Fermigase[2] [25] aus neutralen Atomen als Modellsysteme verwendet, um diese Phänomene genauer zu untersuchen [26]. Der große Vorteil bei diesen Systemen besteht dabei in der Möglichkeit, systemrelevante Parameter, wie das externe Potential als auch die interatomaren Wechselwirkungen, dynamisch und mit hoher Genauigkeit einstellen zu können. Insbersondere die Änderung der interatomaren Wechselwirkungsstärke ermöglicht die Beobachtung des sogenannten BEK-BCS Überganges eines BEKs zu einer fermionischen Supraflüssigkeit [27]. Darüber hinaus verdeutlicht die Realisierung des Übergangs von der Supraflüssigkeit zum Mott-Isolator mit Atomen in einem optischen Gitterpotential die Eignung ultrakalter Gase als Modellsystem für stark wechselwirkende Festkörpersysteme [28–30].

Für die oben angeführten Beispiele wurden ultrakalte Alkali Atome verwendet, deren Eigenschaften durch die kurzreichweitige und isotrope Kontaktwechselwirkung bestimmt werden. Im Gegensatz dazu zeigen dipolare Systeme durch die zusätzliche langreichweitige und anisotrope Dipol-Dipol-Wechselwirkung (DDW) eine höhere Komplexität. Mit der Erzeugung eines Chrom-BEKs im Jahr 2005 wurde die experimentelle Untersuchung von dipolaren Vielteilchensystemen möglich [10]. Hierbei konnten beeindruckende dipolare Effekte wie die Magnetostriktion [31] und der d-Wellen Kollaps [32] beobachtet werden. Obwohl das magnetische Moment von Chrom ($\mu_m = 6\,\mu_B$) bedeutend größer als das von den Alkali Atomen ($\mu_m = 1\,\mu_B$) ist, trägt die DDW dennoch nur 16 % zur gesamten Wechselwirkungsenergie bei [33]. Jedoch kann mittels einer Feshbach-Resonanz die Stärke der Kontaktwechselwirkung reduziert werden und dadurch ein Quantengas mit starker dipolarer Wechselwirkung erzeugt werden [34]. Ein Nachteil sind dabei die wesentlich erhöhten Dreikörperverluste in der Nähe der Feshbach-Resonanz, welche die für Experimente verbleibende Zeit auf wenige Millisekunden reduziert.

[1] Bisher konnten 13 Elemente kondensiert werden: Na [1], Rb [2], Li [3, 4], H [5], He [6], K [7], Cs [8], Yb [9], Cr [10], Ca [11], Sr [12], Dy [13], Er [14].

[2] Ein entartetes Fermigas wurde bisher für folgene Elemente realisiert K [16], Li [17, 18], He [19], Sr [20], Yb [21], Dy [22], Er [23], Cr [24].

Kürzlich wurde mit der Erzeugung eines Dysprosium ($\mu_m = 10\,\mu_B$) [13] und Erbium ($\mu_m = 7\,\mu_B$) [14] BEKs die Familie der dipolaren Quantengase erweitert. Dysprosium ist neben Terbium das Element mit dem größten magnetischen Moment. Zudem wird, entsprechend seiner großen Masse, die Wechselwirkung zwischen Dysprosium Atomen durch die DDW dominiert. Neben den magnetischen Atomen sind heteronukleare Moleküle im Rotations- und Schwingungsgrundzustand vielversprechende Systeme, um dipolare Effekte zu untersuchen, da diese durch ihr induziertes elektrisches Dipolmoment eine noch viel größere DDW aufweisen können. Die Herstellung ultrakalter Moleküle ist jedoch sehr aufwendig, wobei kürzlich mit der Erzeugung bosonischer RbCs- [35, 36] und fermionischer NaK-Moleküle [37] in ihren Rotations- und Schwingungsgrundzuständen auch hier Erfolge erzielt werden konnten. Einen noch stärkeren dipolaren Charakter könnten Grundzustandsatome mit schwach beigemischten Rydbergzuständen aufweisen, welche aber bisher noch nicht realisiert werden konnten [38]. Diese neuen dipolaren Experimente eröffnen eine Vielzahl neuer Möglichkeiten, dipolare Quantensysteme zu erforschen.

Seit der erstmaligen Erzeugung eines dipolaren Kondensates sind dipolare Vielteilchensysteme von großem theoretischen Interesse, da sie die Möglichkeiten bieten, neuartige Quantenphasenübergänge und exotische Materiezustände zu untersuchen. Beispielsweise wurde in einem dipolaren BEK ein sogenanntes Maxon-Roton Anregungsspektrum vorhergesagt [39], welches eng mit dem Auftreten von selbstorganisierten Strukturen in einem dipolaren Quantengas verknüpft ist [40, 41]. Desweiteren zeigen theoretische Studien, dass in Systemen mit starker dipolarer Wechselwirkung kristalline Strukturen [42] als auch neuartige Materiezustände auftreten können [43, 44].

Für mehr als 10 Jahre war die Stuttgarter Chrom-Apparatur das Aushängeschild für die experimentelle Untersuchung von dipolaren Quantengasen, wobei viele faszinierende dipolare Phänomene beobachtet und erforscht werden konnten. Für das Studium von selbstorganisierten Strukturen sowie von neuen Quantenzuständen gelangte die bestehende Apparatur jedoch an ihre technischen Grenzen. Darüber hinaus gab es mit der Realisierung eines Dysprosium-Kondensates ein weiteres dipolares System, das auch ohne den Gebrauch von Feshbach-Resonanzen neuartige dipolare Effekte aufzeigen sollte. Um auch in Zukunft herausragende Forschung an dipolaren Quantengasen betreiben zu können, wurde Ende 2011 die Entscheidung getroffen, nicht nur eine neue Apparatur mit zusätzlichen experimentellen Möglichkeiten aufzubauen, sondern auch von Chrom auf das Element mit dem größten magnetischen Moment, Dysprosium, zu wechseln.

Für das Erzeugen eines Quantengases aus ultrakalten Dysprosium Atomen wurde ein eigenes Verfahren entwickelt. Zuerst werden die Atome mittels eines Zeeman-Abbremsers, wozu Laserlicht mit der Wellenlänge von 421 nm verwendet wird, verlangsamt und in einer magneto-optischen Falle gefangen, wobei die Atome auf wenige Mikrokelvin abgekühlt werden. Für den Betrieb der magneto-optische Falle wird ein optischer Übergang bei 626 nm verwendet. Die kalten Atome werden daraufhin in eine optische Dipolfalle umgeladen und in eine 375 mm entfernte Glaszelle transportiert. Die Atome in der Glaszelle

können mittels eines hochauflösenden Abbildungssystems beobachtet werden. Desweiteren besteht hier auch die Möglichkeit, die Eigenschaften der Quantengase mittels magnetischer Felder und zusätzlichen optischen Potentialen zu beeinflussen. Schlussendlich werden durch Verdampfungskühlung BEKs mit $N \approx 25 \times 10^3$ ($N \approx 30 \times 10^3$) Atome des ^{164}Dy (^{162}Dy) Isotops erzeugt. Desweiteren können mittels dipolarer Stoßvorgänge entartete Fermigase aus spinpolarisierten Dysprosium Atomen hergestellt werden. Bisher war es möglich, Fermigase mit $N \approx 10 \times 10^3$ Atomen und mit Temperaturen von $T/T_F \approx 0.5$ zu realisieren.

Ein wichtiger Parameter, der die Stärke der Kontaktwechselwirkung charakterisiert, ist die s-Wellenstreulänge a, deren Größe durch eine magnetische Feshbach-Resonanz eingestellt werden kann. Durch Vergleich mit den im Experiment erzielten und durch Simulationen vorhergesagten BEK-Atomzahlen für verschiedene Fallengeometrien konnte die bis dato unbekannte Hintergrundstreulänge a_{bg}, die Streulänge abseits einer Feshbach-Resonanz, für das ^{164}Dy Isotop zu $86\,a_0 \lesssim a_{\mathrm{bg}}^{164} \lesssim 93\,a_0$ abgeschätzt werden. Weiterhin deutet die höhere Effizienz bei der Verdampfungskühlung mit Atomen des ^{162}Dy Isotops auf eine größere Hintergrundstreulänge als für das ^{164}Dy Isotop hin. Zusätzlich konnte mittels Stabilitätsuntersuchungen des BEKs aus Atomen des ^{162}Dy Isotops dessen Hintergrundstreulänge auf $a_{\mathrm{bg}}^{164} \lesssim a_{\mathrm{bg}}^{162} \lesssim a_{\mathrm{dd}} = 134\,a_0$ festgelegt werden. Daduch wurde bestätigt, dass für beide untersuchten Dysprosium Isotope die DDW die dominierende interatomare Wechselwirkung ist. Dies bedeutet, dass auch ohne die Verwendung einer Feshbach-Resonanz neuartige dipolare Effekte eines stark wechselwirkenden Quantengases mit Dysprosium Atomen untersucht werden können.

Um weiterführende Erkenntnisse über die Wechselwirkungen zwischen den Dysprosium Atomen zu erhalten, wurden Feshbach-Resonanzen sowohl für das ^{164}Dy als auch für das ^{162}Dy Isotop in einem Magnetfeldbereich zwischen 0 G und 600 G gemessen und analysiert. Daraus ergab sich, dass die große Anzahl von vier Resonanzen pro Gauß auf die komplexe Wechselwirkung zweier Dysprosium Atome zurückzuführen ist. Desweiteren deutet die statistische Auswertung der Resonanzpositionen auf Anzeichen von Quantenchaos im Streuverhalten von Dysprosium Atomen hin. Zusätzliche theoretische Untersuchungen zeigen, dass dieses Verhalten durch die Anisotropie in der kurzreichweitigen Wechselwirkung, welche von der anisotropen Elektronenverteilung des Grundzustandes herrührt, als auch durch eine Zeeman-Kopplung zustande kommt. Neben der großen Anzahl von Resonanzen, die nur eine Breite von wenigen Milli-Gauß aufzeigen, wurden im Feshbach-Spektrum aber auch breite Resonanzen gefunden. Diese breiten Resonanzen wurden im Detail untersucht, indem die Bindungsenergie ihrer dazugehörigen Molekülzustände bestimmt wurde. Unerwartet war dabei, dass diejenigen Zustände, die zu den breiten Resonanzen gehören, von den stark gekoppelten Zuständen, welche die große Anzahl von schmalen Resonanzen erzeugen, entkoppelt sind und einen universalen Charakter über einen großen Magnetfeldbereich aufzeigen. Die Eigenschaften dieser Resonanzen können durch die bekannte Theorie einer s-Wellen-Resonanz beschrieben werden. Weiterhin konnte die Breite zu $\Delta = 31(6)\,\mathrm{G}$ und die Hintergrundstreulänge $a_{\mathrm{bg}} = 91(15)\,a_{\mathrm{bg}}$ der Feshbach-

Resonanz bei $B_0 = 76.9\,\mathrm{G}$ bestimmt werden. Damit kann diese Feshbach-Resonanz in Zukunft benutzt werden, um die Kontaktwechselwirkung im dipolaren Quantengas kontrolliert einzustellen. Der erhaltene Wert für die Hintergrundstreulänge stimmt mit den oben genannten Werten und mit den kürzlich mittels Rethermalisierung gemessenen Werten von $a_{\mathrm{bg}} = 92(8)\,a_0$ und $a_{\mathrm{bg}} = 112(10)\,a_0$ für das ^{164}Dy und ^{162}Dy Isotop überein [45].

Die in dieser Arbeit beschriebenen Studien zeigen die Möglichkeiten, welche die neue Dysprosium-Apparatur bietet, um neuartige Quantenphänomene zu erforschen. Das entwickeltes Vorgehen, Dysprosium Atome zu kühlen und zu fangen, bietet gute Voraussetzungen für weitere experimentelle Untersuchungen von dipolaren Quantensystemen. Besonders durch den Transport in die Glaszelle stehen eine Vielzahl zusätzlicher technischer Möglichkeiten zur Verfügung, wie zum Beispiel ein hochauflösendes Abbildungssystem, mit dem die Eigenschaften der dipolaren Quantengase untersucht werden können.

Abbreviations

Reference for abbreviations used in the text.

AOM	acousto-optical modulator
ADI	anisotropic dispersion interaction
BEC	Bose-Einstein condensate
BO	Born-Oppenheimer
DDI	dipole-dipole interaction
EOD	electro-optical deflector
EOM	electro-optical modulator
GOE	Gaussian-orthogonal ensemble
GPE	Gross-Pitaevskii equation
IGBT	insulated-gate bipolar transistor
MOSFET	metal-oxide-semiconductor field-effect transistor
MOT	magneto-optical trap
MT	magnetic trap
NNS	nearest-neighbor spacing
ODT	optical dipole trap
PDH	Pound-Drever-Hall
RF	radio frequency
RMT	random-matrix theory
TOF	time-of-flight
TF	Thomas-Fermi
ULE	ultra-low expansion
vdW	van-der-Walls
ZS	Zeeman slower

Nomenclature of units and natural constants.

a_0	$5.3 \times 10^{-11}\,\mathrm{m}$	Bohr radius
k_B	$1.38 \times 10^{-23}\,\mathrm{J/K}$	Boltzmann constant
e	$1.60 \times 10^{-19}\,\mathrm{C}$	elementary charge
μ_0	$4\pi \times 10^{-7}\,\mathrm{Tm/A}$	permeability of free space
μ_B	$9.27 \times 10^{-23}\,\mathrm{J/T}$	Bohr magneton ($\mu_\mathrm{B}/h \approx 1.4\,\mathrm{MHz/G}$)
$\hbar$	$1.05 \times 10^{-34}\,\mathrm{Js}$	reduced Planck constant
E_h	$4.36 \times 10^{-18}\,\mathrm{J}$	Hartree energy
1 G	$10^{-4}\,\mathrm{T}$	conversion from Gauss to Tesla

1 Introduction

The observation in the early 20th century of superfluidity and superconductivity, both characterized by an absence of viscosity, opened a completely new field of research in physics of strongly-correlated many-body systems. Understanding the physics behind these phenomena could allow us to design new materials, which would change our daily life. In the past 20 years Bose-Einstein condensates (BEC)[3] [15] as well as degenerate Fermi gases[4] [25] of neutral atoms have been used as highly controllable model systems to investigate these phenomena [26]. The possibility to tune the interaction strength in ultra-cold gases and altering the external confinement almost arbitrarily, even allowing to change the dimensionality of the system, have extended the types of systems that can be studied with ultra-cold atoms. In particular, tuning the interaction strength has allowed to investigate the connection between a BEC and a fermionic superfluid through the study of the so-called BEC-BCS crossover [27]. Another breakthrough was the observation of the superfluid-Mott transition with atoms in an optical lattice showing the feasibility of ultra-cold atoms to successfully model strongly-correlated solid-state systems [28–30]. These examples outline the importance of the interactions on the many-body state of ultra-cold atoms.

In contrast to alkali atoms, which were used for the examples above, whose properties are dominated by the short-range and isotropic contact interaction, dipolar systems show additional complexity due to the long-range and anisotropic dipole-dipole interaction (DDI). With the realization of a BEC of chromium (Cr) atoms in 2005 the experimental investigation of strongly dipolar many-body systems was made possible [10]. Phenomena which are due to the DDI have been observed such as magnetostriction [31], d-wave collapse of the BEC [32], the stabilization of an attractive BEC in a 1-D lattice [46] and spin relaxations in an optical lattice [47]. The magnetic moment of Cr ($\mu_m = 6\,\mu_B$) is large compared to the alkali atoms ($\mu_m = 1\,\mu_B$), but it contributes only about 16 % to the interaction energy in a BEC under normal conditions [33]. To be able to enter the strongly dipolar regime a magnetic Feshbach resonance was used to reduce the contact interaction and thereby enhance the relative contribution of the DDI [34].

Recently, the family of dipolar quantum gases has been extended with the condensation of dysprosium (Dy) ($\mu_m = 10\,\mu_B$) [13] and erbium (Er) ($\mu_m = 7\,\mu_B$) [14] atoms. Dy is beside terbium the element with the largest magnetic moment. In ultra-cold atoms the interaction strength can be characterized by their length scales. By dimensional analysis the corresponding length scale of the DDI is given by $a_{\mathrm{dd}} \propto m\mu_m^2/\hbar^2$, with the atomic mass m, the element's magnetic moment μ_m and $\hbar$ the reduced Planck constant. In Figure (1.1) the periodic table of elements with the product $m\mu_m^2$ is shown. Thanks to the large

[3] So far there are 13 different elements where a BEC could be achieved: Na [1], Rb [2], Li [3, 4], H [5], He [6], K [7], Cs [8], Yb [9], Cr [10], Ca [11], Sr [12], Dy [13], Er [14].

[4] A degenerate Fermi gas has been realized for K [16], Li [17, 18], He [19], Sr [20], Yb [21], Dy [22], Er [23], Cr [24].

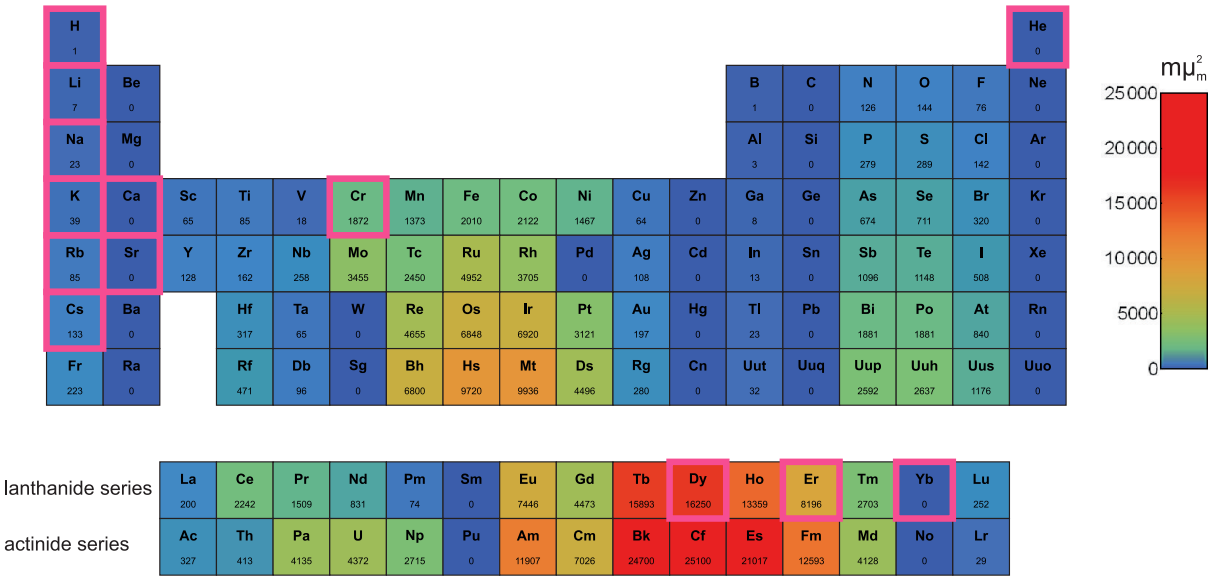

Fig. 1.1, Periodic table of elements: The used color code indicates the element's dipolar character ($\sim m\mu_m^2$) in atomic units while the pink rectangles highlight the elements which have been successfully condensed. Dysprosium (Dy) is the element with the highest magnetic moment and due to its large mass it shows the largest dipolar character beside the transuranic radioactive elements berkelium (Bk), californium (Cf) and einsteinium (Es).

magnetic moment and the high mass of Dy the DDI is dominant even without reducing the contact interaction strength.

In addition to magnetic atoms, also hetero-nuclear ground-state molecules are promising candidates to show strongly dipolar effects, as they have an even stronger and tunable DDI due to their induced electric dipole moments. One way to create ultra-cold molecules is to associate the cold atoms via a Feshbach resonance. Subsequently, the weakly-bound Feshbach molecules have to be transferred into their vibrational and rotational ground-states via a two-photon transition, which was shown the first time for fermionic KRb molecules [48]. Unfortunately, these molecules are unstable due to exothermic two-body chemical reactions [49]. Recently, it was possible to create chemical stable bosonic RbCs molecules [35, 36] and fermionic NaK molecules [37] in their rovibrational ground-state. Furthermore, ground-state atoms with weakly admixed Rydberg states would show an even stronger dipole moment than hetero-nuclear molecules [38]. The emergence of these new systems opens many possibilities for the study and control of dipolar many-body systems.

Since the first realization of a dipolar condensate strongly dipolar many-body systems have been of great theoretical interest for the quest of new quantum phase transitions and new states of matter. For example in quasi-2D geometries a particular excitations spectrum, the maxon-roton excitation spectrum [39], is predicted, which is closely related to self-organized structures in dipolar quantum gases [40, 41]. Furthermore, for strongly

dipolar systems crystalline structures [42] and new exotic quantum phases are predicted [43, 44].

This Thesis

For more than 10 years the Cr BEC apparatus was the "working horse" of the experimental investigation of the physics of dipolar quantum gases and many fascinating phenomena have been observed. However, to investigate self-organized density structures and other novel quantum phases new technical capabilities were required. In addition, with the realization of a Dy BEC in 2011 a new member of the dipolar family was present which should show dipolar effects even without the use of a Feshbach resonance due to the larger dipolar length. Therefore, at the end of 2011 we took the decision to switch from Cr to Dy and to setup a new apparatus with state of the art experimental tools to be able to do outstanding research on dipolar quantum gases.

In this thesis I present the experimental setup of the new apparatus and its cooling and trapping scheme to create dipolar bosonic as well as fermionic quantum gases of Dy atoms. The results of our scheme to create a cold sample of Dy atoms in a magneto-optical trap (MOT) are published in [50]. The new apparatus contains a science cell composed of an octagonal glass cell, which allows for sub-micrometer imaging resolution with a microscope objective and a good magnetic field control to alter the interaction properties of the highly magnetic Dy atoms.

In the framework of this thesis we perform a first study of the BEC properties which allows to estimate the so far unknown background scattering length of Dy. Together with further measurements we confirmed that Dy is in the strongly dipolar regime without the usage of a Feshbach resonance.

Furthermore, we investigate the complex scattering properties of Dy by studying low field Feshbach resonances. By statistical analysis of the resonance positions we can show that the scattering of Dy atoms show indications of quantum chaos. This is studied in detail within a collaboration together with the group of F. Ferlaino and S. Kotochigova and the obtained findings have been published in [51].

By measuring Feshbach resonances for even higher magnetic fields we find that despite the many narrow Feshbach resonances broad features exist. These broad Feshbach resonances can be described by the standard formalism of a s-wave resonance and can be used to control the two-body interaction. We have analyzed the broad resonances in collaboration with the group of P. S. Julienne and the results have been published in [52].

Outline

This thesis is organized as follows. After a short introduction to the element Dy in chapter 2, we review the theoretical descriptions of the scattering behavior of dipolar atoms in chapter 3. In particular, we give a brief introduction to Feshbach resonances and how they can be used to change the properties of a degenerate quantum gas. In addition, we present the concepts of quantum chaos as it will be relevant for the interpretation of the experimental obtained data. We end this chapter with a mean-field description of a dipolar condensate and estimate its stability criterion which constrains the design of our trapping potential. In chapter 4 we give a detailed description of our experimental setup including vacuum chamber, the required laser systems, the feasibility to control the magnetic fields and finally the setup of our high-resolution imaging system. Our scheme to produce a BEC as well as a degenerate Fermi gas of Dy atoms is presented in chapter 5. In chapter 6 our measurement of Feshbach resonances of ^{164}Dy and ^{162}Dy is presented. The observed dense resonance spectrum is analyzed using statistical methods based on random-matrix theory. Further theoretical analysis give insights in the origin of the chaotic scattering behavior of ultra-cold Dy atoms. Broad loss features are analyzed by measuring the binding energy of the underlying molecular state and are further studied using a dipole-modified s-wave scattering model. Finally, in chapter 7 we summarize our findings and give an outlook to the possibilities of further studies of dipolar phenomena with Dy atoms.

2 Dysprosium

The element dysprosium belongs to the group of rare earth elements[5], also known as lanthanides, which consists of 15 chemically similar elements, from atomic number 57 (lanthanum) to 71 (lutetium). The element Dy was first discovered by the French chemist Paul-Emile Lecoq de Boisbaudran in a holmium sample in 1886 [53]. Since the development of ion-exchange chromatography from Frank Spedding in 1950 it is possible to separate Dy from other lanthanides in an efficient way. The Greek expression dysprositos, which means "hard to get at", is the origin of its name and reflects the difficulty to isolate Dy from holmium. Dy has a bright, silver color and can be easily machined. However, the pure metal is not of great industrial importance as it oxidizes rapidly [54]. In contrast, Dy is used together with neodymium, iron and boron to produce the strongest permanent magnets [55].

2.1 General Properties

The nucleus of Dy has 66 protons and there exist seven stable isotopes. Table (2.1) summarizes the mass and the natural abundance of the most common Dy isotopes. Interestingly, besides the bosonic isotopes, also the fermionic isotopes have a high natural abundance, which opens the possibility to study dipolar fermionic quantum gases. In this thesis the results for the bosonic ^{162}Dy and ^{164}Dy isotopes are presented. Additionally, we show first attempts to cool the ^{161}Dy fermion to degeneracy. As many other lanthanide elements Dy has a high melting temperature (1412°C) and boiling point (2560°C) [56]. Beside terbium, Dy is the element with the highest magnetic moment of all elements with $10\,\mu_\mathrm{B}$, where μ_B is the Bohr magnetron. The high magnetic moment alters the properties of the quantum gases and give rise to new physics.

isotope	^{160}Dy	^{161}Dy	^{162}Dy	^{163}Dy	^{164}Dy
mass [a.u.]	159.92	160.93	161.93	162.93	163.93
abundance [%]	2.3	18.9	25.5	24.9	28.3
statistics	boson	fermion	boson	fermion	boson

Tab. 2.1, Natural abundance and statistical properties of the most common stable Dy isotopes [53]

[5]The term rare earth elements is misleading, because these elements are not as rare as it indicates. For example the most abundant lanthanide, the element cer, is as common as copper.

2.1.1 Electron Configuration of the Ground-state

The 66 electrons of Dy are distributed over the possible energy orbitals following Madelung's rule and form the electronic ground-state

$$(1s^2 2s^2 2p^6 3s^2 3p^6 3d^{10} 4s^2 4p^6 4d^{10} 5s^2 5p^6)\, 4f^{10} 6s^2 \ . \tag{2.1a}$$

The expression in brackets represents the electronic configuration of the noble gas xenon. Notice that the $6s$-orbital is completely filled, while the $4f$-orbital is only partly filled with 10 electrons. This configuration is known as a submerged-shell configuration. Using Hund's rules we can obtain the quantum numbers of the ground-state:

(i) Completely filled orbitals do not affect the ground-state quantum numbers. Thus, only the electrons of the $4f$-orbital have to be taken into account.

(ii) The $4f$-orbital has seven sub-states with $m_l = -3, ..., +3$, which have to be filled such that the total spin $\boldsymbol{S}$ is maximized. This results in three m_l states occupied with two electrons with opposite spins and four states which are only singly occupied, therefore we obtain the total electron spin quantum number $S = 4 \cdot 1/2 = 2$.

(iii) Further, the electrons are distributed such that the angular momentum $\boldsymbol{L}$ is maximized which means that the unpaired electrons occupy the states $m_l = 0, +1, +2, +3$, resulting in an orbital angular momentum quantum number $L = 6$.

(iv) Finally, we have to take into account the spin-orbit (LS) coupling. As the $4f$-sub-shell is more than half filled the total angular momentum quantum number is obtained by $|\boldsymbol{J}| = |\boldsymbol{L} + \boldsymbol{S}| = 8$.

In summary, the ground-state of Dy, written in the usual term formalism, is a ${}^5I_8$ state. The high angular momentum of the ground-state is quite different to the usually used alkali and alkaline earth metals. As we shall see later, this anisotropic electronic configuration affects strongly the scattering properties of Dy.

2.1.2 Hyperfine Structure

In contrast to the bosonic Dy isotopes which have no nuclear spin $\boldsymbol{I}$ due to their even numbers of protons and neutrons, fermions show a hyperfine structure as their nuclear spin is $|\boldsymbol{I}| = 5/2$. The coupling between the total angular momentum $\boldsymbol{J}$ and the nuclear spin leads to a hyperfine splitting [57]:

$$\Delta E_{\mathrm{HFS}} = AK + B\frac{3/2K(2K+1) - I(I+1)J(J+1)}{2I(2I-1)J(2J-1)} \ , \tag{2.2}$$

with $K = 1/2(F(F+1) - J(J+1) - I(I+1))$, A, B the hyperfine structure coefficients and the total angular momentum quantum number $F = |\boldsymbol{J} + \boldsymbol{I}| = 21/2$. For the ground-state

g.-s.	A [MHz]	B [MHz]	ν_{is} [MHz]	Refs.
^{161}Dy	-116.2322	1091.5748		
^{163}Dy	162.7543	1153.8684		[58]
e.-s. of 421 nm transition				
^{161}Dy	-86.90	1747.4	1635	
^{162}Dy			913.2	
^{163}Dy	121.62	1844.9	616.3	[59]
e.-s. of 626 nm transition				
^{161}Dy	-187	-317	1727	
^{162}Dy			962	
^{163}Dy	261.7	-334	654	[60]
e.-s. of 684 nm transition				
^{161}Dy	-108.84	2251	-2099	
^{162}Dy			-1091	
^{163}Dy	152.56	2357	-823	[61]
e.-s. of 741 nm transition				
^{161}Dy	-102.09	3883	-2320	
^{162}Dy			-1214	
^{163}Dy	142.91	4105	-915	[62]

Tab. 2.2, Hyperfine A and B coefficients for the ground-state (g.-s.) and for the excited-states (e.-s.) of the 421 nm, 626 nm, 684 nm, 741 nm transition, respectively. In addition, the relative frequency shifts ν_{is} with respect to the transition of the ^{164}Dy isotope are given.

and the needed excited-states the constants A, B are given in Table (2.2). In ^{163}Dy the maximal stretched state ($m_F = 21/2$) of the ground-state is the energetically highest level, in contrast to the ^{161}Dy which shows an inverted hyperfine structure, see Figure (2.1)(b).

2.1.3 Magnetic Moment

The atomic magnetic moment μ_m in the direction of an external magnetic field in the z-direction can be calculated by

$$\mu_m = m_j g_j \mu_B \ , \tag{2.3}$$

where m_j is the magnetic quantum number of the total electronic angular momentum. In Dy its large magnetic moment is mainly due to the large angular orbital momentum $\boldsymbol{L}$. The Landé factor g_j is calculated by following equation [63]

$$g_j = 1 + \frac{J(J+1) - L(L+1) + S(S+1)}{2J(J+1)} \ . \tag{2.4}$$

However, the value calculated by Eq. (2.4) has to be corrected due to the deviation from the pure LS-coupling, additional relativistic and also diamagnetic effects and a value of

$g_j = 1.2370$ is obtained [64]. Experimentally, a value of $g_j = 1.2415867(10)$ was measured [58]. Finally, the magnetic moment of the fully polarized state with $m_j = -8$ of bosonic Dy can be calculated using Eq. (2.3) to $\mu_m = -9.93239\,\mu_B$. For the fermions one has to replace in Eq. (2.3) m_j and g_j by m_F and g_F, accordingly and the Landé factor g_F can be calculated by [63]

$$g_F = g_j \frac{F(F+1) - I(I+1) + J(J+1)}{2F(F+1)} = 0.9459708\ , \tag{2.5}$$

and for the state $m_F = 21/2$ the magnetic moment yields $\mu_m = -9.93239\,\mu_B$.

2.2 Atomic Energy Spectrum

Due to the submerged-shell configuration there are many possibilities to excite the electrons to higher energy levels. Therefore, the atomic energy level structure is quite complex. Figure (2.1)(a) shows a small section of the complete level structure, presented in Figure (A.3). So far, 394 (346) levels with even (odd) parity have been observed [65, 66].

2.2.1 Useful Optical Transitions

As the energy level structure of the lanthanides is quite complex, which results in many possible decay channels, it is not obvious to find a suited optical transition for laser cooling. However, Er was the first lanthanide which could be cooled and trapped in a MOT[6] [67]. The first successful method to laser cool Dy atoms used the $J = 8 \rightarrow J' = 9$ broad transition at a wavelength of 421 nm, which has a transition rate of $\Gamma = 2\pi \cdot 32.2\,\mathrm{MHz}$ [68]. This transition was also used to slow the atoms in a Zeeman slower (ZS) and finally trap them in a MOT [69]. Due to the broad linewidth many photons can be scattered by the atoms, thus this transition is well suited for the operation of the ZS and to image the atoms. On the contrary the high Doppler temperature of $T_{\mathrm{Doppler}} = \hbar\Gamma/(2k_B) = 773\,\mu\mathrm{K}$ requires further cooling steps before the atoms can be efficiently loaded into an optical dipole trap (ODT) to finally perform forced evaporative cooling to degeneracy. One possibility is to use the 741 nm transition, which has a transition rate of $\Gamma = 2\pi \cdot 1.8\,\mathrm{kHz}$. For this transition the Doppler temperature is even below the recoil temperature of $T_{\mathrm{recoil}} = (\hbar k)^2/(mk_B) = 213\,\mathrm{nK}$. The capture velocity of a MOT operating at the 741 nm transition is $v_{\mathrm{capture}} = \Gamma\lambda/(2\pi) = 1.3\,\mathrm{mm/s}$ which is too low to capture the Zeeman slowed atoms. Hence, the atoms first have to be captured in a 421 nm MOT and cooled further in the 741 nm MOT [13]. An alternative solution avoiding the two stage MOT phase and the challenging laser stabilization below 1.8 kHz is to use the 626 nm closed transition, which has a convenient transition rate of $\Gamma = 2\pi \cdot 136\,\mathrm{kHz}$ [70]. This has the advantage

[6] Its large magnetic moment allows to magnetically confine the atoms in the trap region while the excited-states recycles via many meta-stable states to the ground-state.

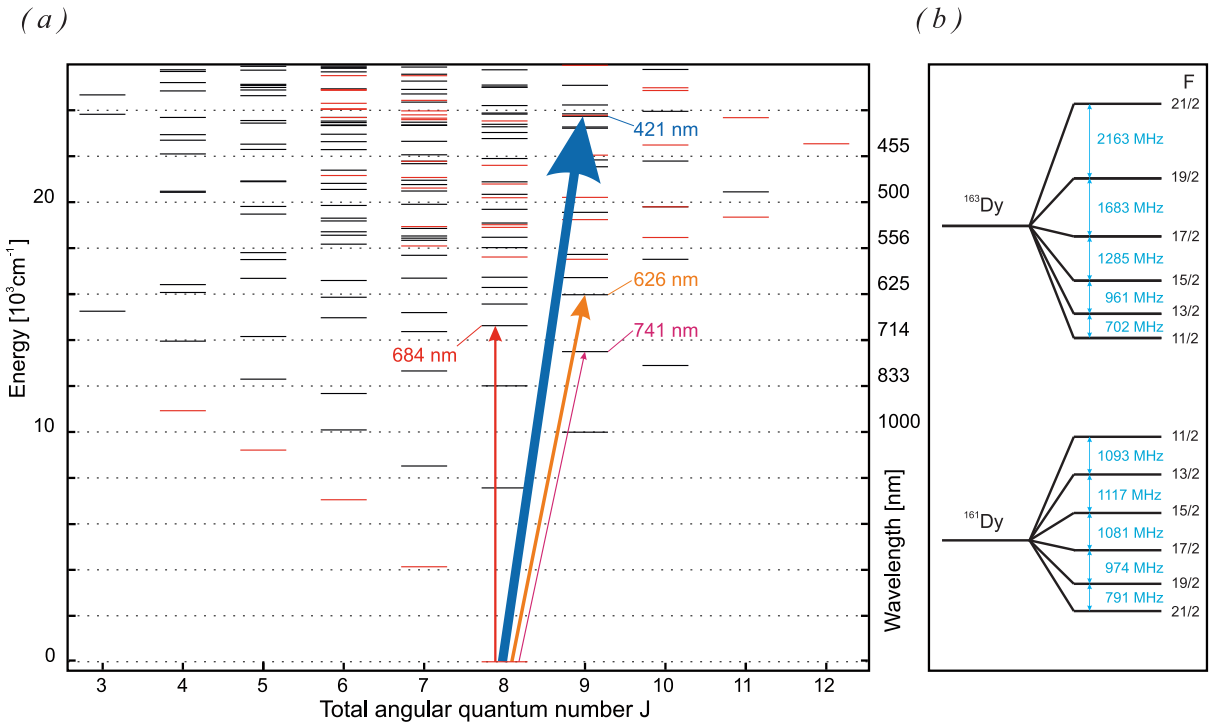

Fig. 2.1, Level structure of Dy: *(a)* Energy states with even (odd) parity are shown in black (red). Useful optically allowed transitions are indicated with arrows. The thickness of the arrows corresponds to their linewidths. The broad 421 nm transition is used to slow down the atoms in the ZS and for transverse cooling. We use the closed cycling 626 nm transition for our MOT. The even narrower 741 nm transition can also be used for a MOT. With the 684 nm transition the atoms can be pumped to different Zeeman sub-states, which would be necessary for demagnetization cooling. *(b)* shows the hyperfine splitting of the ground-state for the two fermionic isotopes calculated with Eq. (2.2).

that the MOT capture velocity allows to directly capture the atoms from the ZS but in addition the Doppler temperature $T_{\mathrm{Doppler}} = 3.3\,\mu\mathrm{K}$ is sufficiently low to transfer the atoms efficiently into the ODT. This scheme is successfully used in Er [71] and Yb [72] experiments. In section 5.2 we show the properties of our MOT operating at the 626 nm closed transition.

The 684 nm transition, which has a transition rate of $\Gamma = 2\pi \cdot 95\,\mathrm{kHz}$, is a $J = 8 \rightarrow J' = 8$ transition. This transition is applicable to optically pump the atoms in different Zeeman sub-states, which is necessary if we want to apply demagnetization cooling. With demagnetization cooling we could use a nearly lossless cooling procedure in the ODT, which would be much more efficient than using the standard forced evaporative cooling method [73]. To investigate the suitability of this transition for demagnetization cooling we performed a high-resolution laser spectroscopy on the 684 nm transition, see Figure (2.2)(c). The resulting data have been published in [61]. In Table (2.3) the properties of the before mentioned transitions are summarized.

	421	626	741	684
λ	421.291 nm	626.082 nm	740.963 nm	683.731 nm
Γ	2.02×10^8	0.85×10^6	11.2×10^3	0.60×10^6
τ	4.94 ns	1.17 µs	89.3 µs	1.68 µs
$\Delta\nu$	32.2 MHz	136 kHz	1.78 kHz	95 kHz
I_{sat}	$56.3\,\mathrm{mW/cm^2}$	$72\,\mu\mathrm{W/cm^2}$	$0.57\,\mu\mathrm{W/cm^2}$	$39\,\mu\mathrm{W/cm^2}$
T_{Doppler}	$773\,\mu$K	$3.3\,\mu$K	43 nK	$2.3\,\mu$K
v_{Doppler}	198 mm/s	12.9 mm/s	1.5 mm/s	10.7 mm/s
T_{recoil}	659 nK	298 nK	213 nK	250 nK
v_{recoil}	5.8 mm/s	3.9 mm/s	3.3 mm/s	3.6 mm/s
v_{capture}	13.6 m/s	85 mm/s	1.3 mm/s	65 mm/s
Refs.	[62]	[70]	[62]	[61]

Tab. 2.3, Relevant parameters of the important optical transitions in Dy including the vacuum wavelength λ, transition rate Γ, lifetime $\tau = 1/\Gamma$, natural linewidth $\Delta\nu = \Gamma/(2\pi)$, saturation intensity $I_{\mathrm{sat}} = 2\pi^2\hbar c\Gamma/(3\lambda^3)$, Doppler temperature $T_{\mathrm{Doppler}} = \hbar\Gamma/(2k_B)$, Doppler velocity $v_{\mathrm{Doppler}} = \sqrt{\hbar\Gamma/(2m)}$, recoil temperature $T_{\mathrm{recoil}} = (\hbar k)^2/(mk_B)$, recoil velocity $v_{\mathrm{recoil}} = 2\pi\hbar/(\lambda m)$ and capture velocity $v_{\mathrm{capture}} = \Gamma\lambda/(2\pi)$, where $\hbar$ is the reduced Planck constant, $k = 2\pi/\lambda$ the wavenumber and $m = 162.5$ a.u. the mean atomic mass of Dy.

The excited-state hyperfine splitting of the fermionic Dy isotopes can be calculated using Eq. (2.2) and the hyperfine constants A and B presented in Table (2.2). Due to the different atomic masses there is an additional isotope shift between the transition frequencies of the different Dy isotopes [74]. The total transition frequency shifts relative to the ^{164}Dy isotope is shown in Figure (2.2). For the $J = 8 \to J' = 9$ ($J = 8 \to J' = 8$) transitions the only observed transitions are the $m_F \to m'_F + 1$ ($m_F \to m'_F$), respectively.

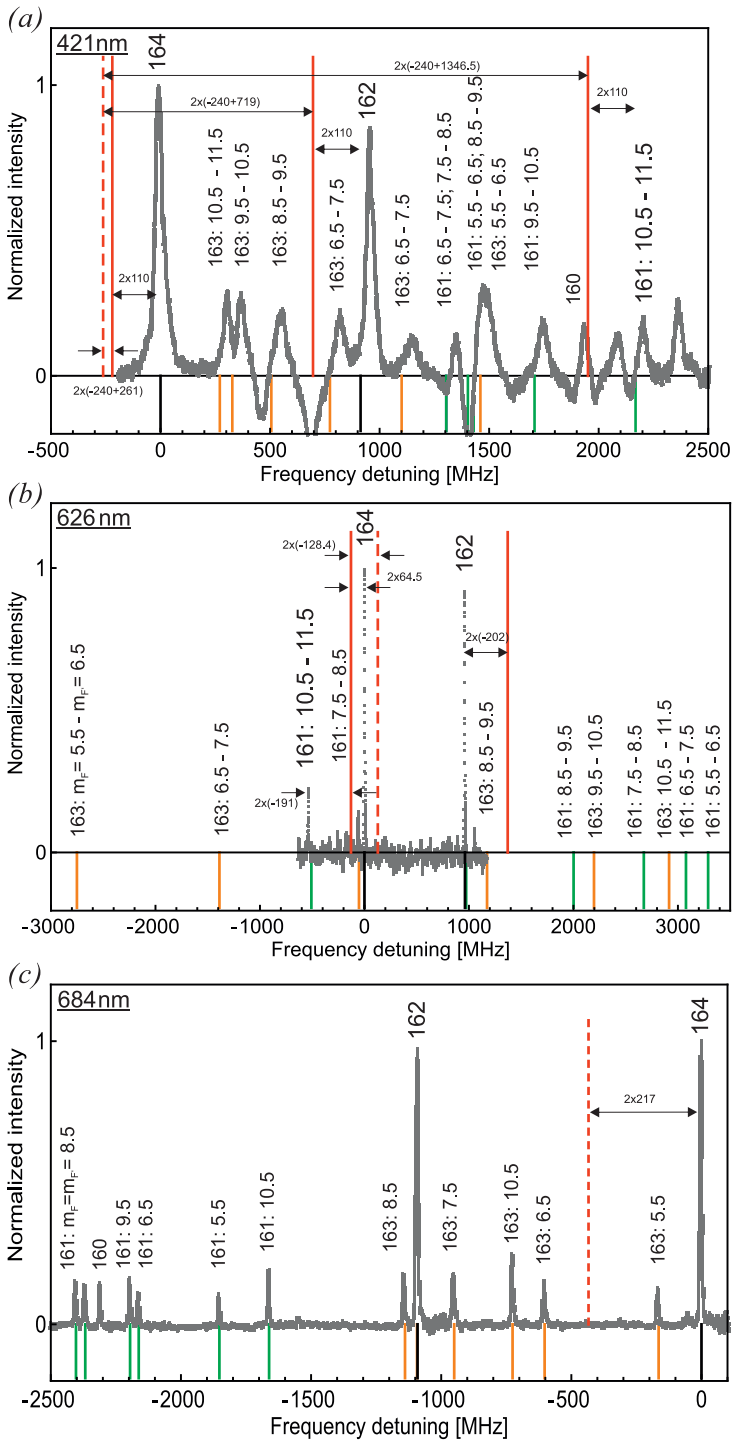

Fig. 2.2, Laser spectroscopy: Spectrum of the most abundant Dy isotopes for the 421 nm *(a)*, 626 nm *(b)* and 684 nm *(c)* transition. The gray data points are the results of the saturation absorption spectroscopy. The resonance positions match nicely with the calculated positions using Eq. (2.2) for the hyperfine shift of the ground- and excited-states. The positions of the ^{161}Dy (^{163}Dy) transitions are shown in green (orange) lines and the position of the bosonic isotopes are indicated in black. The small deviations from the measured positions are due to the non linear scan ramps of the lasers. The dashed red lines mark the position of the cavity resonances which are used to frequency stabilize the lasers. More details on the laser stabilization scheme is given in section 4.3.3.

3 Theory of Dipolar Quantum Gases

In this chapter we briefly introduce the theory of dipolar quantum gases. In the first section we start with the description of the scattering theory between two particles. We will show that the interaction potentials can be approximated by simpler pseudo-potentials. An important tool in cold atom physics are Feshbach resonances which allow to tune the short-range interaction externally and thereby modifying the properties of the degenerate quantum gas. In section 3.2 the theory of Feshbach resonances are discussed and in section 3.3 we give a brief introduction to the subject of quantum chaos as it is relevant for the analysis of the obtained Feshbach spectroscopy data. We conclude this chapter with a mean-field description of dipolar condensates, see section 3.4.

3.1 Few-body Scattering Theory

In the following we discuss the basic collision theory of two colliding Dy atoms. In section 3.1.1 we review the basic concepts of the scattering theory of two atoms interacting via a short-range isotropic interaction potential. For dipolar atoms also the DDI has to be taken into account. Additionally, due to the complex electronic structure of Dy the short-range interaction potential is anisotropic. When accounting for the more complicated interaction potential of dipolar Dy atoms we have to investigate if the basic descriptions for Dy collisions are still valid, this is done in section 3.1.2.

3.1.1 Scattering Theory for Isotropic Short-range Potentials

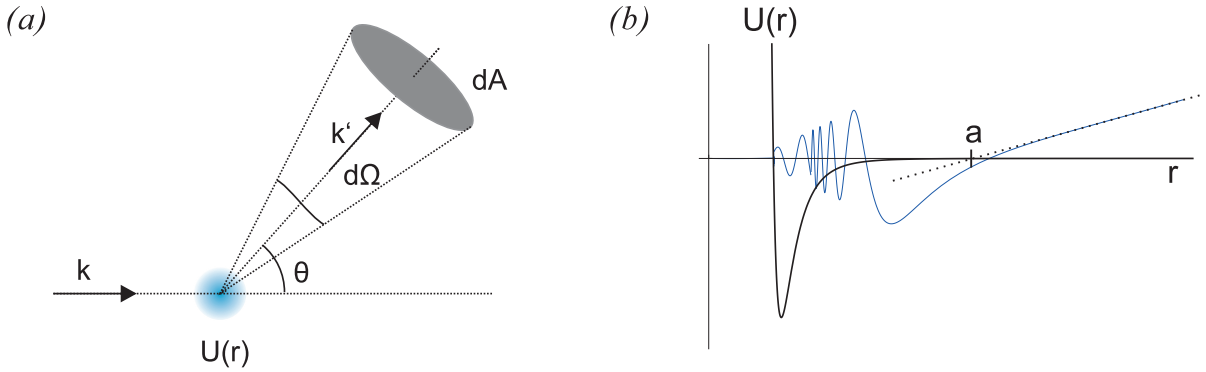

Fig. 3.1, Basic scattering problem: *(a)* An incoming particle, described by a plane wave with wave vector $\boldsymbol{k}$, is scattered on an interaction potential $U(\boldsymbol{r})$ and detected in the shaded area dA under the solid angle $d\Omega$. *(b)* The asymptomatic behavior of the two-body wave-function $\psi(r)$ determines the s-wave scattering length a. Panel *(b)* is taken from [75].

We consider here elastic collisions of two atoms with mass m and position vectors $\boldsymbol{r}_1$, $\boldsymbol{r}_2$ interacting via a finite-range potential $U(\boldsymbol{r}_1, \boldsymbol{r}_2)$. Detailed descriptions can be found in

Refs. [76–79]. For now we do not take the internal structure of the particles into account, thereby we also neglect inelastic scattering processes. For simplicity we transform to center-of-mass and relative coordinates resulting in the scattering of a single particle with the reduced mass $m_\mu = m/2$, relative velocity $\boldsymbol{v}$ and relative momentum $\boldsymbol{p} = \hbar\boldsymbol{k}$ at the potential $U(\boldsymbol{r}_1 - \boldsymbol{r}_2) = U(\boldsymbol{r})$, with $U(r \to \infty) = 0$. Figure (3.1)(a) shows a schematic drawing of two colliding atoms interacting via a short-range potential.

The stationary Schrödinger equation of the relative motion with eigenenergy $E = \hbar^2 k^2/(2m_\mu)$ yields the far-field ($r \to \infty$) solution

$$\psi_{\boldsymbol{k}}(\boldsymbol{r}) \propto \psi_0(\boldsymbol{r}) + \frac{e^{ikr}}{r} f_{\boldsymbol{k}}(\boldsymbol{r}) \,, \tag{3.1}$$

which represents an ingoing wave-function ψ_0 superimposed with a spherical wave modulated in amplitude and phase by the scattering amplitude $f_{\boldsymbol{k}}(\boldsymbol{r})$. The scattering amplitude can be calculated using the first Born approximation [79]

$$f_{\boldsymbol{k}}(\boldsymbol{r}) = -\frac{m_\mu}{2\pi\hbar^2} \int d^3r' \, \mathrm{e}^{-i\boldsymbol{k}'\,\boldsymbol{r}'} \, U(\boldsymbol{r}') \, \psi_{\boldsymbol{k}}(\boldsymbol{r}') \,. \tag{3.2}$$

However, calculating the scattering amplitude iteratively is extremely complicated as the potential $U(\boldsymbol{r})$ contains the complete atomic structure. Therefore, we first restrict ourselves to a finite-range central potential $U(\boldsymbol{r}) = U(r)$, which allows to express the solution of the Schrödinger equation in a superposition of partial waves. This simplifies Eq. (3.2) to

$$f_{\boldsymbol{k}}(\theta) = \frac{1}{2ik} \sum_l (2l+1) \left[(e^{2i\delta_l} - 1) P_l(\cos(\theta)) \right] \,, \tag{3.3}$$

where $l = 0, 1, 2, ...$ is the contribution of the $s, p, d, ...$ partial wave, δ_l the corresponding phase shifts and $P_l(\cos(\theta))$ the Legendre polynomials. To determine the phase shifts δ_l we can take advantage of the fact that in ultra-cold quantum gas experiments the atomic samples are very cold. For decreasing temperature the thermal de-Broglie wavelength λ_{dB} becomes larger and thereby the atoms resolve less details of the two-body interaction potential. The thermal de-Broglie wavelength is defined as

$$\lambda_{\mathrm{dB}} \stackrel{\mathrm{def}}{=} \sqrt{\frac{2\pi\hbar^2}{m k_B T}} \,, \tag{3.4}$$

where $\hbar$ is the reduced Planck constant, k_B the Boltzmann constant and T the temperature of the atomic sample. In addition, each particle wave with an orbital angular momentum $l > 0$ sees a centrifugal barrier $U_{cb} = \hbar^2 l(l+1)/(2mr_0^2)$ with r_0 the characteristic range of the two-body potential[7]. For temperatures typically below $U_{cb,l=2} \approx 1\,\mathrm{mK}$ (d-wave

[7]The characteristic range of a power-law potential $U(\boldsymbol{r}) = C_n/r^n$ can be estimated by using the Heisenberg's uncertainty principle $\Delta p \approx \hbar/\Delta x$ and equating the kinetic energy $(\Delta p)^2/(2m_\mu)$ with the molecular potential, resulting in $r_0 \approx (2m_\mu C_n/\hbar^2)^{1/(n-2)}$, with $\Delta x = r_0$. For most laser cooled elements $r_0 \sim 100\,\mathrm{a_0}$, with $a_0 = 0.05297\,\mathrm{nm}$ the Bohr radius [80].

barrier), which defines the beginning of the ultra-low temperature regime, only the s-wave ($l = 0$) can contribute to the scattering amplitude. Formally, for low energy collisions ($kr_0 \ll 1$), where the thermal de-Broglie wavelength is much larger than r_0, the phase shift for an interaction potential with $U(r) \sim 1/r^n$ varies with $\delta_l \sim k^{2l+1}$ if $l < (n-3)/2$ and $\delta_l \sim k^{n-2}$ otherwise [76, ch. 132]. Thus for the usual short-range potentials with $n = 6$ all scattering amplitudes with $l > 0$ are small compared with the scattering amplitude with $l = 0$. This allows us to neglect all higher partial[8] waves.

Usually to characterize a scattering process the total elastic cross-section is an important quantity. For indistinguishable atoms, one has to take into account, that the wave-function has to be completely symmetric (for boson) or completely antisymmetric (for fermions) with respect to particle exchange. This results in the total elastic cross-section for identical bosons (fermions)

$$\sigma_{\mathrm{tot}_{\substack{B \\ (F)}}} = \int d\Omega \, |f_{\boldsymbol{k}}(\theta) \pm f_{\boldsymbol{k}}(\pi - \theta)|^2 = \frac{8\pi}{k^2} \sum_{\substack{l \,\mathrm{even} \\ (l \,\mathrm{odd})}} (2l+1) \sin^2(\delta_l) \; . \tag{3.5}$$

In the case of ultra-low temperature collisions we have seen that only the s-wave contributes to the scattering and we get the well known isotropic and energy independent total s-wave scattering cross-section for identical bosons

$$\sigma_{\mathrm{tot}} = 8\pi a^2 \; , \tag{3.6}$$

where the *s-wave scattering length* is defined by

$$a \stackrel{\mathrm{def}}{=} \lim_{k \to 0} -\frac{\tan \delta_0(k)}{k} \; . \tag{3.7}$$

In contrast, the Pauli exclusions principle prohibits s-wave collisions between spin polarized fermions leading to a vanishing of the elastic scattering cross-section for low temperatures [81].

The scattered wave-function Eq. (3.1) becomes ($k = 0$) a simple spherically symmetric form

$$\psi(r) \propto 1 - \frac{a}{r} \; , \tag{3.8}$$

which has the same asymptotic behavior as a wave-function taking the full knowledge of the two-body interaction potential into account, see Figure (3.1)(b). Note that the scattered wave-function is spherically symmetric even if the two-body potential is anisotropic, which will be important in the next section.

Summarizing this paragraph, we found that for collisions in the ultra-cold regime the actual small-scale structure of the two-body interaction potential is irrelevant as it can be replaced by a much simpler model. It is usually called pseudo-potential having the

[8] This is not valid for the DDI (n=3), where all partial waves contribute, see next section.

same effective interaction characterized by the s-wave scattering length a, which can be determined experimentally.

3.1.2 Two-Body Interactions between Dipolar Atoms

In the former section we reviewed the basic collision theory of two atoms interacting via a short-range interaction potential. In contrast to alkali atoms for dipolar atoms also the DDI has to be taken into account. As the repulsive part of the molecular potential is only important for very small distances $\boldsymbol{r}$, the main contributions of the interaction potential between two dipolar atoms is the short-range dispersion interaction U_{disp} and the long-range dipole-dipole interaction U_{dd}

$$U_{\mathrm{int}}(\boldsymbol{r}) = U_{\mathrm{disp}}(\boldsymbol{r}) + U_{\mathrm{dd}}(\boldsymbol{r}) \ . \tag{3.9}$$

In the following we study the modifications of the former concepts of two-body collisions due to the more realistic molecular potential $U_{\mathrm{int}}(\boldsymbol{r})$ of two colliding dipolar atoms. In addition, we introduce the concept of pseudo-potentials, which is necessary for studying the properties of a dipolar quantum gas in the mean-field description, see section 3.4.2.

Dispersion Interaction

The attractive short-range part of the molecular potential is caused by induced electric multipoles,

$$U_{disp}(\boldsymbol{r}) = -\frac{C_6}{r^6} - \frac{C_8}{r^8} - \frac{C_{10}}{r^{10}} - \dots \ , \tag{3.10}$$

where r is the distance between the atoms and C_6, C_8 and C_{10} are the dispersion coefficients. The first term in Eq. (3.10) is due to the induced dipole-dipole interaction and is known as the van-der-Walls (vdW) interaction. The other terms represent higher-order contributions. Usually only the first term is used to approximate the full dispersion interaction.

As most laser-cooled atoms have a symmetric electronic distribution of their ground-state configuration also the vdW potential is usually spherically symmetric. The C_6 coefficients can be calculated from spectroscopic data using the Born-Oppenheimer (BO) approximation[9]. The resulting electronic interaction potentials are known as BO potentials. In the case of lanthanide atoms, the calculation of the BO potentials is more difficult, as the electronic ground-state configuration has an unfilled inner $4f$-shell shielded by a closed $6s$-shell. Nevertheless, the group of S. Kotochigova pioneered in calculating the BO potentials for Dy and Er [82]. In the ground-state of a lanthanide atom the electron spin $\boldsymbol{S}$ is coupled to the electron orbital angular momentum $\boldsymbol{L}$, forming a total angular momentum $\boldsymbol{j} = \boldsymbol{S} + \boldsymbol{L}$. The collision state of two colliding atoms is defined by the total angular momentum $\boldsymbol{J} = \boldsymbol{j}_1 + \boldsymbol{j}_2$ and its quantum number $\Omega = m_1 + m_2$, which is the

[9]The electronic part of the wave-function is decoupled from the nuclear part.

projection along the internuclear axis. During the collision the quantum numbers m_1 and m_2 can be changed as long as $\Omega = m_1 + m_2 = m_1' + m_2'$ stays conserved. Each configuration of $\boldsymbol{j}_1$ relative to $\boldsymbol{j}_2$, illustrated in Figure (3.2), results in a separate BO potential which means that the $C_6(m_1, m_2, m_1', m_2')$ coefficients depend on the quantum numbers m_1, m_2, m_1', m_2'. For each Ω there exists $(\boldsymbol{J}+1) - \Omega$ equivalent BO potentials. For Dy ($\boldsymbol{j}_1 = \boldsymbol{j}_2 = 8$) there are 81 (72) gerade (ungerade) BO potentials. The dependence of C_6 on Ω is caused by the anisotropic coupling of the f-shell electrons of the two atoms. This results in an anisotropic vdW interaction which depends on the relative orientation

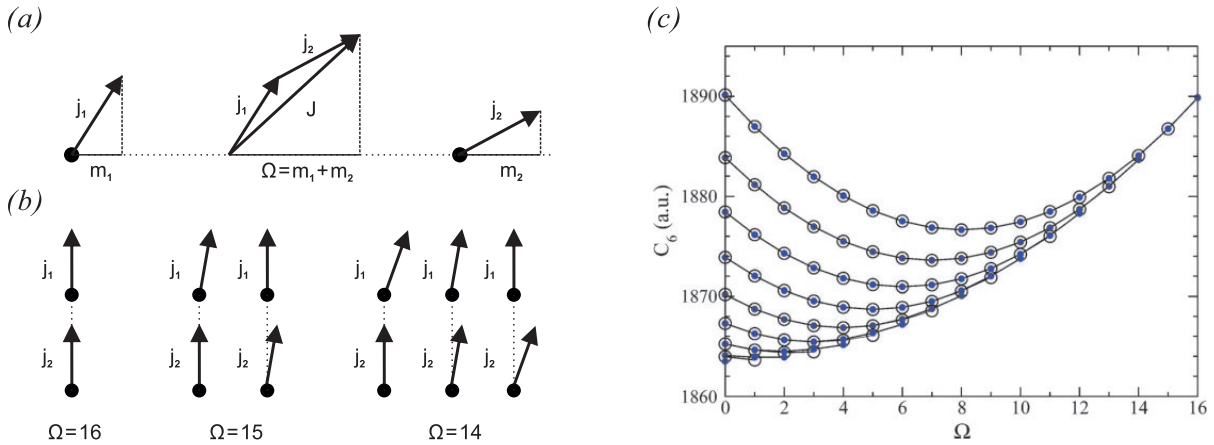

Fig. 3.2, Anisotropic dispersion interaction: *(a)* The atomic total angular momenta $\boldsymbol{j}_1$ and $\boldsymbol{j}_2$ form the total angular momentum $\boldsymbol{J} = \boldsymbol{j}_1 + \boldsymbol{j}_2$ of two colliding atoms, which processes around the internuclear axis. The quantum number Ω is the projection of $\boldsymbol{J}$ onto the internuclear axis. *(b)* Possible relative orientations of $\boldsymbol{j}_1$ and $\boldsymbol{j}_2$ results in different values of Ω. *(c)* Gerade (filled cicles) and ungerade (open circles) vdW C_6 coefficients for different Ω. Panel *(c)* is taken from [82].

of the atoms. The amount of anisotropy in the C_6 coefficients is defined by its spread[10], see Figure (3.2)(c).

For the two-body collision, without coupling between different internal states, the physics stays the same even with an anisotropic short-range potential. This is based on our findings in section 3.1.1 where we have seen that independently of the details of the short-range potential the scattered wave-function for ultra-cold collisions is spherically symmetric and characterized by the s-wave scattering length a. The anisotropy of the short-range interaction plays a major role in the context of anisotropy-induced Feshbach resonances, see section 3.2.2.

[10]The recently updated values for ^{164}Dy are $C_6 = 2003\, E_h a_0^6$ and $\Delta C_6 = 188\, E_h a_0^6$ [51]. Where $E_h = 4.360 \times 10^{-18}$ J is the Hartree energy.

A Contact Interaction Pseudo-potential

As it is possible to experimentally measure the s-wave scattering length a, it is not necessary to know the real shape of the short-range interaction potential and we can replace it by a spherically symmetric pseudo-potential, which is especially useful for the mean-field description of a BEC. One of the simplest pseudo-potentials describing the two-body short-range interaction is the so called zero-range contact interaction potential

$$V_{\text{contact}}(\boldsymbol{r}) \stackrel{\text{def}}{=} g\,\delta(\boldsymbol{r}) \tag{3.11a}$$

with the so called *contact coupling strength*

$$g \stackrel{\text{def}}{=} \frac{4\pi\hbar^2}{m}\,a \tag{3.11b}$$

for indistinguishable particles of mass m.

Dipolar Interactions

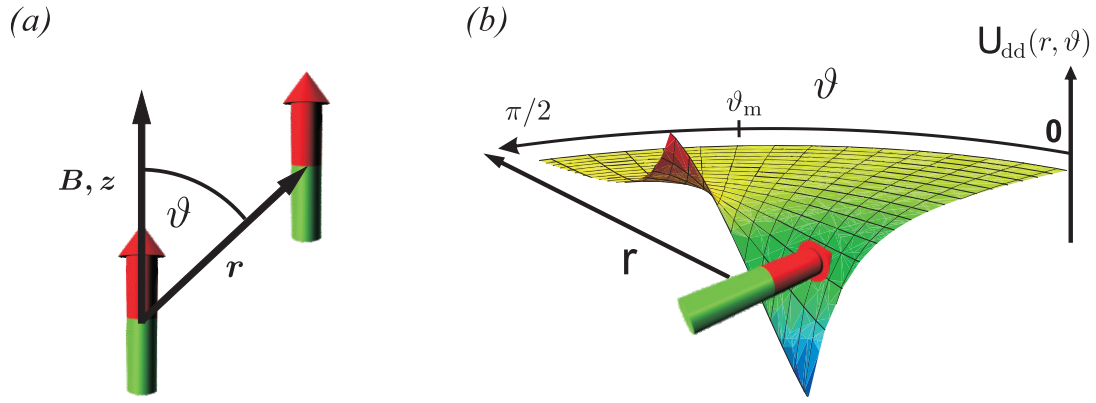

Fig. 3.3, Dipole-dipole interaction: *(a)* The DDI of two polarized dipoles depend on the relative orientation ϑ and on the relative distance $\boldsymbol{r}$. *(b)* The DDI can be attractive in the head-to-tail ($\vartheta < \vartheta^*$) or repulsive in side-by-side configuration ($\vartheta > \vartheta^*$). At the magic angle $\vartheta^* \approx 55°$ the interaction vanishes. The Figure is taken from [75].

In dipolar atoms the DDI adds an additional ingredient which leads to new fascinating physics, like the d-wave collapse of a dipolar BEC [32]. In the following we introduce the properties of the DDI. The long-range part of the interaction potential of two dipoles, aligned by an external field, can be described as

$$U_{dd}(r,\vartheta) = \frac{C_{dd}}{4\pi}\frac{1-3\cos^2\vartheta}{r^3}\,, \tag{3.12}$$

where $r = |\boldsymbol{r}|$ is the distance between the dipole and ϑ is the angle between $\boldsymbol{r}$ and the external field. Due to the $1/r^3$ dependency the DDI is a long-range interaction[11]. Additionally, the DDI is anisotropic as it depends on the angle ϑ. Thus, it can be either attractive or repulsive, see Figure (3.3). The coupling constant C_{dd} is either $C_{\mathrm{dd}} = \mu_0 \mu_m^2$ for magnetic[12] or $C_{\mathrm{dd}} = d^2/\epsilon_0$ for electric dipoles[13], where μ_m and d are the corresponding dipole moments. Magnetic moments of atoms range from $\mu_m = 0\,\mu_{\mathrm{B}}$ (e.g. Sr) to $\mu_m = 10\,\mu_{\mathrm{B}}$ (e.g. Dy). Whereas heteronuclear molecules can have induced dipole moments on the order of a few Debye[14]. Therefore, the dipolar coupling constant of polar molecules is much larger than for magnetic atoms. In this thesis we focus on atomic magnetic dipoles polarized by an external magnetic field.

In the presence of DDI the elastic collisions between two atoms change fundamentally. The scattering phase shift δ_l with $l > 0$ for potential with $1/r^n$ varies as $\delta_l \propto Ak^{2l+1} + Bk^{n-2}$, with A, B constants depending on the short-range details of the potential [76, 79]. The first term is due to the short-range potential, while the latter is due to the scattering outside of the centrifugal barrier [85]. For the DDI ($n = 3$) all partial waves have to be considered and the phase shifts do not vanish for low energies. Rather, in the limit of low energies they acquire finite values [86]. According to [85, 87] an universal scattering behavior can be observed for low enough collision energies $E < E_D$, where

$$E_D = \frac{C_{dd}}{4\pi D^3} = \frac{16\pi^2\hbar^6}{m_\mu^3 \mu_0^2 \mu_m^4} \tag{3.13a}$$

and D is the *dipolar length*

$$D \overset{\text{def}}{=} \frac{m_\mu C_{dd}}{4\pi\hbar^2} \,. \tag{3.13b}$$

For indistinguishable bosons the total elastic cross-section of two dipolar atoms is composed of[15]

$$\sigma_B = \frac{32\pi}{45} D^2 + 8\pi a^2 \,, \tag{3.14a}$$

[11] There exist different methods [83] trying to define whether a potential has short-range or long-range character, depending also on the dimensionality of the system. We simply define a long-range potential if the potential decreases slower than $1/r^n$, with $n \leq 3$.

[12] $\mu_0 \overset{\text{def}}{=} 4\pi \times 10^{-7}\,\mathrm{T\,m/A}$ is the vacuum permeability.

[13] $\epsilon_0 \overset{\text{def}}{=} 1/(\mu_0 c^2)$ is the permittivity, where c is the speed of light.

[14] The unit Debye is defined in SI units as $1\,\mathrm{D} = 1/\mathrm{c} \cdot 10^{-21}\,\mathrm{C/m}$, where c is the speed of light. The conversion factor between magnetic and electric dipole moment is $1\,\mu_{\mathrm{B}} \approx 9.274 \times 10^{-3}\,\mathrm{D}$ [84].

[15] This is not valid anymore if $D \gg a$ as in general the scattering length depends on the dipolar length, see next section.

whereas for indistinguishable fermions it only depends on the dipolar length

$$\sigma_F = \frac{32\pi}{15} D^2 \ . \tag{3.14b}$$

The non vanishing and temperature independent scattering cross-section allows to cool polarized dipolar fermions by forced evaporative cooling to degeneracy, which was first observed for fermionic Dy atoms in the group of B. Lev [22] and is used to cool down fermionic Er to temperatures of $T/T_F = 0.2$ with T_F the Fermi temperature in the group of F. Ferlaino [23]. In section 5.3.4 we present the first attempt to cool spin-polarized fermionic Dy atoms in our apparatus.

A Pseudo-potential for Dipolar Atoms

Due to the long-range character of the DDI it is not possible to describe the DDI by a pseudo contact interaction potential as it was done in section 3.1.2, but it is possible to define a dipole-dipole pseudo-potential [88, 89]. Defining the pseudo-potential as in Eq. (3.11a) would cause trouble if a wave-function does not vanish at the origin ($\psi(r = 0) \neq 0$), because there the pseudo-potential would diverge. Hence, we have to prevent this by adding an additional term proportional to $\mu_m^2 \delta(\boldsymbol{r})$ [90], which has the same characteristics as the pseudo contact interaction potential. This would not be necessary from a physical point of view as for small distances the strong Coulomb forces ensure that the wave-function has a zero amplitude at the origin. However, it is important for mathematical treatments. The full pseudo-potential for contact and dipolar interactions can be therefore written as

$$V_{\text{int}}(\boldsymbol{r}, \vartheta) = \frac{4\pi\hbar^2}{m} a(\mu_m)\delta(\boldsymbol{r}) + \frac{\mu_0 \mu_m^2}{4\pi} \frac{1 - 3\cos^2\vartheta}{r^3} \ , \tag{3.15}$$

which consists of a short-range part and a long-range part. Notice that $a(\mu_m)$ is now the effective scattering length, in general, it depends on the DDI. But the dependency is usually week and as the scattering length a is determined experimentally it automatically accounts for this additional small fraction [91, 92].

For further discussions of dipolar systems we now introduce some useful parameters. In analogy to the scattering length a we can define a *characteristic dipolar length*[16]

$$a_{\text{dd}} \overset{\text{def}}{=} \frac{\mu_0 \mu_m^2 m}{12\pi\hbar^2} \tag{3.16a}$$

[16]Note that the relation between the dipolar length and the characteristic dipolar length is $D = 3/2\, a_{dd}$.

and the *dipolar strength*

$$g_{\mathrm{dd}} \overset{\mathrm{def}}{=} \frac{4\pi\hbar^2}{m}\, a_{\mathrm{dd}} = \frac{\mu_0\mu_m^2}{3}\ . \tag{3.16b}$$

The characteristic dipolar length is defined such that a three-dimensional, homogeneous dipolar condensate becomes unstable when $a = a_{\mathrm{dd}}$, see section 3.4.4. Finally, we define the *relative dipolar strength*

$$\epsilon_{\mathrm{dd}} \overset{\mathrm{def}}{=} \frac{g_{\mathrm{dd}}}{g} = \frac{a_{\mathrm{dd}}}{a} = \frac{\mu_0\mu_m^2 m}{12\pi\hbar^2 a} \tag{3.16c}$$

for indistinguishable particles. To observe effects, which are dominated by the DDI, in degenerate gases both interactions have to be equally strong such that $\epsilon_{\mathrm{dd}} \gtrsim 1$. For comparison the relative dipolar strength of Cr has a value of $\epsilon_{\mathrm{dd}} \approx 0.16$ at its background scattering length of $a_{\mathrm{bg}} \approx 100\, a_0$, whereas Dy has a value of $\epsilon_{\mathrm{dd}} \approx 1.3$ at an assumed background scattering length of $a_{\mathrm{bg}} \approx 100\, a_0$. An important tool in ultra-cold quantum gas experiments are Feshbach resonances which can be used to tune the scattering length and thereby modifying the two-body interaction potential. Hence, we briefly discuss in the following section the theory of Feshbach resonances.

3.2 Theory of Feshbach Resonances in Ultra-cold Gases

Feshbach resonances were first theoretically studied independently by Feshbach, in the context of nuclear physics [93], and by Fano, who approached the problem on the background of atomic physics [94]. Nowadays, Feshbach resonances are a standard tool to control the interactions in ultra-cold quantum gas experiments. They are used to study many-body systems, such as ultra-cold fermions in the BEC to BCS crossover [95] or few-body physics like the Efimov effect [96]. Furthermore, Feshbach resonances can be used to create Feshbach molecules, which open the way to produce ultra-cold ground-state molecules [48, 97]. For dipolar atoms a Feshbach resonance can be used to alter the contact interaction and thereby modifying the relative dipolar strength. For example in Cr a Feshbach resonance was used to reduce the strength of the contact interactions thereby it was possible to go from a regime where the DDI plays only a perturbative effect [98] to a regime where strong dipolar effects can be observed [34].

3.2.1 Basic Concepts of Feshbach Resonances

In the previous sections we studied the ultra-cold collisions of two atoms. It was shown that despite the complicated molecular interaction potential the scattering process can be described by a simple s-wave collision, characterized only by the s-wave scattering length a. So far we have taken into account only one single molecular potential. But there exist

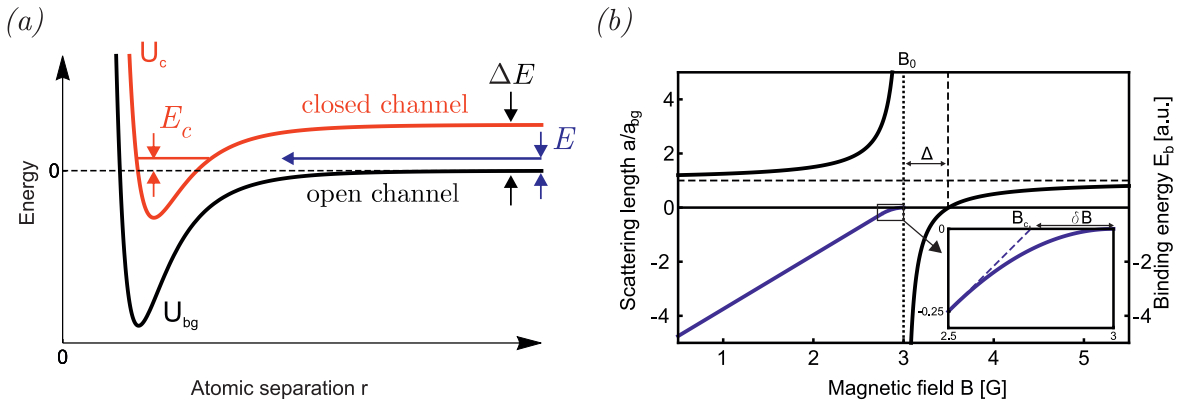

Fig. 3.4, Feshbach resonance: *(a)* Due to the coupling between different molecular states a Feshbach resonance occurs when the energy E of the incident particles matches with the bound-state energy E_c. The relative energy difference ΔE between the closed channel (red) and open channel (black) can be controlled by an external magnetic field. *(b)* Dependency of the scattering length (black) in the vicinity of a Feshbach resonance, with its position B_0 and width Δ. The molecular binding energy (blue) shows a linear dependency far away from the resonance and bends close to the pole due to the coupling.

more molecular potentials depending on the internal structure of the colliding particles. If there is a coupling between different molecular potentials, the scattering behavior is strongly modified. To understand the basic concepts of Feshbach resonances we assume two molecular interaction potential $U_{\mathrm{bg}}(r)$ and $U_c(r)$, where their molecular states differ at least in one quantum number, see Figure (3.4)(a). The background potential $U_{\mathrm{bg}}(r)$ connects asymptotically two free atoms and the energy E of the colliding atoms is close to its threshold. This potential is usually known as the open channel. The potential $U_c(r)$ is called closed channel, since E is less than its asymptotic value, but it supports at least one molecular bound-state near the threshold of the open channel. If the energy of the incident particles ($E \sim 0$) is close to the energy of the bound-sate E_c, the former weak coupling gets resonantly enhanced, leading to a strong mixing between the channels and a short-lived diatomic weakly-bound molecule is formed. This causes a divergence of the scattering length and a so called Feshbach resonance occurs [99]. The energy difference ΔE between the two channels can be controlled via a magnetic field[17] if the two channels have different magnetic moments [101]. In the following we only consider magnetically tuned Feshbach resonances in the limit of small kinetic energies ($E \to 0$). Due to the resonant coupling the s-wave scattering length a depends on the magnetic field B

$$a(B) = a_{bg}\left(1 - \frac{\Delta}{B - B_0}\right) , \tag{3.17}$$

[17] Also strong DC-electric fields can be used [100].

where a_{bg} is the background scattering length, B_0 the resonance position and Δ the resonance width [102]. The resonance width depends on the coupling strength and on the difference in magnetic moments, furthermore the resonance position $B_0 = B_c + \delta B$ is shifted due to the coupling. Figure (3.4)(b) shows the binding energy of the weakly-bound molecular state. Far away from the resonance position the energy $E_b = \delta\mu_m(B - B_c)$ depends linear on the magnetic field B with a slope given by the difference in magnetic moments $\delta\mu_m = \mu_{\mathrm{atoms}} - \mu_c$ of the closed and open channel[18]. The energy E_b would be zero at a magnetic field equal to B_c, but due to the coupling of the two channels the molecular state bends in the vicinity of the resonance. For large positive values of the scattering length the binding energy is given by the universal expression

$$E_b = \hbar^2/(2m_\mu a^2) \,, \tag{3.18}$$

with m_μ the reduced mass, see inset of Figure (3.4)(b). In this region, where the binding energy depends quadratically on the magnetic field, the state can be simply described by an effective molecular potential having a scattering length a. The state is called a halo state and its wave-function extends over a large size on the order of a, which is far beyond the outer classical turning point of the potential. Feshbach resonances can be classified by the dimensionless strength parameter [80]

$$s_{\mathrm{res}} = \frac{a_{\mathrm{bg}}\Delta\delta\mu}{\overline{a}\overline{E}} \,, \tag{3.19}$$

with $\overline{a} = 0.955978\, R_{\mathrm{vdW}}$ the mean scattering length and its corresponding energy scale $\overline{E} = 1.09422\, E_{\mathrm{vdW}}$[19]. Resonances with $s_{res} \gg 1$ are called entrance channel dominated resonance. Here, the threshold scattering and bound-states have the spin character of the entrance channel over a large fraction of the width. The bound-state energy follows the universal Eq. (3.18). Usually these resonances have a large width and are conventionally called *broad resonances*. Resonances with $s_{res} \ll 1$ are called closed channel dominated resonances. The universal regime lasts only over a small fraction of the resonance width. Typically these resonances have a width $\Delta < 1\,\mathrm{G}$ and are known as *narrow resonances*[20].

The coupling between the open channel and closed channel plays a fundamental role for the appearance of Feshbach resonances. In the following we want to study the coupling mechanism between different collision states. Formally, the elastic collision between two atoms in the presence of an external magnetic field B can be described by preparing the atoms at large distance in state q_1 and q_2, then let them collide (they interact with each other) and afterward they end up again in the same state $q_1\prime$,$q_2\prime$=q_1,q_2 at large distances. Hence, the scattering channels are defined by the internal states of the two atoms q_i, their

[18] $\mu_{\mathrm{atoms}} = 2\mu_m$ is the magnetic moment of the separated atoms.

[19] The characteristic length scale of a C_p/R^p long-range potential is $R_p = \left(\frac{2\mu C_p}{\hbar^2}\right)^{\frac{1}{p-2}}$ with its corresponding characteristic energy scale $E_p = \frac{\hbar^2}{2\mu R_p^2}$ [103].

[20] Exceptions exists, i.e. the resonance at 737 G in ^{7}Li has a $s_{\mathrm{res}} \lesssim 1$ but its width is $\Delta = 192\,\mathrm{G}$ [80].

relative orbital momentum l and its projections $m_F = m_{F1} + m_{F2}$ and m_l. The scattering process can be described by the following Hamiltonian

$$H = -\frac{\hbar^2}{2m_\mu}\frac{\mathrm{d}^2}{\mathrm{d}r^2} + \frac{\hbar^2 l(l+1)}{2m_\mu r^2} + \sum_{n=1}^{2}(U_n^{HF} + U_n^Z) + U_{\mathrm{int}}(\boldsymbol{r}) \;, \tag{3.20}$$

where U^{HF} is the hyperfine interaction, U^Z is the Zeeman interaction and $U_{\mathrm{int}} = U^{\mathrm{el}} + U^{\mathrm{SS}}$ the two-body interaction, which has been described in section 3.1.2. In the following we summarize the different interactions:

(i) **Hyperfine interaction**
The total angular momentum $\boldsymbol{j}$ is coupled to the nuclear spin $\boldsymbol{i}$. Thus, the hyperfine interaction is given by

$$U_n^{HF} = \frac{a_n^{\mathrm{HF}}}{\hbar^2}\boldsymbol{j}\cdot\boldsymbol{i} \;, \tag{3.21}$$

with a_n^{HF} the hyperfine constant.

(ii) **Zeeman interaction**
The Zeeman interaction is given by

$$U_n^Z = g_F\mu_B m_{Fn}B \;, \tag{3.22}$$

with g_F the Landé factor.

(iii) **Electronic interaction**
The electronic interaction, also called Coulomb interaction, consists of the exchange potential and the vdW potential. Usually it is isotropic and therefore it is diagonal in l and m_l, but it is off-diagonal in the atomic channel quantum number q_1, q_2. This means, that only molecular potentials with $\Delta l = 0$ and $\Delta m_l = 0$ can be coupled together. The coupling due to the electronic interaction is often responsible for the appearance of broad Feshbach resonances [80].

(iv) **Spin-spin interaction**
The spin-spin interaction includes the magnetic DDI as well as second-order spin-orbit interactions. The two contributions are both anisotropic and off-diagonal in q_1, q_2 and l, this means that the spin-spin interaction can also couple different partial waves with $\Delta l = 2$. Usually the spin-spin coupling is responsible for the existence of narrow resonances [80]. The coupling due to the spin-spin and second-order spin-orbit interactions induces the Feshbach resonances in Cr [104].

By analyzing possible coupling schemes one gets a qualitative understanding of the origin of Feshbach resonances for different elements. Note that the Hamiltonian (3.20) conserves the total magnetic quantum number $M_{tot} = m_{F1} + m_{F2} + m_l$ during collision and is invariant under parity operation, thus only even or odd partial waves l are coupled together.

In alkali atoms (e.g. Rb), which have a hyperfine structure, the electronic interaction is the dominant interaction leading to Feshbach resonances. In ^{52}Cr this is not the case as it has no hyperfine splitting. Since for the electronic interaction $\Delta m_l = 0$ has to be fulfilled, resulting in $\Delta m_s = 0$, the electronic interaction can only couple molecular sates with the same magnetic moment. As they shift in an external magnetic field equally, the electronic interaction could not be used to induce magnetic Feshbach resonances. Hence, Feshbach resonances in Cr are due to the spin-spin interaction as it is a factor 36 larger than for alkalis. The situation is more complex when we now consider lanthanide atoms, like Er and Dy, which have an even stronger DDI, but in addition the electronic interaction is anisotropic (not anymore diagonal in l), shown in section 3.1.2. Due to the large number of BO potentials, which can be coupled by the DDI and the anisotropic part of the vdW interaction to the open channel, the lanthanides have a dense spectrum of Feshbach resonances. The next section discusses the origin of Feshbach resonances in the lanthanides Er and Dy.

3.2.2 Anisotropy-induced Feshbach Resonances

So far we have studied the basic concepts of Feshbach resonances. We have seen that they occur due to the coupling between different molecular states caused by the electronic and spin-spin interactions. To explain the Feshbach resonances in alkali elements few molecular potentials have to be taken into account. This is in strong contrast to lanthanide atoms where many molecular potentials exist which can be coupled to the open channel due to the anisotropy of the DDI as well as of the electronic interaction. In the following we present an analysis of the occurrence of Er and Dy Feshbach resonances based on coupled-channels and multichannel bound-state calculations done by the group of S. Kotochigova. More details on the theoretical model can be found in [51, 105, 106].

The calculation assumes Dy atoms prepared in the lowest Zeeman sublevel with a total angular momentum $j_1 = j_2 = 8$ and its projection along the magnetic field $m_{\mathrm{j1}} = m_{\mathrm{j2}} = -8$. As the bosonic isotopes have no hyperfine structure the radial part of the Hamiltonian (Eq. (3.20)), describing the scattering process can be simplified and is given by

$$H = -\frac{\hbar^2}{2m_\mu}\frac{\mathrm{d}^2}{\mathrm{d}r^2} + \frac{\hbar^2 l(l+1)}{2m_\mu r^2} + g_j\mu_B(m_{\mathrm{j1}} + m_{\mathrm{j2}})B + U_{\mathrm{int}}(\boldsymbol{r}) \;, \tag{3.23}$$

assuming a homogenous magnetic field B along the z-direction. The first two terms describe the kinetic and rotation energy followed by the term of the Zeeman interaction energy. The interaction Potential $U_{\mathrm{int}}(\boldsymbol{r})$ is anisotropic and consists of the dispersion interaction, the magnetic dipole-dipole and the quadrupole-quadrupole interaction as introduced in section 3.2.1. For $B = 0$ the total angular momentum $\boldsymbol{J_{tot}} = \boldsymbol{j_1} + \boldsymbol{j_2} + \boldsymbol{l}$, consisting of the two atomic $\boldsymbol{j_1}, \boldsymbol{j_2}$ and the relative orbital angular momentum $\boldsymbol{l}$, is conserved. In contrast, for $B > 0$ only the projection $M_{\mathrm{tot}} = m_{\mathrm{j1}} + m_{\mathrm{j2}} + m_{\mathrm{l}}$ of $\boldsymbol{J_{tot}}$ along $\boldsymbol{B}$ is conserved. In addition, the Hamiltonian (Eq. (3.23)) is invariant under parity operation so that only

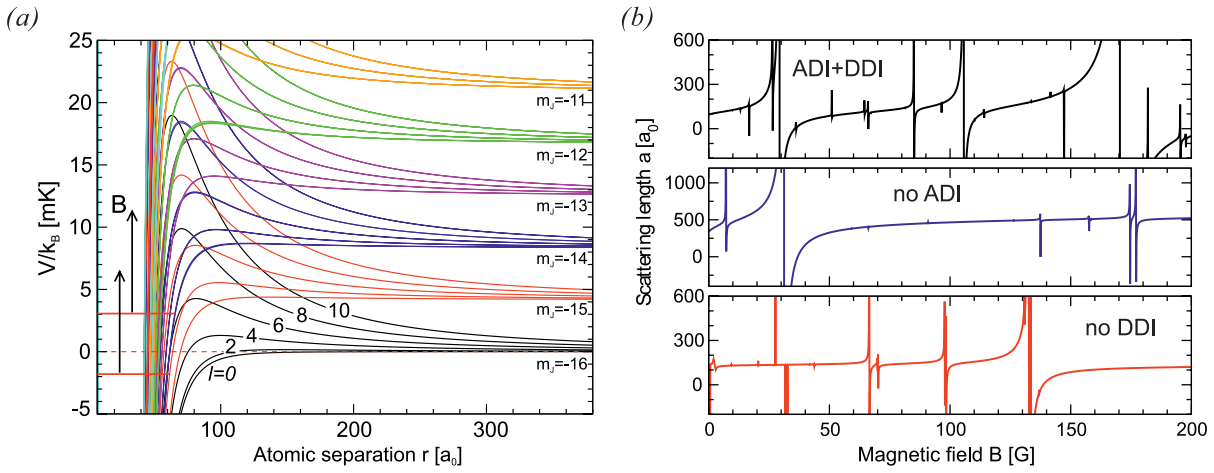

Fig. 3.5, Anisotropy-induced Feshbach resonances: *(a)* Potential energy curves for two colliding ^{164}Dy atoms for a magnetic field of $B = 50\,\mathrm{G}$ as a function of internuclear distance r. For simplicity only one of the 81 even molecular potentials ($\Omega = 16$) for each value of l is shown. The red horizontal lines indicate the bound-state energies of different molecular potentials, which can be shifted in energy due to the Zeeman effect. A Feshbach resonance can appear if the bound-state energy is equal to the energy of the incident particle. *(b)* Predicted scattering length as a function of magnetic field. In the top panel all anisotropic interactions are included, whereas in the middle the anisotropic dispersion (ADI) and in the lower panel the DDI is switched off. Here, only channels with $l \leq 10$ are included. To observe the same density as in the experiment channels up to $l > 40$ have to be included. Figures taken from [105] with slight modifications.

even or odd l states are coupled. For ultra-cold bosonic spin-polarized gases only even-l channels with $M_{\mathrm{tot}} = -16$ have to be considered. The coupling between the different states is due to the anisotropic interaction potential $U_{\mathrm{int}}(\boldsymbol{r})$. In Figure (3.5)(a) the long-range potential energy curves of interacting ^{164}Dy atoms are shown. Whereas for interatomic separation of $r > 200\,a_0$ the Zeeman interaction dominates the collisions dynamics, the potential curves of higher partial waves overlap for $r < 200\,a_0$ indicating the possibility of coupling between potentials with higher partial waves l [106].

The anisotropic DDI as well as the anisotropic part of the dispersion relation, characterized by the ΔC_6-coefficient, contribute to the appearance of the Feshbach resonances. The DDI can couple rotational states with $\Delta l = 2$ and the anisotropic dispersion interaction (ADI) with $\Delta l = 4$. In the calculation it is possible to switch-off different parts of the interaction. The results of the coupled-channels calculation including coupling to partial waves up to $l = 10$ show that the Feshbach resonances observed in Dy are induced by the anisotropy of the interaction potential [105]. Figure (3.5)(b) shows the dependence of the resonance distribution on the DDI and on the ADI by switching on and off the two parts independently. Note that the resonance density observed in the experiment, see section 6.3.4, is much higher than the one shown in Figure (3.5)(b). In the calculations

the couplings of partial waves up to $l > 40$ have to be included to resemble the same density as observed in the experiment [51].

3.3 Quantum Chaos in Ultra-cold Collisions

Recently, a dense Feshbach spectrum has been observed for Er atoms in the group of F. Ferlaino in Innsbruck. They could show using statistical arguments that Er collisions show signatures of quantum chaos [107]. In a joint cooperation consisting of the theory group of S. Kotochigova, the group of F. Ferlaino and our group we could demonstrate that Dy shows similar chaotic behavior as Er. In addition, our theoretical and experimental studies have provided more insights on the origin of this chaotic behavior. In the following sections we first give a short introduction to quantum chaos (section 3.3.1) and random matrix theory (section 3.3.2). Whereas the presentation of the results of our joint effort is postponed to section 6.2.1 and section 6.2.2.

3.3.1 An Introduction to Quantum Chaos

The term chaos for deterministic dynamical systems is used in many different fields to describe irregular, unpredictable and apparently random behavior. A classical deterministic system is completely described by the differential equations of motion. The initial condition of position and momentum determines uniquely the motion of a particle for all times in the future as well as in the past. Although the motion is deterministic the solution of the differential equations can be extremely sensitive on the choice of the initial conditions, leading to an exponential deviation in time of former closely spaced trajectories. The Lyapunov exponent characterizes the rate of separation of infinitesimally close trajectories in phase space. For regular motion the Lyapunov exponent vanishes. Hence, the Lyapunov exponent can be used to distinguish between the regular motion of an integrable system and the chaotic motion of non-integrable systems [108].

Due to Bohr's correspondence principle the quantum and the classical behavior should coincide for macroscopic systems. In quantum systems the Lyapunov exponent cannot be used as the notion of a phase-space trajectory looses its meaning. This is due to the fact that the initial conditions can be only defined within the limit of the uncertainty relation. For bound quantum systems neither the wave-function nor any observable quantity show the extreme sensitivity to initial conditions that defines classical chaos [109]. Therefore, it is challenging to define quantum chaos as a property of a quantum system which is related to the description of chaos in the classical meaning. Note that often the term quantum chaos is referred to the study and description of the properties of quantum systems for which the corresponding classical system is chaotic.

A prominent example is the hydrogen atom in a strong magnetic field. Due to the Zeeman interaction, the atomic energy levels split up with increasing magnetic fields.

Usually this splitting is well described by quantum perturbation theory. However, in large magnetic fields, where the magnetic forces on the electron become comparable to the Coulomb interaction, perturbation theory breaks down and the energy level distribution shows a quantitative difference to the low field region. The required magnetic field for ground-state atoms to see a transition between regular and irregular behavior is very large ($\approx 10^8\,\mathrm{G}$). But due to the $1/n^3$ dependency of the Coulomb interaction, magnetic fields of approximately $6 \times 10^4\,\mathrm{G}$, which can be realized in laboratories, are sufficient for highly excited atoms with principle quantum numbers of $n = 30 - 40$. On the other hand, this system can be also analyzed classically. In the same magnetic field range the corresponding classical system changes its behavior from regular to chaotic [110, 111]. To get a quantitative measure to be able to distinguish between regular and irregular behavior of a quantum system a statistical analysis was used, which was introduced for the characterization of complex and irregular energy-level spectra of excited nuclei. These statistical analysis methods are based on random-matrix theory which will be introduced in the following section.

3.3.2 Basic concepts of Random-matrix Theory

Starting in the 1930s, experiments on neutron and proton scattering have shown many narrow resonances in their cross-sections [112, 113]. For this complex and strongly interacting system an exact theoretical description was not possible in the 1950s. To describe the statistical properties of the system, Wigner and Dyson developed a theory called random-matrix theory (RMT), where the resonance spectra are characterized by their fluctuation properties [114, 115].

RMT suggests to substitute the actual complex Hamiltonian by an ensemble of randomly generated Hamiltonians. The ensemble is defined by a certain probability distribution for their matrix elements, which depends on the symmetry of the underlying system. In case of a time-reversal system such as nuclei and neutral atoms, the Hamiltonians belong to the Gaussian-orthogonal ensemble (GOE). As RMT only provides insights in the global properties of the system it is a phenomenological theory like classical thermodynamics. Similar to classical thermodynamics it has been applied to many different complex systems: atomic physics [116], neural networks [117] and financial mathematics [118].

RMT provides measures to probe the statistical properties of the system by analyzing their eigenenergy spectra [119]. The spectral fluctuations are connected to the level correlations of the systems eigenstates. In the following we only discuss two of the most important statistical analysis methods of RMT. The first measure is the analysis of the nearest-neighbor spacing (NNS) distribution, which probes short-range correlations. The dimensionless quantity $s = \delta E/\overline{d}$ is defined, where δE is the spacing between any two adjacent energy levels and $\overline{d} = 1/\overline{\rho}$ the mean level spacing. The NNS distribution $P(s)$ of

non-interacting levels is given by a Poissonian distribution

$$P_{\mathrm{P}}(s) = \exp(-s). \tag{3.24}$$

For strongly-correlated levels, e.g. for energy eigenvalues of the GOE, the NNS distribution follows the so-called Wigner-Dyson distribution

$$P_{\mathrm{WD}}(s) = \frac{\pi}{2}\, s\, \exp(-\pi s^2/4). \tag{3.25}$$

Note that Eq. (3.25) is obtained for 2×2 matrices, however it is still a good approximation with errors at the percent level for larger matrices. Both distributions are normalized with $\int ds\, P(s) = 1$ and by definition have the same mean value of $\int ds\, sP(s) = 1$. To interpolate between the Poissonian and the Wigner-Dyson distribution an empirical function, called Brody distribution, was introduced and is defined by [120]

$$P_{\mathrm{B}}(s, \eta) = A s^{\eta} \exp(-\alpha s^{\eta+1}) \,, \tag{3.26a}$$

$$A = (\eta + 1)\alpha \,, \tag{3.26b}$$

$$\alpha = \left[\Gamma\left(\frac{\eta+2}{\eta+1}\right)\right]^{\eta+1} \,, \tag{3.26c}$$

where Γ is the Gamma function and η is a single fitting parameter. Notice that η quantifies the tendency to the Poissonian ($\eta = 0$) or the Wigner-Dyson ($\eta = 1$) distributions but not the degree of correlation.

The analysis of the fluctuations in the number of levels Σ^2 within an energy level interval ΔE is a further statistical measure. The number variance probes the long-range correlation of the spectrum. For uncorrelated levels the fluctuations would grow linearly with the interval $\Sigma^2_{\mathrm{P}} = \Delta E$ indicating large fluctuations around a mean value. In contrast, if the system is strongly correlated the fluctuations are suppressed. This suppression is often called spectral rigidity. For a GOE spectrum the number variance follows the dependency of $\Sigma^2_{\mathrm{WD}} = 2/\pi^2 \ln(\Delta E) + 0.442$ [115]. The two signatures, on the one hand the level repulsion and on the other hand the large spectral rigidity are central properties of systems with strong correlations.

The statistical analysis of the energy levels of the hydrogen atom in a strong magnetic field agrees with the prediction of RMT for GOE if the classical system is chaotic, see Figure (3.6). Also other quantum systems which have a chaotic classical analog, e.g. Stadium-Billiard or Sinai-Billiard, show the same correlation between RMT and classical chaotic behavior [121]. Nuclear physicist have even proposed in the so called Bohigas-Giannoni-Schmitt conjecture that statistical properties based on RMT, which indicates level fluctuations should be used to define quantum chaos in general [122]. So far the conjecture was not generally proven, but it is numerically well established. Ref. [119] even proposed to speak of quantum chaos (or of chaos) whenever in a system the spectral

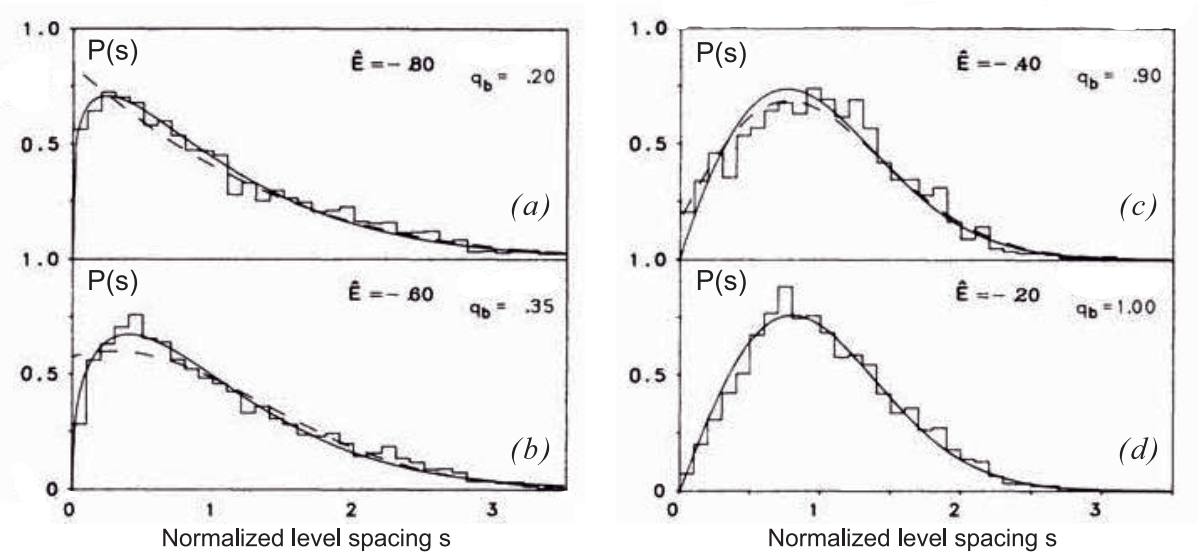

Fig. 3.6, Hydrogen atom in a strong magnetic field: NNS distribution $P(s)$ of energy levels calculated for different values of scaled energy $\widehat{E}$. The solid line is a fit to the Brody distribution with parameter q_b, which interpolates between the Poissonian ($q_b = 0$) and Wigner-Dyson ($q_b = 1$) distribution, see section 3.3.2. By decreasing the scaled energy $\widehat{E}$, which corresponds to an increase in magnetic field strength, one can see clearly the transition from a regular *(a)* to a chaotic system *(d)*. The figure is taken from [110] with slight modifications.

fluctuation measure agrees with the RMT prediction of a GOE. For an introduction to quantum chaos see Refs. [109, 111] and more details can be found in Refs. [108, 123, 124]. Note that also other quantum mechanical distinction criteria exist, which are based on energy eigenvectors or temporal evolution of suitable expectation values, see Refs. [109, 111]. So far we have described the two-body interactions between dipolar atoms. Now we are able to discuss many-body effects of dipolar quantum gases.

3.4 Dipolar Bose-Einstein Condensates

In this section we give a brief introduction to the physics of dipolar bosonic quantum gases. The theoretical description allows us to predict properties of a Dy BEC, which are important to consider during the designing phase of the apparatus. Furthermore, we provide the formalism to describe our experimental findings. For more details on dipolar many-body physics see the review articles [39, 86].

We start this section with a description of the phenomenon of Bose-Einstein condensation. In section 3.4.2 we use a mean-field approach to solve the many-body problem, resulting in the Gross-Pitaevskii equation (GPE) of a dipolar condensate. In general the GPE is not analytically solvable, but for special cases exact expressions can be obtained, see section

3.4.3. Finally, in section 3.4.4 we study the stability of a Dy condensate in different trap configurations using a variational calculation approach.

3.4.1 Bose-Einstein Condensation

Bose-Einstein condensation was theoretically predicted by Einstein in 1925 [125], based on the statistical arguments of Bose to describe the black-body radiation spectrum [126]. Bose-Einstein condensation is a purely statistical effect. In the last 35 years there has been huge progresses in cooling and trapping of neutral atoms, especially of alkali atoms. Finally in 1995 BECs of rubidium, sodium and lithium atoms were achieved[21] [1–4]. The BEC region of a dilute-atomic gas lays in the thermodynamically forbidden regime of the phase diagram. This means that the BEC in fact is metastable and can decay via molecular recombination to the ultimately stable solid-state condition. Therefore, low densities are necessary, where the two-body collision rate dominates the three-body loss rate, hence the gas will reach kinetic equilibrium before it decays to the absolute ground-state [135]. To get an intuitive picture of the formation of a BEC one uses the following brief description:

We start with a gas containing N particles at room temperature and low densities confined in an external potential with volume V, where the atoms can be described fully classically. Cooling down the sample increases the thermal de-Broglie wavelength, which is the coherence length of the wave packets. For temperature below a critical temperature T_c the de-Broglie wavelength is on the order of the mean inter-particle distance and overlapping wave packets are formed. To characterize the BEC phase transition one defines the phase space density

$$\mathcal{D} = n\lambda_{dB}^3 \,, \tag{3.27}$$

where $n = N/V$ is the particle density and λ_{dB} the de-Broglie wavelength. In a harmonic trap it is given by

$$\mathcal{D} = n\lambda_{dB}^3 = N\left(\frac{\hbar\bar{\omega}}{k_B T}\right)^3 \,, \tag{3.28}$$

where $\bar{\omega} = (\omega_x\omega_y\omega_z)^{1/3}$ is the geometric mean of the trap frequencies. For $\mathcal{D} > \zeta(3/2) \approx 2.6$ the ground-state[22] is populated macroscopically and the atoms loose their individual properties [79]. Using this criterion we can define the critical temperature of bosonic atoms in a harmonic trap to be

$$k_B T_c \stackrel{\text{def}}{=} \hbar\bar{\omega}\left(\frac{N_{\text{tot}}}{\zeta(3)}\right)^{1/3} \,, \tag{3.29}$$

[21] There exist not only BEC of neutral atoms, but also of photons [127], excitons [128], polaritons [129, 130] and molecules: K_2 [131], Li_2 [132, 133] and Na_2 [134].

[22] $\zeta(x)$ is the Riemann zeta function.

where N_{tot} is the sum of the number of condensed and thermal atoms. In the experiment we typically have $N_{\mathrm{tot}} = 10^5$ atoms with a trapping confinement with $\bar{\omega} = 2\pi \cdot 100\,\mathrm{Hz}$, resulting in a critical temperature of $T_c = 200\,\mathrm{nK}$.

3.4.2 Mean-Field Description of a Dipolar BEC

To solve the many-body problem of N interacting particles confined in an external potential V_{ext} we use a mean-field approach. Here, we only give a short review while a detailed description can be found in [79, 136, 137].

The full many-body Hamiltonian is given by

$$\begin{aligned}\hat{\mathrm{H}} = &\int \mathrm{d}^3 r\, \hat{\Psi}^\dagger(\boldsymbol{r}) \left[-\frac{\hbar^2}{2m}\boldsymbol{\nabla}^2 + V_{\mathrm{ext}}(\boldsymbol{r})\right] \hat{\Psi}(\boldsymbol{r}) \\ &+ \frac{1}{2}\int \mathrm{d}^3 r \int \mathrm{d}^3 r'\, \hat{\Psi}^\dagger(\boldsymbol{r})\hat{\Psi}^\dagger(\boldsymbol{r}')\, V_{\mathrm{int}}(\boldsymbol{r},\boldsymbol{r}')\, \hat{\Psi}(\boldsymbol{r})\hat{\Psi}(\boldsymbol{r}')\ ,\end{aligned} \tag{3.30}$$

where $V_{\mathrm{int}}(\boldsymbol{r},\boldsymbol{r}')$ is the two-body interaction potential and $\hat{\Psi}(\boldsymbol{r}), \hat{\Psi}^\dagger(\boldsymbol{r})$ are the bosonic field operators, creating or annihilating a particle at position $\boldsymbol{r}$, respectively. In the mean-field description a single particle interacts with a mean-field potential, which includes the interactions of all other particles. Therefore, the condensate's wave-function $\psi(\boldsymbol{r})$ can be defined as the expectation value of the field operator $\left\langle \hat{\Psi}(\boldsymbol{r}) \right\rangle = \psi(\boldsymbol{r})$, which is related to the experimentally accessible condensate density distribution $n(\boldsymbol{r}) = |\psi(\boldsymbol{r})|^2$. Using the Heisenberg equation we obtain the time-dependent GPE of a dipolar condensate

$$\begin{aligned}i\hbar\frac{\partial}{\partial t}\psi(\boldsymbol{r},t) = \Big[&-\frac{\hbar^2}{2m}\boldsymbol{\nabla}^2 + V_{\mathrm{ext}}(\boldsymbol{r}) \\ &+ g\,|\psi(\boldsymbol{r},t)|^2 + \int \mathrm{d}^3 r'\, V_{\mathrm{dd}}(\boldsymbol{r}-\boldsymbol{r}')\,|\psi(\boldsymbol{r}',t)|^2\Big]\psi(\boldsymbol{r},t)\ .\end{aligned} \tag{3.31}$$

We use the ansatz $\psi(\boldsymbol{r},t) = \psi(\boldsymbol{r})\exp(-i\mu t/\hbar)$, where μ is the chemical potential, to separate the time dependence in order to obtain the stationary GPE

$$\mu\,\psi(\boldsymbol{r}) = \left[-\frac{\hbar^2}{2m}\boldsymbol{\nabla}^2 + V_{\mathrm{ext}}(\boldsymbol{r}) + \Phi_{\mathrm{contact}}(\boldsymbol{r}) + \Phi_{\mathrm{dip}}(\boldsymbol{r})\right]\psi(\boldsymbol{r})\ , \tag{3.32a}$$

with the mean-field potentials of the contact interaction

$$\Phi_{\mathrm{contact}}(\boldsymbol{r}) \stackrel{\mathrm{def}}{=} g\,|\psi(\boldsymbol{r})|^2 \tag{3.33a}$$

and dipolar interaction

$$\Phi_{\mathrm{dip}}(\boldsymbol{r}) \stackrel{\mathrm{def}}{=} \int \mathrm{d}^3 r'\, V_{\mathrm{dd}}(\boldsymbol{r}-\boldsymbol{r}')\,|\psi(\boldsymbol{r}')|^2\,. \tag{3.33b}$$

In the following we discuss the possible solutions of the GPE for different cases.

3.4.3 Solutions of the Gross-Pitaevskii Equation

Due to the non-locality of the kinetic term and the non-local, non linear dipolar interaction term the stationary GPE is only numerically solvable. But for special cases there exists approximations, which will be discussed in the following. In general, the atoms are trapped in harmonic potentials of the form

$$V_{\text{ext}}(\boldsymbol{r}) = \frac{m}{2}\left(\omega_x^2 x^2 + \omega_y^2 y^2 + \omega_z^2 z^2\right) , \tag{3.34}$$

depending on the trap frequencies ω_i $(i = x, y, z)$.

GPE for Non-interacting BEC

Neglecting the interaction terms the GPE becomes

$$\psi(\boldsymbol{r}) = \left[-\frac{\hbar^2}{2m}\boldsymbol{\nabla}^2 + \frac{m}{2}\left(\omega_x^2 x^2 + \omega_y^2 y^2 + \omega_z^2 z^2\right)\right]\psi(\boldsymbol{r})\,. \tag{3.35}$$

The solution of this equation is well known as it is the textbook problem of a three dimensional quantum-mechanical harmonic oscillator. Therefore, the ground-state of a non-interacting BEC is described by a Gaussian function

$$\psi(\boldsymbol{r}) = \sqrt{\frac{N}{\pi^{3/2} l_x l_y l_z}}\exp\left[-\frac{x^2}{2l_x^2} - \frac{y^2}{2l_y^2} - \frac{z^2}{2l_z^2}\right] , \tag{3.36}$$

with the widths $l_i = \sqrt{\hbar/(m\omega_i)}$ $(i = x, y, z)$. The characteristic size, the so-called harmonic oscillator length, of a non-interacting BEC can be defined as

$$a_{\text{ho}} \stackrel{\text{def}}{=} \sqrt{\frac{\hbar}{m\bar{\omega}}} , \tag{3.37}$$

where $\bar{\omega} = (\omega_x\omega_y\omega_z)^{1/3}$ is the geometric mean of the trap frequencies. For a non-interacting BEC in a trap with a mean trap frequency of $\bar{\omega} = 2\pi \cdot 100\,\text{Hz}$ the harmonic oscillator length is $a_{\text{ho}} \approx 0.8\,\mu\text{m} \approx 15000\,\text{a}_0$.

GPE for Contact-interacting BEC

In the case of a contact-interacting BEC the kinetic term in the GPE can be neglected if the condition $Na/a_{\text{ho}} \gg 1$ is fulfilled and we find a linear equation in the Thomas-Fermi

(TF) approximation [79]

$$\mu\,\psi(\boldsymbol{r}) = \left[V_{\text{ext}}(\boldsymbol{r}) + g\,|\psi(\boldsymbol{r})|^2\right]\psi(\boldsymbol{r})\;. \tag{3.38}$$

We finally obtain the well-known parabolic density distribution of a BEC with contact interactions

$$\begin{aligned} n_{\text{TF}}(\boldsymbol{r}) = |\psi(\boldsymbol{r})|^2 &= \frac{\mu - V_{\text{ext}}(\boldsymbol{r})}{g} \\ &= n_0 \;\cdot\; \max\left\{\left(1 - \frac{x^2}{R_x^2} - \frac{y^2}{R_y^2} - \frac{z^2}{R_z^2}\right), 0\right\}, \end{aligned} \tag{3.39a}$$

where $n_0 = 15N/(8\pi R_x R_y R_z)$ is the central density and

$$R_{x,y,z} = \sqrt{\frac{2\mu}{m\omega_{x,y,z}^2}} \tag{3.40}$$

the TF radii in the respective directions. Due to the normalization condition $N = \int \mathrm{d}\boldsymbol{r}\,|\psi(\boldsymbol{r})|^2$ the particle number and the chemical potential are related and we obtain the chemical potential

$$\mu = \frac{\hbar\bar{\omega}}{2}\left(\frac{15Na}{a_{\text{ho}}}\right)^{2/5}\;, \tag{3.41}$$

which is only large compared to the harmonic oscillator energy if $Na/a_{\text{ho}} \gg 1$. The latter condition defines the regime in which the TF approximation is valid and is in agreement with our earlier assumption. The TF radius of a contact interacting BEC with $N = 10000$ atom in a spherical symmetric trap with a mean trap frequency of $\bar{\omega} = 2\pi \cdot 100\,\text{Hz}$ is around $R = 3\,\mu\text{m}$. To image the BEC in trap the resolution of our imaging system has to be $\lesssim 1\,\mu\text{m}$, which requires a high-resolution microscope objective, see section 4.5.

TF Approximation for a Dipolar BEC

The non-local character of the DDI complicates the former situation. Nevertheless, Refs. [138, 139] showed that it is possible to calculate the density distribution of a dipolar BEC in the TF approximation. To simplify the problem we use cylindrical coordinates $\boldsymbol{r} = (\rho, z)$, where the cylindrical symmetry is along the polarization direction of the dipoles. In addition, we define the trap radio $\lambda \overset{\text{def}}{=} \omega_\rho/\omega_z$ and the cloud aspect ratio $\kappa \overset{\text{def}}{=} R_z/R_\rho$ with the radial (axial) trap frequencies $\omega_\rho\,(\omega_z)$ and TF radii $R_\rho\,(R_z)$, respectively. The dipolar mean-field potential reads

$$\Phi_{\text{dip}}^{(\text{TF})}(\boldsymbol{r}) = n_0 g_{\text{dd}}\left[\frac{\rho^2}{R_\rho^2} - \frac{2z^2}{R_z^2} - f_{\text{dip}}(\kappa)\left(1 - \frac{3}{2}\frac{\rho^2 - 2z^2}{R_\rho^2 - R_z^2}\right)\right], \tag{3.42a}$$

with the *dipolar anisotropic function* $f_{\mathrm{dip}}(\kappa)$ given by

$$f_{\mathrm{dip}}(\kappa) = \frac{1+2\kappa^2}{1-\kappa^2} - \frac{3\kappa^2 \operatorname{artanh}\left(\sqrt{1-\kappa^2}\right)}{(1-\kappa^2)^{3/2}} \,. \tag{3.42b}$$

The dipolar anisotropic function $f_{\mathrm{dip}}(\kappa)$ decreases monotonically and it asymptotically reaches $f(\kappa \to 0) = 1$, $f(\kappa \to \infty) = -2$ and vanishes for $\kappa = 1$. Remarkably, the density distribution of the dipolar BEC still has a parabolic distribution but the TF radii now depend on the contact interaction strength g_{dd} as well as on the relative dipolar strength ϵ_{dd}. But first the aspect ratio κ has to be calculated for a given trap ratio λ by solving the transcendental equation [139]

$$3\kappa\epsilon_{\mathrm{dd}}\left[\left(\frac{\lambda^2}{2}+1\right)\frac{f_{\mathrm{dip}}(\kappa)}{1-\kappa^2} - 1\right] + (\epsilon_{\mathrm{dd}}-1)\left(\kappa^2-\lambda^2\right) = 0 \tag{3.43a}$$

and finally one can determine the TF radii

$$R_\rho = \left[\frac{15gN\kappa}{4\pi m\omega_\rho^2}\left\{1+\epsilon_{\mathrm{dd}}\left(\frac{3}{2}\frac{\kappa^2 f_{\mathrm{dip}}(\kappa)}{1-\kappa^2}-1\right)\right\}\right]^{1/5} \tag{3.43b}$$

and the chemical potential

$$\mu = gn_0[1-\epsilon_{\mathrm{dd}} f_{\mathrm{dip}}(\kappa)] \,, \tag{3.43c}$$

with $R_z = R_\rho/\kappa$. To get a more intuitive picture how the DDI alters the properties of a BEC we assume a spherically symmetric contact-interacting BEC ($\kappa = 1$) and add some weak DDI ($\epsilon_{\mathrm{dd}} \ll 1$). In this case the dipolar mean-field potential has the simple form [39]

$$\Phi_{\mathrm{dip}}^{(\mathrm{TF})}(\boldsymbol{r}) = \epsilon_{\mathrm{dd}}\frac{m\omega^2}{5}\left(1-3\cos^2\vartheta\right)\begin{cases} r^2 & \text{if } r \le R \\ R^5/r^3 & \text{if } r > R \end{cases} . \tag{3.44}$$

Due to the fact that the dipolar mean-field potential Φ_{dip} has a minimum along the polarization axis and a maximum perpendicular to it a contact-interacting BEC with additional weak DDI is elongated along the magnetic field axis, which is known as the magnetostriction effect and has been observed with Cr condensates [31].

3.4.4 Stability of a Dipolar BEC

The stability criterion of a dipolar BEC was studied extensively within our group with Cr atoms, see Refs. [46, 75, 140, 141]. In the case of Cr, and also in the recently condensed dipolar atom Er, the DDI only plays a perturbative role and has to be enhanced using a Feshbach resonance to study strongly dipolar physics. That is different for Dy, due to the higher magnetic moment and higher mass, already at a background scattering

length of around $a \approx 100\,a_0$, resulting in a relative dipolar strength $\epsilon_{\mathrm{dd}} > 1$, the DDI affects strongly the properties of a Dy BEC. In this section we will discuss the stability diagram of a Dy condensate and we will see that it is only possible to condense Dy atoms in particular trap configurations, which is not the case for Cr and Er.

The main instability mechanism for a dipolar condensate is due to long-wavelength phonon excitations. The excitation spectrum of a homogeneous dipolar BEC is given by [39]

$$E(q) = \hbar\omega(q) = \sqrt{\left(\frac{\hbar^2 q^2}{2m}\right)^2 + \frac{\hbar^2 q^2}{2m} 2n_0[g + g_{\mathrm{dd}}(3\cos^2\alpha - 1)]}\,, \tag{3.45}$$

with the quasi-momentum q and the angle α between the excitation and the polarization direction of the dipoles. In the limit of low momenta Eq. (3.45) shows a linear dispersion relation (sound waves) hence these low momenta excitations are called phonon excitations. Due to the DDI the energy spectrum is anisotropic and it depends on the alignment of the dipoles with respect to the traveling sound wave. The condensate is stable as long as the excitations frequencies are real and positive, but for imaginary excitations the BEC collapses. Therefore, the phonon instability occurs if $\epsilon_{\mathrm{dd}} = g_{\mathrm{dd}}/g > 1$, consequently if $a < a_{\mathrm{dd}}$ for excitations perpendicular to the alignment of the dipoles ($\alpha = \pi/2$). For excitations parallel to the alignment of the dipoles ($\alpha = 0$) the condensate is stable as long as $a > -2a_{\mathrm{dd}}$.

In the following we want to study the stability of a dipolar condensate confined in an external trap. A convenient method to study this is to evaluate the GPE energy functional, for simplicity we restrict ourselves to cylindrical symmetries. The total energy for a wave-function $\psi(\boldsymbol{r}) \stackrel{\mathrm{def}}{=} \langle \boldsymbol{r} | \psi \rangle$ is given by

$$\begin{aligned} E[\psi] &\stackrel{\mathrm{def}}{=} \langle\psi|\,\hat{\mathrm{H}}\,|\psi\rangle \\ &= \int \mathrm{d}^3 r \left[+\frac{\hbar^2}{2m} |\boldsymbol{\nabla}\psi(\boldsymbol{r})|^2 + V_{\mathrm{ext}}(\boldsymbol{r})\ |\psi(\boldsymbol{r})|^2 + \frac{\Phi_{\mathrm{contact}}(\boldsymbol{r}) + \Phi_{\mathrm{dip}}(\boldsymbol{r})}{2}\ |\psi(\boldsymbol{r})|^2 \right] . \end{aligned} \tag{3.46}$$

A natural choice is a Gaussian trial function [142]

$$\psi(\boldsymbol{r}) = \sqrt{\frac{N}{\pi^{3/2}\sigma_r^2\sigma_z a_{\mathrm{ho}}^3}} \exp\left[-\frac{1}{2a_{\mathrm{ho}}^2}\left(\frac{r^2}{\sigma_r^2} + \frac{z^2}{\sigma_z^2}\right)\right] \tag{3.47}$$

to evaluate the energy functional. Here, σ_r, σ_z are the radial and axial dimensionless widths. In a trap with a trap ratio of $\lambda = \omega_z/\omega_\rho$ and the external field pointing in z-direction we obtain the total energy per particle [140]

$$\begin{aligned} \widetilde{E}(\sigma_\rho, \sigma_z) &\stackrel{\mathrm{def}}{=} \frac{E}{N\hbar\bar{\omega}} \\ &= \frac{1}{4}\left(\frac{2}{\sigma_\rho^2} + \frac{1}{\sigma_z^2}\right) + \frac{1}{4\lambda^{2/3}}(2\sigma_\rho^2 + \lambda^2\sigma_z^2) + \frac{N a_{\mathrm{dd}}}{\sqrt{2\pi} a_{\mathrm{ho}}\sigma_\rho^2\sigma_z}\left(\frac{a}{a_{\mathrm{dd}}} - f(\kappa)\right)\,, \end{aligned} \tag{3.48}$$

which corresponds to the sum of the energies due to the quantum pressure, the external trapping potential and a combination of the contact and dipolar interaction.

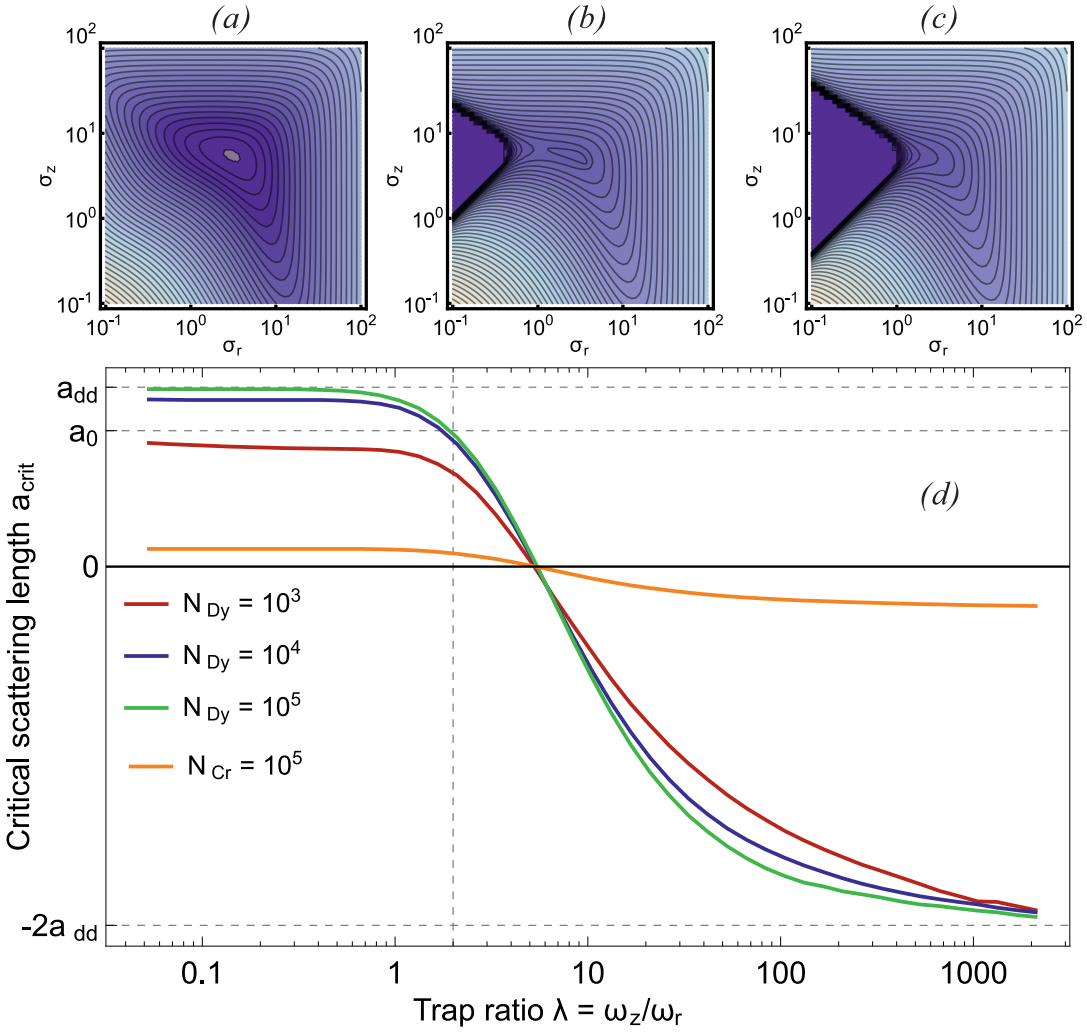

Fig. 3.7, Stability diagram of a Dy BEC: *(a)-(c)* Energy landscape $\widetilde{E}(\sigma_r, \sigma_z)$ with $a = (150, 125, 100)\, a_0$ for an isotropic trap ($\lambda = 1$), $\bar{\omega} = 2\pi \cdot 100\,\mathrm{Hz}$ and $N = 20000$ atoms, resulting in $a_{\mathrm{crit}} = 122\, a_0$. *(a)* Well above a_{crit} the energy landscape has a global minimum. *(b)* Close to the instability point the cloud is compressed radially and only a small barrier separates the local minimum from the global one. *(c)* Finally, below a_{crit} the BEC is collapsed. *(d)* The solid lines show the critical scattering length $a_{\mathrm{crit}}(\lambda)$ depending on the trap ratio λ with a mean trap frequency $\bar{\omega} = 2\pi \cdot 100\,\mathrm{Hz}$ obtained by a variational calculation. A Dy BEC is only stable in a trap with $\lambda > 2$ (vertical dashed line). For comparison the critical scatting length of a Cr BEC is shown (orange solid line). For Cr the situation is different as $a_{\mathrm{dd}} = 15\, a_0$ which is far below its background scattering length of $a_{\mathrm{bg}} \approx 100\, a_0$. Thus, a Cr BEC can be created in any trap configuration.

In Figure (3.7)(a)-(c) the energy landscapes $\widetilde{E}(\sigma_\rho, \sigma_z)$ for different scattering lengths a are shown. A stable condensate correspondents to a global minimum, which is found for a

scattering length above a_{dd}. If the scattering length is below a_{dd} but well above a critical value a_{crit} the energy has a clear local minimum, which corresponds to a metastable state at finite widths. By decreasing the scattering length further the barrier insulating the metastable state gets smaller. At the value $a = a_{\mathrm{crit}}$ the barrier vanishes completely and the BEC shrinks towards the point-like ground-state. Thereby the density increases dramatically and finally the BEC collapses.

Figure (3.7)(d) shows the critical scattering length a_{crit} for different trap ratios λ. The diagram can be separated into two regimes. For prolate traps ($\lambda < 1$) the DDI destabilizes the condensate, because the dipoles mainly attract each other, lowering the total energy of the system and a sufficient strong contact interaction is needed to stabilize the condensate. In contrast, for oblate traps ($\lambda > 1$) the DDI stabilizes the condensate due to the repulsion of the dipoles. In this regime it is possible to create a stable purely dipolar condensate ($a = 0$) or even a condensate with negative contact interactions $a < 0$ [46]. For Dy condensates the situation is different compared to other dipolar elements, like Cr, as the characteristic dipolar strength has a value of $a_{\mathrm{dd,Dy}} = 134\,a_0 \gg 15\,a_0 = a_{\mathrm{dd,Cr}}$. If we assume a background scattering length $a_{\mathrm{bg}} \approx 100 a_0$ for Dy, we find that a Dy condensate is only stable in a trap which has a trap ration of $\lambda > 2$. This constraint has to be taken into account during the cooling procedure of Dy atoms to degeneracy, see section 5.4.

Conclusion

In this chapter we have studied the scattering properties of Dy atoms. We have seen that despite the complicated electronic structure of Dy the short-range potential can be approximated by a pseudo-potential completely characterized by a single parameter, the s-wave scatting length a. Using a Feshbach resonance the s-wave scattering length can be tuned and thereby the balance between the contact interaction and DDI can be modified. Additionally, we have seen by using the mean-field approximation that a dipolar BEC shows also a bimodal density distribution like for a standard contact interacting alkali BEC. By analyzing the stability criterion of a Dy condensate we found that there are constraints on the trap configuration ($\lambda > 2$) for a stable BEC, which we have to take into account during the cooling process. Note that the validation of the mean-field model so far has been confirmed in many experiments with alkalies and also with Cr atoms. Due to the strong DDI and its complex short-range interaction it could be that the GPE is not suitable to describe the physics of Dy BECs in some situations[23]. Very recently we have observed an effect that cannot be explained by the GPE [143].

[23] See Ref. [75] for a summery of the validation criteria of the mean-field model.

4 Experimental Setup

In Stuttgart the experimental study of dipolar quantum gases started with the realization of the first Cr BEC in 2005 [10]. Due to a complex cooling scheme, the optical access was limited for further experimental tools, e.g for a high-resolution imaging system or to confine the atoms in tailored optical potentials. To overcome this limitation a new Cr apparatus including an attached science cell with high optical access was planned. During the planning phase Dy, the element with the largest magnetic moment, was condensed in the group of B. Lev mid of 2011 [13]. Additionally, beginning of 2012 a new member of the dipolar quantum gas family was added by the condensation of Er in the group of F. Ferlaino [14].

In Cr the dipolar interactions are weak and induce only perturbative effects. To enhance the dipolar effects the contact interaction has to be reduced by using a Feshbach resonance. However, inelastic three-body losses are also enhanced close to Feshbach resonances, which limited the lifetime of the condensate and thereby the time available for experiments. Due to its larger magnetic moment and its higher mass, Dy is in the strongly dipolar regime ($\epsilon_{\mathrm{dd}} > 1$) even without using a Feshbach resonance.

Having this advantage in mind and the possibility to study dipolar fermionic systems, at the end of 2011 the decision was taken to switch from Cr to Dy. In this section we introduce our experimental setup, which allows us to study dipolar bosonic as well as fermionic systems of Dy atoms.

Cr (Stuttgart)	Dy (Stanford)	Er (Innsbruck)
ZS (425nm, 5 MHz)	ZS (421nm, 32 MHz)	ZS (401nm, 27 MHz)
MOT (425nm, 5 MHz)	bMOT (421nm, 32 MHz)	MOT (583nm, 190 kHz)
	rMOT (741nm, 1.8 kHz)	
Magnetic Trap (MT)		
Doppler Cooling (425nm, 5 MHz)		
Evaporation in MT		
Transfer to ODT	Transfer to ODT	Transfer to ODT
Optical Pumping (427nm, 5 MHz)	RF Transfer	
Evaporative Cooling	Evaporative Cooling	Evaporative Cooling
BEC	BEC	BEC
[10], [75, ch. 3]	[13], [144, ch. 9]	[14], [84, ch. 7]

Tab. 4.1, Benchmark of different cooling and trapping methods of state of the art dipolar quantum gas experiments.

4.1 Experimental Requirements and Tools

When we started to think about the possibilities to bring Dy to degeneracy there were different approaches available to cool dipolar atoms presented in Table (4.1). First of all there was the already existing quite challenging approach of the Stanford group and the more convenient way which was used to create an Er condensate by the Innsbruck group. As we have worked for many years with Cr we wanted to use our elaborated knowledge of cooling and doing experiments with Cr combining the most suited methods of the different approaches. Based on this we summarize the following requirements to efficiently cool Dy atoms to degeneracy:

(i) **Effusion Cell**
For Dy a temperature of around 1200 °C is needed to have high atomic flux with an average velocity of around 500 m/s. This is also the case for Cr, hence the same high-temperature effusion cell can be used.

(ii) **Zeeman Slower**
To decelerate the atoms to reach the capture velocity of the MOT a ZS is needed. Using the strong 421 nm transition (natural transition rate of 32.2 MHz) ensures an efficient slowing of the atoms. Additionally, this wavelength is close to the 425 nm wavelength which was used in Cr allowing us to recycle the laser system for the Dy experiment.

(iii) **Magneto-optical Trap**
To cool and trap the atoms in a MOT we can use different approaches[24]. The possible methods are adapted from the approaches presented in Table (4.1):

1. **Cr approach**
Using the 421 nm transition we would be able to trap many atoms, but due to the broad linewidth the Doppler temperature is around 700 μK [145]. To reach adequate temperatures to load the ODT the atoms have to be cooled further in a magnetic trap (MT) using forced radio frequency (RF)-evaporative cooling. In addition, the narrow 626 nm or 741 nm transition could be used to Doppler cool the atoms in the MT [146]. The disadvantage of this method is that many steps are required, which would increase the cycle time and influence the stability of the system.

2. **Stanford approach**
Using a narrow transition ($\hbar\Gamma < E_{\text{recoil}}$) the atoms can be cooled to the recoil limit allowing an efficient direct loading in an ODT. A MOT operating at the 741 nm transition would be a good choice, but its low linewidth induces a too low capture velocity to load the MOT directly from the ZS. Thus, atoms have to be captured in a MOT working at the 421 nm transition and then further

[24]The experiment is planned in a way such that we can use any of the mentioned approaches.

cooled in the 741 nm MOT [13]. Advantageous is the availability of diode lasers to generate the 741 nm light, however stabilizing the laser below 1.8 kHz is challenging.

3. **Innsbruck approach**
A transition with an intermediate linewidth would allow to capture efficiently the atoms of the ZS by the MOT and the achieved low temperatures would be sufficient to load directly the ODT. In Dy the closed transition at 626 nm with a linewidth of 136 kHz leads to a Doppler temperature of around 3 μK.

(iv) **Optical dipole Trap**
As the DDI does not conserve the magnetic quantum number m_j, dipolar relaxation processes are allowed, which heat up the sample [147]. To prevent dipolar relaxations the atoms have to be prepared in the lowest magnetic sub-state, which is not magnetically trappable. Hence, it is not possible to reach BEC temperatures in a MT for dipolar atoms which makes the usage of an ODT necessary. The Er narrow-line MOT automatically prepares the atoms in the lowest Zeeman sub-state [14]. If the 626 nm MOT does not spin-polarize the atoms into the lowest magnetic sub-state an optical pumping transition at 684 nm is available. Note that the narrow-line 741 nm MOT in Dy pumps the atoms to the highest magnetic sub-state and the atoms have to be transferred to the lowest state using RF adiabatic rapid passage [13].

In addition to the required experimental methods mentioned above we also planned for further experimental tools which will allow us to do outstanding experiments on dipolar quantum gases:

(v) **Science Cell**
To have better optical access and magnetic field control a science cell has to be attached to the MOT chamber. The atoms have to be transported from the MOT chamber to the science cell by an optical tweezer. In addition, the science cell shall provide the possibility for a high-resolution imaging system.

(vi) **High-resolution Imaging + Electro-optical deflector System**
Taking time-of-light (TOF) absorption images are a standard method in quantum gas experiments to extract properties of the ultra-cold gas. However, an in-trap imaging provides the possibility to search directly for local density variations due to the DDI which could indicate new physical phenomena, e.g. the Rosensweig instability [148] or the supersolid phase. For this we have designed an imaging system which consists of a high-resolution objective with a resolution below 1 μm. This objective will also be used together with an electro-optical deflector system (EOD) to create time-averaged tailored potentials.

(viii) **Frequency Stabilization**
The stabilization scheme of all laser, especially the 421 nm and 626 nm laser system,

are designed in a way such that different isotopes can be addressed easily. In addition, it is possible to change the frequencies from the bosonic ^{164}Dy to the fermionic ^{161}Dy isotope in the experimental sequence to be able to study Bose-Fermi mixtures.

The experiment was planed to fulfill the upper mentioned requirements. As the vacuum chamber design was already in an advanced planning stage when we decided to switch from Cr to Dy we only adapted the crucial parts, e.g. the ZS. We also installed the cloverleaf coils for the MT as their fixtures were already integrated. We decided to follow the approach using the MOT operating at the 626 nm transition. In parallel we setup the 741 nm and 684 nm diode lasers to be able to adapt our method if necessary to create a cold sample mentioned above.

4.2 Experimental Apparatus

The Dy apparatus, shown in Figure (4.1), consist of three main parts: The oven chamber, the MOT chamber and the science cell, which can be separated by vacuum valves to pump them individually. The oven chamber (high vacuum section, $p_{\mathrm{Oven}} \propto 10^{-9}$ mbar) is connected by the ZS with the MOT chamber (ultra-high vacuum section (UHV), $p_{\mathrm{MOT}} < 10^{-11}$ mbar). The ZS tube serves as a differential pumping stage and bridges the two pressure regimes. The low pressures in the MOT chamber and in the science cell is required to reduce the collisions between Dy atoms and the background gas. In the following sections we discuss the important technical parts of the setup.

Oven Chamber

The oven chamber can be separated from the UHV section by a pneumatic valve[25]. Thus after refilling Dy only the oven chamber has to be pumped[26]. To heat up the Dy granulate[27] to 1250°C we use a high temperature effusion cell[28]. We fill 15 g of Dy granulate in a molybdenum crucible[29]. To transversely cool the atomic beam the oven chamber provides an optical access from two orthogonal directions. In addition, a shutter can block the atomic beam. This is only necessary for experiments in the MOT chamber which require long lifetimes in the ODT.

[25] MDC Vacuum Products: E-GV-1500M-P-03.
[26] Ion getter pump: Agilent Technologies: VacIon Plus 75 (Diode).
[27] Supplier: HMW Hauner.
[28] Createc Fischer: HTC-40-10-2000-WK-SHM.
[29] We tried different materials for the crucible: ZrO_2, ZrO_2 (stabilized by Y_2O_3), ZrO_2 (stabilized by CaO), Y_2O_3 and finally Mo. Before we found out that molybdenum is a suitable material we used a tungsten crucible to hold the inner crucible to protect the effusion cell. Replacing it by a bigger molybdenum crucible allows to increase the operation time. 8 g of Dy allows to operate the system for around 3 months (Note, during this time we often measured day and night).

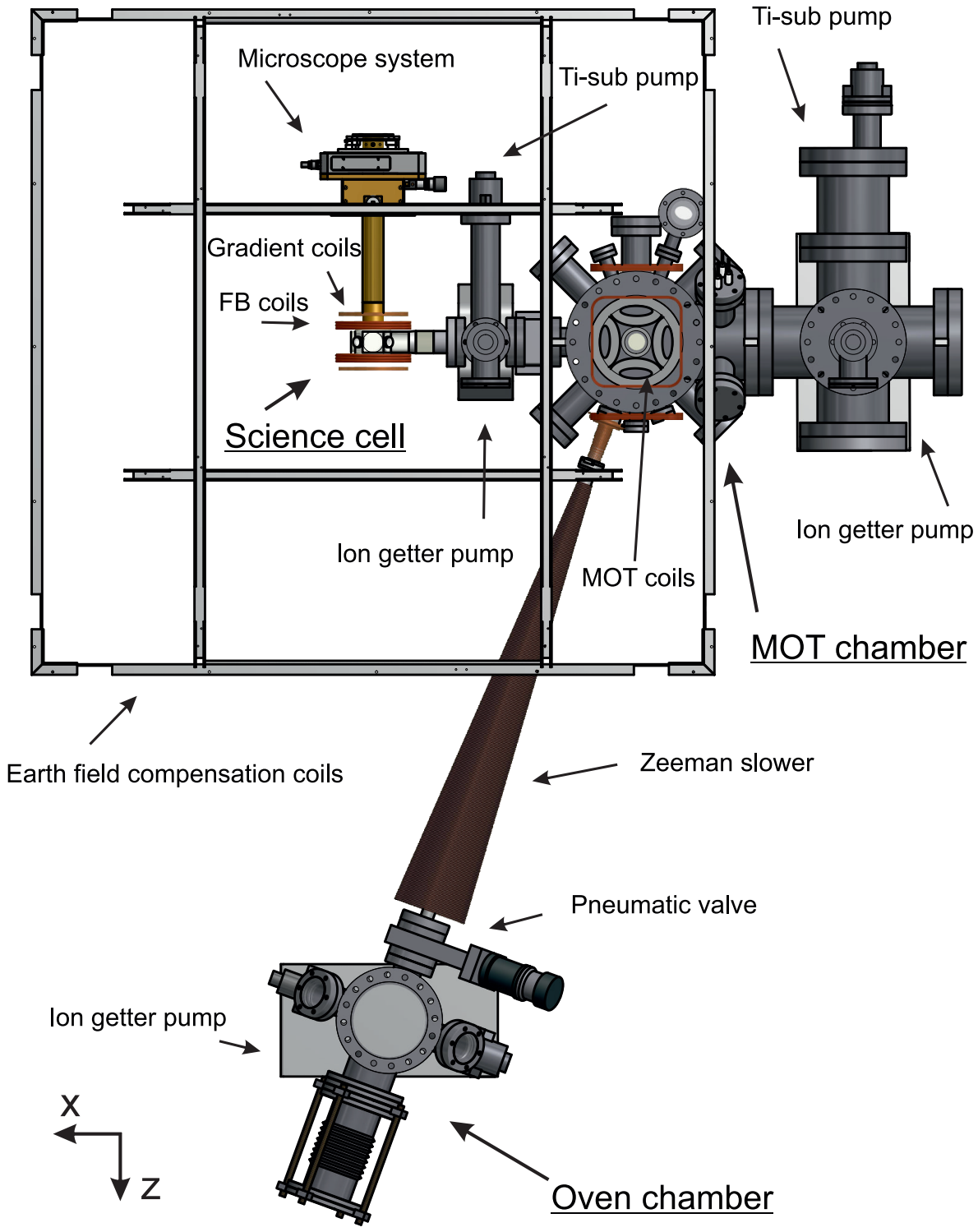

Fig. 4.1, Experimental Setup: The vacuum apparatus consists of three main parts: the oven chamber, the MOT chamber and the science cell.

MOT Chamber

The atoms are slowed down in the ZS and enter the trapping region of the MOT. The MOT chamber is pumped by a 75 l/s ion getter pump[30]. To reduce the pressure we have an additional titanium sublimation pump. The chamber design provides optical access for the MOT beams, the transport beam, a path to image[31] the atoms and one to supervise[32] the loading behavior of the MOT. The MOT chamber was designed to use clover leaf coils to create a MT and it provides the possibility to perform RF evaporative cooling.

Science Cell

To cool atoms to ultra-low temperatures, advanced cooling methods are required, which restrict the optical access for further experiments. To overcome this limitation a science cell is attached to the MOT chamber. It can be separated from the MOT chamber by a gate valve. An additional ion getter[33] and Ti-sublimation pump allow to independently adapt and pump the science cell to new experimental requirements. The atoms are transported by an optical tweezer from the MOT chamber to the science cell. Figure (4.2)(a) shows a schematic drawing of the science cell.

The octagonal glass cell combines both requirements of high optical access and the reduction of magnetic parts around the highly magnetic atoms[34]. It consists of a blown quartz glass frame[35] onto which high quality windows[36] are bonded. This allows to use an anti-reflection coating on both sides of the window to avoid aberrations and stray light. The two large main windows (clear aperture of 38.1 mm) allow a large optical access for the high-resolution imaging of the atoms with a theoretical numerical aperture of $NA \approx 0.76$. The length of the cell as well as the dimensions of the three side windows (clear aperture of 25.4 mm) are given by the demands of the optical transport: at the position of the MOT the minimal beam waist of the transport beam should be approximately 35 μm and the maximal travel range of the transport translation stage is 400 mm. Four additional small side windows (clear aperture of 11.0 mm) allow for further optical access, e.g. usable for an optical lattice. Furthermore, the glass cell has to be suited for UHV and the glass-metal transition[37] has to be non-magnetic to ensure the possibility of transporting the atoms. See appendix A.2 for a technical drawing of the octagonal glass. More details on the design of the glass cell can be found in Ref. [149].

[30] Ion getter pump: Agilent Technologies: VacIon Plus 75 (Diode).
[31] PCO: pco.pixelfly.
[32] UniBrain: Fire-i 530b.
[33] Agilent Technologies: 8 l/s VacIon pump.
[34] Eddy currents limit the switch-off time of the magnetic fields, see Ref. [141].
[35] Precision Glassblowing (TechGlass).
[36] Gooch & Housego: surface roughness < 1 Å, flatness: $\lambda/20$.
[37] Only Pyrex glass and stainless steel (SS 316L) was used.

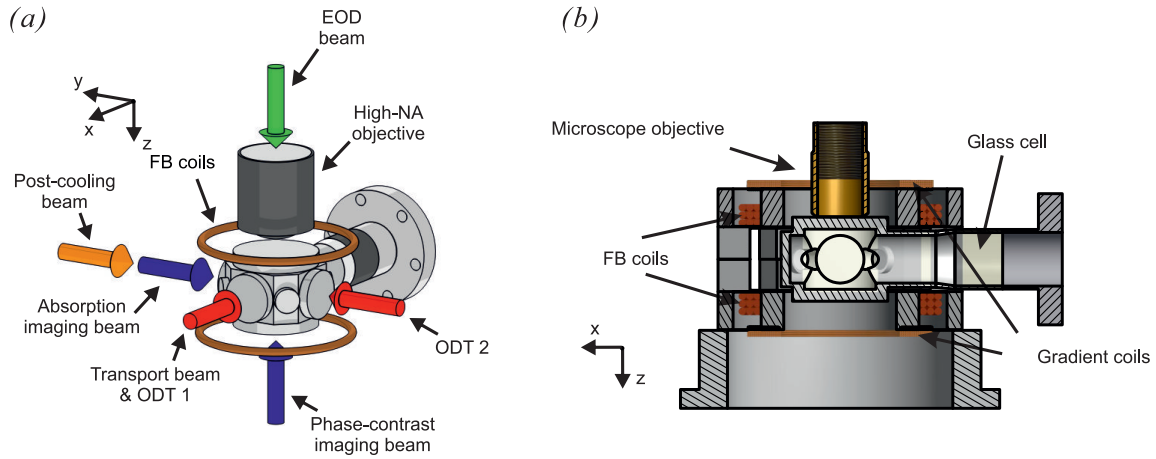

Fig. 4.2, Science Cell: *(a)* Schematic drawing of the science cell. An optical tweezer transports the atoms from the MOT chamber to the science cell, where they are transferred to a crossed ODT. The atoms can be imaged using the high-resolution objective with phase-contrast imaging or by standard absorption imaging. In addition, the combination of objective and EOD system allows to create time-averaged potentials. *(b)* Sectional view of the science cell. The Feshbach coils and gradient coils are mounted in a plastic holder. The objective has a working distance of 25 mm, thus the margin between the objective and the window surface is 2.63 mm.

4.3 Laser Systems

Several laser systems are necessary to create a degenerate Dy quantum gas. The 421 nm laser system is used to produce the light for the ZS, transverse cooling, absorption and phase contrast imaging. The 626 nm laser system is used for the MOT. It was not clear at the beginning that the MOT operating at the 626 nm transition would work. To be able to use the other cooling approaches (mentioned earlier) we also setup the 684 nm and 741 nm laser systems. As the 626 nm transition MOT works, these systems can be used for future experiments or more efficient cooling procedures, e.g. demagnetization cooling [73]. All our lasers, except the dipole trap lasers, are stabilized to reference cavities using the Pound-Drever-Hall (PDH) technique [150, 151] which allows us to switch between different isotopes easily. In Figure (2.2) we show the measured spectra for the most abundant isotopes together with the cavity resonances (red dashed lines) and the frequency difference between the cavity resonances and the atomic resonances are indicated. Frequency shifter can bridge the frequency gaps such that we can access the atomic transition with the locked laser. The laser systems are planned such that we can easily access the needed frequencies to cool and trap the ^{164}Dy, ^{162}Dy and ^{161}Dy ($m_F = 10.5 \rightarrow m_F\prime = 11.5$) isotopes. In the following we present the setup of the 421 nm, 626 nm and the ODT laser system.

4.3.1 Blue (421 nm) Laser System

To create the blue laser light at a wavelength of $\lambda = 421.291\,\text{nm}$ we use a multi-step process. First we optically pump a Ti:sapphire crystal inside a ring cavity[38] with 18 W of green light at a wavelength of $\lambda = 532\,\text{nm}$ generated by a diode-pumped solid state (DPSS) laser[39]. We get around 4.5 W infrared light at a wavelength of $\lambda = 842.582\,\text{nm}$ at the output of the Ti:sapphire system, which is further frequency doubled using a lithium triborate (LBO) crystal inside a home-build monolithic ring cavity[40]. Finally, we obtain 1.5 W of blue laser light at the output of the doubling cavity, which is mainly used for the transverse cooling and for the absorption imaging. To have enough blue laser light for the ZS we use a nearly identical second system[41]. The only difference between the master and the slave system is that we use an optically pumped semiconductor laser (OPSL), providing 20 W of $\lambda = 532\,\text{nm}$ light[42] to pump the Ti:sapphire crystal and we obtain 6.5 W of infrared light, resulting in 2 W of blue laser light usable for the ZS.

The 421 nm master system is stabilized to a passively stable ultra-low expansion cavity (ULE) with an electronic feedback to the external cavity of the Ti:sapphire system. To be able to shift the frequency of the laser over a large range it is stabilized on a moveable sideband created by a fiber-EOM[43]. The fiber-EOM is modulated with two frequencies. The first frequency[44] $\nu_{\text{PDH}} = 20\,\text{MHz}$ is used to obtained fixed sidebands needed for the PDH scheme. Together with the second variable frequency[45] ν_{sweep} three error signals are created one at the position of the carrier frequency and two are shifted through $\pm\nu_{\text{sweep}}$. Locking the laser to one of them allows to shift the laser frequency by ν_{sweep}. The shift of the locked laser is limited to $\nu_{\text{sweep}} = 60 - 700\,\text{MHz}$ by the free-spectral range of the ULE cavity of $\nu_{\text{FSR}} = 1.5\,\text{GHz}$ (TM_{00} mode), else counter propagating sidebands would interfere and unlock the laser. To be able to study mixtures of the bosonic ^{164}Dy and fermionic ^{161}Dy isotope we have to shift the frequency of the 421 nm light in the experimental sequence by 2168 MHz, therefore an additional cavity[46] (FPI), see Figure (4.5)(b), was setup which has a free-spectral range of $\nu_{\text{FSR}} = 8\,\text{GHz}$ (TM_{00} mode). As we currently only work with single species it is more convenient to lock the 421 nm master system to the ULE cavity. The needed frequencies[47] to address the different isotopes are shown in Figure (2.2)(a). The slave blue laser system is stabilized relative to the master

[38] Coherent: MBR 110.
[39] Coherent: Verdi V18.
[40] More detail to the master system can be found in Ref. [152] and to the slave system in Ref. [153]. The length of the cavity is actively stabilized using the Hänsch-Couillaud locking scheme [154].
[41] Note that Ref. [145] reported the need of 1 W blue laser light to operate the ZS.
[42] Coherent: Verdi G20.
[43] EOSPACE: PM-0K5-20-PFA-PFA-842 -S3mmFS.
[44] Toptica: PDD 110^F is used to provide the $\nu_{\text{PDH}} = 20\,\text{MHz}$ and to generate the PDH error signal.
[45] Windfreak Technologies: Synthesizer v2.0, based on ADF4350 ($137.5 - 4400\,\text{MHz}$)
[46] Toptica: FPI 100.
[47] Notice that the required frequencies in the blue have to be divided by two to calculate the needed shifts in the infrared, this is due to the frequency doubling technique. An AOM shifts the frequency additionally by $-240\,\text{MHz}$ resulting in a frequency shift in blue by $2 \times (-240 + \nu_{\text{sweep}})$.

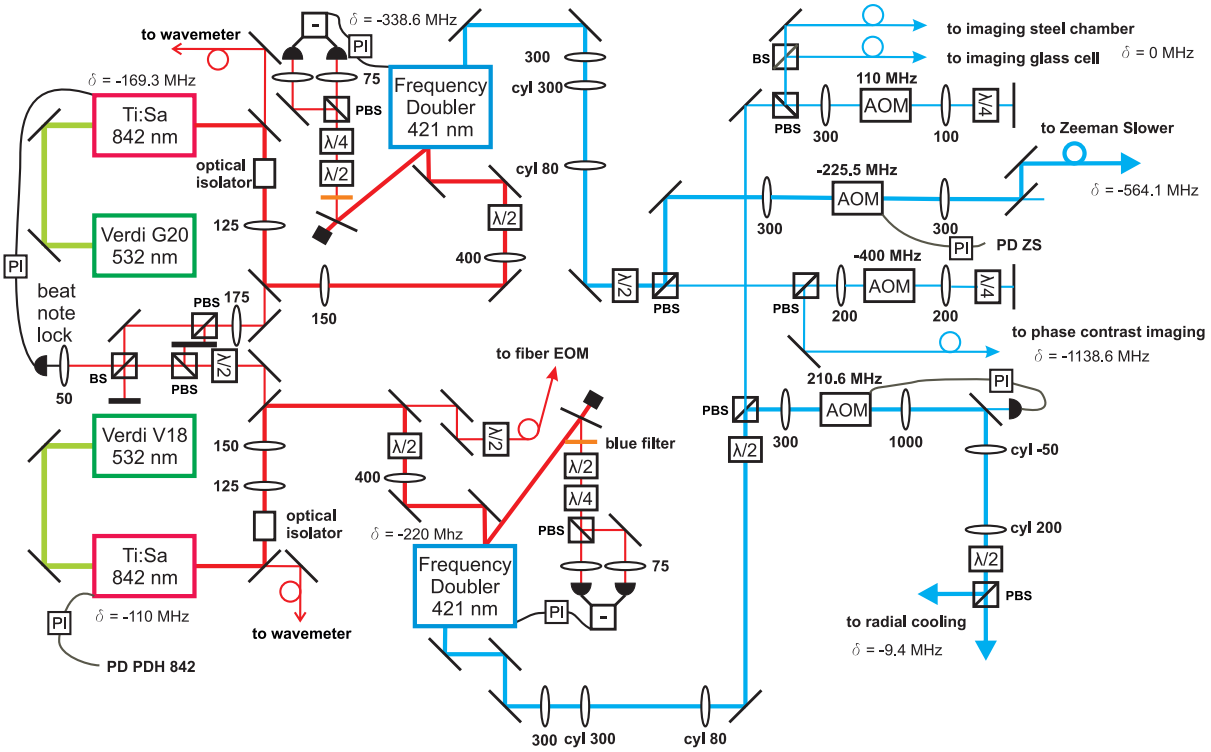

Fig. 4.3, 421 nm laser system: The 421 nm light is generated by frequency doubling the infrared light of two Ti:sapphire laser systems. The master system is locked to the ULE cavity and the slave system is stabilized relative to the master by a beat-note lock. The master generates the light for the transverse cooling and for absorption imaging. The light of the slave laser system is used for the ZS and for phase contrast imaging. On several occasions the frequency shift δ to the atomic resonance is indicated. The absorption imaging light is resonant ($\delta = 0$) for zero magnetic field.

system by the offset-lock technique [155]. This is a convenient way to reach the $18\,\Gamma_{421}$ detuning to the atomic resonance required for the ZS, see section 5.1. The ZS light is coupled into an optical fiber to increase the pointing and polarization stability of the ZS beam[48]. We not only use acousto-optic modulators (AOM) to shift the frequencies for the transverse cooling, the ZS and the imaging, but also to actively stabilize the light intensities improving the stability of the whole experiment[49]. In Figure (4.3) a schematic drawing of the 421 nm laser system is shown. More details on the slave system and on the offset-lock can be found in Ref. [153].

[48] Schäfter+Kirchhoff: Optical fiber: PMC-E-460Si-2.7-NA013-3-APC.EC-200-P.

[49] We operate the 421 nm system not at the maximum ratings. Usually we work with $P_{\text{master}} = 700\,\text{mW}$ and $P_{\text{slave}} = 500\,\text{mW}$, which is sufficient to stabilize the powers to $P_{\text{TC}} = 600\,\text{mW}$ and $P_{\text{ZS}} = 300\,\text{mW}$.

4.3.2 Orange (626 nm) Laser System

When we started to think about the different methods to cool and trap Dy a curial point was the generation of 626 nm light. At that time no suitable commercial solution was available. Fortunately the group of D. J. Wineland reported on the creation of 626 nm light, which they frequency double to achieve 313 nm light to study $^9Be^+$ ions [156]. We use the same approach based on the sum frequency generation of a 1050 nm[50] and a 1550 nm[51] fiber laser in a periodically poled lithium niobate (PPLN) crystal[52]. Both fiber lasers have a maximal output power of 5 W leading to 2 W of 626 nm light. A more detailed description on the creation of the 626 nm light can be found in section A.1. The 626 nm laser system is frequency stabilized by coupling the orange light to the ULE cavity and using the feedback signal to stabilize the 1050 nm fiber laser, while the 1550 nm system is free running. We could estimate the linewidth to be less than 30 kHz for the locked orange light.

We use an additional EOM[53] to broaden the linewidth of the orange laser to approximately $70\,\Gamma_{626}$ which increases the capture rate and the atom number of the MOT, see section 5.2. To be able to cool and trap the bosonic ^{164}Dy and the fermionic ^{161}Dy isotope sequentially we use two AOMs[54] in double pass configuration, subsequently the light is coupled into optical fibers and guided to the experimental chamber. The frequency of the bosonic ^{162}Dy isotope is accessible by locking the orange laser system to the next ULE cavity resonance +1.5 GHz apart and using the fermion AOM with a slightly different center frequency. See Figure (4.4) for a schematic drawing of the orange system.

4.3.3 Laser Frequency Stabilization Scheme

In atomic physic experiments usually the cooling lasers are locked directly to atomic transitions, therefore polarization spectroscopy on atomic vapor has to be performed. In Dy this could be either done directly at the atomic beam before the entrance of the ZS, or using a hollow cathode lamp to provide the atomic Dy vapor. As the optical access of our oven chamber is limited the first option would be challenging for all required wavelengths. Thus, we tried to use the hallow cathode lamp but due to pressure broadening the linewidth of the transition lines were to broad to be used for laser stabilization, see Ref. [157] for more details. Alternatively one can use reference cavities providing resonance lines with their linewidth $\Delta_{1/2}$ given by the length of the resonator d and the reflectivity of the mirrors R:

$$\Delta_{1/2} = \frac{\nu_{\mathrm{FSR}}}{\mathcal{F}} \,, \tag{4.1}$$

[50] NKT Photonics: Koheras Boostik HPA Y10 System, Linewidth < 10 kHz (120 μs).
[51] NKT Photonics: Koheras Boostik HPA E15 System, Linewidth < 1 kHz (120 μs).
[52] Covesion: MSFG626-0.5-40.
[53] Qubig: EO-F0.1M3-VIS.
[54] We use DDS frequency sources (e.g. based on AD9959) for all AOMs of the 626 nm, 684 nm and 741 nm laser systems.

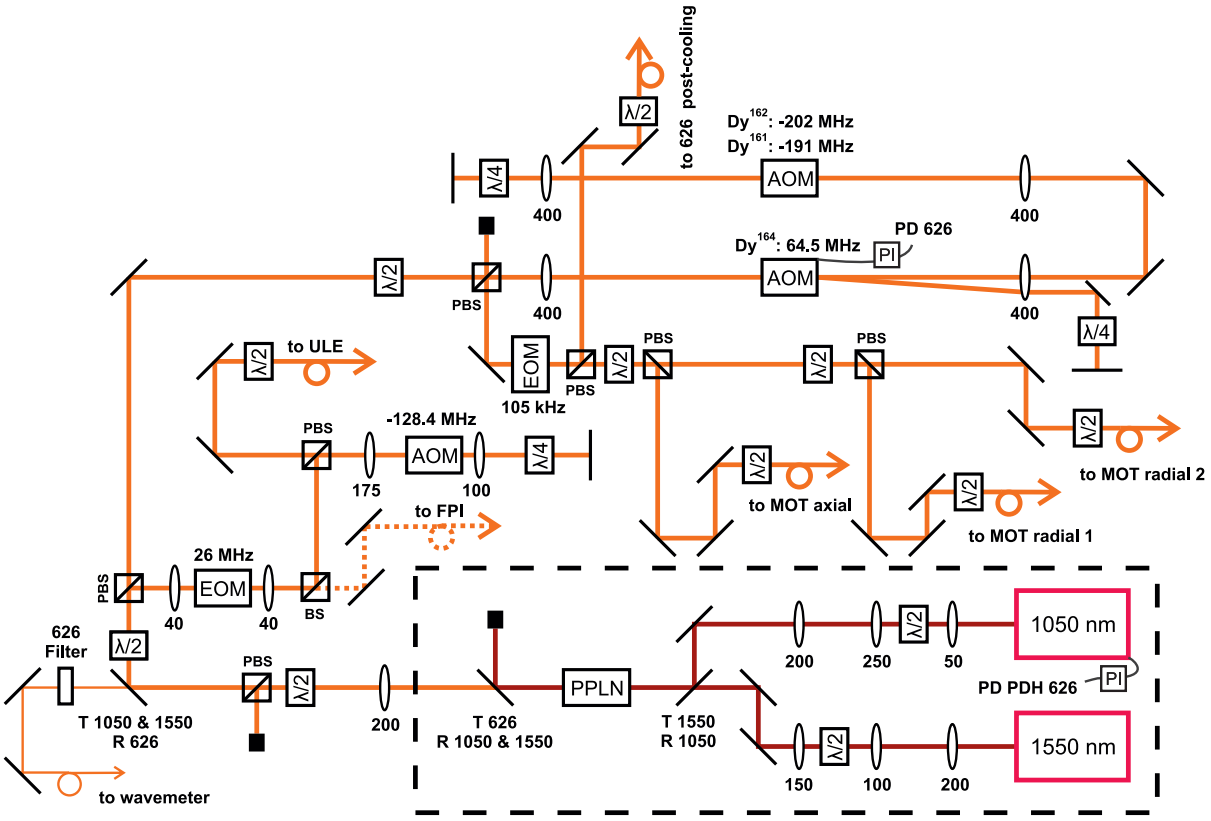

Fig. 4.4, 626 nm laser system: We use a sum-frequency generation of two infrared fiber lasers to create 626 nm light. After the AOMs, which are necessary to bride the gap between the ULE cavity resonance and the atomic resonance for the different isotopes, the light is coupled into optical fibers for the axial and radial beams of the MOT. A small fraction of light is used to further Doppler cool the atoms after the atoms are transported to the science cell.

where $\nu_{\mathrm{FSR}} = c/(2d)$ is the free spectral range and $\mathcal{F} = (\pi R^{1/2})/(1-R)$ the finesse. To stabilize the 421 nm, 626 nm and 684 nm laser system we use a ULE cavity[55], see Figure (4.5)(a). The mirror spacers are made out of ULE glass, which has a zero-crossing of the linear thermal expansion coefficient around room temperature[56]. The cavity has to be actively temperature stabilized to reach high thermal stability [158]. In addition, the ULE spacer is inside a vacuum can (pressure below 10^{-8} mbar) to shield it from the environment[57]. The cavity has one planar mirror and one mirror with a curvature of 500 mm. Both mirrors are reflection coated for the wavelength of 626 nm (684 nm) with a transmission of $T = 0.013793\,\%$ ($T = 0.016627\,\%$) leading to a theoretical linewidth of $\Delta_{1/2} \approx 66\,\mathrm{kHz}$ ($\Delta_{1/2} \approx 80\,\mathrm{kHz}$), respectively. As the natural transition rate of 421 nm transition is $\Gamma_{421} = 2\pi \cdot 32.2\,\mathrm{MHz}$ the requirements for the mirror coating at 842 nm is

[55] Stable Laser Systems: cavity length $d = 100.08\,\mathrm{mm} \rightarrow FSR = 1.498\,\mathrm{GHz}$ (TM_{00} mode).
[56] In our case at $T = 33.3°\mathrm{C}$.
[57] Ion getter pump: Agilent Technologies: 2 l/s pump. We see a drift of $\approx 20\,\mathrm{kHz/day}$ of the atomic resonance in respect to the locked laser. This could be due to an increase of pressure in the ULE can. This could be solved using an ion pump with a higher pumping rate.

not curial. Here, the transmission of $T = 1.058415\,\%$ leads to a theoretical linewidth of $\Delta_{1/2} \approx 5\,\mathrm{MHz}$.

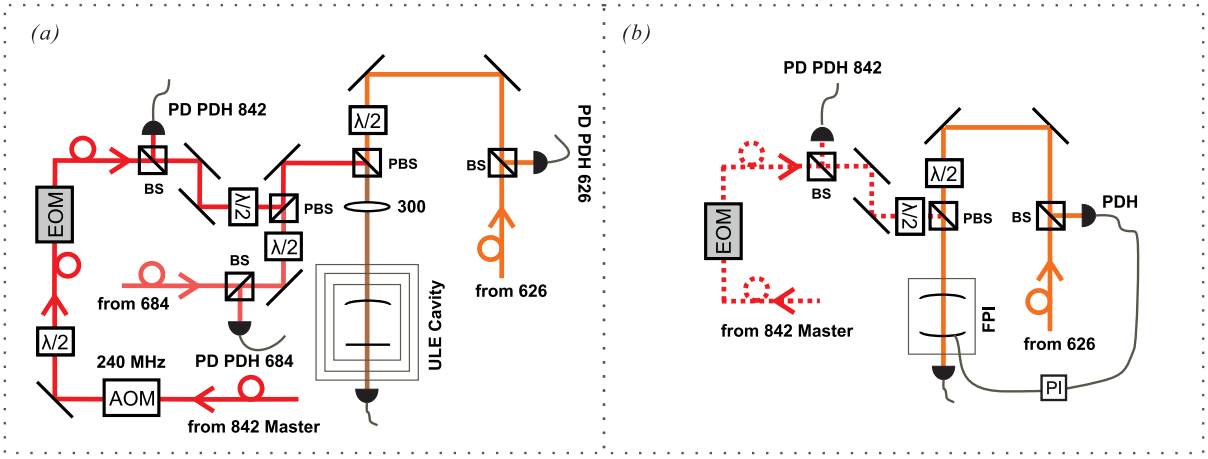

Fig. 4.5, Laser stabilization: *(a)* The 421 nm (via the 842 nm maser laser), 626 nm and 684 nm laser systems are locked to the passively stable ULE cavity using the PDH technique. *(b)* In future a transfer resonator (FPI) will be used to stabilize the 421 nm system, as its free spectral range $FSR = 8\,\mathrm{GHz}$ (TM_{00} mode) allows to change the frequency between the bosonic and fermionic isotope using the fiber EOM in the experimental sequence. The length of the transfer resonator is actively stabilized by the 626 nm laser.

4.3.4 Optical Dipole Traps (1070 nm + 1064 nm) Laser Systems

After the MOT phase the atoms are loaded into a single beam ODT. To efficiently transfer the atoms from the MOT chamber to the science cell a deep potential is needed. Therefore, we use a ytterbium fiber laser[58] at 1070 nm with 100 W output power[59], see Figure (4.6)(a). The transport beam has a measured beam waist of $w_0 = (37.3 \pm 1.2)\,\mu\mathrm{m}$ and an estimated maximum power of 72 W at the atoms. The last lens of the transport beam is mounted on a computer-controlled air bearing translation stage[60] allowing us to transport the atoms from the MOT chamber to the science cell. More details on the transport can be found in section 5.3.2. However, this laser is only used for the transport as the longitudinal frequency modes of the laser drive two-photon Raman transitions, which heat up the atomic sample and thus this laser cannot be used for evaporative cooling, see Figure (4.6)(b-c).

In the science cell the atoms are transferred to a crossed ODT to be able to evaporatively cool the atoms to degeneracy. The crossed ODT consists of ODT 1, which is superimposed

[58] IPG Laser: YLR-100-LP-WC, linewidth $\Delta\lambda = 2.5\,\mathrm{nm}$.
[59] Controllable by an analog signal between 100 % and 5 % of the output power and a TTL signal to switch-off the laser in 25 μs.
[60] Aerotech: Stage: ABL15040, 40 cm travel range, 0.5 μm accuracy, Controller: ENSEMBLE HLE10-60-A-MXH-B.

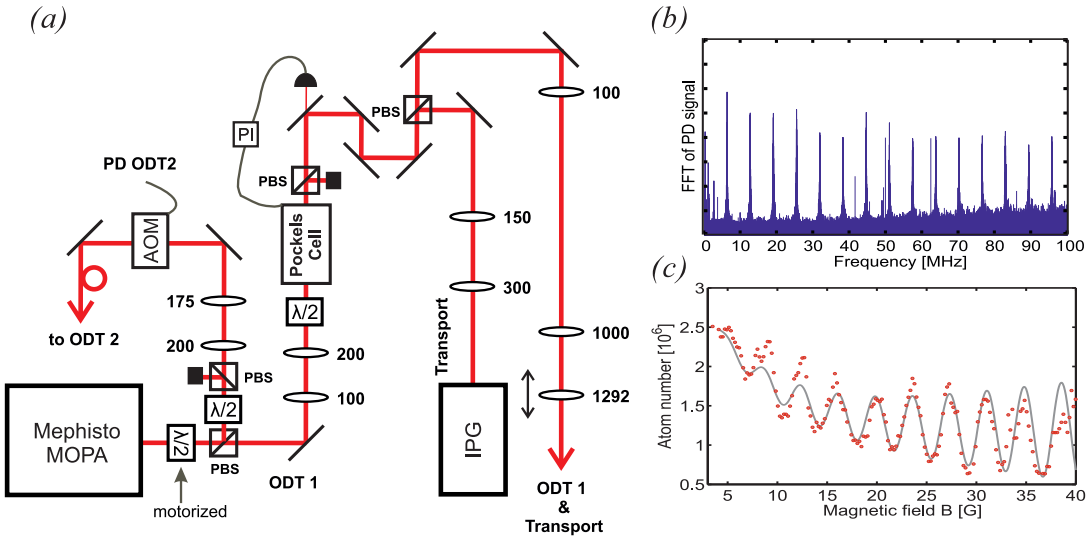

Fig. 4.6, ODT Laser Setup: *(a)* We use a fiber laser (IPG) with 100 W output power to transport the atoms from the MOT chamber to the science cell. After the transport the atoms are loaded into a crossed ODT, created by solid-state laser (Mephisto MOPA). The powers of ODT 1 (ODT 2) are controlled and actively stabilized by a Pockels cell (AOM), respectively. We use a high-power fiber to guide ODT 2 directly to the science cell. *(b)* Longitudinal mode structure of the fiber laser with a spacing of 6.4 MHz leading to two-photon Raman transitions between different Zeeman levels which heats up the sample and causes atom losses. *(c)* Atom loss of a thermal cloud in the transport beam depending on the external magnetic field. An artificial fit function (gray) gives a period of $\Delta B = 3.75\,\mathrm{G}$ corresponding to a Zeeman splitting of $\Delta f = 6.5\,\mathrm{Mhz}$.

with the transport beam and ODT 2 being perpendicular to it. Both traps are created by a 55 W solid-state laser[61] at a wavelength of 1064 nm. The power distribution between ODT 1 and ODT 2 can be adjusted by a motorized rotating waveplate[62]. The power of ODT 1 is actively intensity stabilized using a Pockels cell[63] while ODT 2 is controlled by an AOM[64]. Furthermore, ODT 2 is coupled into a high-power polarization-maintaining optical fiber[65]. We have 28 W (8 W) of maximum power of ODT 1 (ODT 2) at the atoms in the science cell. In order to reach the needed trap ratio the beam waists of ODT 1 and ODT 2 have to be adjusted using cylindrical lenses. In addition, we use quartz lenses to minimize the effect of thermal lensing. Figure (4.6)(a) shows the dipole trap setup. Lately, also ODT 1 is guided by a high-power fiber directly to the science cell and actively

[61] Coherent: Mephisto MOPA 55 W, linewidth $\Delta\nu = 1\,\mathrm{kHz}$ (100 ms).
[62] UAB ALTECHNA: 8MRU-1.
[63] Pockels Cell: Qioptiq Photonics: DBBPC5; Controller: FLUDICON: RheCon 2.0. The controller limits the bandwidth to 150 Hz. To be able to switch-off ODT 1 we use a high voltage Behlke switch, Model: HTS 61-03-GSM.
[64] AA Opto Electronic: AA.MT.15, 80 MHz center frequency, 4 kHz bandwidth of the intensity stabilization. In order to minimize the beam movement during the evaporation ramps, we use a two-frequency driver for the AOM providing a constant RF driving power [159].
[65] OZ Optics: PMJ-A3HPC,A3HPC-1064-10/125-5AS-2-1-LMA.

controlled by an AOM, which allows to decouple the transport beam from the ODT improving the beam shape of ODT 1 and the stability of the system.

4.3.5 Laser Light Distribution on the Apparatus

Figure (4.7) and Figure (4.8) show how the different laser lights are distributed around the vacuum chamber. Most of the light is guided by optical fibers to the apparatus and additionally, wherever it is possible, we actively control the laser intensity, which improves the overall stability of the system. The atoms are imaged in the MOT chamber by standard absorption imaging after TOF[66]. Using the transport beam the atoms are moved from the MOT chamber to the science cell. Here, we have the possibility to either do standard absorption imaging in the x-z-plane[67] or high-resolution imaging in the x-y-plane[68].

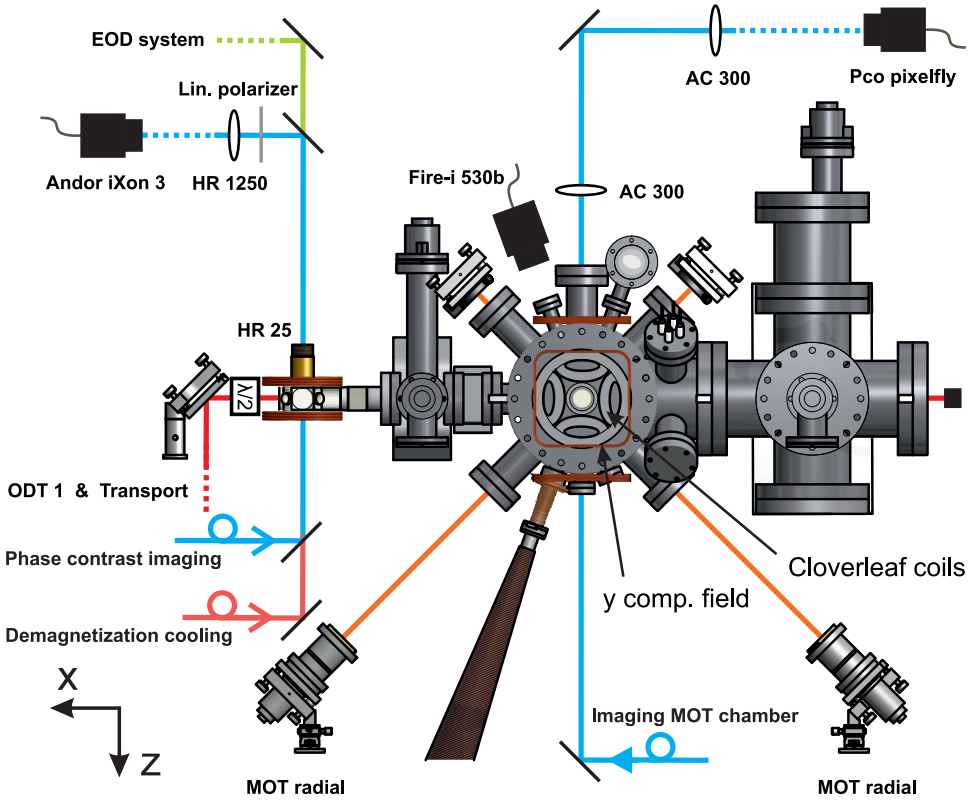

Fig. 4.7, Experimental Setup (front view): Schematic drawing of the experimental setup. Most of the different laser lights are coupled into optical fibers and guided to the apparatus, which increases the stability of the system. For the imaging telescopes we use achromat (AC) lenses to minimize lens aberration effects.

[66] PCO: pco.pixelfly, pixel size: $6.45 \times 6.45\,\mu$m.
[67] PCO: pco.pixelfly usb, pixel size: $6.45 \times 6.45\,\mu$m.
[68] Andor Technology: Andor iXon 897, pixel size: $16 \times 16\,\mu$m.

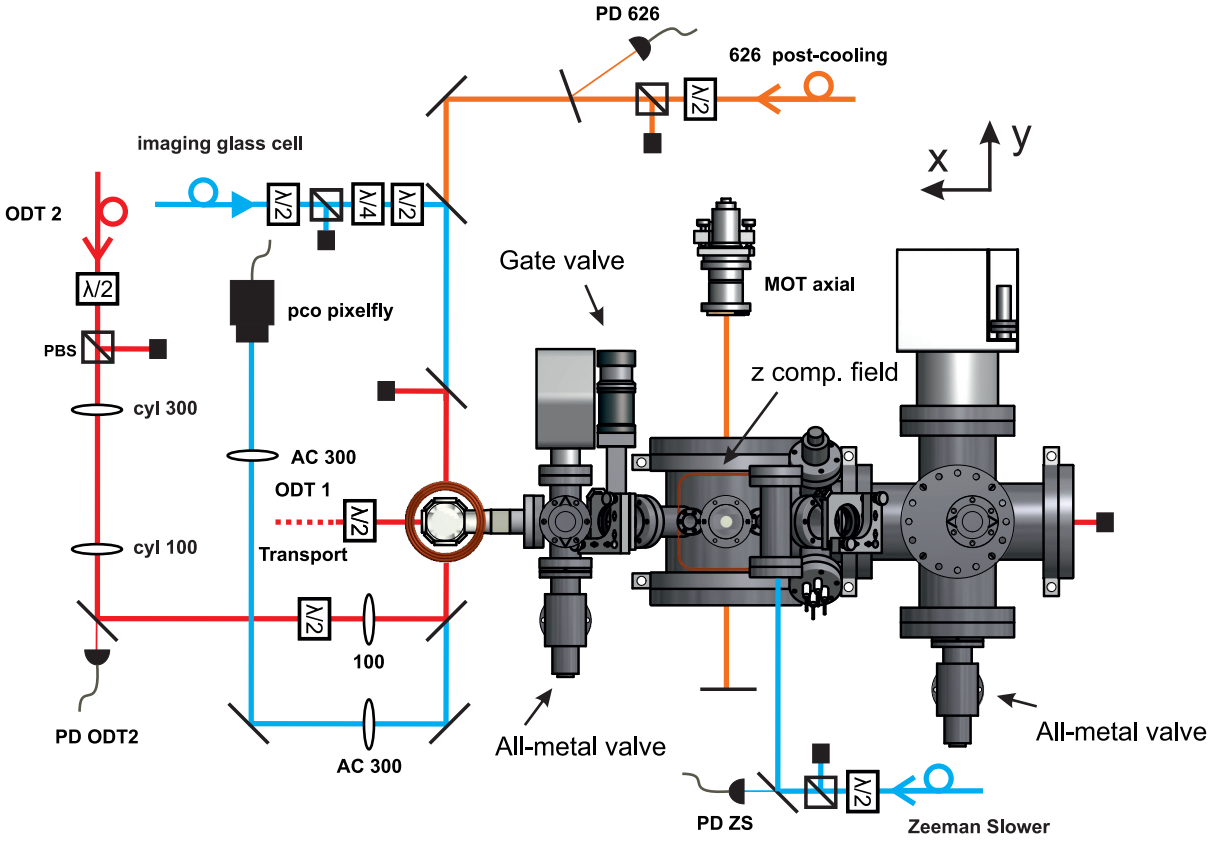

Fig. 4.8, Experimental Setup (top view): Schematic drawing of the experimental setup. A gate valve separates the MOT chamber from the science cell, such that this part can easily be exchanged and pumped individually. In the science cell the atoms are further Doppler cooled using the 626 nm transition.

4.4 Magnetic Field Control

Magnetic fields are an important experimental tool to trap and externally manipulate ultra-cold atoms. On the other hand for atoms with large magnetic moments it is essential to be able to compensate unwanted magnetic fields. Different magnetic field coils were designed to achieve the needed requirements:

MOT Coils

The MOT chamber has the same magnetic field coils configuration as it was used in the old Cr experiment [160]. As we did not know which cooling approach will work best we also implemented an Ioffe-Pritchard MT in the clover leaf configuration consisting of the clover leaf coils, the pinch coils and the offset coils [161]. The coils are water cooled and can be operated with up to 300 A, creating a MT with a maximum axial (y-direction) curvature of 319 G/cm^2 and maximal radial gradient of 211 G/cm. We do not use the MT as the MOT at the 626 nm transition works.

To produce the magnetic gradient field for the MOT we use the above mentioned offset coils (5×3 windings) in anti-Helmholtz configuration, giving an axial (radial) gradient of $0.36\,\mathrm{G/(A\,cm)}$ ($0.18\,\mathrm{G/(A\,cm)}$), respectively. We typically operate the MOT coils only with a current of up to 15 A, thus a power supply with moderate output power is sufficient[69]. We use an IGBT[70] to be able to fast switch-off the trap before doing the absorption imaging.

Compensation Coils

Around the MOT chamber we have installed magnetic field compensation coils[71] in the z- and y-directions, which produce almost homogenous offset fields. The z-compensation coils (4×10 windings) produce an offset field of $1\,\mathrm{G/A}$. These coils are also used to create an offset field of 10 G when we image the atoms in the MOT chamber. In the y-direction the compensation coils (4×10 windings) produce an offset field of $-0.4\,\mathrm{G/A}$. These compensation coils are also used to slightly modify the MOT position with respect to the transport beam to optimize the loading efficiency on a daily basis.

For many experiments with highly magnetic atoms, e.g. demagnetization cooling and spinor physics with fermionic Dy, the magnetic field in the science cell has to be well controlled or even compensated to approximately zero field. A magnetic field compensation cage is implemented around the glass cell, consisting of three pairs of coils in x-, y- and z-direction (each coil has 5×3 windings). The coils create a homogenous offset field of $0.27\,\mathrm{G/A}$, $-0.2874\,\mathrm{G/A}$ and $-0.35\,\mathrm{G/A}$ in the x-, y- and z-directions[72], respectively. Within 10 mm around the center of the glass cell the fields have a calculated homogeneity of $< 1\,\mu\mathrm{G/mm}$. We use self-build bipolar current sources[73] for these compensation coils. In combination with a self build magnetic field sensor we will be able to actively stabilize the magnetic field to $\delta B \leq 500\,\mu\mathrm{G}$ [162]. In addition, they can also be used to change the magnetic field direction while the absolute value stays constant. This changes the polarization direction of the magnetic dipoles which modifies the properties of the dipolar quantum gas, see section 5.4.

Feshbach Coils

Feshbach resonances are an important tool in ultra-cold quantum gas experiments to externally control the interaction properties. As we are working with magnetic Feshbach resonances a homogenous magnetic field is required. The design of our science cell provides

[69] EA ELEKTRO-AUTOMATIK: EA-PS-3016-20-B (16V,20A).
[70] Insulated-gate bipolar transistor (IGBT).
[71] Power supplies: EA ELEKTRO-AUTOMATIK: EA-PS-3016-10-B (16V,10A).
[72] So far only the coils in y-direction were calibrated using RF transitions between two Zeeman sub-states (calculated value: -0.2653 G/A).
[73] Based on OPA549.

the possibility to have different coil configurations depending on the field direction and the maximal needed absolute field value.

To study Feshbach resonances up to 100 G we used Feshbach coils creating a field in y-direction. It consist of two coils in Helmholtz configuration, both have a diameter of around 78 mm and 10×10 windings. The magnetic field created by the coils was calibrated by RF-spectroscopy and results in the conversion factor of 20.13 G/A. The current is provided by a highly stable current source[74]. To estimate the magnetic field stability we measured[75] the relative noise $(\delta I/I)_{\mathrm{rms}} = 2.2 \times 10^{-5}$ at 5A of the current source, resulting in a magnetic field noise of $\delta B < 2.2$ mG at the maximum field of 100 G[76]. Due to the high inductance of $L \approx 10$ mH of the coils the switch-off time is limited to around 4 ms.

A second configuration allows to study Feshbach resonances up to 600 G. The field of this configuration points in z-direction which is essential for a stable BEC configuration. The high field Feshbach coils have 3×3 windings and are in a Helmholtz configuration with a diameter of around 88 mm, creating a magnetic field of 1.76 G/A (calibrated by RF-spectroscopy). Furthermore, the wires are water cooled, such that a maximum current of 350 A does not heat up the coil significantly. The coils are mounted in a plastic holder, which still provides the optical access through all glass windows of the glass cell, see Figure (4.2)(b). Small magnetic field gradients can expel the atoms from the trap. Therefore, the coils have to be positioned within a volume of (1 cm × 1 cm × 1 cm) with respect to the atoms, see Figure (4.9)(b). We use two power supplies[77] in master-slave configuration operating at a maximum voltage of 11 V to guarantee a fast switch-off time. The current is actively controlled by a high precision current transducer[78], a home build PI controller and an MOSFET[79], see Figure (4.9)(a) [141]. The magnetic field resolution over the full range up to 600 G is less than 10 mG (estimated by current noise measurement) and the switch-off time with around 2 ms is mainly limited by the settings of the PI controller[80].

[74] HighFinesse: Bipolar Current Source BCS 6/12, Current stability and reproducibility: $< 2.5 \times 10^{-5} \times I_{\max}$.

[75] Using the same devices as in [141].

[76] The current source is controlled by an analog voltage 10 V ≡ 6 A. The voltage provided by our computer control (NI PCI-6713 card) has a limited resolution of 4.9 mV, yielding a magnetic field resolution of 59 mG. This could be increased by using two channels of the NI card, where the voltage of the second one is attenuated by a factor of 49.9 and added to the first channel, resulting in a theoretical magnetic field resolution of 1.2 mG.

[77] Agilent: 6682A (21V, 240A).

[78] Danfysik: Ultrastab 860R.

[79] Metal-oxide-semiconductor field-effect transistor (MOSFET): Dynex: DIM 1200DDM12-E000; To limit the dissipated power the maximum voltage of the power supplies was restricted to 11 V.

[80] The current transducer measures the current and provides a proportional voltage, which is stabilized by the PI in respect to the desired voltage given by the computer control adapting the variable resistance of the MOSFET. The conversion factor is 68.4 G/V. Using two channels of the NI card the theoretical resolution is 6.34 mG.

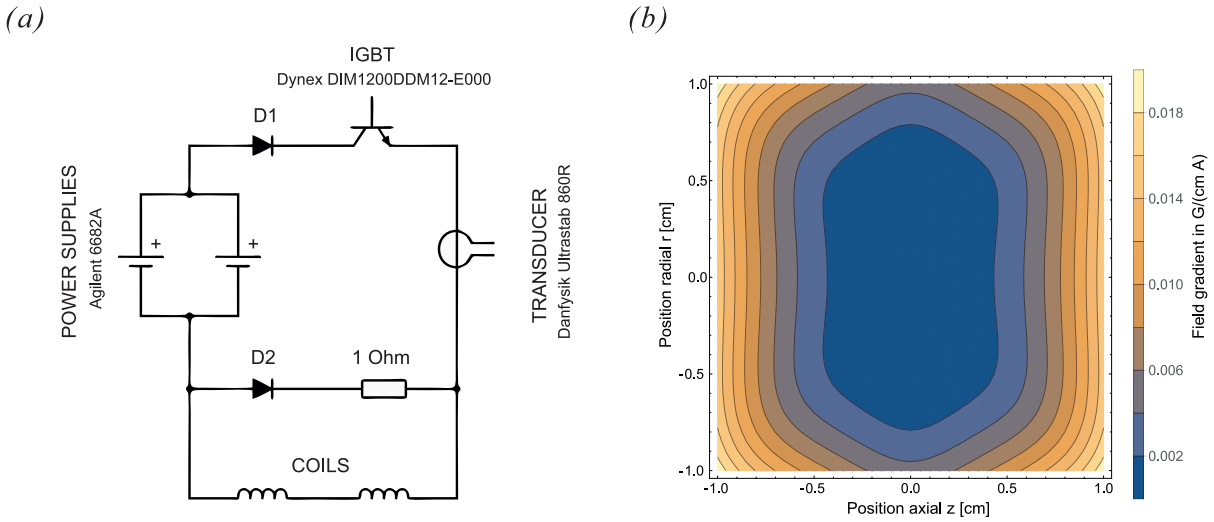

Fig. 4.9, Feshbach coils: *(a)* Circuit diagram of the Feshbach coils. *(b)* If the highly magnetic atoms are not centered to the middle of the Feshbach coil the resulting magnetic field gradient can lead to atom losses.

Gradient Coils

An additional pair of coils (10×10 windings) with a diameter of around 105 mm and a separation of 52.5 mm in anti-Helmholtz configuration provides an axial (radial) gradient of 3.6 G/(A cm) (1.8 G/(A cm)), respectively. These coils can be used to compensate gravity, as any gradient strongly modifies the trapping potential created by the ODT lasers, see section 5.3.1. In a controlled way this can be used to change the trap depth of the crossed ODT without changing its confinement resulting in a more efficient forced evaporative cooling process [163].

4.5 High-resolution Imaging System

In our experiment the microscope objective is used to combine two important experimental tools. On the one hand it is used to perform in-trap images of the quantum gas and on the other hand together with an EOD system time-averaged tailored potentials can be created. The typical size of a BEC is on the order of a few μm, thus the resolution of the objective for the imaging light $\lambda = 421\,\text{nm}$ and also for the light which is used to trap the atoms $\lambda = 532\,\text{nm}$ has to be around $1\,\mu\text{m}$.

The diffraction-limited spot size d given by the Rayleigh criterion can be calculated by [164]

$$d = 1.22\,\frac{f\lambda}{D} = \frac{1.22}{2}\,\frac{\lambda}{NA}\,, \tag{4.2}$$

where D is the lens diameter, f the focal length of the lens and $NA = n\sin\alpha$ the numerical aperture, calculated with the refraction index n and α the half of the opening angle of the lens aperture. The clear aperture of the largest window of the glass cell limits the maximum numerical aperture to $NA \approx 0.78$ (assuming the atoms in the center of the glass cell), resulting in a theoretical minimal spot size of $d \approx 350\,\text{nm}$ ($\lambda = 421\,\text{nm}$). Accounting for the possibility to move the objective in the lateral directions and for some margin between the objective and the window surface ($\approx 2\,\text{mm}$) the aperture is limited to $D = 17\,\text{mm}$ and the focal length of the objective to $f_1 = 25\,\text{mm}$, yielding a numerical aperture of $NA = 0.32$ and a minimal theoretical spot size of $d = 803\,\text{nm}$ ($d = 1014\,\text{nm}$) for $\lambda = 421\,\text{nm}$ ($\lambda = 532\,\text{nm}$), respectively. Figure (4.2)(b) shows a schematic drawing of the glass cell including the Feshbach holder and the objective. Additionally, the objective has to be corrected for the refraction of the glass window (6.35 mm thick quartz glass) for both wavelengths. To fulfill these requirements we use a diffraction-limited custom-made microscope objective[81], where the housing and spacers are made out of polyimide[82] to avoid any magnetic material. To be able to align the objective with respect to the atoms and the glass window it is mounted in a brass tube, which is attached to translation stages. For a rough alignment a home-made xyz-translation stage can be used. Fine adjustments can be done by a piezo xyz-stage[83] and a tilt stages[84], see Figure (4.10).

For the high-resolution imaging we use an EMCCD camera which has a pixel size of $16\,\mu\text{m}$, thus a magnification of $M = 50$ is sufficient to achieve high-resolution images of the quantum gas. For this a second diffraction-limited objective[85] with a focal length of $f_2 = 1250\,\text{mm}$ is necessary. Both objectives are anti-reflection coated for the imaging light ($\lambda = 421\,\text{nm}$) and the EOD trapping light ($\lambda = 532\,\text{nm}$).

[81] Special Optics: 54-17-25-532/421nm.
[82] Ultem 2300
[83] Physik Instrumente (PI): stage: P-563.3CD, travel range: $300 \times 300 \times 300\,\mu\text{m}$, resolution: 2 nm (closed loop), controller: E-725.3CDA.
[84] Newport Spectra-Physics: M-TTN80.
[85] Special Optics: 54-17-1250-532/421nm.

To experimentally investigate the performance of the microscope objective for the two wavelengths we used different test targets. A standard method to estimate the resolving capacity is to illuminate an USAF resolution test chart[86] and acquire an image with the EMCCD camera. For both wavelength we were able to resolve the smallest pattern, which gives us an upper limit of the resolution to 1.56 μm [165]. In addition, we use a pinhole[87] with a diameter of 500 nm to approximate a point source to extract the resolution of the objective. We get a resolution according the Rayleigh criterion of $(0.99 \pm 0.03)\mu$m for the $\lambda = 421$ nm imaging light and $(1.36 \pm 0.05)\mu$m for the $\lambda = 532$ nm trapping light [166]. More details on the performance testing of the microscope objective can be found in Ref. [167]. In Ref. [166] the setup and the performance of the EOD system is described.

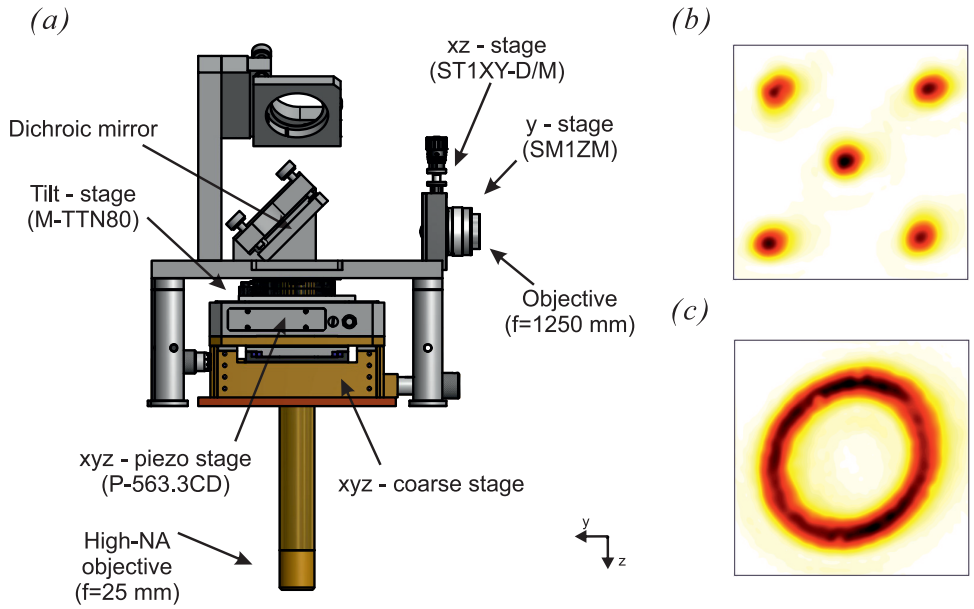

Fig. 4.10, Microscope objective: *(a)* Schematic drawing of the microscope stack. Both objectives are mounted on translation stages to have an optimum of alignment freedoms. A dichroic mirror separates the $\lambda = 421$ nm imaging from the $\lambda = 532$ nm trapping light. *(b-c)* Examples of different intensity patterns created by the EOD system. The images are recorded after the deflector with a CCD camera. Images *(b)* and *(c)* are taken from [166].

[86] Edmund Optics: Positive target 58-198.
[87] National Aperture: 1-0.5HS.

5 Cooling Dysprosium Atoms to Quantum Degeneracy

In this chapter we describe our procedure to create BECs as well as degenerate Fermi gases of Dy atoms. We first use a ZS to slow down the atoms longitudinally (section 5.1) and subsequently they are trapped in a MOT (section 5.2). Afterwards, the cooled and trapped atoms are transferred into an ODT which is used to transport the atoms from the MOT chamber to the science cell. To cool the sample further the atoms are loaded into a crossed ODT where a degenerate quantum gas is achieved by forced evaporative cooling (section 5.3). Finally, in section 5.4 we present a first study of the Dy BEC properties and a first in-situ image of a dipolar BEC is shown in section 5.5.

5.1 Creation of a Slow Atom Beam

To obtain a Dy beam with a high atom flux we have to heat up Dy granulate in an effusion cell to 1250°C. The atoms leaving this oven have a velocity distribution with a maximum at around 500 m/s. As the capture velocity of a typical MOT is on the order of a few m/s a ZS is necessary to slow down the atoms.

To estimate the atomic flux at the MOT position the temperature dependence of the saturated vapor pressure p_{sat} is required. P_{sat} of Dy for different temperatures can be found in Ref. [168] and approximated by the Antoine equation [84]

$$p_{\mathrm{sat}}(T) = 10^{A-\frac{B}{C+T}} \ , \tag{5.1}$$

where p_{sat} is in mbar, T in °C and $A_{\mathrm{Dy}} = 6.92$, $B_{\mathrm{Dy}} = 10169.5$, $C_{\mathrm{Dy}} = 36.94$ are empirical constants. In Figure (5.1)(a) the vapor pressures of the magnetic atoms Dy, Er and Cr are shown. These elements have in common that they require high temperatures to reach the needed vapor pressures for ultra-cold quantum gas experiments. In the effusive regime where the oven diameter is much smaller than the mean free path of the atoms inside the oven, the longitudinal velocity distribution of atoms emitted inside a small solid angle of azimuth θ_{em} can be calculated by [169]

$$f_{\mathrm{em}}(v,T) = \left(\frac{\pi D_{\mathrm{em}}}{2}\right)^2 \frac{p_{\mathrm{sat}}(T)}{k_{\mathrm{B}}T} \left(\frac{m}{2\pi k_{\mathrm{B}}T}\right)^{3/2} v^3 \exp\left(-\frac{mv^2}{2k_{\mathrm{B}}T}\right) \sin^2(\theta_{\mathrm{em}}). \tag{5.2}$$

Here, v is the longitudinal velocity of the beam and D_{em} the diameter of the oven aperture. Velocity distributions for different temperatures are shown in Figure (5.1)(b). The maximum velocity is located at $v_{\mathrm{max}} = \sqrt{\frac{3k_{\mathrm{B}}T}{m}} = 480\,\mathrm{m/s}$ for a temperature of $T_{\mathrm{oven}} = 1250°\mathrm{C}$.

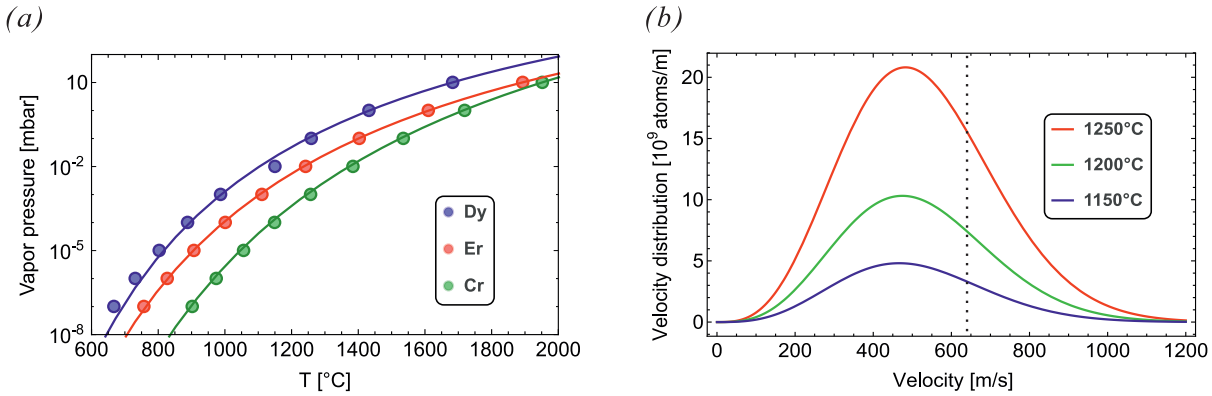

Fig. 5.1, Creation of an atom beam: *(a)* Saturated vapor pressure of the magnetic atoms Dy, Er and Cr. For these elements a high temperature effusion cell is necessary to reach the required vapor pressures. *(b)* Longitudinal velocity distribution for different temperatures with $D_{\mathrm{em}} = 2\,\mathrm{mm}$ and $\theta_{\mathrm{em}} = 0.0076$ at the position of the MOT. The ZS capture velocity is around 650 m/s which is highlighted by the dotted line.

Slowing down Atoms by a Zeeman Slower

Only a small fraction ($\approx 10^{-6}$ for $v_{\mathrm{c}}^{\mathrm{MOT}} \approx 15\,\mathrm{m/s}$) of the atoms have a velocity such that they can be directly trapped by the MOT. Thus, a ZS has to be used to reduce the longitudinal velocity of the atoms. Atoms entering the ZS with a velocity smaller than its capture velocity $v_{\mathrm{c}}^{\mathrm{ZS}}$ are slowed down to a final value v_f using strong light forces.

The maximum acceleration obtained by the radiation force due to a resonant laser beam with a wavelength λ collinear and counter-propagating to the atomic beam is given by [170]

$$a_{\mathrm{max}} = \frac{\hbar k}{m}\frac{\Gamma}{2}\,, \tag{5.3}$$

where Γ is the transition rate of the used transition and $k = 2\pi/\lambda$ the wave vector. It assumes that the atom absorbs a photon with the maximal possible rate of $\Gamma/2$. For a constant deceleration a_{ZS} the velocity at position x in the ZS can be calculated by

$$v(x) = v_{\mathrm{c}}^{\mathrm{ZS}}\sqrt{1 - \frac{x}{l_0}}\,. \tag{5.4}$$

Here, l_0 is the required length of the slower to reduce the entrance velocity $v_{\mathrm{c}}^{\mathrm{ZS}}$ to a final velocity v_f, given by

$$l_0 = \frac{(v_{\mathrm{c}}^{\mathrm{ZS}})^2 - v_f^2}{2a_{\mathrm{ZS}}}\,. \tag{5.5}$$

As the atoms are slowed down the resulting Doppler shift has to be compensated such that the transition frequency ω_0 at zero magnetic field matches the constant laser frequency ω. This is done using the Zeeman shift induced by an external magnetic field. To fulfill the

resonance condition over the full length of the ZS the magnetic field has to vary with

$$B(x) = B_{\text{bias}} + B_0\sqrt{1 - \frac{x}{l_0}}\,, \tag{5.6}$$

where $B_{\text{bias}} = \frac{\hbar\delta}{\mu'}$ is the magnetic bias field and $B_0 = \frac{\hbar k v_c^{\text{ZS}}}{\mu'}$ the overall height of the magnetic field profile. Here, $\delta = \omega - \omega_0$ is the detuning of the ZS laser light. The difference of the magnetic moments between the ground- and excited-state is given by $\mu' = (g_e m_e - g_g m_g)\mu_B$ with the magnetic quantum numbers $m_g = 8, m_e = 9$ and the Landé factors $g_g = 1.24, g_e = 1.22$.

In Dy a suitable transition to operate the ZS is the 421 nm transition which has a transition rate of $\Gamma = 2\pi \cdot 32.2\,\text{MHz}$. This results in a high acceleration of $a_{\text{max}} = 5.9 \times 10^5\,\text{m/s}^2$. The difference of the magnetic moments between ground- and excited-state is $\mu' = 1.047\,\mu_B$. The maximal rate at which atoms can absorb photons and be cooled imposes an upper limit on the field gradient [171]. To ensure that no atoms are getting out of resonance on the way through the slower we use a security factor of $\alpha_{\text{ZS}} = 0.78$, resulting in lower acceleration of $a_{\text{ZS}} = \alpha_{\text{ZS}} \cdot a_{\text{max}}$. To minimize the effect of the ZS light on the MOT we use a large detuning of $\delta = -18\,\Gamma_{421}$, which sets the magnetic bias field to $B_{\text{bias}} = -395\,\text{G}$. Our ZS is designed for a capture velocity of $v_c^{\text{ZS}} = 645\,\text{m/s}$, resulting in an overall magnetic field height of $B_0 = 1045\,\text{G}$. To have a large capture velocity with moderate absolute field values a spin-flip ZS is used. For a final velocity of $v_f = 13.5\,\text{m/s}$ the length of the ZS can be calculated to $x_0 = 0.45\,\text{m}$. Hence, the atom flux Φ at the position of the MOT can be estimated by integrating Eq. (5.2) up to v_c^{ZS}, which results in an atomic flux of around $\Phi = 10^{12}$ atoms/s.

The Dy ZS consists of two parts. The first part was already planned and built in 2008 for the new Cr experiment [172]. We decided to use this already existing part and adapt it to be usable for Dy atoms by adding a second part. The first part consists of two independent coils wound around a double-walled (for water cooling) CF16 tube. The first coil has six layers disconnected from the second coil with ten layers. In addition, a compensation layer over both coils is used to correct for all major imperfections. The first part[88] produces a positive decreasing magnetic field and has a length of 65.5 cm. The second part[89] has a length of 6.7 cm and creates a negative magnetic field to reach a final velocity of $v_f = 13.5\,\text{m/s}$. Due to the fact that we used the already existing part the ZS is much longer than necessary. In Figure (5.2) the resulting magnetic field of the ZS is shown.

In the inset of Figure (5.2) one can see that at some positions the gradient of the measured field is slightly higher than the gradient of the calculated field with maximal acceleration, but due to the broad linewidth of the 421 nm transition the resonance condition is still fulfilled.

[88] $R_{1-6} = 1.38\,\Omega$, $R_{7-16} = 1.31\,\Omega$, $R_{\text{comp}} = 0.14\,\Omega$
[89] $R_{\text{small}} = 0.28\,\Omega$

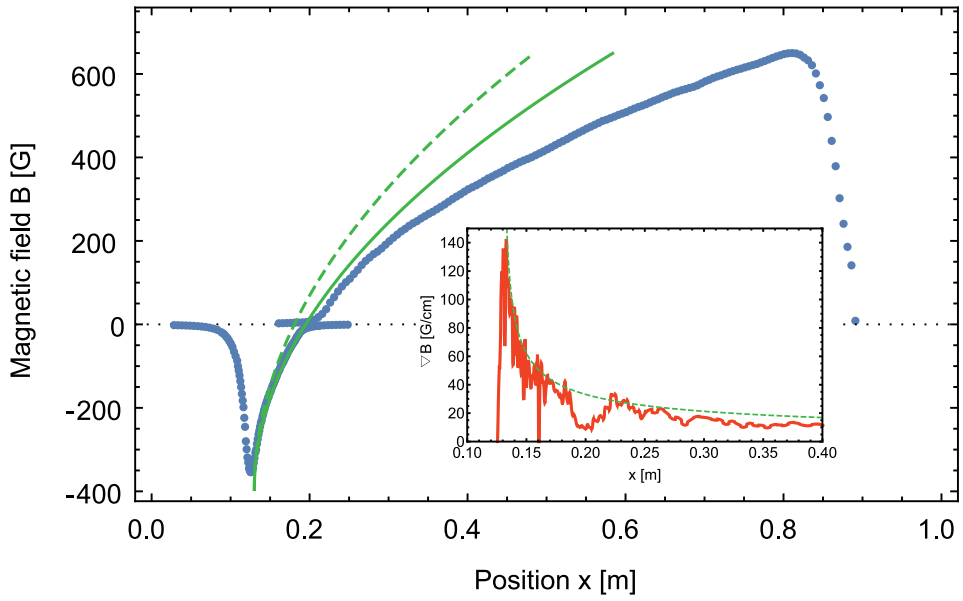

Fig. 5.2, Magnetic field of the Dy spin-flip ZS: The atoms are slowed down from a capture velocity of $v_c^{ZS} = 645\,\mathrm{m/s}$ to a final velocity of $v_f = 13.5\,\mathrm{m/s}$. The MOT position is situated at the origin of the graph. The measured magnetic field (blue circles) is created by the first part consisting of three layers ($I_{1-6} = 10.76\,\mathrm{A}$, $I_{7-16} = 5.66\,\mathrm{A}$ and $I_{\mathrm{comp}} = -4.7\,\mathrm{A}$) and the second part ($I_{\mathrm{short}} = 9.6\,\mathrm{A}$). The dashed (solid) green line indicates the theoretical magnetic field for a maximal (with a security factor of $\alpha_{ZS} = 0.78$) acceleration. The inset shows the gradient of the magnetic field (red) and of the maximal field (dashed green).

For the ZS we use positive circular polarized 421 nm light ($m_J = 8 \rightarrow m_J = 9$). The light is focused on the aperture of the effusion cell and has an estimated diameter of 18 mm at the position of the MOT. We use a power of $P_{ZS} = 100\,\mathrm{W}$ which results in a light intensity of $I_{ZS} = 0.75\,I_{s,421}$. To achieve a higher stability we couple the ZS light in a fiber and use an AOM for intensity stabilization. We have optimized the flux by adjusting the different currents of the ZS coils[90].

5.2 Magneto-optical Trap for Dysprosium Atoms

Magneto-optical traps are a standard tool in ultra-cold quantum gas experiments to produce a sample of cold neutral atoms [173]. The lowest temperature achievable with a MOT is the Doppler temperature $T_D = \frac{\hbar\Gamma}{2k_B}$ which depends on the transition rate Γ of the used cooling transition. For example the cooling transition of Rubidium has $\Gamma = 2\pi \cdot 6\,\mathrm{MHz}$ resulting in a Doppler temperature of $T_D = 146\,\mu\mathrm{K}$. To reach quantum degeneracy, further cooling methods have to be applied. A standard way is to use forced evaporative cooling in a magnetic or optical trap. Due to dipolar relaxation processes

[90] $I_{1-6} = 8.2\,\mathrm{A}$, $I_{7-16} = 5.2\,\mathrm{A}$, $I_{\mathrm{comp}} = 0\,\mathrm{A}$ and $I_{\mathrm{short}} = 9.7\,\mathrm{A}$

it is not possible to reach quantum degeneracy for dipolar atoms in a MT, therefore an ODT has to be used. To efficiently transfer the atoms from the MOT into the ODT the temperature of the atomic sample has to be on the order of a few microkelvin. Using a transition with a small Γ offers a simple way to reach this temperature regime. For example, MOTs in ytterbium (erbium) with $\Gamma = 2\pi \cdot 200\,\mathrm{kHz}$ ($\Gamma = 2\pi \cdot 190\,\mathrm{kHz}$) have Doppler temperatures of $T_D = 4.8\,\mu\mathrm{K}$ ($T_D = 4.6\,\mu\mathrm{K}$) [71, 72]. It is even possible to reach temperatures of a few hundreds of nanokelvin for example in strontium (dysprosium) with $\Gamma = 2\pi \cdot 7.6\,\mathrm{kHz}$ ($\Gamma = 2\pi \cdot 1.8\,\mathrm{kHz}$) [13, 174]. In these cases the atoms cannot be trapped directly from the ZS as the capture velocities of narrow-line MOTs are too small, hence the atoms are first trapped in a standard MOT and then further cooled in the narrow-line MOT.

To avoid this extra step we use the 626 nm transition with a transition rate of $\Gamma = 2\pi \cdot 136\,\mathrm{kHz}$ ($T_D = 3.3\,\mu\mathrm{K}$) for trapping the atoms in the MOT, inspired by Er and Yb experiments. The MOT beams are retroreflected and two beams are aligned under an angle of 45° with respect to the horizontal and vertical axis. They have a diameter of 22.5 cm to accomplish a large trapping volume and the light intensity is about $I_{\mathrm{MOT}} = 370\,I_{\mathrm{s},626}$ per beam. See Figure (4.7) and Figure (4.8) for a schematic drawing of the MOT chamber.

In the following we mainly focus on the ^{164}Dy isotope, while the other isotopes are qualitatively similar. We load more than 1.5×10^8 atoms at a temperature of $500\,\mu\mathrm{K}$ in 4 s at a detuning of $\delta_{626} = -35\,\Gamma_{626}$ and with an axial magnetic field gradient of $\nabla B = 3\,\mathrm{G/cm}$. As the cooling light is far red detuned, the obtained temperature is much higher than the Doppler limit. To reduce the temperature the MOT is compressed in 170 ms using two linear ramps. The compression is done by decreasing the 626 nm light intensity to $I_{\mathrm{cMOT}} = 0.15\,I_{\mathrm{s},626}$ and the detuning to $\delta_{cMOT} = -2.75\,\Gamma_{626}$. We note that we can avoid atom losses during the compression ramp when we open the magnetic field gradient to $\nabla B = 1.5\,\mathrm{G/cm}$. Finally, we end up with 1.5×10^8 atoms at a temperature of $6\,\mu\mathrm{K}$ and an atomic number density of about $n = 8.6 \times 10^{10}\,\mathrm{cm}^{-3}$, resulting in a phase-space density of $\mathcal{D} = 1.5 \times 10^{-5}$. We are not able to reach the Doppler temperature as we have to be further red detuned than the optimal detuning of $\delta = -0.5\,\Gamma_{626}$ to hold the atoms against gravity. We also have observed that MOT temperatures between $6\,\mu\mathrm{K} \lesssim \mathrm{T_{cMOT}} \lesssim 20\,\mu\mathrm{K}$ don't effect the loading efficiency of the ODT.

Figure (5.3) shows the atom number as a function of the MOT detuning. The atom number increases for higher detunings as the capture volume gets larger. After reaching its maximum the atom number decreases rapidly because of the finite size of the trapping beams. In addition, we can broaden the 626 nm light with an EOM which has a resonance frequency of 105 kHz. At a detuning of $\delta_{626} = -35\,\Gamma_{626}$ the EOM provides frequency components from $0\,\Gamma_{626}$ to $-70\,\Gamma_{626}$, see inset of Figure (5.3)(a). The usage of the EOM allows us to go to higher detunings resulting in a higher atom number in the MOT. Between $-28\,\Gamma_{626}$ and $-35\,\Gamma_{626}$ the detuning curve shows a drop in atom number. This is presumably due to stray magnetic fields restricting the cloud's elongation.

We are also able to create a MOT for the ^{162}Dy isotope with $N = 1.3 \times 10^8$ atoms. The lower atom number in comparison to the ^{164}Dy isotope is due to its lower natural abundance. Additionally, we can trap $N = 2.1 \times 10^7$ atoms of the fermionic ^{161}Dy isotope without any additional repumpers. The reached atom number is even higher than one would expect from taking into account its natural abundance and also the fact that only the $F = 21/2$ hyperfine state is trappable by the MOT.

We can prove by state selective imaging using 626 nm light that most of the atoms are automatically pumped by the MOT light to the lowest Zeeman sub-state $m_J = -8$. An explanation can be found if one considers the fact that a narrow-line MOT is strongly influenced by gravity. For higher detunings the cloud shifts downward in the direction of gravity and increases its volume. This has been already seen in Er [71, 175] and strontium [174, 176]. The MOT then stays at a finite magnetic field and there the natural optical pumping of a red-detuned MOT to high-field seeking states takes place. A homogenous magnetic field during the compression and also during the transfer to the ODT prevents spin flips and keeps the sample spin-polarized.

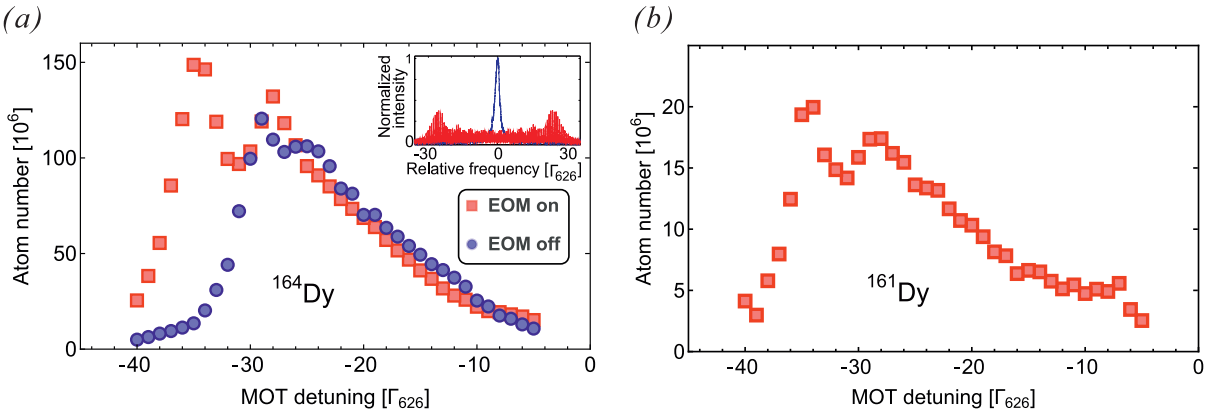

Fig. 5.3, Dy MOT operating at the 626 nm transition: *(a)* Atom number as a function of the 626 nm light detuning. A spectral broadener allows us to achieve higher detunings and consequently increases the atom number (squares). The orange light frequency is broaden up to $\approx 70\,\Gamma_{626}$ by an EOM (inset). *(b)* Due to the natural abundance and also the fact that only one hyperfine state is trappable, the reached atom number of the fermionic isotope is lower than for the bosonic isotopes.

Before the atoms enter the ZS we provide a transverse cooling stage based on a two-dimensional optical molasses. The 421 nm beams are elliptically shaped ($w_x = 6.8$ mm and $w_y = 1.7$ mm) to achieve a higher spacial overlap with the atomic beam. We typically use a power of $P_{\text{trans}} = 100$ mW resulting in an intensity of $I_{\text{trans}} = 9\,I_{\text{s,421}}$. To analyze the effect of the transverse cooling we fit a standard rate equation $N(t) = N_{\text{ss}}(1 - e^{-\gamma t})$ to the measured loading curves, see Figure (5.4)(a). Here, $N_{\text{ss}} = R/\gamma$ is the steady-state value, R the capture rate and γ the decay rate. For the maximum available transverse cooling light power of $P_{\text{trans}} = 165$ mW ($I_{\text{trans}} = 15\,I_{\text{s,421}}$) per beam, we obtain a steady-state

value of $N_{ss} = 2.0 \times 10^8$ atoms, a capture rate $R = 3.1 \times 10^8\,s^{-1}$ and a decay rate of $\gamma = 1.6\,s^{-1}$. The transverse cooling increases the atom number by a factor of 5 and the capture rate by a factor of 8, see Figure (5.4)(b-c).

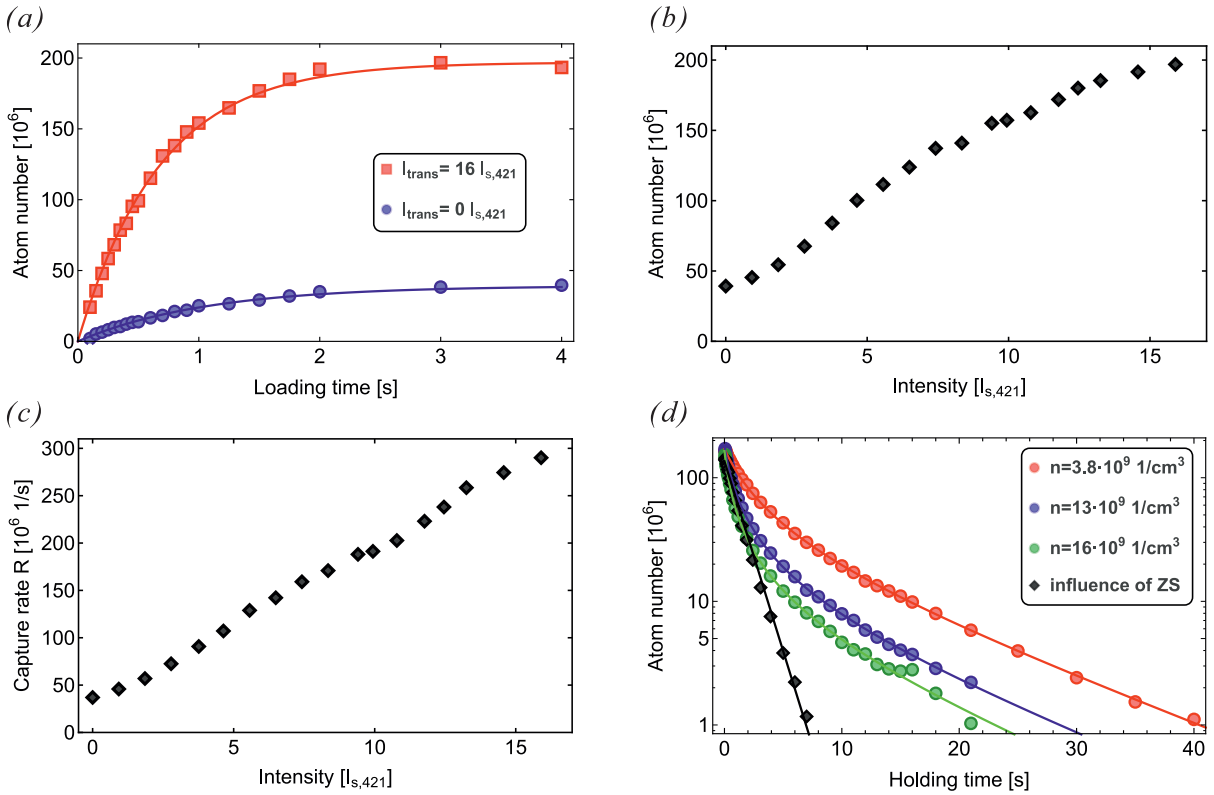

Fig. 5.4, Properties of the 626 nm MOT: *(a)* Atom number as a function of the loading time at $\delta_{626} = -35\,\Gamma_{626}$. By fitting the standard loading rate equation one can extract the atom number and the capture rate R shown in *(b-c)* for different transverse cooling light intensities. Due to the transverse cooling the capture rate is increased by a factor of 8 and the maximum atom number by a factor of 5. *(d)* Atom number as a function of the holding time at a detuning of $\delta_{626} = -35\,\Gamma_{626}$. The fast decay is caused by the ZS light (diamonds). We use Eq. (5.7) to extract the two-body loss rate. After the fast two-body decay, we observe an one-body loss rate of around $1/\gamma = 12\,s$, still limited by one-body scattering processes of the 626 nm light.

We studied the decay rate of the MOT depending on the atom density and ZS light by measuring the decay dynamics of our MOT. After loading the MOT for 4 s we block the atomic beam. We observe that the maximum atom number is mainly limited by losses caused by the ZS light. The fast decay of the atom number ($\gamma = 1.4\,s^{-1}$) is due to off-resonant pumping of the ZS light to excited-states. To avoid this one has to spatial separate the atomic cloud from the ZS light [71]. We observe the fast decay for any detuning δ_{626} which means that in our configuration, where the ZS light propagates at an angle of 20° with respect to gravitational direction, the spatially separation of the cloud from the ZS in not possible.

To further investigate the loss mechanism we switch-off the ZS light and field resulting in a slower decay dynamic. Even without the ZS light we see a fast decay at the beginning, which we attribute to two-body losses due to light-induced collisions. The two-body loss rate β can be extracted using the following equation for the atom number evolution [177]:

$$N(t) = \frac{N_{\mathrm{ss}}\gamma e^{-\gamma t}}{\gamma + \frac{\beta N_{\mathrm{ss}}\rho_{\mathrm{ee}}(1-\rho_{\mathrm{ee}})}{\bar{V}}(1-e^{-\gamma t})}\,, \tag{5.7}$$

where N_{ss} is the steady-state atom number, γ the one-body loss rate, ρ_{ee} the relative excited-state population and $\bar{V} = 2\sqrt{2}\pi^{3/2}\sigma_x^2\sigma_y$ the effective volume with σ_y the axial and σ_x the radial cloud size. To study the density dependence we took decay curves for three different atomic number densities $n = N_{\mathrm{ss}}/\bar{V}$ by changing the trapping volume with the magnetic field gradient at a detuning of $\delta_{626} = -35\,\Gamma_{626}$, see Figure (5.4)(d). Furthermore, we investigated the decay rate of the compressed MOT, where we have a ten-times lower relative excited-state population due to the smaller detuning and lower light intensity. As a result we estimated the two-body loss rate to $\beta = 3.0(3) \times 10^{-9}$ which is independent of the atomic number density and the relative excited-state population of $\rho_{\mathrm{ee}} = 0.037$.

The slow decay ($1/\gamma = 12\,\mathrm{s}$) at longer times is caused by one-body scattering processes of the orange light for all densities. To investigate this we reduced the intensity after the loading phase to different intensities between $1\,I_{\mathrm{s},626} \leq I_{626} \leq 18\,I_{\mathrm{s},626}$. At low intensities we are able to achieve decay rates of $1/\gamma = 35\,\mathrm{s}$.

To summarize, with our MOT operating at the 626 nm transition we reach atom numbers $N > 10^8$ for the bosonic ^{164}Dy and ^{162}Dy isotopes at a temperature of $6\,\mu$K. These are good starting conditions for transferring the atoms into the ODT and creating a BEC. In addition, the atom number of the fermionic ^{161}Dy isotope $N = 2.1 \times 10^7$ is sufficient to reach a degenerate Fermi gas. The results presented in this section have also been published in [50].

5.3 Dysprosium Atoms in Optical Dipole Traps

Optical dipole traps are an important tool in ultra-cold quantum gas experiments. For dipolar atoms an ODT is essential as this technique allows to trap atoms in the lowest Zeeman state where dipolar relaxation is suppressed. The atoms are transferred from the compressed MOT in the first ODT created by the high-power transport beam. By moving the focusing lens of this beam the atoms are transported from the MOT chamber to the science cell. In this ODT forced evaporative cooling is not possible because its mode structure causes heating. To circumvent this limitation once in the science cell the atoms are transferred into a crossed ODT created by a narrow-linewidth laser and finally a degenerate Dy quantum gas is achieved.

5.3.1 General Description and Trap Properties

Optical dipole traps for neutral atoms are based on the electric dipole interaction with a far-detuned light field. In this section we give the needed expressions to discuss the properties of our ODTs. A detailed description can be found in Ref. [178]. The strong electric field $\boldsymbol{E}(t)$ created by a laser induces a dipole moment $\boldsymbol{p}(t) = \alpha \boldsymbol{E}(t)$ with α the scalar complex polarizability of the atom. The dispersive interaction energy U_{dip} of the induced dipole moment with the light field can be calculated by

$$U_{\mathrm{dip}}(\boldsymbol{r}) = -\frac{1}{2}\left\langle \boldsymbol{p}(t)\boldsymbol{E}(t)\right\rangle = -\frac{1}{2\epsilon_0 c}\mathrm{Re}\left\{\alpha\right\}\mathrm{I}(\boldsymbol{r})\ , \tag{5.8}$$

where $I = 2\epsilon_0 c\left|E\right|^2$ is the intensity of the field. On the other hand, the light field can also induce heating of the atomic sample as photons are absorbed and spontaneously re-emitted. The rate of the scattering events is given by

$$\Gamma_{\mathrm{sc}}(\boldsymbol{r}) = \frac{P_{\mathrm{abs}}}{\hbar\omega} = \frac{\left\langle \dot{\boldsymbol{p}}(t)\boldsymbol{E}(t)\right\rangle}{\hbar\omega} = \frac{1}{\hbar\epsilon_0 c}\mathrm{Im}\left\{\alpha\right\}\mathrm{I}(\boldsymbol{r})\ . \tag{5.9}$$

This means that the interaction potential U_{dip} and also the scattering rate Γ_{sc} depend on the complex polarizability $\alpha(\omega)$ and the intensity distribution $I(\boldsymbol{r})$ of the light field.

The polarizability $\alpha(\omega)$ can be calculated using the Lorenz model which describes a neutral two-level atom in an oscillating electric field. Thereby, the following expressions for the interaction potential and the scattering rate can be obtained [178]:

$$U_{\mathrm{dip}}(\boldsymbol{r}) = -\frac{3\pi c^2}{2\omega_0^3}\left(\frac{\Gamma}{\omega_0-\omega}+\frac{\Gamma}{\omega_0+\omega}\right)I(\boldsymbol{r}), \tag{5.10a}$$

$$\Gamma_{\mathrm{sc}}(\boldsymbol{r}) = \frac{3\pi c^2}{2\hbar\omega_0^3}\left(\frac{\omega}{\omega_0}\right)^3\left(\frac{\Gamma}{\omega_0-\omega}+\frac{\Gamma}{\omega_0+\omega}\right)^2 I(\boldsymbol{r})\ , \tag{5.10b}$$

with Γ the spontaneous decay rate of the exited state, ω_0 the transition frequency and ω the laser frequency. For real atoms which have more than only one optical transition the dipole potential and the scattering rate can be estimated by summing over all (Γ_i/ω_i) terms of the possible transitions and from this the polarizability $\alpha(\omega)$ can be obtained using Eq. (5.8)[91]. Usually the laser is tuned relatively close to the resonance at ω_0 such that the rotating wave approximation can be used ($\delta \ll \omega_0$) and one can simplify Eq. (5.10a) and Eq. (5.10b) to

$$U_{\mathrm{dip}}(\boldsymbol{r}) = \frac{3\pi c^2}{2\omega_0^3}\frac{\Gamma}{\delta}I(\boldsymbol{r})\ , \tag{5.11a}$$

$$\Gamma_{\mathrm{sc}}(\boldsymbol{r}) = \frac{3\pi c^2}{2\hbar\omega_0^3}\left(\frac{\Gamma}{\delta}\right)^2 I(\boldsymbol{r})\ , \tag{5.11b}$$

[91] The spectroscopy data of most elements can be found in the NIST database.

where $\delta = \omega - \omega_0$ is the laser frequency detuning. If the laser frequency is below the transition frequency ($\delta < 0$) the potential energy U_{dip} is negative and the atoms are trapped in the region of higher intensities. Comparing both equations one finds that it is better to use higher intensities than smaller detunings to keep the scattering rate low and still achieve a sufficient trapping potential. Note that the presented equations are only valid for a two-level atom.

Single Beam Trap

Usually ODTs are created by a tightly focused laser beam at a far-red detuned wavelength of around $\lambda \approx 1\,\mu$m. A focused laser beam with power P is well described by a Gaussian intensity distribution:

$$I(r,z) = \frac{2P}{\pi w(z)^2} \exp\left(-\frac{2r^2}{w(z)^2}\right). \tag{5.12}$$

The waist $w(z)$ can be obtained by

$$w(z) = w_0 \sqrt{1 + \left(\frac{z}{z_R}\right)^2}\,, \tag{5.13a}$$

with the minimum beam radius w_0 and the Rayleigh length $z_R = \frac{\pi w_0^2}{\lambda}$.

The trapping potential can be calculated by inserting the intensity distribution Eq. (5.12) in Eq. (5.8). For low temperatures the atoms are trapped in the harmonic regime of the potential and we can approximate the potential to

$$U_{\mathrm{dip}} \approx -U_0 + \frac{m}{2}(\omega_r^2 + \omega_z^2)\,, \tag{5.14a}$$

where the trap depth is defined as

$$U_0 = \frac{\mathrm{Re}\,\{\alpha\}\,\mathrm{P}}{\epsilon_0 \pi c w_0^2} \tag{5.14b}$$

The polarizability $\mathrm{Re}\,\{\alpha\}$ can be either calculated using spectroscopy data (see section above) or by measuring the trap frequencies (see the following section). By determining the radial and axial trap frequencies

$$\omega_r = \sqrt{\frac{4U_0}{m w_0^2}} \quad \omega_{\mathrm{z}} = \sqrt{\frac{2\mathrm{U}_0}{\mathrm{m z}_{\mathrm{R}}^2}} \tag{5.15}$$

the trap is fully characterized.

Crossed Beam Configuration

A higher forced evaporative cooling efficiency can be reached if the local density of the atoms is increased. This we can obtain using a crossed ODT created by two perpendicular crossed laser beams. To be able to obtain different trap geometry it could be necessary to use elliptical beams. Thus, we have to extend Eq. (5.12) to obtain the intensity distribution for the k'th beam [166]:

$$I_k(x,y,z) = \frac{2P_k}{\pi w_{x,k}(z) w_{y,k}(z)} \exp\left[-2\left(\frac{x^2}{w_{x,k}(z)^2} + \frac{y^2}{w_{y,k}(z)^2}\right)\right] \tag{5.16}$$

along the optical axis z. Our crossed trap is created by ODT 1 ($I_1(y,z,x)$) pointing along the x-direction and by ODT 2 ($I_2(x,z,y)$) perpendicular aligned to the first beam along the y-direction[92]. The trapping potential created by both beams can be described in the harmonic approximation by

$$U_{\text{trap}}(x,y,z) \approx -\underbrace{\frac{\text{Re}\{\alpha\}}{\epsilon_0 \pi c}\left(\frac{P_1}{w_{1,y}w_{1,z}} + \frac{P_2}{w_{2,x}w_{2,z}}\right)}_{U_0} + \frac{m}{2}(\omega_x^2 + \omega_y^2 + \omega_z^2)\,, \tag{5.17}$$

with the adapted trap frequencies in the corresponding directions $\omega_x, \omega_y, \omega_z$. See Ref. [166] for their exact expressions. For a non-radially symmetric trap two trap ratios can be defined along the x and y axis $\lambda_{x,y} = \omega_z/\omega_{x,y}$.

In general, the trapping potential is modified by gravity and by any magnetic gradient which results in an additional force acting on the strongly magnetic atom. Especially, the potential in z-direction is lowered by gravity. We have installed additional gradient coils to be able to compensate for gravity, see section 4.4. The effective trapping potential U_{trap} created by the optical dipole potential U_{dip} is superimposed by the gravitational potential U_{gravity} and modified by any further magnetic gradient U_{mag}. It can be calculated as

$$U_{\text{trap}}(x,y,z) = U_{\text{dip}}(x,y,z) + U_{\text{gravity}}(x,y,z) + U_{\text{mag}}(x,y,z). \tag{5.18a}$$

In the z-direction one obtains:

$$U_{\text{trap}}(z) = U_{\text{dip}}(z) + m g_{\text{earth}} z + \mu_m B_{\text{grad}}(z)\,, \tag{5.18b}$$

with the magnetic moment μ_m of the atom, the earth gravitational constant g_{earth} and magnetic gradient field B_{grad} created by the gradient coils. For low laser powers gravity tilts the trapping potential and the effective trapping depth is strongly reduced. The gradient coils can be used to compensate gravity as shown in Figure (5.5). On the other hand the gradient coils can also be used to lower the trap depth in a controlled way

[92] in Lab coordinates, see Figure (4.2).

without changing the trap frequencies significantly. This can be used for a more efficient forced evaporative cooling process [163].

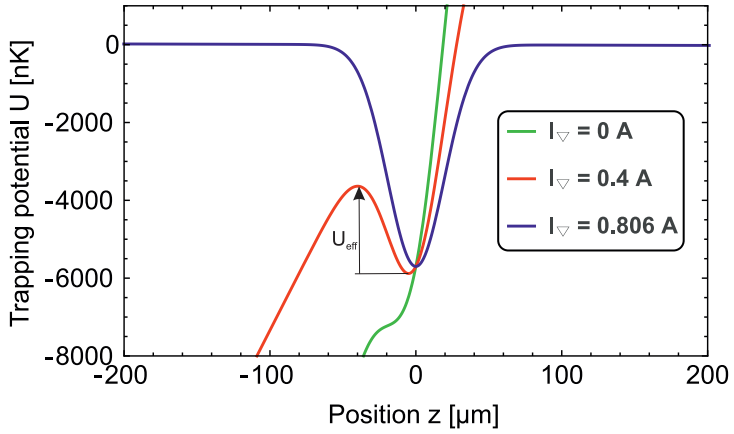

Fig. 5.5, Effective trapping potential in the vertical direction: Gravity strongly modifies the trapping potential and lowers the trap depth to U_{eff}. Using the gradient coils we can externally control the trap depth while only changing weakly the trap frequencies.

In our experiment we use different dipole traps for different purposes. To transport the atoms from the MOT chamber to the science cell we create an ODT by a fiber laser operating at a wavelength of $\lambda = 1070\,\text{nm}$. Subsequently, we perform evaporative cooling in a crossed ODT, created by two laser beams at a wavelength of $\lambda = 1064\,\text{nm}$. And finally a laser operating at a wavelength of $\lambda = 532\,\text{nm}$ is used to create tailored potentials together with the EOD system. As the polarizability for Dy was not known, we first used Eq. (5.11a) to calculate the trap depth based on spectroscopy data, summarized in Table (5.1). Due to its complex electronic structure the energy level spectrum of Dy is quite rich. In addition, many transition properties are not known, hence the obtained polarizability is only a rough estimate. Furthermore, we experimentally determined the trap frequencies of the different traps and used the above mentioned equations to estimate the polarizabilities for the different wavelengths. We obtained a value of $\text{Re}\{\alpha\} = (102 \pm 20)\,\text{a.u.}$[93] for the polarizability of ^{164}Dy at 1070 nm by measuring the trap frequencies in the single transport beam [166]. Note that the measured polarizability depends strongly on the measured beam waist ($\text{Re}\{\alpha\} \propto w^{-4}$). To determine the polarizability at 1064 nm we measured the trap frequencies for different powers of ODT 1 and ODT 2 in the crossed trap. By minimizing the standard deviation of the fitted polarizability we obtain the polarizability of $\text{Re}\{\alpha\} = (136 \pm 15)\,\text{a.u}$ at 1064 nm. For the polarizability at 532 nm we only have one trap frequency measurement, therefore we can only roughly estimate the polarizability to $\text{Re}\{\alpha\} \approx 11\,\text{a.u.}$

[93] Atomic unit of electric polarizability is $1\,\text{a.u.} = 1\,(\text{e}^2\text{a}_0^2)/\text{E}_\text{h}$, with $E_h = 4.360 \times 10^{-18}\,\text{J}$ the Hartree energy, $a_0 = 0.05297\,\text{nm}$ the Bohr radius and $e = 1.602 \times 10^{-19}\,\text{C}$ the elementary charge.

wavelength	calculated	measured	relative deviation
1070 nm	167 a.u.	(102 ± 20) a.u.	39 %
1064 nm	167 a.u.	(136 ± 15) a.u	19 %
532 nm	350 a.u.	11 a.u.	-

Tab. 5.1, Comparison of measured and calculated polarizabilities for different trapping wavelengths.

5.3.2 Optical Transport

The transport beam is created by the tightly focused light of a fiber laser to a minimal waist of 37.3 μm. Due to thermal lensing the waist is increased to $w_0 = 40.5\,\mu$m for laser powers $P > 40\,$W. The maximum laser power at the atoms is $P = 72\,$W which results in a maximal trap depth of

$$U_0 = \frac{\mathrm{Re}(\alpha_{1070})\mathrm{P}}{\epsilon_0 \pi c w_0^2} \approx 640\,\mu\mathrm{K}\ . \tag{5.19}$$

While the potential of the ODT is deep enough to trap the atoms, the spacial overlap between the compressed MOT ($1/e^2$ radius around 400 μm) and the ODT is too small to efficiently transfer the atoms to the ODT. As the last lens of our transport beam is mounted on an air bearing translation stage we can slightly move the focal position of the transport beam by $\Delta x = 15\,\mathrm{mm} \approx 3\,\mathrm{z_R}$ which leads to an increase of the waist to $w(\Delta x) \approx 170\,\mu$m. Hence, the trapping area is enlarged by a factor $(170/40.5)^2 \approx 17.6$, but also the potential depth is decreased by the same amount. After the compression stage the MOT and the ODT are superimposed for 120 ms to transfer the atoms to the ODT. To optimize the transfer efficiency the position of the compressed MOT can be slightly shifted with respect to the ODT position by using the compensation coils. In addition, the transferred atom number depends strongly on the polarization direction of the linear polarized trapping light. A possible explanation for this behavior is the dependency of the heating rate Γ_{sc} on the light polarization with respect to the quantization axis as it was theoretically shown for Er atoms [179]. After the transfer we switch-off the MOT fields and beams. As the atoms are trapped in an out-of-equilibrium position of the optical potential we have to move the focus position of the transport beam in 47 ms back to the zero position such that the potential minimum is at the prior MOT position. Due to the initial potential energy at the loading position and due to the compression the sample heats up[94]. In average we can load around 15×10^6 atoms into the transport beam.

By moving the last lens ($f = 1292\,$mm) of the transport beam we transport the atoms over a range of 375 mm from the MOT chamber to the science cell within 1.9 s. The full laser power of the fiber laser is needed to achieve a transport efficiency close to 100 %. The trapping frequency in the axial direction is only 8 Hz which limits the maximum acceleration of the translation stage. In Figure (5.6)(a) we show the trapezoidal

[94] Another method to increase the loading efficiency without showing strong heating effects is to enlarge the ODT potential temporally by fast scanning the laser beam horizontally using an AOM [180].

acceleration profile of the translation stage. This results in a velocity profile consisting of two linear ramps smoothed by a quadratic behavior at the beginning and at the end. The efficiency of the transport strongly depends on the magnetic offset fields applied during the transport. The Zeeman splitting has to be larger than the thermal energy of the atoms to prevent dipolar relaxation processes. We get the highest efficiency when we apply a magnetic offset field of 1.4 G in the y-direction. We typically end up with $N = 10 \times 10^6$ atoms at a temperature of $T = 120\,\mu$K in the science cell. This is mainly limited by the lifetime of the atoms in the trap. A faster transport would increase the atom number but also induces sloshing of the atoms in the trap. We also see that during the transport the atoms undergo plain evaporation, see Figure (5.6)(b)

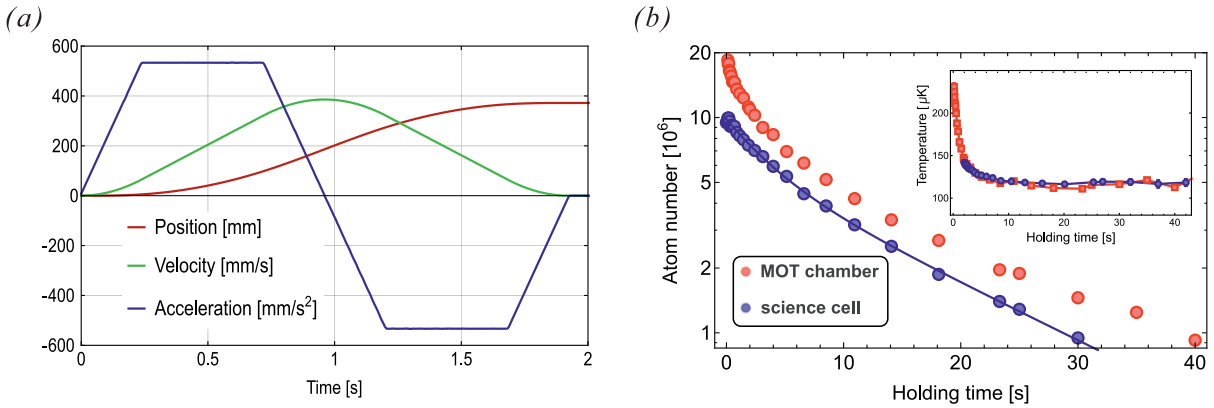

Fig. 5.6, Optical transport: *(a)* To transport the atoms we choose a trapezoidal acceleration profile (blue) with a maximum acceleration of 535 mm/s^2. The maximum velocity (green) of 390 mm/s is reached after 0.95 s and results in a s-curved position profile (red). *(b)* Lifetime measurement of the trapped atoms in the MOT chamber (red) and in the science cell (blue). The lifetime in the MOT chamber and in the science cell is 20 s and 16 s, respectively. The temperature dependence on the holing time is shown in the inset. During the transport time the atoms undergo plain evaporative cooling.

After the atoms are transported to the science cell, forced evaporative cooling has to be performed to reach quantum degeneracy. Unfortunately this is not possible in the transport beam as the mode structure of the laser induces heating. Thus, we have to transfer the atoms from the transport beam in a second ODT created by a laser with a narrow linewidth. Both beams use the same path (see Figure (4.6)) and have approximately the same beam waists to maximize the spacial overlap. The transfer process is done by linearly ramping down the power of the transport beam to 20 % of its initial power in 100 ms and afterwards ramping up the ODT 1 power in 100 ms. Thereby we can transfer about 90 % of atoms from the transport beam into ODT 1. The lifetime in ODT 1 is increased to 25 s, which is still shorter than we expect from our background pressure $< 10^{-11}$mbar. One possible loss mechanism could be the micro motion of the translation stage, thus in a new setup also ODT 1 is guided via a high-power fiber to the science cell and overlapped with the transport beam directly in front of the glass cell.

5.3.3 Doppler Cooling in the Dipole Trap

For evaporative cooling, a high collision rate is essential. We use a second dipole trap ODT 2 superimposed perpendicular to ODT 1 to create a crossed ODT. Here, the density and thus the collision rates are increased. We ramp up ODT 2 simultaneously with ODT 1. But the atoms are too hot to be trapped in the crossed region. By applying a further laser cooling step using σ^- polarized 626 nm light we can cool the atoms in the crossed trap. Our approach is inspired by the Doppler cooling phase which was applied for magnetically trapped Cr atoms [146].

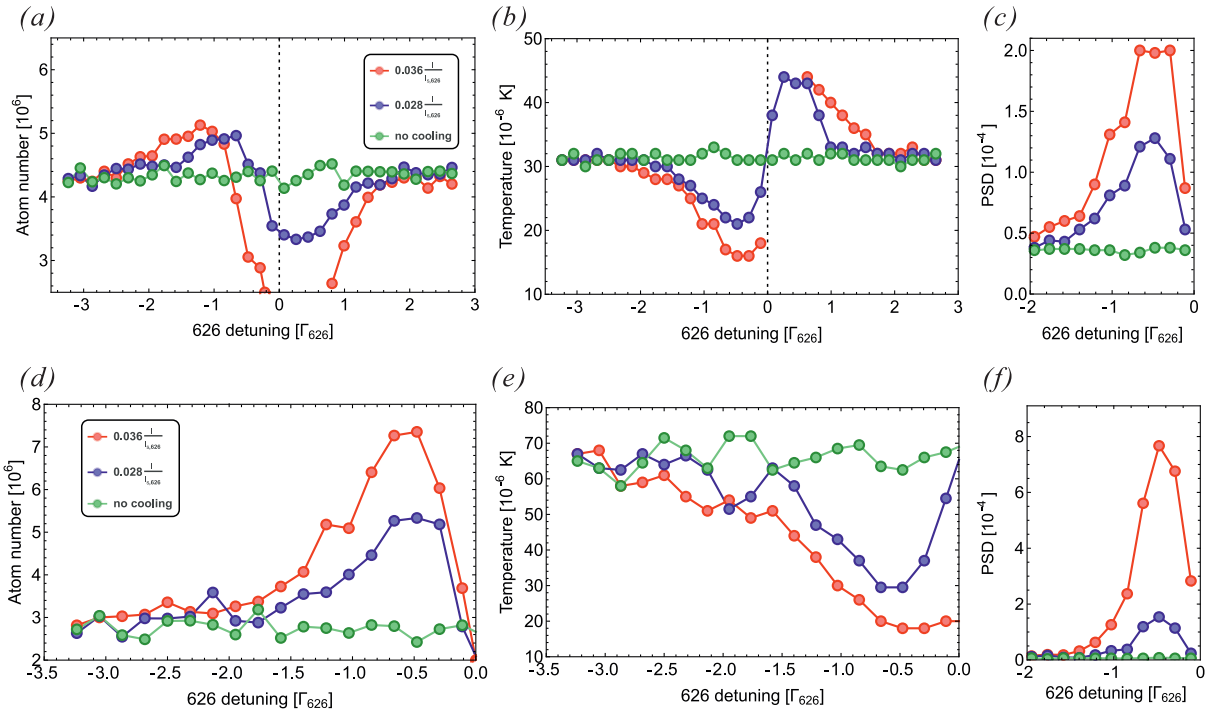

Fig. 5.7, Doppler cooling in the ODT: *(a,d)* Atom number, *(b,e)* temperature and *(c-f)* phase-space density of ODT 1 *(a-c)* and of the crossed ODT *(d-f)* as a function of the 626 frequency detuning δ after the Doppler cooling. At $\delta = -\Gamma_{626}/2$ the atom number of the crossed ODT has its maximum and its temperature is minimal without loosing many atoms from ODT 1. The increase in atom number in *(a)* is caused by the fact that the atoms which are far out in the wings of the ODT (not recordable by the image) move to the center of the trap and the reduction of evaporation due to the cooling.

To perform Doppler cooling in the crossed ODT the atoms are illuminated for 500 ms with the cooling light (beam waist $w_0 = 3.0\,\text{mm}$) along the y-direction and a magnetic offset field of 2.3 G is applied. The atoms are Doppler cooled by the light only in one direction, but due to the collisions the whole sample equilibrates at a lower temperature. In Figure (5.7) the effect of the cooling light for the ODT 1 (a-c) and for the crossed ODT (d-f) for different cooling powers is shown[95].

[95] We also actively stabilize the 626 nm Doppler cooling power which increases the stability of the system.

Without the cooling light we have $N = 4 \times 10^6$ atoms in ODT 1 at around $T = 30\,\mu$K. By applying the additional Doppler cooling procedure we reach temperatures below $20\,\mu$K without loosing many atoms. The lowest temperature is obtained at a frequency detuning of $\delta = -\Gamma_{626}/2$, which is in nice agreement with the textbook prediction of Doppler cooling [170]. But even more important is that due to the Doppler cooling the atom number in the crossed ODT is increased to $N_{\mathrm{cODT}} = 700 \times 10^3$ atoms.

The efficiency of a cooling method can be analyzed using the factor

$$\chi = -\frac{log(\mathcal{D}_{k+1}/\mathcal{D}_k)}{log(\mathcal{N}_{k+1}/\mathcal{N}_k)}\,, \tag{5.20}$$

which compares the increase in phase-space density $\mathcal{D}_{k+1}/\mathcal{D}_k$ per atom number loss $\mathcal{N}_{k+1}/\mathcal{N}_k$ in the cooling step $k \to k+1$. For the Doppler cooling the used intensity and the frequency detuning has to be chosen in a trade-off between an increase in phase-space densities and loss of atoms. Using Eq. (5.20) we can estimate a cooling efficiency of $\chi \approx 15$ for the Doppler cooling in ODT 1. The lowest temperature we can reach is around $16\,\mu$K which is far above the Doppler limit of $T_{\mathrm{Doppler}} = 3.3\,\mu$k. We found that the light shift of the excite-state of the 626 nm transition is reversed to the ground-state shift which means that we can cool the hot atoms in the wings but by decreasing the frequency detuning we heat up the atoms trapped in center of the potential. Hence, to further cool the atoms we have to use the standard approach of forced evaporative cooling described in the next section.

A cooling method, which has a higher efficiency than forced evaporative cooling and no Doppler temperature limit, is demagnetization cooling. Here, due to inelastic dipolar collisions the atom can transfer its thermal energy into Zeeman energy by populating a higher Zeeman level, thereby the sample cools down. Using an optical pumping transition (in Dy the 684 nm transition would be a good choice) the atoms can be transferred back to the initial stage, leaving the temperature nearly unchanged. If the temperature of the sample is lower than the Zeeman energy the cooling stops and the Zeeman splitting has to be lowered using an external magnetic offset field and the cooling cycle can start again. This was already studied in Cr where a cooling efficiency of $\chi > 11$ was observed and will be soon implemented in our setup [73, 181].

5.3.4 Forced Evaporative Cooling of Bosonic and Fermionic Dy

To finally reach a degenerate quantum gas we have to use the well established method of forced evaporative cooling [15]. The basic idea of forced evaporative cooling is to remove the high-energy atoms from the thermal cloud which results in a lower temperature of the sample due to elastic collisions among the remaining atoms. An atom in an ODT can leave the trap if its total energy $E_{\mathrm{kin}} + E_{\mathrm{pot}}$ exceeds the trap depth $U_0 \propto P$ (see Eq. (5.14b)). For a constant trap depth the evaporation rate however stagnates and the trap depth has

to be lowered. In a dipole trap evaporative cooling can be forced by reducing the laser power slowly. Unlike in MTs where the trap depth can be lowered by a RF-knife also the trap frequencies decrease as they are related to the trap depth, see Eq. (5.15). Hence, density and the elastic collision rate are reduced for lower trap depths.

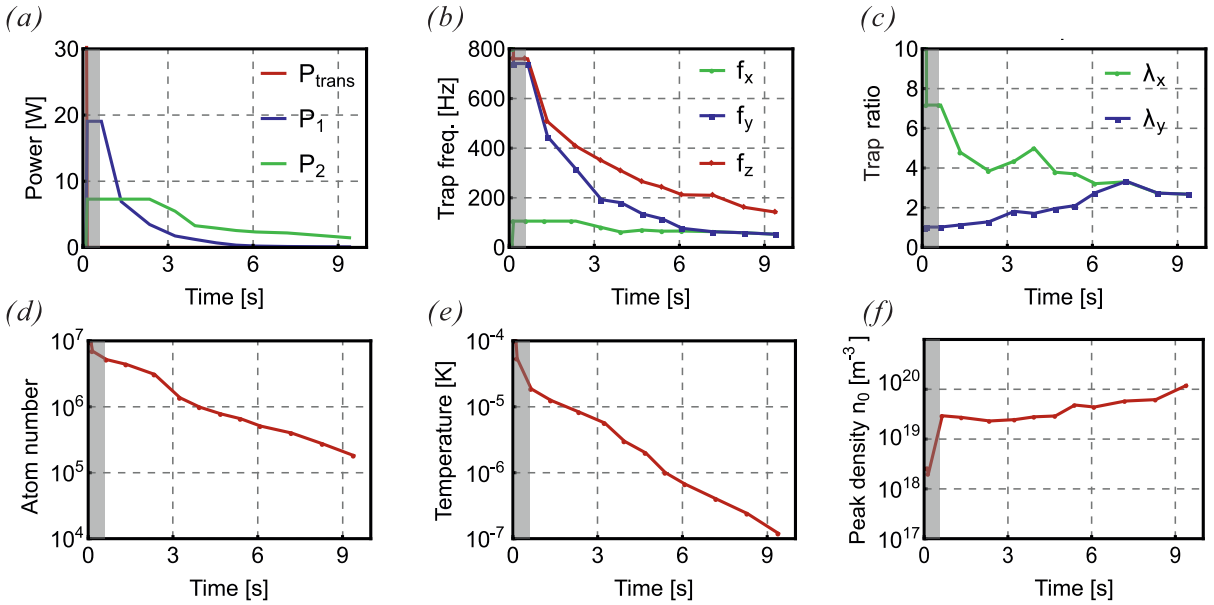

Fig. 5.8, Forced evaporative cooling: The trap parameters *(a-c)* and the evolution of the atom number *(d)*, the temperature *(e)* and the peak density *(f)* of the evaporation ramps are presented. The shaded area indicates the Doppler cooling phase. After 9.4 s we obtain a BEC in a radially symmetric trap with a trap ratio of $\lambda = 2.7$.

The presented results in this section are for traps created by ODT 1 with $(w_{0,y}, w_{0,z}) = (40, 35)\,\mu$m and ODT 2 to $(w_{0,x}, w_{0,z}) = (105, 36)\,\mu$m. Typically we start with $N_{\mathrm{cODT}} \approx 900 \times 10^3$ atoms at a temperature of $T_{\mathrm{cODT}} \approx 20\,\mu$K in the crossed region and still $N_{\mathrm{ODT}} \approx 4000 \times 10^3$ atoms are present in the wings of ODT 1. By forced evaporative cooling we have to increase the phase-space density from $\mathcal{D} = 9 \times 10^{-4}$ four orders of magnitude to finally reach the BEC transition ($\mathcal{D} = 2.6$). We reduce the power of ODT 1 in an exponential-like piecewise linear ramp. After the second ramp we also decrease the power of ODT 2 to reduce the trap depth. The time duration of each linear ramp is optimized by maximizing the cooling efficiency χ (Eq. (5.20)). During the evaporation ramp we apply a magnetic offset field of $B = 1.25$ G pointing in the z-direction. With this field we are not in the vicinity of any Feshbach resonance (see section 6.1). In Figure (5.8) the experimental sequence in the science cell with the typical trap parameters and achieved values of the atom number, temperature and peak density are shown. For the last ramps the powers of ODT 1 and ODT 2 have to be adjusted such that a trap ratio of $\lambda > 2$ is obtained to be in the stable region of the stability diagram of a Dy BEC (see section 3.4.4). After around 9 s we observe the onset of the phase transition in a oblate

trap with a final trap ratio $\lambda = f_z/\sqrt{f_x f_y} = 2.7$. Here, the symmetry axis is defined by the external magnetic field, which points in z-direction.

Figure (5.9) shows the increase of the phase-space density. The cooling efficiency can be analyzed using a double-logarithmic plot of the phase-space density over the atom number. The slope of the graph is directly related to the efficiency χ. The overall efficiency is indicated by the linear fit resulting in an efficiency of $\chi = 2.9$. The sudden initial increase of the phase-space density is due to the Doppler cooling in the crossed ODT with 626 nm light.

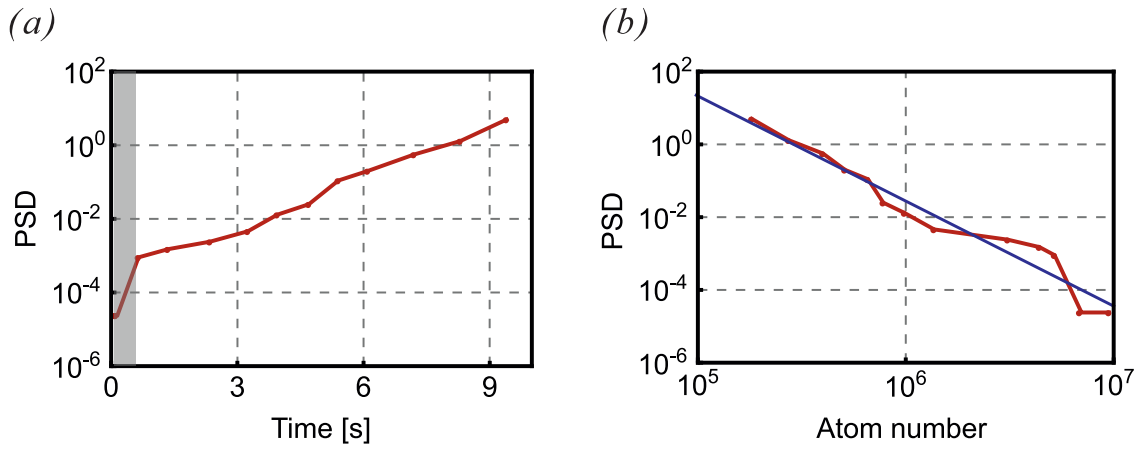

Fig. 5.9, Cooling efficiency: *(a)* Increase of phase-space density (PSD) of each cooling step. *(b)* To analyze the cooling efficiency the phase-space density is plotted over the atom number. The slope of a linear fit according Eq. (5.20) (blue line) gives the overall efficiency $\chi = 2.9$ of the cooling process.

Evaporative cooling of Spin-polarized Fermionic Dy Atoms

The elastic cross-section of two colliding dipolar atoms is modified by the DDI as we have seen in section 3.1.2. For fermions, in contrast to non-dipolar gases the elastic cross-section does not vanish for low temperatures, it even tends to a constant value. This opens the possibility to evaporative cool polarized dipolar fermions. In the following we present the first attempts of forced evaporative cooling of the fermionic ^{161}Dy isotope in our apparatus. To have a high collision rate we need a tighter trap, which we can realize by changing the minimal waist of ODT 1 to $(w_{0,y}, w_{0,z}) = (40, 35)\,\mu$m and of ODT 2 to $(w_{0,x}, w_{0,z}) = (30, 30)\,\mu$m.

When the thermal energy ($k_B T$) of the fermionic gas, reaches the Fermi energy E_F a smooth crossover to quantum degeneracy appears. The corresponding temperature is called Fermi temperature [25]

$$T_F = \frac{E_F}{k_B} = \frac{\hbar\bar{\omega}(6N)^{1/3}}{k_B}\,, \tag{5.21}$$

with $\bar{\omega}$ the mean trap frequency and N the particle number. For temperatures $T < T_F$ the gas is quantum degenerated.

In an optimized sequence we start with 30×10^6 ^{161}Dy atoms in the compressed MOT and we transport in 1 s $N = 1500 \times 10^3$ atoms to the glass cell. The cooling procedure in the science cell is the same as for the bosons. We first apply the Doppler cooling and further cool the atoms by forced evaporative cooling. In Figure (5.10) we present the obtained values. In summary, we can reach a degenerate Fermi gas with $T/T_F \approx 0.5$ and

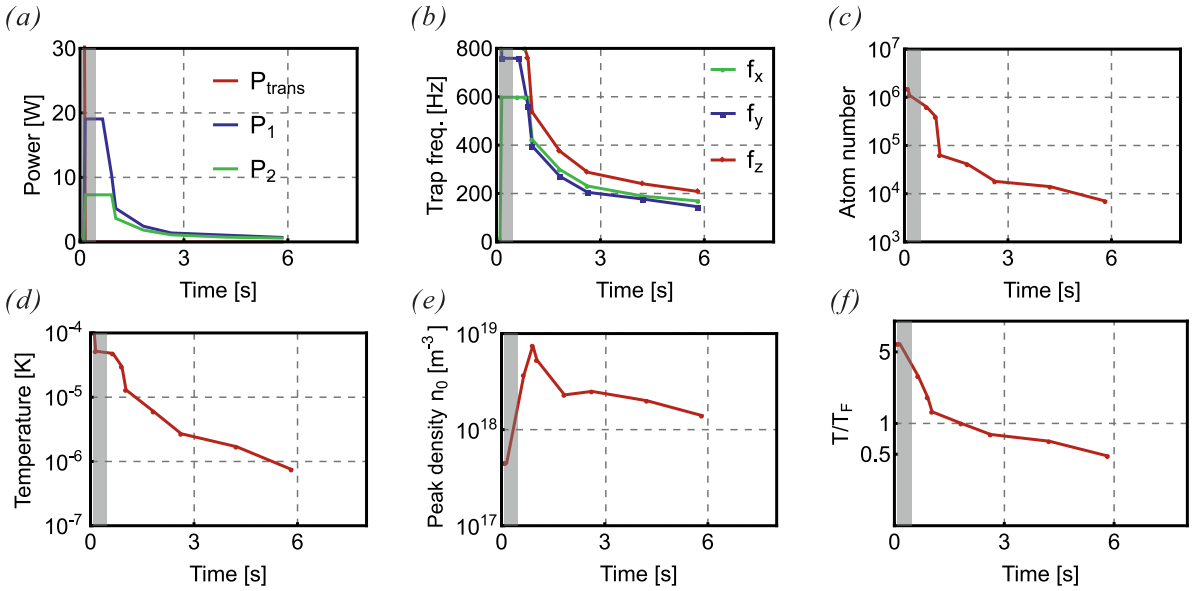

Fig. 5.10, Cooling efficiency of the fermionic ^{161}Dy isotope: To cool the fermionic isotope we use in principle the same methods as for the bosons. The trap parameters are shown in panel *(a,b)*. In panel *(c-f)* one can see that at the beginning the cooling efficiency is sufficient but as soon as the density drops the elastic collision rate decreases and the cooling becomes very inefficient.

$N \approx 10 \times 10^3$ atoms. The overall cooling efficiency is at the moment not very good as the collision rates are already very small at the beginning. To increase the collision rate one has to use a even tighter trap. For example the Innsbruck group uses a crossed ODT with beam waists of 15 μm and 33 μm for the trapping beams and obtains cooling efficiencies of $\chi = 3.5$. They are able to reach $T/T_F = 0.11$ with $N = 3 \times 10^4$ Er atoms [23].

5.4 Bose-Einstein Condensation of Dysprosium Atoms

Using the evaporative cooling method we finally reach the phase transition to a Dy BEC. At temperatures $< 200\,\mathrm{nK}$ we see the first indication of Bose enhancement, which is a slight increase in the density distribution caused by the shift from the Maxwell-Boltzmann distribution towards zero energy close to the critical temperature. Reducing the temperature further we observe the appearance of a narrow peak in the center of the density distribution which we extract from TOF images taken after $t_{\mathrm{TOF}} = 20\,\mathrm{ms}$[96]. The density distribution is well described by a bimodal distribution consisting of a Gaussian background accounting for the thermal atoms and the quadratic behavior within the TF approximation of the condensed atoms. Figure (5.11) illustrates the phase transition to a ^{164}Dy BEC.

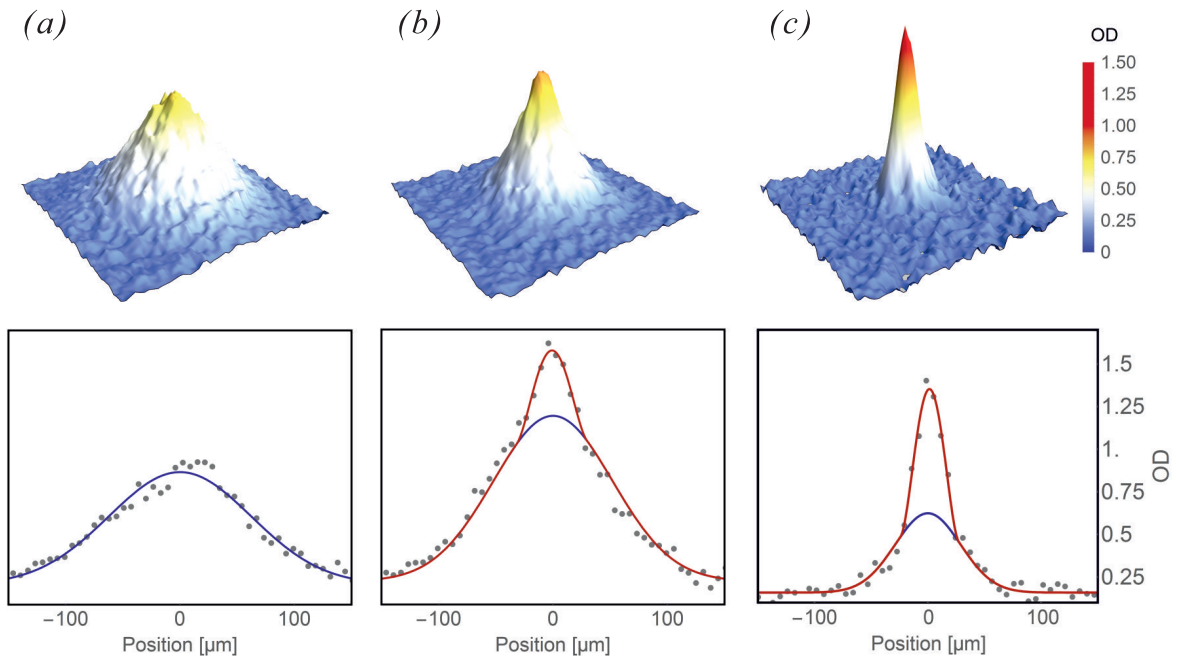

Fig. 5.11, Phase transition to a ^{164}Dy BEC: Optical density profiles (top) and corresponding horizontal cuts (bottom) extracted from absorption images taken after 20 ms of expansion. *(a)* At a temperature of 240 nK the density profile of the atom cloud ($N_{\mathrm{th}} = 270 \times 10^3$) is well described by the Maxwell-Boltzmann distribution. *(b)* Decreasing the temperature further ($T = 180\,\mathrm{nK}$) the onset of the condensation appears ($N_{\mathrm{th}} = 170 \times 10^3$). The density distribution can now be described by a bimodal distribution (red). *(c)* Finally, we obtain $N_{\mathrm{BEC}} = 14 \times 10^3$ condensed atoms with still $N_{\mathrm{th}} = 30 \times 10^3$ in the thermal cloud. The temperature of $T = 50\,\mathrm{nK}$ is obtained by a Gaussian fit to the wings of the distribution (blue).

[96] The cycle time to produce the Dy BEC is around 16 s.

By lowering the trap depth we can increase the BEC atom number as expected. But the condensed atom number saturates at a value of around $N = (10 - 15) \times 10^3$ despite the fact that many atoms are still present in the thermal cloud. The calculated trap frequencies after the last ramp are $(f_r, f_z) = (48, 132)\,\mathrm{Hz}$, which corresponds to a mean trap frequency of $\bar{\omega} = 67\,\mathrm{Hz}$ and a trap ratio of $\lambda = f_z/f_r = 2.75$.

To study the limitation of the BEC atom number we change the trap to be more oblate. This we can do be changing the waists of the ODT 1 to $(w_{0,y}, w_{0,z}) = (36, 36)\,\mu\mathrm{m}$ and ODT 2 to $(w_{0,x}, w_{0,z}) = (150, 30)\,\mu\mathrm{m}$. A higher BEC atom number $N \approx 22 \times 10^3$ can be obtained using a trap with a calculated trap frequencies of $(f_r, f_z) = (50, 248)\,\mathrm{Hz}$ leading to a trap ratio of $\lambda \approx 5$.

In section 3.4.4 we estimated the stability of a Dy BEC using the Gaussian ansatz. Figure (5.12) shows a zoom of the stability diagram. In addition, the results of a numerical calculation is shown[97]. Here, the stability border is shifted to higher trap ratios. Our finding of the reduced BEC atom numbers in a trap with $\lambda = 2.75$ compared to a trap with $\lambda = 5$ can be explained by the fact that the background scattering length a_{bg} is smaller than $100\,a_0$. Based on our obtained BEC atom numbers for different trap geometries we can estimate the background scattering length of the ^{164}Dy isotope to $86\,a_0 < a_{\mathrm{bg}} < 93\,a_0$.

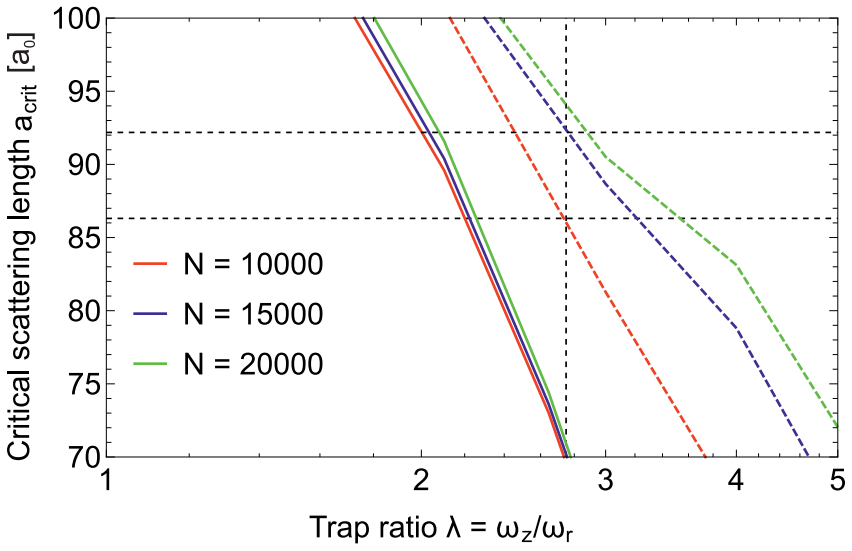

Fig. 5.12, Stability diagram of a ^{164}Dy BEC: Critical scattering length a_{crit} as a function of the trap ratio λ and for different atom numbers. The solid lines show the results of a variational calculation for a mean trap frequency of $\bar{\omega} = 2\pi \cdot 67\,\mathrm{Hz}$. The colored dashed lines represent the solutions of a full numerical simulation of the GPE. The trap ratio of $\lambda = 2.75$ is highlighted by the vertical black dashed line.

Recently, we were also able to condense the ^{162}Dy isotope. For this isotope we used the same trap configuration and cooling procedure as descried in the previous sections

[97] GPE simulations were done by Damir Zajec.

only the final evaporation ramp is slightly different. The final trap frequencies in the crossed ODT are $f_x = f_y = 42\,\mathrm{Hz}$ and $f_z = 143\,\mathrm{Hz}$ resulting in a mean trap frequency of $\bar{\omega} = 2\pi \cdot 63\,\mathrm{Hz}$ with a trap ratio of $\lambda = f_z/\sqrt{f_x f_y} = 3.4$. In this configuration we obtain up to $N_{\mathrm{BEC}} = 30 \times 10^3$ condensed atoms with $N_{\mathrm{th}} = 30 \times 10^3$ thermal atoms at a temperature of $T = 60\,\mathrm{nK}$. Furthermore, using similar evaporation ramps as for the ^{164}Dy isotope we observe a more efficient forced evaporative cooling behavior of the ^{162}Dy isotope. Both the higher BEC atom number and the more efficient evaporative cooling indicate a larger scattering length a of the ^{162}Dy compared to the ^{164}Dy isotope which was also observed in Ref. [182].

We further studied the stability of a Dy condensate by changing the polarization direction of the dipoles. Recalling Eq. (3.16c) a quantum gas is strongly dipolar if the dipolar length a_{dd} is larger than the scattering length a. As mentioned earlier we can observe a ^{162}Dy condensate with $N_{\mathrm{BEC}} = 30 \times 10^3$ atoms in a trap with a trap ratio of $\lambda = f_z/\sqrt{f_x f_y} = 3.4$. Here, the dipoles are aligned by an external magnetic field B along the z-direction. If we tilt the magnetic field by 90° such that the field points in y-direction the trap ratio along the new polarization axis changes to $\lambda = f_y/\sqrt{f_x f_z} = 0.54$ and we are in the instability region for a strongly dipolar BEC. In concordance to this prediction we cannot observe a condensate if the magnetic field is tilted in the y-direction, only $N_{\mathrm{th}} = 15 \times 10^3$ thermal atoms are left. This has been also observed for the ^{164}Dy isotope in Ref. [13].

Based on our previous analysis we can estimate the background scattering length of the ^{164}Dy and the ^{162}Dy isotope within some limits. The background scattering length of ^{164}Dy isotope is between $86\,a_0 \lesssim a_{\mathrm{bg}}^{164} \lesssim 93\,a_0$ and of the ^{162}Dy isotope it is $a_{\mathrm{bg}}^{164} \lesssim a_{\mathrm{bg}}^{162} \lesssim a_{\mathrm{dd}}$. Most recently the background scattering length $a_{\mathrm{bg}} = 92(8)\,a_0$ for ^{164}Dy and $a_{\mathrm{bg}} = 112(10)\,a_0$ for the ^{162}Dy isotope were measured by cross-dimensional rethermalization [45]. The measured values are in good agreement with our findings presented in this section. Using the measured values for the background scattering length together with the dipolar length of $a_{\mathrm{dd,Dy}} = 134\,a_0$ we can calculate the relative dipolar strength for both isotopes to $\epsilon_{\mathrm{dd}}^{164} = 1.47(14)$ and $\epsilon_{\mathrm{dd}}^{162} = 1.20(10)$. Hence, the element Dy is well suited to study strongly dipolar effects even without the usage of Feshbach resonances.

5.5 High-resolution Image of a Dipolar BEC

To extract the density profile $n(x, y, z)$ of the atomic cloud we expose the atoms with 421 nm light and register the intensity profile $I(x, y, z)$ by a CCD camera. A standard method in quantum gas experiments is the absorption imaging technique. Here, the intensity of the probe light with frequency ω_p passing through the atomic cloud is reduced by

$$I(x, y, z) = I_0 e^{-\sigma(\omega_p)\int_{-\infty}^{x} n(x', y, z)dx'}\,, \tag{5.22}$$

which is equal to Beer's law $I(x) = I_0 e^{-OD\,x}$ for a constant density n and with the optical density OD. For low intensities ($I \ll I_{\mathrm{sat}}$) the light scattering cross-section of resonant imaging light can be estimated with

$$\sigma(\omega_p) = \frac{6\pi c^2}{\omega_p^2} \,. \tag{5.23}$$

As a result the registered intensity distribution by the CCD camera after passing the atomic cloud contains information on the column density of the atoms

$$n(y,z) = \int_{-\infty}^{\infty} n(x',y,z)dx' = \frac{1}{\sigma(\omega_p)}\, OD \,. \tag{5.24}$$

To be independent of the CCD camera properties we take three different pictures. The first image with the intensity profile $\tilde{I}_1$ is taken with atoms, the second one with $\tilde{I}_2$ without atoms and finally the third one with $\tilde{I}_3$ without the resonant probe light. Based on this the optical density can be calculated by [166]

$$OD = \ln\left(\frac{\tilde{I}_2 - \tilde{I}_3}{\tilde{I}_1 - \tilde{I}_3}\right) \,. \tag{5.25}$$

Due to the limited dynamic range of the CCD camera low intensity absorption imaging is limited to $OD \approx 3$. To extract the density profile of a BEC we usually take an image after a long TOF of around $t_{\mathrm{TOF}} = 20\,\mathrm{ms}$, such that the remaining thermal cloud is expanded and the bimodal distribution is clearly visible. Thus, the optical density is usually on the order of $OD \approx 1$.

Because of the much higher in-trap densities absorption imaging cannot be used to take in-trap images. However, we can use the so called phase-contrast polarization imaging, which was first introduced in Ref. [183]. It relies not on the absorption of the atoms but on the dispersive phase shift to extract the optical density. Here, the atoms are exposed with linear polarized light. In addition, an external magnetic field parallel to the imaging axis is applied which splits the linear polarization into equal parts of σ^+ and σ^- light. Due to the different Clebsch-Gordan coefficients only the σ^- part is affected by the atoms. After the atomic cloud a linear polarizer with an angle θ to the initial linear polarization combines the different circular polarizations and the resulting intensity depends on the dispersive phase shift caused by the atoms. To extract the optical density also three images are taken and one can calculate [166]

$$OD = 8\left(\frac{\delta}{\Gamma}\right)\left[\theta - \arccos\left(\sqrt{\frac{\tilde{I}_1 - \tilde{I}_2}{\tilde{I}_2 - \tilde{I}_3} + 1}\;\cdot\;\cos(\theta)\right)\right] \,, \tag{5.26}$$

where δ is the frequency detuning from resonance of the imaging light and Γ the natural transition rate of the used transition.

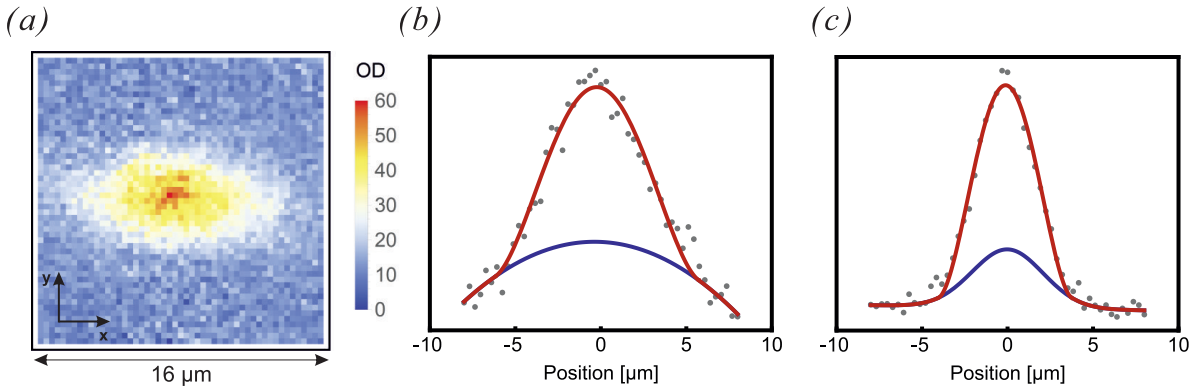

Fig. 5.13, In-situ image of a Dy BEC: *(a)* Phase-contrast polarization image of a nearly pure BEC with $N_{\mathrm{BEC}} = 17 \times 10^3$ atoms. Here, the imaging detuning is $\delta \approx 35\,\Gamma$ and the angle of the polarizer is $\theta = 15°$. In *(b-c)* we show the integrated density distribution in y- and x-direction, respectively. From the bimodal fit (red) one can see that the thermal fraction (blue) is quite small and the condensate shows the well known parabolic behavior.

Figure (5.13) shows an in-situ image of an almost pure Dy BEC with $N_{\mathrm{BEC}} = 17 \times 10^3$ atoms[98]. In-trap images allow to extract directly the BEC properties like the TF radii from the pictures, which can be compared to full numerical simulations of the GPE. Ongoing measurements try to extract the scattering length a from the TF radii. This would be a direct method despite the standard technique of cross-dimensional rethermalization where the elastic scattering cross-section is determined. Furthermore, the possibility to take in-trap images is currently used to study the formation of self-organized density patterns. So far the phase-contrast imaging is destructive, however using further detuned imaging light of around $\delta \approx 300\,\Gamma$ would allow to take multiple images from the same atomic sample to investigate dynamic processes of the degenerate quantum gas.

Conclusion

In this chapter we presented our procedure to create a degenerate strongly dipolar quantum gas of Dy atoms. We start with a MOT operating at the 626 nm transition which provides good starting conditions to load the atoms in our ODT. After transporting the atoms to the science cell we perform forced evaporative cooling to quantum degeneracy. By analyzing the saturation of the BEC atom number together with a full numerical simulation of the GPE we could estimate the background scattering length of the ^{164}Dy isotope to be between $86\,a_0 \lesssim a_{\mathrm{bg}}^{164} \lesssim 93\,a_0$ and of the ^{162}Dy isotope $a_{\mathrm{bg}}^{164} \lesssim a_{\mathrm{bg}}^{162} \lesssim a_{\mathrm{dd}}$. This constrains the final trap ratio to $\lambda > 4$ to be able to create a stable condensate with $N \approx 20 \times 10^3$ of ^{164}Dy atoms. Furthermore, we are able to cool fermionic ^{164}Dy atoms to quantum degeneracy by dipolar collisions. The cooling efficiency of the fermions could be

[98] To have a higher BEC atom number the image was taken in the vicinity of a Feshbach resonance at 65.5 G, see section 6.3.

increased by using tighter beams of the ODT such that the collision rates are higher. In addition, we have shown a first in-situ picture of a dipolar condensate which allows to study directly new interesting dipolar phenomena like the Rosensweig instability. To have additional control of the internal properties of the dipolar atoms we study in the next chapter Feshbach resonances.

6 Feshbach Spectrum of Dysprosium

Two-body interactions play an important role in the properties of a degenerate quantum gas. In the case of magnetic Dy the interactions consist of the long-range DDI and the short-range dispersion interaction. We have seen in section 3.1.2 that at low temperatures the short-range potential can be replaced by the contact interaction pseudo-potential, which is fully determined by the scattering length a. Magnetically tunable Feshbach resonances, introduced in section 3.2.1, are an important tool to externally control the contact interaction strength and thereby changing the properties of the dipolar system. In this chapter we present the study of Feshbach resonances of the ^{164}Dy and ^{162}Dy isotopes based on atom-loss spectroscopy (section 6.1). The complexity of the molecular potentials are reflected in the observation of a dense Feshbach spectrum. In section 6.2 we apply a statistical analysis of the spacing between resonances which shows that the resonance positions are strongly correlated and coupled to each other. In addition, we observe broad loss features in this dense set of narrow resonances. The states corresponding to the broad features are decoupled from the states causing the many narrow resonances. Further analysis allows us to assign the broad features to textbook-like s-wave halo states, see section 6.3.

6.1 Feshbach Spectroscopy for Dysprosium Atoms

Due to the high number of BO potentials of Dy, theoretical calculations are so far not able to predict the positions and widths of its Feshbach resonances. However, the calculations show that the resonances are induced by the anisotropic interactions of Dy, see section 3.2.2. Feshbach resonances in Dy have been already studied in the group of B. Lev up to a magnetic field of 6 G [184]. In this section we present Feshbach spectroscopy measurements in a magnetic field region from 0 G to 600 G.

6.1.1 Field Calibration

To study magnetic Feshbach resonances the magnetic field has to be known precisely, thus we have to calibrate our Feshbach coils using RF-spectroscopy[99]. This is done by applying a constant RF radiation for 500 ms with a frequency between 25 and 1000 MHz and varying the magnetic field value by changing the current of the coils. If the Zeeman splitting $\Delta E_Z = g_J \mu_B = 1.7377\,\mathrm{MHz/G}$ matches the energy of the applied radio-frequency, the atoms are transferred to higher m_J states. In the energetically higher states they undergo dipolar relaxation processes which heat up the sample and the atoms are lost from the trap. In Figure (6.1) we show the measured data for the calibration of the high field coils. We find that the field up to 600 G depends linearly on the applied current with

[99] RF source: Keithley Instruments, Inc: 3390 Function Generator, Amplifier: Mini-Circuits: ZHL-2-W

a slope of 1.76 G/A. The same method was used to calibrate the second pair of Feshbach coils, which we used to do the high-resolution spectroscopy up to a magnetic field of 70 G.

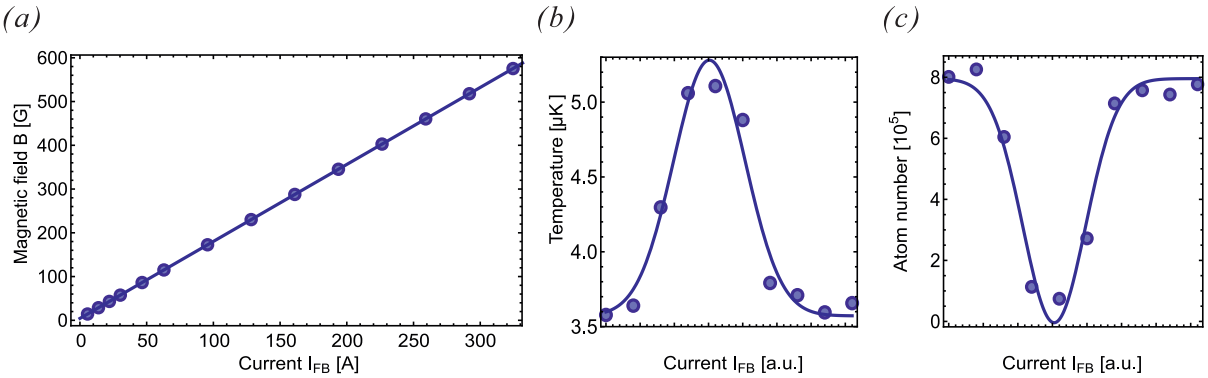

Fig. 6.1, Feshbach field calibration: We perform RF-spectroscopy on an atomic sample of typically $N = 8 \times 10^5$ atoms at a temperature of $T = 3.5\,\mu$K to calibrate the homogenous magnetic field created by the Feshbach coils. *(a)* A linear fit (solid line) to the measured data points (cycles) gives a slope of 1.76 G/A. If the applied RF radiation matches the Zeeman splitting the atomic sample is heated up *(b)* and strong atom losses occur *(c)*. To extract the resonance value we fit a Gaussian (solid line) to the temperature and atom loss feature.

6.1.2 Atom-loss Spectroscopy

To detect the position of the Feshbach resonances we used the well-established method of atom-loss spectroscopy [80]. This is done by studying atom losses for given wait times as a function of an applied magnetic field. Locally, the time evolution of the density n is given by

$$\dot{n} = -L_1 n - L_2 n^2 - L_3 n^3 \,, \tag{6.1}$$

with L_1, L_2 and L_3 the one-, two-, and three-body loss coefficients, respectively. The one- and two-body losses are in general very slow and can be neglected for the holding times needed to perform atom-loss spectroscopy to detect Feshbach resonances. To describe atom losses we have to integrate Eq. (6.1) over the trap volume:

$$\dot{N} = -L_3 \left\langle n^2 \right\rangle N \,, \tag{6.2}$$

where $\langle n^2 \rangle = 1/N \int n^3(\boldsymbol{r})\, d^3r$ is the mean square density.

On a Feshbach resonance the three-body losses are amplified due to the coupling between the atomic-threshold state and a molecular state. In general the three-body loss rate scales as $L_3 \sim a^4$, with a being the s-wave scattering length [80]. Because of the divergence of the scattering length close to the pole of a Feshbach resonance, see Figure (3.4)(b), the field location of maximum atom loss can be identified as the position of the Feshbach resonance.

We perform atom-loss spectroscopy in the crossed ODT in the science cell. To prepare a sample of Dy atoms at a temperature of choice we use the methods described in the previous chapter 5. The final temperature is controlled by adjusting the beam powers. We recompress the trap to reduce residual evaporation induced by increased elastic collisions. This also minimizes a weakening of the trap confinement caused by a residual field gradient created by our Feshbach coils. The recompression is done by increasing the ODT beam powers by a factor of approximately 2 in 100 ms. Finally, we increase the bias magnetic field in 15 ms to the desired target value. After a given wait time at a constant magnetic field we record the atom number by standard TOF absorption imaging. See Figure (6.2) for an example of the atom-losses in dependence of applied magnetic field close to a Feshbach resonance.

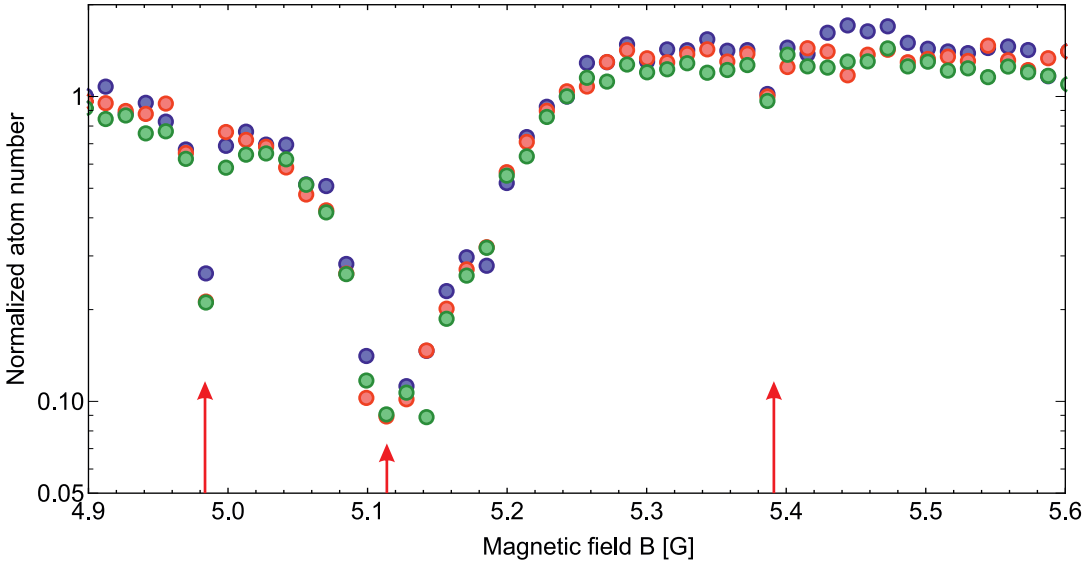

Fig. 6.2, Atom-loss spectroscopy: The normalized atom number is plotted versus the magnetic field with a resolution of $\Delta B = 14.5\,\mathrm{mG}$. To detect a Feshbach resonance we record the atom number for a given wait time at different magnetic field values. Due to the resonantly increased three-body loss rate at a Feshbach resonance we can identify the field with maximum atom loss as the Feshbach resonance position (indicated with red arrows). For the Feshbach spectroscopy we average the data of three different measurements (blue, red, green circles). Data points are taken in a random order. In this scan we can clearly observe three loss features.

We use different starting conditions and wait times for the Feshbach spectroscopy data sets presented throughout this chapter. The initial conditions for the ^{164}Dy isotope are $N_0 = 1.8 \times 10^5$ atoms at a temperature of $T_0 = 2.4\,\mu\mathrm{K}$. For the ^{162}Dy isotope the initial conditions are $N_0 = 1.0 \times 10^5$ and $T_0 = 1.5\,\mu\mathrm{K}$. In Figure (6.3)(a) we show the atom-loss spectroscopy data for the ^{164}Dy as well as for the ^{162}Dy isotope with a magnetic field resolution of $\Delta B = 500\,\mathrm{mG}$ and a wait time of 2 s. Figure (6.3)(b) shows the high-resolution atom-loss spectroscopy of the ^{164}Dy isotope as a function of magnetic field

between B=0 to 70 G with $\Delta B = 14.5\,\mathrm{mG}$ resolution and a wait time of 500 ms. Here, the starting conditions are $N_0 = 250 \times 10^3$ atoms and temperatures of $T = 600\,\mathrm{nK}$.

In the presented spectra of both isotopes we see an irregular pattern of several broad features appearing on top of a dense set of narrow resonances. For the ^{162}Dy isotope we can identify distinct broad loss features at a magnetic field of around 141 G and 160 G and for the ^{164}Dy isotope at 80 G and 180 G. In the high-resolution scan of the ^{164}Dy isotope we can observe 309 resonances up to a magnetic field of 70 G. Most of the features have a width of only a few mG. In the following sections we study these narrow resonances in more detail using a statistical approach based on the RMT which is well known in the framework of nuclear physics. The analysis of the broad features is presented in section 6.3.

6.2 Quantum Chaos in Ultra-cold Er and Dy Collisions

In this section we present the results of our joint cooperation with the theory group of S. Kotochigova and the Er group of F. Ferlaino to get more insights in the scattering behavior of ultra-cold Er and Dy atoms. The element Er also belongs to the lanthanides and has a similar anisotropic electronic configuration as Dy. It has a magnetic moment of $7\,\mu_\mathrm{B}$ and a large electronic and total angular momentum of $L = 5$ and $J = 6$, respectively. Their bosons have no hyperfine structure, whereas the fermion have additional hyperfine levels due to a nuclear spin of $I = 7/2$ [84]. Our investigation is based on the statistical analysis of the Feshbach resonance positions for magnetic fields from $B = 0\,\mathrm{G}$ to 70 G for both elements. In addition, the theoretical study of a microscopic coupled-channels model leads to an understanding of the origin of the observed resonance distribution.

6.2.1 Statistical Analysis of the Resonance Position

In this section we present the analysis of the Feshbach spectrum observed experimentally as well as obtained from theoretical calculations of Dy and Er collisions according to RMT. Note that we modify the RMT methods presented in section 3.3.2 to be able to analyze the Feshbach resonance spectra as it was introduced in [84, 107]. To use the universal statistical methods suggested by RMT we first have to adimensionalize the spectra using the mean resonance density $\overline{\rho}$. Therefore, we construct the staircase function [119]:

$$\mathcal{N}(B) = \int_0^B dB' \sum_i \delta(B' - B_i)\,, \tag{6.3}$$

which counts the number of resonances below a magnetic field value B. In Figure (6.4)(a) the staircase functions for both elements are shown. Both species are fitted by a linear dependence. Their slopes correspond to the resonance densities of $\overline{\rho} = 4.3\,\mathrm{G}^{-1}$ for ^{164}Dy, $\overline{\rho} = 2.7\,\mathrm{G}^{-1}$ for ^{168}Er at $T = 350\,\mathrm{nK}$, $\overline{\rho} = 3.4\,\mathrm{G}^{-1}$ for ^{168}Er at $T = 1,4\,\mu\mathrm{K}$ and

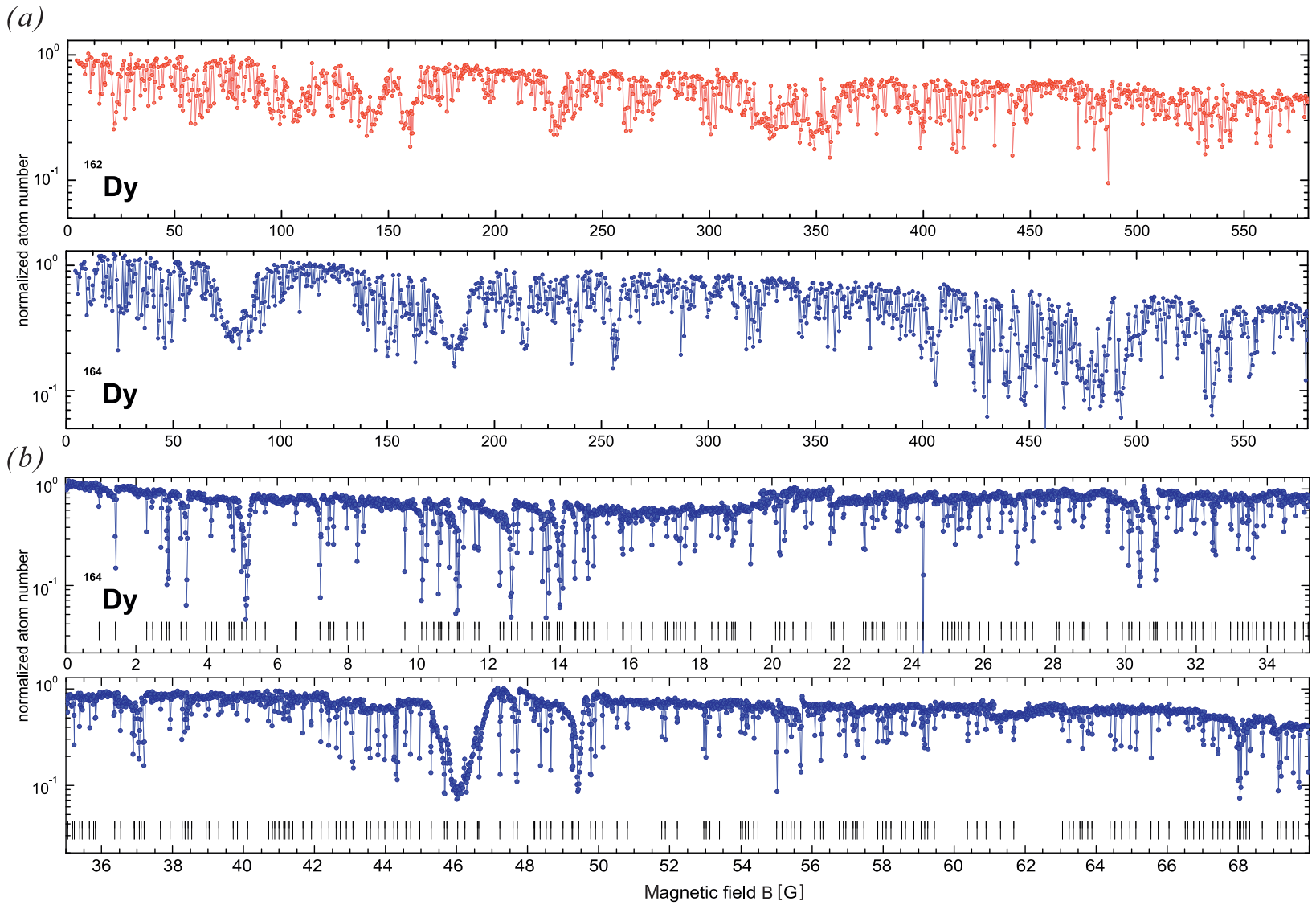

Fig. 6.3, Atom-loss spectroscopy of Dy atoms: Each data point is averaged over three measurements and normalized to a reference number taken at low field. *(a)* Spectrum for the ^{164}Dy and ^{162}Dy isotope up to 600 G with a resolution of 500 mG. *(b)* High-resolution scan of the ^{164}Dy isotope from B=0 to 70 G with 14.5 mG resolution.

$\overline{\rho} = 25.6\,\mathrm{G}^{-1}$ for ^{167}Er. The density $\overline{\rho}$ of Dy is about 50 % higher than for Er caused by a larger number of collision channels, due to its larger total angular momentum. The much larger density $\overline{\rho}$ for the fermionic ^{167}Er isotope is due to its additional hyperfine structure. The temperature dependence and also the higher density for fermionic than bosonic isotopes have also been observed in Dy for magnetic fields up to 6 G [184]. Recently, the temperature dependence of the resonance density for ^{168}Er could be explained using a theoretical model describing the three-body recombination via the formation of a trimer. It cannot be simply explained in terms of high-partial wave two-body collisions since the d-wave barrier height $U_{l=3} \approx 250\mu\,\mathrm{K}$ is well above the temperature of the sample. Rather, the origin of temperature-dependent resonances lies in the "partial wave" of the corresponding three-atom entrance channel. Three-body channels with a total orbital angular momentum of $\mathcal{N} = 0$ show a decreasing recombination rate with temperature, whereas those with $\mathcal{N} = 2$ show the opposite behavior and are responsible for the vanishing of resonances with decreasing temperature [51].

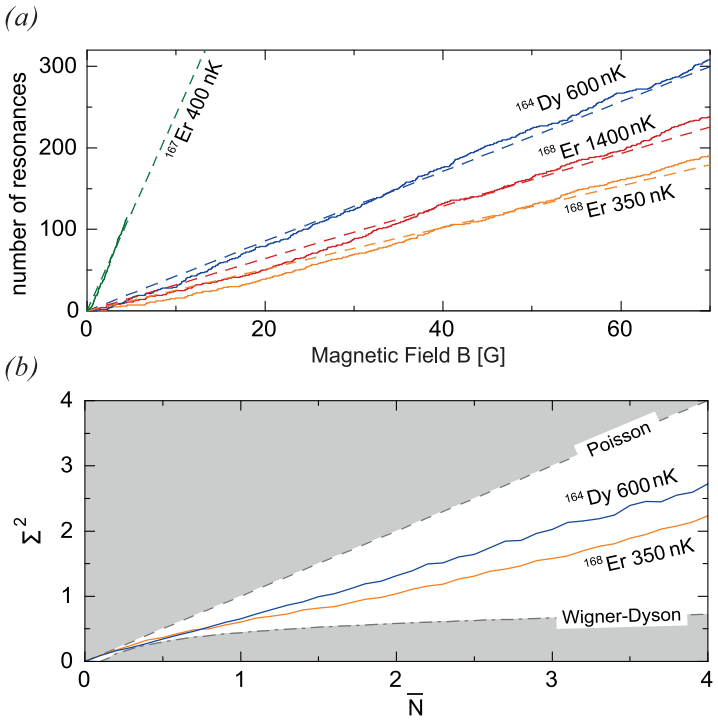

Fig. 6.4, Statistical analysis according to RMT: *(a)* Staircase function for the number of resonances as a function of magnetic field for ^{164}Dy, ^{168}Er at two different temperatures and for fermionic ^{167}Er. The dashed lines show linear fits. The slopes correspond to the mean resonance densities $\overline{\rho}$. *(b)* Number variance calculated from the experimental Feshbach spectra for ^{168}Er at $T = 350\,\mathrm{nK}$ (orange line) and ^{164}Dy (blue line) as a function of the scaled magnetic field interval $\overline{N} = \Delta B\overline{\rho}$. The number variance of both species lies between the variances of an uncorrelated Poissonian (dashed line) and the correlated Wigner-Dyson (dot-dashed line) distribution.

To probe long-range correlations we first study the fluctuations in the number of resonances within a magnetic field interval ΔB. We use a dimensionless description of the number variance such that we are able to compare both elements with the RMT prediction, see section 3.3.2. Formally, the number variance is defined by

$$\Sigma^2 = \overline{N^2} - \overline{N}^2 \ , \tag{6.4}$$

where $\overline{N} = \sum_{i=0}^{M-1} N_i/M$ is the mean value of resonances in a normalized field interval and $\overline{N^2} = \sum_{i=0}^{M-1} N_i^2/M$ its corresponding quadratic mean value. N_i is the number of resonances in the magnetic field interval $[i\Delta B, (i+1)\Delta B]$ with $i = 0, \cdots, M-1$, such that $M\Delta B = B_{\max} = 70\,\mathrm{G}$. Thus, the dimensionless value $\overline{N} \equiv \Delta B \overline{\rho}$ is the magnetic field interval ΔB rescaled by the mean resonance density $\overline{\rho}$. In Figure (6.4)(b) we show the number variance for Er and Dy as a function of $\overline{N}$. For both elements the fluctuations increase monotonically with ΔB, but less than one would expect for uncorrelated levels ($\Sigma^2 = \overline{N}$). This behavior has already been observed in Er [107], but it is the first evidence of correlations in Dy and indicates similarities between the species.

To calculate the NNS distribution of the resonance positions one generates a histogram of the number of resonances within a spacings s between $i\delta s$ and $(i+1)\delta s$, where $i = 0, 1, \cdots$ and the bin size $\delta s \approx 0.35$. It is usually calculated by $\delta s = \Delta i_{\max}/(\sqrt{N_{\mathrm{res}}}\,\overline{d})$, where $\Delta i_{\max}$ is the maximum difference in position between two neighboring resonances and N_{res} the number of observed resonances [84]. Figure (6.5) presents the NNS distribution of the experimental data for both elements, which have a clear deviation from the Poissonian $P_{\mathrm{P}}(s)$ as well as from the Wigner-Dyson distribution $P_{\mathrm{WD}}(s)$. The intermediate behavior of both species is also indicated by the fitted Brody parameter η, see Eq. (3.26a). The fitted value is $\eta = 0.45(7)$ ($\eta = 0.68(9)$) for Dy (Er), respectively. In Figure (6.5)(c,d) we show the magnetic field resolved Brody parameter $\eta(B)$. For this purpose we fit the NNS distribution of resonances located in moving intervals $[B - \Delta B/2, B + \Delta B/2]$ with $\Delta B = 20\,\mathrm{G}$. In the case of Dy we find that the Brody parameter η increases linearly with fields for small B until a saturation value of $\eta \approx 0.5$ for $B > 30\,\mathrm{G}$ is reached. In the case of Er the Brody parameter fluctuates around ≈ 0.5. Interestingly, the resonance spectrum obtained from theoretical scattering calculations, see next section, show the same statistical behavior in the NNS distribution, shown as gray data points and lines in Figure (6.5). Also the slow increase of the Brody parameter η with increasing magnetic fields is reproduced by the theory. This indicates that a sufficiently strong magnetic field is needed to change from an uncorrelated to a correlated system.

6.2.2 Emergence of Chaotic Scattering in Ultra-cold Er and Dy

In the following we use the possibility offered by the calculations to tune the anisotropy of the interaction potentials to study their effects on the level distribution of the most-weakly-bound energy levels at $B = 0$. The full potential can be separated in an isotropic

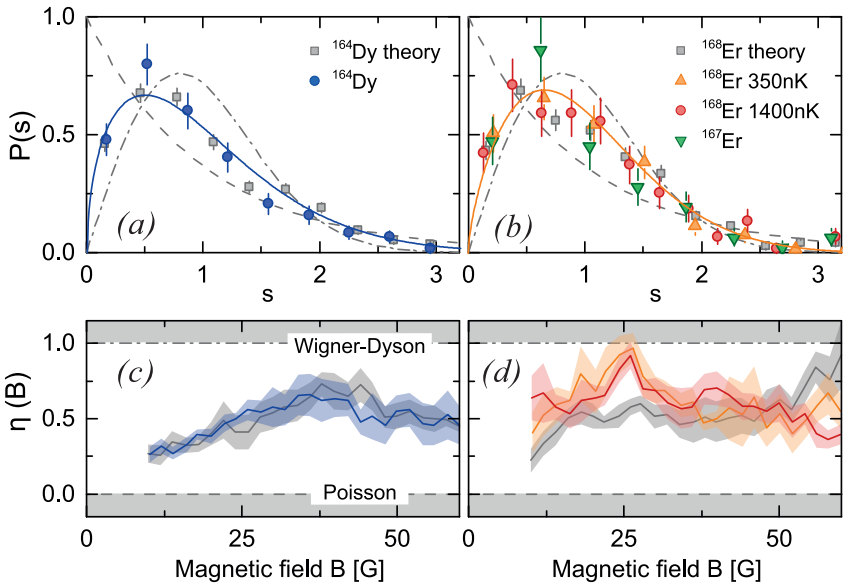

Fig. 6.5, Analysis of the NNS distribution: *(a)* NNS distribution of the Dy Feshbach resonance spectra (blue markers). The dashed and dot-dashed curves are the Poissonian and Wigner-Dyson distribution, respectively. The solid line is a fitted Brody distribution with $\eta = 0.45(7)$. *(b)* NNS distribution for different Er spectra. The solid line is a Brody distribution with $\eta = 0.68(9)$ fitted to the Er data at $T = 350\,\mathrm{nK}$. *(c-d)* Magnetic field resolved Brody parameter $\eta(B)$ as a function of magnetic field for Dy and ^{168}Er at $T = 350\,\mathrm{nK}$. Gray markers and lines in all four panels are results from the coupled-channels calculation. The 1σ error bars correspond to Poissonian counting errors and the shaded band are 1σ statistical uncertainties of the fits to the data.

part $U_i(\boldsymbol{r})$ and an anisotropic part $U_a(\boldsymbol{r})$:

$$U_{\mathrm{int}}(\boldsymbol{r}) = U_i(\boldsymbol{r}) + U_a(\boldsymbol{r}) \;, \tag{6.5}$$

where the anisotropic part consists of the anisotropic dispersion $U_{\Delta C_6}(\boldsymbol{r})$ and the magnetic dipole-dipole $U_{\mathrm{MDD}}(\boldsymbol{r})$ contribution. Thus, we can define

$$U_a(\boldsymbol{r}) = \lambda_{\Delta C_6}\, U_{\Delta C_6}(\boldsymbol{r}) + \lambda_{\mathrm{MDD}}\, U_{\mathrm{MDD}}(\boldsymbol{r}) \;. \tag{6.6}$$

The strength of the anisotropic parts can be tuned independently by the parameter $\lambda_{\Delta C_6}$ and λ_{MDD}. For $\lambda_{\mathrm{MDD}} = \lambda_{\Delta C_6} = 1$ the potential corresponds to the real physical potential. In Figure (6.6)(b) and (d) the energy levels for $B = 0$ of the most-weakly-bound levels of ^{164}Dy$_2$ with $J_{\mathrm{tot}} = 16$ as a function of λ_{MDD} and $\lambda_{\Delta C_6}$ are shown. For $\lambda_{\mathrm{MDD}} = \lambda_{\Delta C_6} = 0$ the binding energies are regularly structured and correspond to the ro-vibrational levels of the isotropic centrifugal potential. For small λ_{MDD} and $\lambda_{\Delta C_6}$ the degeneracy of the energy levels is lifted and the levels shift linearly. The linear dependence for increasing strength of the DDI is approximately valid up to a value of $\lambda_{\mathrm{MDD}} = 1$. Hence, the DDI does not lead to the observed level distribution. This is confirmed in Figure (6.6)(a) as

the NNS distribution of the energy levels at $\lambda_{\mathrm{MDD}} = 1$ and $\lambda_{\Delta C_6} = 0$ follows a Poissonian distribution.

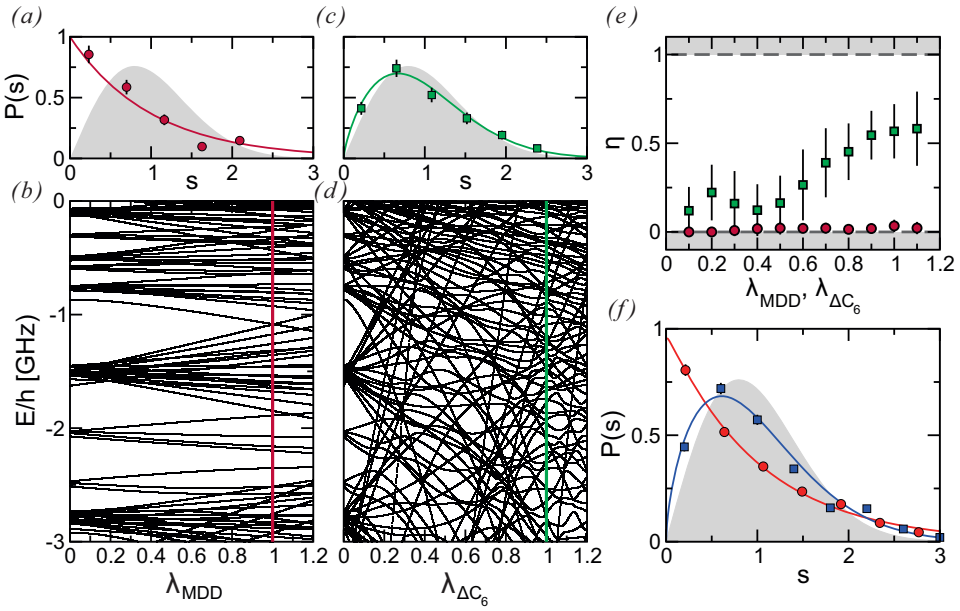

Fig. 6.6, Anisotropy induced chaos of $B = 0$ near-threshold bound-states: *(b)* Bound-state energies of $^{164}Dy_2$ with $J_{\mathrm{tot}} = 16$ as a function of the anisotropy scale parameter λ_{MDD} with $\lambda_{\Delta C_6} = 0$. *(a)* NNS distribution (red circles) of the energy levels in panel *(b)* at $\lambda_{\mathrm{MDD}} = 1$. The solid red line is a Brody distribution fit to the data and agrees well with a Poissonian distribution. *(d)* Bound-state energies of $^{164}Dy_2$ with $J_{\mathrm{tot}} = 16$ as a function of the anisotropy scale parameter $\lambda_{\Delta C_6}$ with $\lambda_{\mathrm{MDD}} = 0$. *(c)* Analysis of the NNS distribution of energy levels in panel *(d)* at $\lambda_{\Delta C_6} = 1$. The Brody fit (solid green line) is close to a Wigner-Dyson distribution. *(e)* Brody parameter η as a function of $\lambda_{\Delta C_6}$ (green squares) and λ_{MDD} (red squares) with $\Delta\lambda = 0.2$ obtained by fitting the NNS distribution of the bound-states in panel *(b)* and *(d)* to a Brody distribution, respectively. The horizontal lines at $\eta = 1$ and $\eta = 0$ correspond to the Brody parameter for a Poissonian and Wigner-Dyson distribution. The 1σ error bar contains the statistical and fitting uncertainties. *(f)* NNS distribution $P(s)$ of the normalized energy spacing s for individual-J (blue squares) and combined-J (red circles) at $\lambda = 1$. Here, the error bars reflect the 1σ statistical uncertainties. The gray shaded areas in panel *(a)*, *(c)* and *(f)* indicate the Wigner-Dyson distribution.

On the other hand, for a relatively small anisotropic dispersion strength $\lambda_{\Delta C_6} \approx 0.1$ levels start to avoid each other. At $\lambda_{\Delta C_6} = 1$ and $\lambda_{\mathrm{MDD}} = 0$ most levels have undergone multiple avoided crossings and the levels can not be described by a single dominant partial wave. Analyzing the NNS distributions of the energy levels confirms the non-Poissonian level spacing, see Figure (6.6)(c). The situation for $\lambda_{\mathrm{MDD}} = \lambda_{\Delta C_6} = 1$ has also been computed and the level distribution is similar to the one shown in Figure (6.6)(c). Note that similar results have been also obtained for $^{168}Er_2$.

In Figure (6.6)(e) we quantify our observation so far by showing the Brody parameter η extracted from the NNS distribution of the $B = 0$, $J_{\mathrm{tot}} = 16$ $^{164}\mathrm{Dy}_2$ levels as a function of λ_{MDD} and $\lambda_{\Delta\mathrm{C}_6}$. For increasing DDI strength λ_{MDD} and no anisotropic dispersion ($\lambda_{\Delta\mathrm{C}_6} = 0$) the Brody parameter is always zero indicating the prevalence of small level spacings. On the other hand, in the absence of the DDI an increase of $\lambda_{\Delta\mathrm{C}_6}$ leads to an increase of η starting for values of $\lambda_{\Delta\mathrm{C}_6} \gtrsim 0.4$. For $\lambda_{\Delta\mathrm{C}_6} = 1$ the Brody parameter saturates at a value of $\eta \approx 0.7$ indicating a depopulation of small energy spacings but a Wingner-Dyson distribution with $\eta = 1$ is not reached.

So far we have analyzed the NNS distribution of the energy levels for a single $J_{\mathrm{tot}} = 16$. To obtain the same resonance density as measured experimentally also the coupling to higher partial waves l, resulting in high J_{tot}, has to be taken into account. Thus we compare now the NNS distribution for $\lambda_{\mathrm{MDD}} = \lambda_{\Delta\mathrm{C}_6} = 1$ and $B = 0$ of individual Js with that obtained by combining all bound-states ($|E/h| < 3\,\mathrm{GHz}$) with $J_{\mathrm{tot}} = 16, \cdots, 25$. For $J_{\mathrm{tot}} > 25$ the number of bound-states are too small to calculate the NNS distribution. Figure (6.6)(f) shows that the NNS distribution of an individual J is non-Poissonian (as we have seen before). However, the combined-J distribution does follow a Poissonian distribution indicating that the energy levels of different Js are uncorrelated. This means that even the Hamiltonians of different Js have the same coupling strength the coupling between the individual Js leads to uncorrelated eigenenergies.

With increasing magnetic field B the energy levels shift upwards due to the Zeeman effect and when they reach the threshold at $E = 0$ Feshbach resonances appear. We observe that for both species the level structure differs quantitatively in the low field region (0 G to 10 G) from the larger field region (50 G to 60 G), see Figure (6.7). For small fields the avoided crossings are substantially narrower than for larger B. In addition, at small fields the levels cluster whereas at higher fields they are more uniformly distributed. This is caused by the linear increase of the coupling between vibrational levels with different J as a function of B. This change can also be observed by analyzing the B-field resolved Brody parameter for the Feshbach resonance locations obtained from the coupled-channels calculation, see Figure (6.5)(c-d). For ^{164}Dy the theoretical Brody parameter $\eta(B)$ increases linearly from zero for small fields and saturates at $\eta(B) \approx 0.5$ for magnetic fields higher than $B = 35\,\mathrm{G}$. It shows excellent agreement with $\eta(B)$ obtained from the experimental data. For ^{168}Er we see a much faster increase of $\eta(B)$ at small fields, which saturates at $\eta(B) \approx 0.5$ for fields $B > 20\,\mathrm{G}$. Furthermore, the NNS distribution of the Feshbach resonance location from 0 G to 70 G agrees nicely with NNS distribution of the experimental data, shown in Figure (6.5)(a-b). The initial rise of $\eta(B)$ for both species is due to the Zeeman interaction which couples the primary uncoupled and randomly distributed weakly-bound molecular vibrational levels at $B = 0$ with increasing strength for increasing magnetic fields. The reason for the saturation of the Brody parameter at $\eta(B) \approx 0.5$ is not yet explained and is probably determined by the complex interplay between the Zeeman shifts and anisotropic inter-atomic interaction.

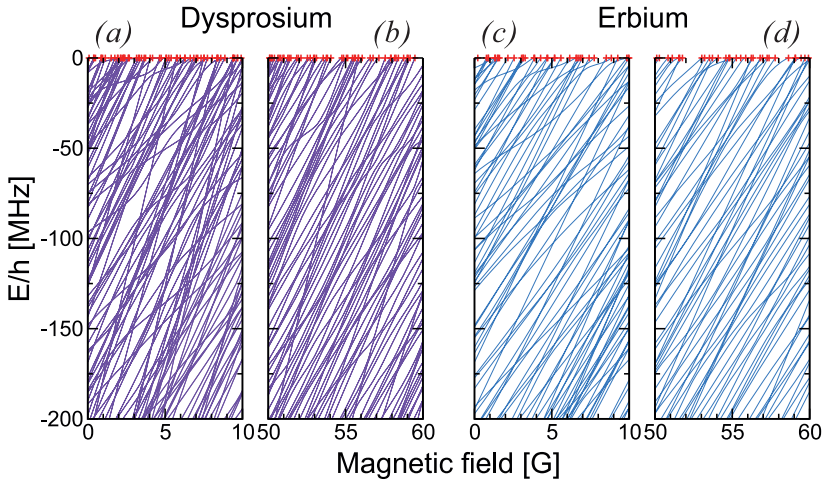

Fig. 6.7, Near-threshold-bound-states of Dy and Er: Panels *(a,c)* show the region between $B = 0\,\mathrm{G}$ to $10\,\mathrm{G}$ while panels *(b,d)* show the region between $B = 50\,\mathrm{G}$ to $60\,\mathrm{G}$. The calculations have been performed with $\lambda = 1$ for $^{164}\mathrm{Dy}_2$ and for $^{168}\mathrm{Er}_2$. Red crosses indicate the position of Feshbach resonances.

In this section we have experimentally and theoretically studied resonant collisions of Dy and Er atoms in a magnetic field. By analyzing the NNS distributions as well as the number fluctuations of the Feshbach resonance positions we could show that both species show signatures of quantum chaos. The theoretical simulations could show that the chaotic distribution of resonances emerges due to the anisotropy of the molecular dispersion interaction caused by their large electron orbital angular momenta. This finding is unique to colliding magnetic lanthanides and has not been observed in any other ultra-cold system. Furthermore, we found that a sufficiently strong magnetic field is necessary to fully develop the chaotic behavior. We could show that the NNS distribution for Er and Dy is very similar, as it can be expected from their similar ratio between anisotropic to isotropic dispersion interaction of $\Delta C_6/C_6 \approx 10\%$.

6.3 Broad Feshbach Resonances

The atom-loss spectra of the ^{164}Dy and ^{162}Dy isotope (see Figure (6.3)) show both a few distinct broad loss features with a width of several Gauss. Usually, these broad features correspond to single broad Feshbach resonances, as it is known for instance for the elements Na [101], Cs [185] and for the interspecies sample of ^{6}Li-^{133}Cs [186, 187]. However, this is not obvious in Dy due to the dense chaotic Feshbach spectrum. To analyze the broad loss features in more detail we perform magneto-association to measure the binding energy of the weakly-bound dimer in dependence of the magnetic field.

6.3.1 Binding Energy Measurements

Our binding energy measurements are focused on the two broad loss features of the ^{164}Dy isotope around a magnetic field of $B \approx 80\,\mathrm{G}$ and $B \approx 180\,\mathrm{G}$. The binding energy of the weakly-bound Feshbach dimer is experimentally obtained based on the method of magneto-association which was first used by Thompson *et al.* to produce shallow dimers composed of ^{85}Rb atoms [188]. An oscillating magnetic field with frequency ν_{ass} induces a stimulated emission of an atom pair to emit a low frequency photon while forming a lower energy weakly-bound molecule if the modulation energy matches its binding energy $E_b = h\nu_{\mathrm{ass}}$. By colliding with an additional single atom the newly formed molecule relaxes to a deeply-bound-state which releases sufficient kinetic energy for the atom and the molecule to be lost from the trap [189], see the schematic drawing in Figure (6.8).

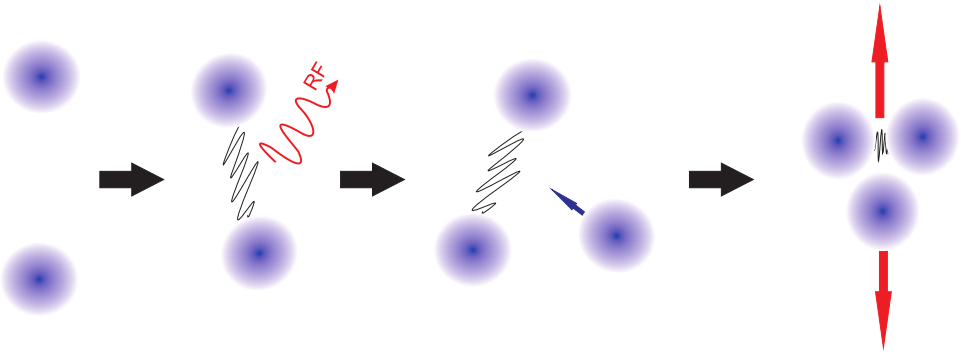

Fig. 6.8, Measurement of the binding energy: By modulating the magnetic field we stimulate an atom pair to emit a photon while forming a lower energy weakly-bound molecule. This molecule relaxes to a deeply-bound molecular state if it collides with an additional atom. Its binding energy is converted in kinetic energy and both are lost from the trap.

The modulation of the magnetic field around its bias value is done by applying an additional RF field along the magnetic field direction[100]. The antenna consisting of 8 windings with a diameter of 5 cm is placed close to the bottom window of the glass cell.

[100]RF source: Keithley Instruments, Inc: 3390 Function Generator, Amplifier: RFPA: AP 001220-10

With an oscillating current in the antenna we can induce an oscillating magnetic field with a typical amplitude between 100 mG and 500 mG. The modulation time lies between 100 ms and 500 ms. This spectroscopy is done with a thermal cloud at a temperature T of 400 nK $\leq$ T $\leq$ 700 nK.

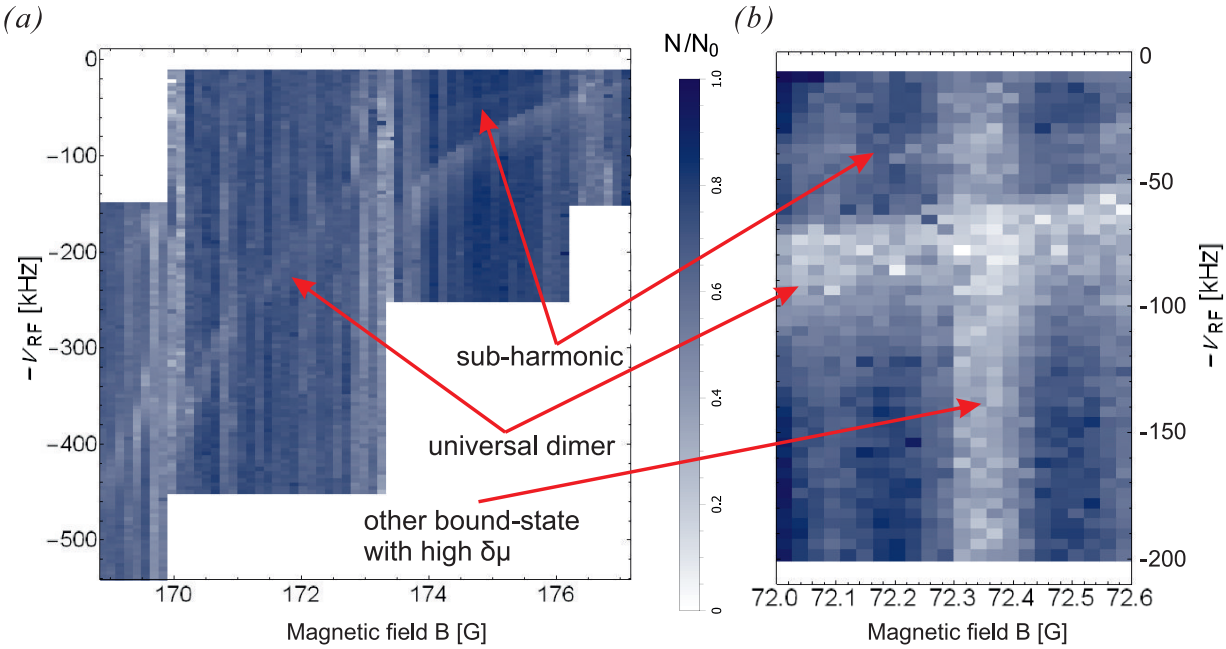

Fig. 6.9, Measurement of the binding energy: *(a)* We use magnetic-field modulation spectroscopy to measure the binding energy of the weakly-bound dimer. The normalized remaining atom number is plotted as a function of magnetic field and modulation frequency. By changing the modulation frequency for constant bias magnetic fields we observe one narrow, slowly varying feature and many localized broad features. The former is the signature of the weakly-bound-state creating the broad Feshbach resonance at 180 G. The broad features are responsible for the narrow Feshbach resonances. At $B \approx 170$ G and $B \approx 174$ G we observe avoided crossings. Additionally, one can observe a weak association feature at low frequencies which is a sub-harmonic of the main association line. For magnetic fields $B < 169$ G and $B > 177$ we loose the signal of the weakly-bound dimer. *(b)* Zoom of the magnetic-field modulation spectroscopy of the 76 G resonance. The association line of the broad resonance is clearly visible. Most of the states with a high energy-vs.-magnetic field slope crosses the former line without showing any coupling behavior.

In Figure (6.9) we show the remaining atom number left after the field modulation as a function of frequency and bias field. We observe two kinds of spectra, either the losses are in a narrow or in very broad frequency band. As for the latter the frequency is resonant over a large frequency range but only for distinct magnetic fields the responsible bound-states have a high energy-vs.-magnetic field slope. On the opposite, the center frequency of the narrow loss feature evolves slowly with the magnetic field. The line shapes of the narrow loss features are caused by the relative kinetic energy of the two

associated atoms. By fitting a Maxwell-Boltzmann distribution to the narrow loss features we can extract their corresponding binding energies $E_b(B)$, see Figure (6.10).

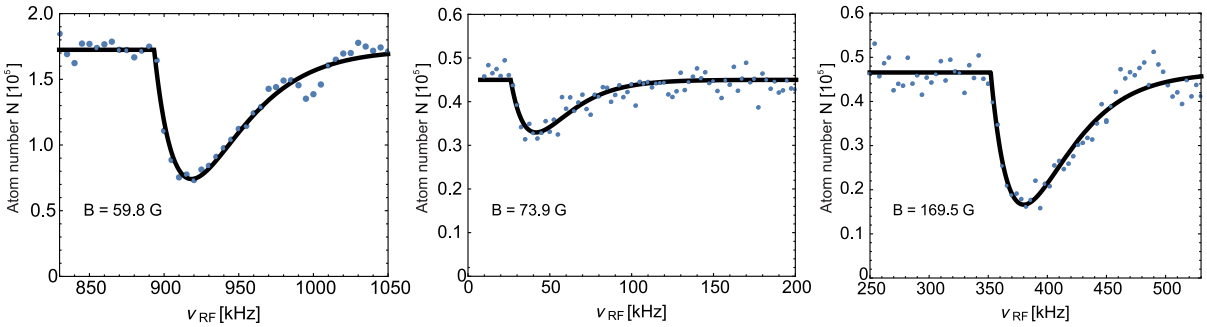

Fig. 6.10, Measurement of the binding energy: Examples of magnetic field modulation spectra of both broad resonances. By fitting a Maxwell-Boltzmann distribution (solid line) we extract the binding energy shown in Figure (6.11).

In Figure (6.11) (b) the obtained binding energies (red circles) are plotted as a function of magnetic field combined with a high-resolution ($\Delta B = 20\,\mathrm{mG}$) atom-loss spectra. One can see that inside the broad features the dense background of narrow resonances remains. We can assign some of the states with high energy-vs.-magnetic field slope to narrow loss features in the atom-loss spectroscopy. For both broad resonances we observe a slow variation of the binding energy with magnetic field ($< 1\,\mathrm{MHz}$ over $10\,\mathrm{G}$) and a quadratic behavior over several Gauss, which indicates the coupling of the bound-state with the two-atom continuum, which is usually termed open channel [80]. This is a strong evidence that the observed bound-state is in both cases the s-wave halo state that is found in the vicinity of Feshbach resonances.

6.3.2 Theoretical Analysis of the Broad Resonances

In section 6.2 we have seen that the anisotropic dipolar and vdW interactions mix many different electronic symmetries and partial waves leading to strongly coupled levels. Therefore, the appearance of a broad feature showing the properties of an universal state which is decoupled from all the other states is quite surprising. In the following section we present the theoretical analysis to support the assumption of a long-range s-wave halo state creating a broad resonance embedded in a "sea" of chaotic levels which are responsible for all the narrow resonance. This analysis was done with theory support of K. Jachymski and P. S. Julienne. Here, we only give a brief summary of the theoretical findings. More details on the applied theoretical models can be found in Ref. [52].

First we analyze the influence of the many narrow resonance on the properties of the broad resonance. There exist also alkali atom systems which have broad s-wave resonances superimposed with one ore more much narrower resonances of higher partial waves. This is the case for example in Cs + Cs [190] or in Rb + Cs collisions [191]. Our collaborators have developed an analytic treatment based on multichannel quantum defect theory to

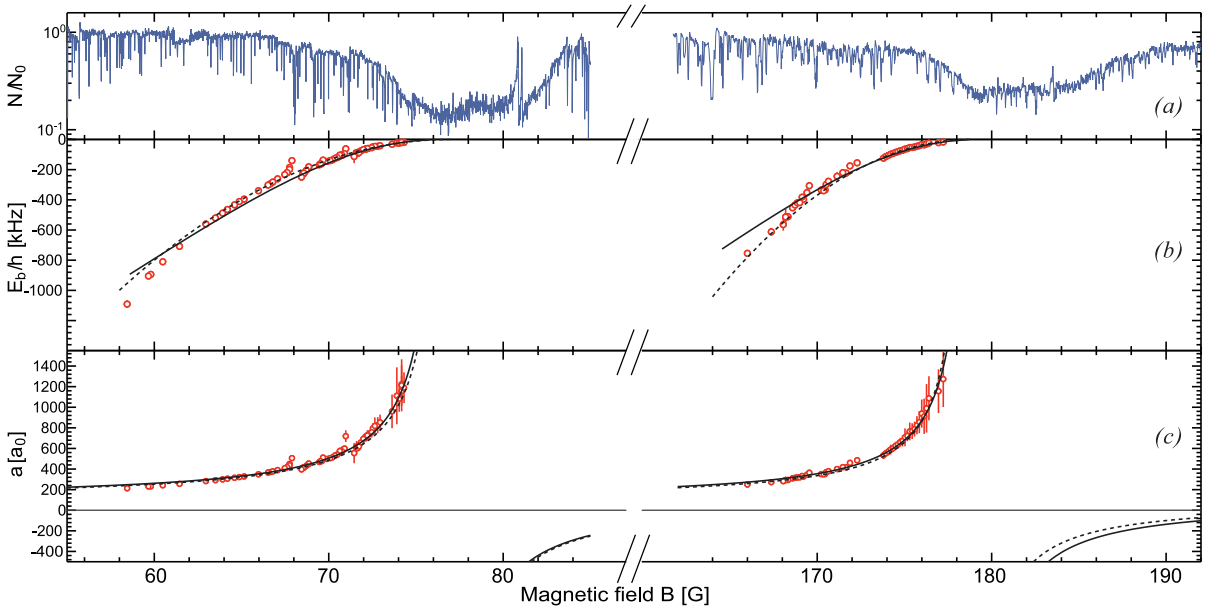

Fig. 6.11, Broad Feshbach resonances of ^{164}Dy: *(a)* Atom-loss spectroscopy at $T = 500\,\mu$K with a magnetic field resolution of $\Delta B = 20\,$mG. The spectra show that the two broad features are overlapped with many narrow resonance. *(b)* Binding energy measurement (red cirles) of a weakly-bound dimer. The solid (dashed) lines are obtained by fits of our measured data to the coupled-channel calculation (universal quadratic expression). Form these fits we can extract $a_{\rm bg}\Delta$ (see Table (6.1)). *(c)* The circles are obtained by converting the $E_b(B)$ data using the results of the coupled-channels calculation for $a(E_b)$. The solid lines are fits using Eq. (3.17). The dashed lines are the scattering length using the values obtained from the fit of $E_b(B)$ by the universal quadratic expression and assuming $a_{\rm bg} = 91\,a_0$.

characterize overlapping resonances [192]. They found that a broad resonance provides the local background scattering length for all the narrow resonances. The range over which a narrow resonance perturbs the underlying background due to the strong resonance depends on their widths. In the binding energy measurement (see Figure (6.9) and Figure (6.12)) we observe some avoided crossings that modify the halo dimer binding energy. This is due to the stronger-than-usual coupling between the halo dimer and another state, which influence the scattering length and thereby show a stronger effect in the atom loss spectroscopy. Apart from these stronger resonances all others are very narrow ($\lesssim 20\,$mG in the atom-loss spectrum) and perturb the scattering length only very locally. With this analysis we can conclude that the narrow resonances only locally perturb the properties of the universal state which allows us to use the universal equation for the magnetic field dependency of the scattering length (Eq. (3.17)) in the vicinity of the broad resonance.

To describe the collisions of two Dy atoms in the same Zeeman level the methods introduced by Ref. [85] were used. Here, only a single s-wave entrance channel with its off-diagonal coupling to d-wave channels is required. The many other electronic and

partial wave channels only generate a dense set of threshold-crossing levels with very different magnetic moments that are weakly-coupled to the s-wave halo state. The dipolar interaction vanishes in the diagonal s-wave potential. But due to the off-diagonal coupling between the s-wave and the d-wave an effective adiabatic potential, which varies at long range as $-C_4/R^4$, is induced. To account for this a hybrid interaction potential consisting of the vdW and the effective adiabatic potential was used in the calculations.

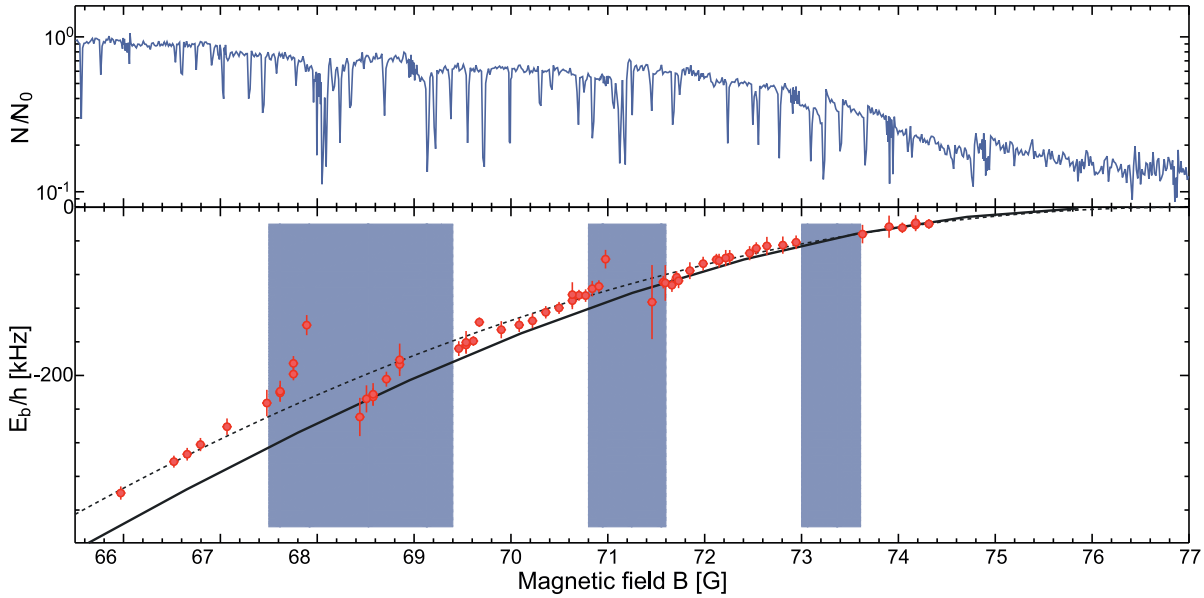

Fig. 6.12, Zoom on the 77 G resonance: The region with strong avoided crossings in the binding energy as well as stronger-than-usual narrow Feshbach resonances are highlighted in blue. In these regions the scattering length is unknown. Away from these regions, resonances are very narrow and modify the scattering length induced by the broad one only very locally. The solid (dashed) lines are obtained by fits of our measured data to the coupled-channels calculation (universal quadratic expression), respectively.

We analyze the broad resonance using a coupled-channels approach. As a fully coupled-channels model is too complicated due to the many electronic potential and the couplings to higher partial waves, we use a simplified two-channel description neglecting the influence of the narrow resonances. This assumption is valid as the experimental binding energy measurement shows that the universal s-wave state seems to be decoupled from the states which are responsible for all the narrow resonances. Our two-channel model is based on the methods described in Refs. [193–195].

In Figure (6.13) we compare the results of the coupled-channels calculation with the measured binding energies for the two broad resonances. As we do not clearly observe the linear increase of the measured binding energies with magnetic field we cannot extract $\delta\mu$ from the measurement. Therefore, the fit to the data is not unique as s_{res} and $\delta\mu$ are not independent. The figure shows fits with different assumed $\delta\mu$ and s_{res} values. Assuming a reasonable minimum value of $\delta\mu = g\mu$ with $g = 1.24159$ a resonance strength

parameter of $s_{\mathrm{res}} = 16.17$ can be obtained from the fit for the 76 G resonance. As the ratio $s_{\mathrm{res}}/(\delta\mu) = (a_{\mathrm{bg}}\Delta)/(\overline{a}\overline{E})$ is constant we can extract $a_{\mathrm{bg}}\Delta$ from the fits. A second method to obtain $a_{\mathrm{bg}}\Delta$ is to convert the measured binding energy data $E_b(B)$ to $a(B)$ using the results of the coupled-channels calculation for $a(E_b)$ and to fit the usual expression Eq. (3.17) to the converted data, shown in Figure (6.11)(c). For the 76 G resonance the obtained value of $a_{\mathrm{bg}}\Delta$ agrees with the value extracted from the fit to $a(B)$. Good agreement with the data can be also obtained for the 180 G resonance using the same s_{res} values for the fit and assuming $\delta\mu$ to be 6 % larger. This shows that both resonances have similar pole strength.

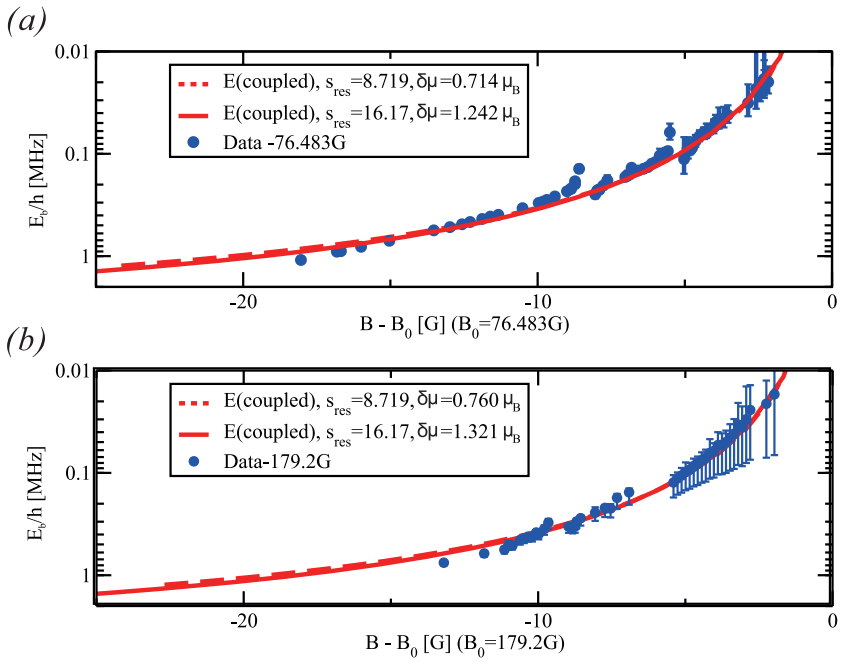

Fig. 6.13, Analysis of the broad resonances with coupled-channels calculation: Comparison of the coupled-channels model with the experimental obtained binding energies for the 76 G *(a)* and the 180 G *(b)* resonance. Fits with different combinations of $s_{\mathrm{res}} \gg 1$ and $\delta\mu$ such that $s_{\mathrm{res}}/(\delta\mu)$ is constant are possible.

In addition, we fit our measured data $E_b(B)$ by the universal quadratic expression ($E_b(B) = -(B - B_0)^2/(a_{\mathrm{bg}}\Delta)^2$) in the vicinity of the pole ($B > 66$ G and $B > 173$ G for the two resonances respectively) to extract $a_{\mathrm{bg}}\Delta$. The fit results (dashed line) are shown in Figure (6.11)(b). Interestingly, the results of the coupled-channels theory and the universal theory are in close agreement with each other for the lower-field resonance and in reasonable agreement for the higher-field one. We further assume a background scattering length of $a_{\mathrm{bg}} = 91\, a_0$ (will be justified in the next section) to calculate $a(B)$ using Eq. (3.17) with $a_{\mathrm{bg}}\Delta$ given by the universal fit. The resulting curve (dashed line in Figure (6.11)(c)) is in close agreement with the result from the coupled-channels calculation (solid line). In

universal B_0	universal $a_{\rm bg}\Delta$	numerical CC B_0	numerical CC $a_{\rm bg}\Delta$
76.9(5) G	2810(100) G a_0	76.8(5) G	2700(100) G a_0
178.8(6) G	2150(150) G a_0	179.1(6) G	2540(110) G a_0

Tab. 6.1, Resonance parameters obtained from fitting the binding energy data to the universal expression (Eq. 3.18) and to numerical coupled-channels calculation.

Table (6.1) we summarize the results of the universal expressions and coupled-channels calculation.

We can conclude that the observed broad resonances strongly modify the scattering properties over a large magnetic field range, although multiple couplings to other states can be found in the data. Our analysis show that the binding energy of the *s*-wave halo dimer is well approximated in the pole vicinity by the universal quadratic expression (Eq. (3.18)). Furthermore, we can use the usual expression of an isolated magnetically tunable near threshold Feshbach resonance given by Eq. (3.17) to calculate the scattering length as a function of the magnetic field.

6.3.3 Localization of the Zero-crossing

To calculate the background scattering length based on the obtained $a_{\rm bg}\Delta$ value we have to estimate the width Δ of the Feshbach resonance. Therefore, we have to find the magnetic field position where the scattering length a is zero, see Figure (3.4)(b). A convenient method to locate the zero-crossing is to analyze the evaporative cooling efficiency as it depends on the elastic cross-section. For a non-magnetic gas the elastic collision cross-section goes to zero for a vanishing a resulting in an ineffective evaporation [196]. In case of magnetic atoms due to the dipolar collisions the total scattering cross-section does not vanish for $a \to 0$, rather reaches a constant value for low temperatures, see Eq. (3.14a). Nevertheless, when $a = 0$ the total elastic cross-section and thus the thermalization is minimal, leading to a slower evaporation which is characterized by a maximum in the background (between narrow resonances) atom number and temperature after a holding time in a constant trap. In Figure (6.14) we show the temperature and atom number on the higher magnetic field side of the $B = 76.9\,\mathrm{G}$ resonance. We observe that the maximum atom number and temperature varies slowly with magnetic field. The maximum in atom number and in temperature can be located at $B_{\rm max,N} = 109(5)\,G$ and $B_{\rm max,T} = 107(5)\,G$, respectively.

A second method to locate the zero-crossing is to examine the asymmetric line shapes of the narrow Feshbach resonances. The line shape and in particular its symmetry depends on the sign of its "local" background scattering length $\tilde{a}_{\rm bg}$ [192]. The sign of the local background scattering length determines the side on which the local zero-crossing takes place, if $\tilde{a}_{\rm bg} > 0$ ($\tilde{a}_{\rm bg} < 0$) it is on the high- (low-) field side of the resonance. As the zero-crossing corresponds to a minimum in the three-body recombination the atom number

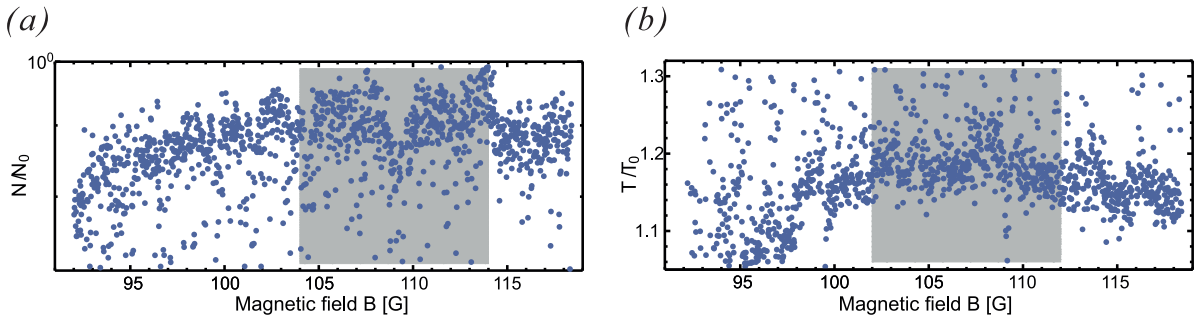

Fig. 6.14, Analyzing evaporation efficiencies to locate the zero-crossing: The background atom number *(a)* and temperature *(b)* show a maximum at $B_{\mathrm{max,N}} = 109(5)\,G$ and $B_{\mathrm{max,T}} = 107(5)\,G$, respectively, indicating the zero-crossing of the scattering length a.

has a maximum in its vicinity leading to an asymmetric line shape in the loss feature, see Figure (6.15). For magnetic fields up to the position of the broad resonance at $B = 76.6\,\mathrm{G}$ all the line shapes of the isolated narrow resonances correspond to $\tilde{a}_{\mathrm{bg}} > 0$. On the other side of the broad resonance the line shapes are inverted. At a magnetic field of $B = 109\,\mathrm{G}$ we observe a resonance with a very symmetric line shape, which suggests that $\tilde{a}_{\mathrm{bg}} \approx 0$. We

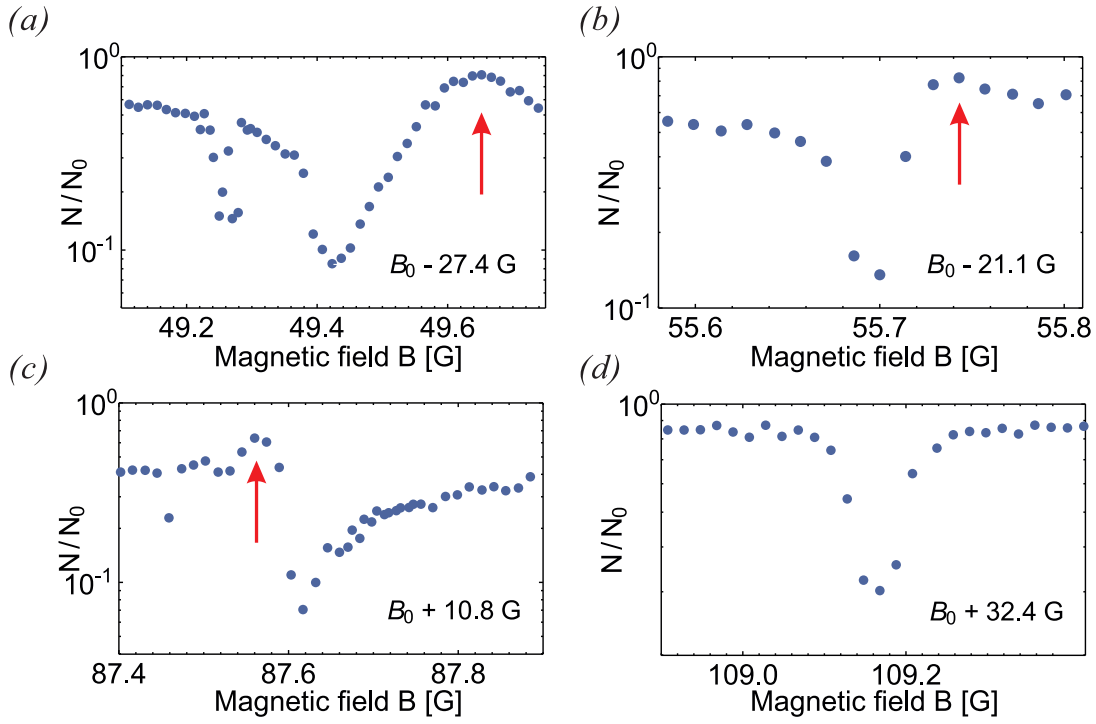

Fig. 6.15, Line shape analysis: For magnetic fields $B < B_0 = 76.9\,G$ *(a,b)* the loss features show a maximum in atom number (zero-crossing, indicated by red arrows) on their high field side ($\tilde{a}_{\mathrm{bg}} > 0$). On the other side of the broad resonance ($B > B_0$) their line shape is inverted, for example in *(c)*, implying $\tilde{a}_{\mathrm{bg}} < 0$. *(d)* At a magnetic field of $B = 109\,G$ we observe a resonance with a symmetric line shape corresponding to $\tilde{a}_{\mathrm{bg}} \approx 0$.

do not clearly observe distinct resonances between 110 G and 120 G and for even higher fields the local background scattering length could be already influenced by the second broad resonance at $B = 178.7$ G. In addition, the observation of a zero-crossing of the background scattering length near $B = 109$ G corresponds with the finding of the first method. Combining both methods we estimate the zero-crossing to be at $B = 108(5)$ G.

If we assume that the broad s-wave halo resonance provides the local B-dependent background to the narrow resonances, the universal model then implies a width of $\Delta = 31(6)$ G and a background scattering length of $a_{\mathrm{bg}} = 91(15)\, a_0$ for this resonance. This justifies the assumption we made above. While the data suggests the persistence of such a strong s-wave halo state across the dense set of narrow resonances, further experimental and theoretical work has to be done to explore this effect in more detail. The extracted background scattering length agrees within the errors with the value obtained by thermalization measurements of Ref. [45]. It also agrees with the estimated value based on the study of the atom number limitation of Dy condensates in different trap geometries, see section 5.4. In Figure (6.16) we compare the 77 G resonance with Feshbach resonances of other elements.

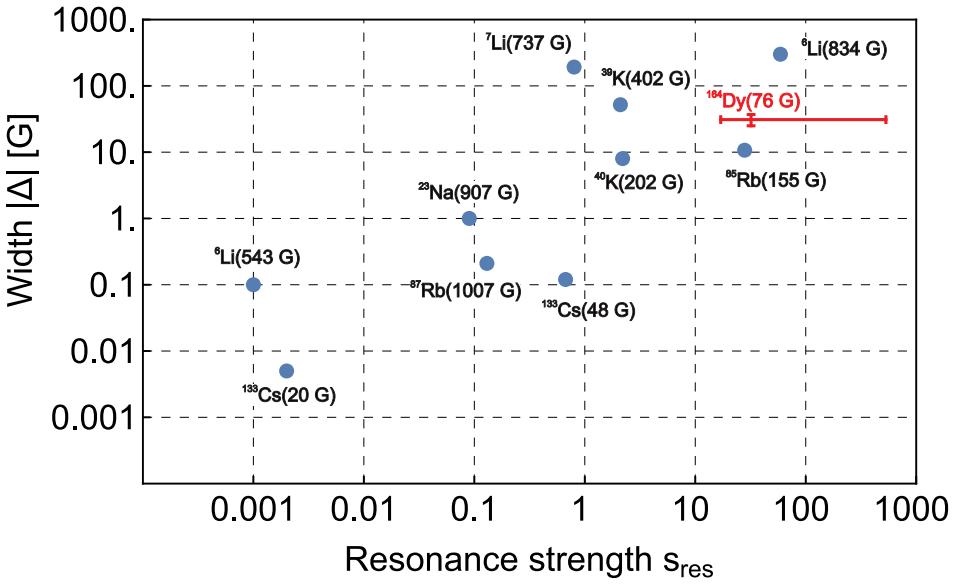

Fig. 6.16, Classification of Feshbach resonances: Comparison of the 76 G resonance with other Feshbach resonances in terms of the pole strength s_{res} and the width Δ. We used the lowest value obtained from the fits for the lower boundary of the s_{res} parameter, whereas the upper boundary is obtained using the largest possible value of $\delta\mu = 16 g_j \mu_{\mathrm{B}}$. Values for the other resonances are taken from [80].

data set	N_0 [10^5]	T_0 [nK]	$\nu_{x,y,z}$ [Hz]	η	t_{wait} [ms]
green	1.8 (2)	2400 (200)	70 (10)	7.0 (1.5)	2000
			123 (15)		
			263 (25)		
red	0.46 (2)	500 (100)	44 (5)	4.0 (1.5)	500
			87 (10)		
			145 (15)		
blue	1.0 (2)	450 (100)	52 (5)	5.0 (1.5)	500
			23 (5)		
			260 (25)		

Tab. 6.2, Summary of the experimental conditions used for the atom-loss spectroscopy. N_0 and T_0 are the initial atom number and temperature, η the trap ratio, $\nu_{x,y,z}$ the trapping frequencies in the three directions and t_{wait} the holding time of the atoms in the final trap.

6.3.4 Universal Loss Dynamics

So far we could prove that our broad resonances have resonance strength parameters of $s_{\mathrm{res}} \gg 1$ and that their properties are well described by the universal expressions of the binding energy Eq. (3.18) and scattering length Eq. (3.17). Thus, we expect to observe further characteristics for broad resonances. In this section we show strong evidence that our observation of atom losses in the vicinity of the pole are indeed comparable with universal loss dynamics found at the center of broad resonances, for example observed in ^{133}Cs [197] and ^{39}K [198].

For this we study atom-losses around the broad resonances at different temperatures. We observe that close to the poles the final atom number reaches a minimum which is the same for both resonances, see Figure (6.17). Furthermore, we find that at lower temperature the saturation is reached in a narrower magnetic field region and at a lower level.

The change in atom number for a given wait time is described by Eq. (6.2) and depends on the three-body loss coefficient L_3. For small scattering lengths ($|a| \ll \lambda_{\mathrm{dB}}$) the loss coefficient scales as $L_3 \sim a^4$. Since a diverges close to the pole of a Feshbach resonance it is no longer a relevant parameter and another length scale is necessary to describe L_3. This is the thermal wavelength λ_{dB} resulting in a scaling of the loss coefficient as $L_3 \sim \lambda_{\mathrm{dB}}^4 \sim 1/T^2$. An exact expression for the temperature dependent three-body loss coefficient in the unitary regime ($a/\lambda_{\mathrm{dB}} \gg 1$) was calculated by Ref. [199] and is given by

$$L_3 = \frac{\hbar^5}{m^3} 36\sqrt{3}\pi^2 \frac{1 - e^{-4\eta_*}}{(k_{\mathrm{B}}T)^2} \,, \tag{6.7}$$

where η_* is the loss coefficient when three atoms are close to each other. For $\eta_* = 0$ there is no three-body loss whereas in the limit of $\eta_* \to \infty$ all particles are lost.

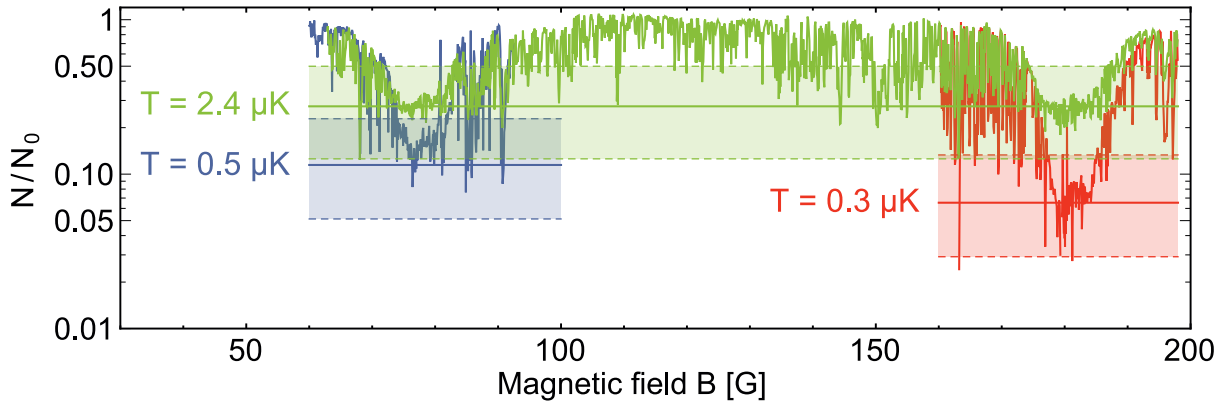

Fig. 6.17, Universal loss dynamics: Atom loss spectroscopy for different initial conditions. Final atom number N normalized to the initial N_0 as a function of magnetic field with a resolution of $\Delta B = 100\,\mathrm{mG}$. See Table (6.2) for the experimental conditions of the different data sets. The temperature dependence of the saturation is well reproduced by the model of universal loss dynamics of a Bose gas of Ref. [200] (solid horizontal lines). The shaded regions represent the uncertainty on the result of the model given a one-standard deviation on all experimental parameters.

We analyze our data with the model developed in Ref. [200]. This model predicts the final atom number taking into account two-body evaporation and three-body recombination. The model requires the knowledge of the trap depth, trap frequencies, initial atom number and temperature.

We use forced evaporation to cool the atomic sample down to the required temperatures T. The trap depth U can be expressed through the trap ratio $\eta = U/(k_\mathrm{B}T)$. It can be estimated with the knowledge of the beam waist of the crossed ODT and the effect of gravity. The trap ratio strongly depends on the knowledge of the trapping potential. In addition, since Dy is strongly magnetic any residual magnetic field gradient can change the trap depth. We improved our estimations of this parameter using a statistical analysis of final temperature and atom number in our atom-loss spectroscopy. For this we used loss dynamics equations adapted from [200] for a finite s-wave scattering length and including universal dipolar scattering. Doing this we obtained a knowledge of η with an uncertainty of 20 %. In Table (6.2) we summarize the initial conditions and parameters for the three different data sets presented in Figure (6.17). Using these parameters we obtain the expected final atom number for unitary-limited two- and three-body losses in a Bose gas. These predictions are compared to our measured data in Figure (6.17). The shaded areas represent the range where the calculated final atom number is obtained by varying the input parameters of the model by one standard deviation. The only unknown parameter of the model is η_*. By comparing the model with a fixed η_* to our measured three data sets we obtain η_* to be

$$\eta_* = 0.07^{+0.17}_{-0.05}. \tag{6.8}$$

Since the saturation levels of both resonances are similar, also η_* takes the same value. Further systematic studies of $L_3(T)$ at the resonances would yield a more precise measure of η_*, which would indicate the possibility to observe Efimov states in the vicinity of the two broad resonances [201].

Conclusion

In this chapter we presented the Feshbach spectroscopy data for the ^{164}Dy and ^{162}Dy isotope in a magnetic field range from 0 G to 600 G. We could show that the dense spectrum of 4 resonances per Gauss is caused by the complex molecular structure. The anisotropic DDI as well as the ADI induce the Feshbach resonances but only the anisotropic dispersion interaction is responsible for the chaotic scattering behavior. It is remarkable that despite the many narrow resonances isolated states can decouple from this background and form broad resonances at $B_0 = 76.9(5)\,\mathrm{G}$ and $B_0 = 178.8(6)\,\mathrm{G}$ for the ^{164}Dy isotope. In addition, these broad resonances maintain their universal properties, with $s_{\mathrm{res}} \gg 1$ over a large magnetic field range. For the 77 G resonance we could obtain a width of $\Delta = 31(6)\,\mathrm{G}$ and a background scattering length of $a_{\mathrm{bg}} = 91(15)\,a_0$. The simple universal description allows us to control the scattering properties of the dipolar gas in a controlled way [34] and we can obtain pure BECs at a magnetic field of $B = 63\,\mathrm{G}$ (between narrow resonances) with up to $N = 25 \times 10^3$ atoms with $\gtrsim 1\,\mathrm{s}$ lifetimes. The broad resonances are promising candidates to allow the study of few-body physics like Efimov states [202]. Additionally, the observed bound-states of the broad resonances have magnetic moments of $\mu_m \approx 20\,\mu_B$ close to that of two free atoms, which is the highest reported magnetic dipole moment [203].

7 Summary and Outlook

Summary

The main subject of this thesis was the creation of a dipolar quantum gas of Dy atoms and the investigation of its two-body interactions. For this purpose we setup a new experimental apparatus which allows us to study dipolar many-body systems with ultra-cold bosonic ^{164}Dy, ^{162}Dy as well as fermionic ^{161}Dy atoms.

Our cooling and trapping scheme to create a degenerate gas of Dy atoms consists of a ZS operating at the 421 nm transition and a MOT using the 626 nm transition. Following this, we use an ODT to transport the atoms over a range of 375 mm to a science cell. Here, we have the possibility to take in-trap images as well as to manipulate the atoms with magnetic fields and further optical potentials. In the crossed ODT we employ a further Doppler cooling stage to increase the phase space density and finally we perform forced evaporative cooling to reach degeneracy. With our system we can produce BECs with $N \approx 25 \times 10^3$ ($N \approx 30 \times 10^3$) atoms of the ^{164}Dy (^{162}Dy) isotope, respectively. In addition, we can create degenerate Fermi gases of spin-polarized Dy samples thanks to dipolar scattering. So far a degenerate Fermi gas with $N \approx 10 \times 10^3$ and $T/T_F \approx 0.5$ could be realized.

By comparing the saturation of the BEC atom number for different trap ratios with the predictions of GPE simulations we could estimate the hitherto unknown background scattering length of the ^{164}Dy isotope to be between $86\,a_0 \lesssim a_{\mathrm{bg}}^{164} \lesssim 93\,a_0$. The more efficient evaporative cooling and the higher obtained BEC atom number indicate a larger scattering length of the ^{162}Dy than the ^{164}Dy isotope. We also investigated the stability of a ^{162}Dy condensate by changing the magnetic field direction which effectively transforms an oblate ($\lambda > 1$) to a prolate ($\lambda < 1$) trap. As the condensate was not stable we could conclude that the scattering length of the ^{162}Dy isotope is $a_{\mathrm{bg}}^{164} \lesssim a_{\mathrm{bg}}^{162} \lesssim a_{\mathrm{dd}} = 134\,a_0$. This means that for both isotopes the DDI compared to the contact interaction at background scattering length is the dominant interaction ($\epsilon_{\mathrm{dd}} = a_{\mathrm{dd}}/a > 1$). This allows to study strongly dipolar effects with Dy atoms without the necessity to reduce the contact interaction by a Feshbach resonance.

To investigate the scattering properties of Dy we measured and analyzed Feshbach resonances for the ^{164}Dy as well as for the ^{162}Dy isotope in a magnetic field range from 0 G to 600 G. We could show that the dense spectrum of four resonances per Gauss is caused by the complex molecular structure. Using statistical methods to analyze the resonance positions based on RMT we found signatures of quantum chaos in the scattering behavior of Dy atoms. Further theoretical simulations could indicate that the joint effect of anisotropy of the dispersion interaction and the Zeeman coupling is responsible for the chaotic behavior. Despite the many narrow resonances we found for both isotopes broad distinct features in the Feshbach spectrum. By measuring the binding energy of

their molecular-state we could prove that the loss-features correspond to broad Feshbach resonances showing universal behavior with a resonance strength $s_{\mathrm{res}} \gg 1$ over a large magnetic field range. It is quite surprising that states which are responsible for the broad resonances decoupled from the strongly coupled states causing all the narrow resonances. By estimating the zero-crossing of the scattering length we could calculate the width $\Delta = 31(6)\,\mathrm{G}$ and the background scattering length $a_{\mathrm{bg}} = 91(15)$ of the resonances located at $B_0 = 76.9\,\mathrm{G}$. The obtained value for the background scattering length agrees with our estimations above and with the recently by cross-dimensional rethermalization measured values of $a_{\mathrm{bg}} = 92(8)\,a_0$ for ^{164}Dy [45].

The studies presented in this thesis show the possibilities of our new Dy apparatus. Our developed scheme to create ultra-cold fermionic as well as bosonic Dy samples provides good starting conditions for further experiments on dipolar many-body systems. In particular, the transport of the atoms to the science cell allows the usage of the in-trap imaging system as well as the possibility to create tailored time-averaged trapping potentials using the EOD system, which will be of great benefit for further studies.

Ongoing Work

Very recently we were able to directly observe, using our high-resolution imaging system a spontaneous transition from an unstructured superfluid to an ordered arrangement of long-lived droplets in a Dy condensate [143]. Structure formation has been studied with classical ferrofluids and is known as the normal-field instability or the Rosensweig instability [148, 204]. For example, a magnetized ferrofluid forms stable droplet patterns on a super-hydrophobic surface due to a competition between gravity, surface tension and magnetic forces [205]. The analysis of the dispersion relation of surface excitations displays a minimum at finite momentum. In a quantum ferrofluid like a Dy condensate a similar competition between the harmonic trapping, contact interaction and dipolar interaction exists. For a large relative dipolar interaction the excitation spectrum shows also a minimum at finite momentum which can lead to a periodic perturbation of the atomic density distribution, known as the roton instability [206]. So far it was believed that these rotonic structures would be unstable due to an instability of the forming droplets [207].

To investigate the droplet formation in a ^{164}Dy condensate we use the Feshbach resonance at $B_0 = 7.117(3)\,\mathrm{G}$. We create an almost pure BEC with $N = 15 \times 10^3$ atoms at a scattering length of $a \approx a_{\mathrm{dd}}$ in a radially symmetric trap with trapping frequencies of $(f_x, f_y, f_z) = (46, 44, 133)\,\mathrm{Hz}$ and the magnetic dipoles are aligned in z-direction. By reducing the scattering length to $a = a_{\mathrm{bg}} < a_{\mathrm{dd}}$ we likely induce an angular roton instability [41] and trigger the transition to an ensemble of droplets mostly arranged in a triangular lattice, presented in Figure (7.1).

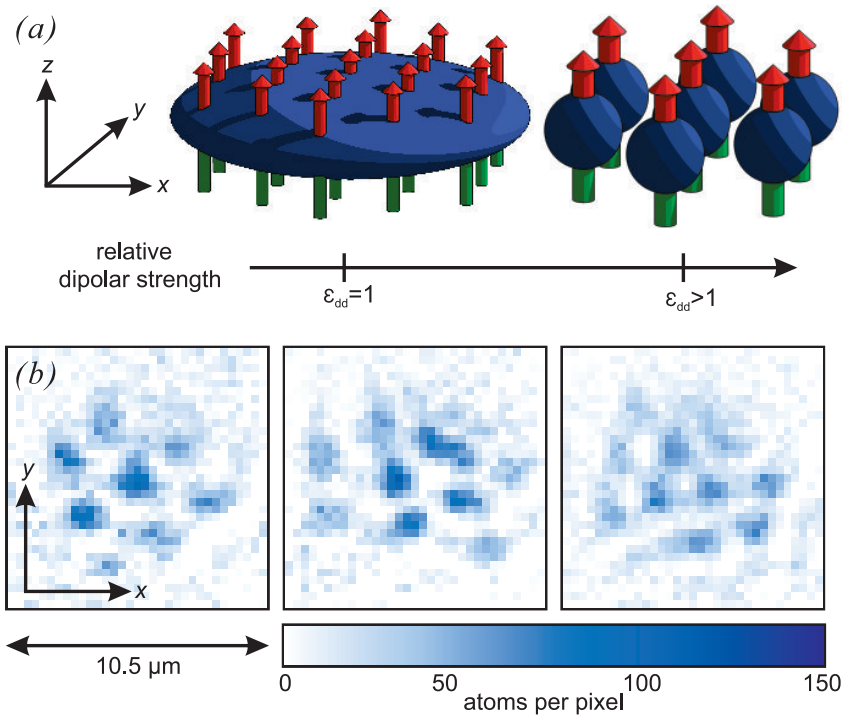

Fig. 7.1, Microscopic droplets in a quantum ferrofluid: *(a)* Schematic of the experimental sequence: We create a Dy condensate at $\epsilon_{\mathrm{dd}} = a_{\mathrm{dd}}/a \approx 1$. By increasing the relative dipolar strength ($\epsilon_{\mathrm{dd}} > 1$) we induce a roton instability and subsequently the atoms cluster to droplets in a triangular lattice. *(b)* High-resolution single-shot in-situ image of the droplets pattern. Figure with small modifications taken from [143].

The coexistence of superfluidity and spatial long-range order defines the supersolid state [208–210]. The observation of this state has been claimed for the first time in helium [211], but had to be withdrawn recently [212]. So far we could not probe the superfluidity in the structured states, but if we can show in further experiments that the droplets have a common phase this system is a very good candidate for a supersolid ground-state. Note that so far GPE simulations could not explain the stability of the droplets, which means that our observation represents a novel state of matter.

Future Perspectives

With our system we may be able to observe further self-organized structures of dipolar quantum gases in different trapping geometries. To create time-averaged tailored optical potentials we can use our microscope objective together with an EOD system. With this combined system it is possible for example to study dipolar condensates in a toroidal trap. By alining the dipoles in the plane of the trap the DDI is breaking the rotational symmetry of the system and the atoms may accumulate at two opposite sites of the ring-trap and a

self-induced Josephson-junction is created. For an imbalanced population the atoms may coherently tunnel though the weak links analog to Josephson oscillations [213].

Additionally the investigation of a dipolar quantum gas in multi-well potentials could show interesting dipolar effects. For example a system of three wells could be able to support non-trivial phases in its ground-state depending on the interplay between tunable on-site and inter-site interaction as well as a tunable tunnel coupling between the wells [214]. For a system with a linear arrangement of the three wells the repulsive DDI can lead to a depopulation of the middle well. This would not be observable if only short-range interactions are present [215].

Here, I have only presented a small selection of possible dipolar many-body effects that can be studied with our new apparatus. In addition, the observed broad resonances provide the possibility to observe few-body phenomena like Efimov states [202]. Furthermore, we are not restricted to only investigate bosonic quantum gases. With our cooling and trapping scheme we can also create ultra-cold fermionic samples to study for example universal three-body physics [216] or it may be even possible to study dipolar Bose-Fermi mixtures.

A Appendix

A.1 Sum-frequency Generation of 626 nm Light

To create 626 nm light we setup a home-build laser system as it was introduced in Ref. [156]. We create a 626 nm photon by sum frequency generation (SFG) of two infrared photons at 1550 nm and 1050 nm in a periodically poled lithium niobate (PPLN) crystal. To mix three different electromagnetic waves second nonlinear processes are required. Therefore, usually nonlinear crystals where the dielectric polarization $\boldsymbol{P}$ response nonlinear in the electric field $\boldsymbol{E}$ of the light field are used.

To efficiently generate 626 nm photons the phase matching condition $\hbar\boldsymbol{k}_{626} \approx \hbar\boldsymbol{k}_{1050} + \hbar\boldsymbol{k}_{1550}$ has to be fulfilled over the whole crystal length. Otherwise the generated photons will destructively interfere with each other, which limits the total number of photons leaving the crystal. The PPLN crystal is designed in a way such that quasi-phase matching is achieved. Lithium niobate is a ferroelectric crystal meaning that each unit cell has a small electric dipole moment. The quasi-phase matching is engineered by the periodically inversion of these dipole moments by strong electric fields during the crystal production. The inverted regions of the crystal generate photons that are 180° out of phase with respect to the generated photons in the non-inverted regions. With the right periodicity the newly generated photons will mostly interfere constructively with the previous ones. By changing the temperature of the crystal the periodicity of the poling can be altered slightly to adjust the phase match condition to account for slight frequency changes.

As the PPLN crystal is a nonlinear material the highest conversion efficiency is obtained for high light intensities. This is usually done by focusing the light into the center of the crystal. For a laser beam with a Gaussian beam profile good conversion efficiencies are obtained for the condition $z_0 = 1/2\,l$, where z_0 is the Rayleigh length and l the length of the crystal[101]. This results in high light intensities over the full length of the crystal. Our used PPLN crystal has dimensions of $(l \times w \times h) = (40 \times 10 \times 0.5)$ mm and three gratings with $11.12, 11.17$ and $11.22\,\mu$m periods. We use the $11.22\,\mu$m period and optimize the conversion efficiency by adjusting the temperature to $T = 172.22$°C. The input as well as the output facets are anti-reflection coated with reflectivity $< 1\%$ for all three wavelengths. To realize the condition for high conversion efficiency we have to focus the 1050 nm (1550 nm) light to $w_0 = 55\,\mu$m ($w_0 = 66.6\,\mu$m), respectively[102]. The used lens system is shown in Figure (4.4). An optimum of the sum frequency generation is achieved for vertical polarization of both infrared beams. In Figure (A.1) we show the SFG output power as a function of the product of the pump and signal input power. We fit the data by a linear function forced to go through the origin and from the slope we can estimate

[101] This condition was recommended by Covesion, whereas the Boyd-Kleinman model predicts $l/(2z_0) = 2.84$.

[102] Refractive index of the crystal: $n_{1550} = 2.222$, $n_{1050} = 2.203$.

the SFG efficiency to be

$$\eta_{SFG} = \frac{P_{626}}{P_{1050}\, P_{1550}\, l} = 2.07(3)\,\%\,\mathrm{W}^{-1}\mathrm{cm}^{-1}, \tag{A.1}$$

which is approximately 20% smaller than the efficiency obtained in Ref [156]. Typically, we operate the system at a lower output power of $P_{626} = 1\,\mathrm{W}$, which is sufficient to run the Dy quantum gas experiment.

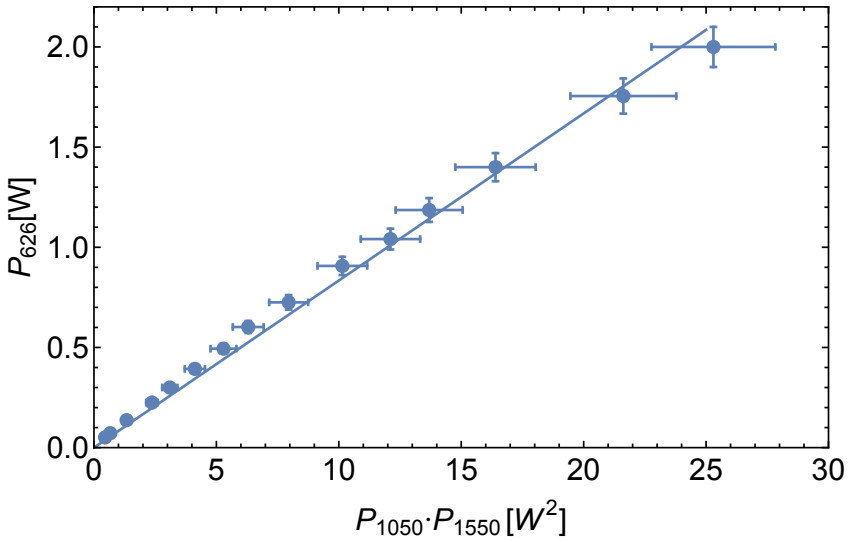

Fig. A.1, Sum-frequency generation of 626 nm light: SFG output power as a function of the product of the powers of the 1050 nm and 1550 nm light.

A.2 Octagonal Glass Cell

Our octagonal glass cell consist of a blown quart glass frame with nine bonded high quality windows to provide optimum optical access to the atoms. In Figure (A.2) we show a detail technical drawing of the glass cell.

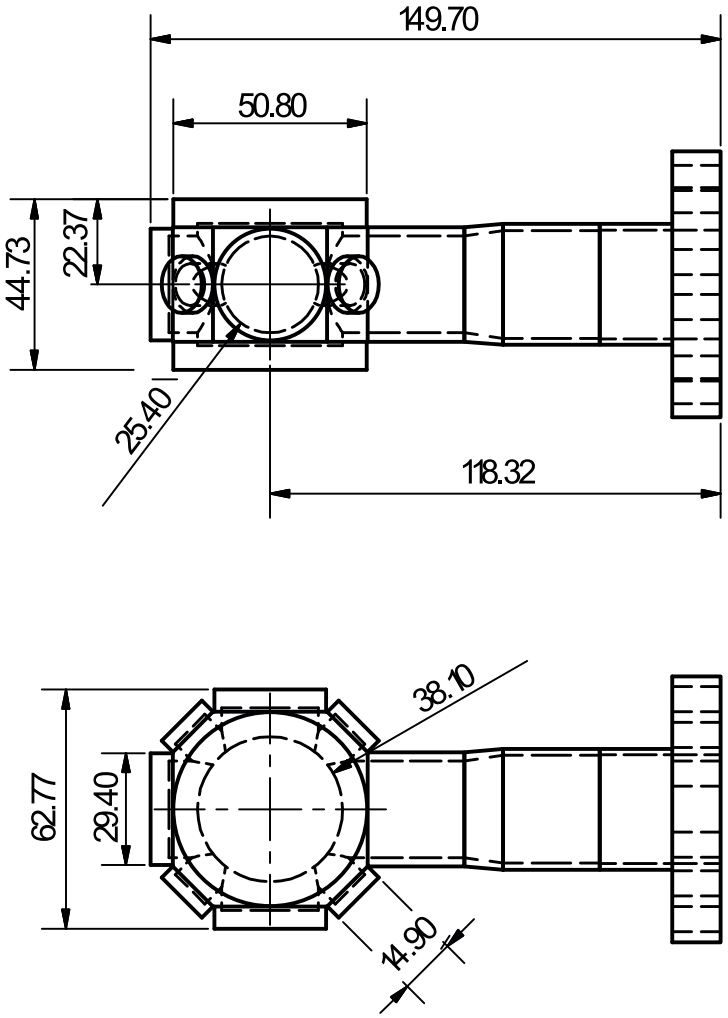

Fig. A.2, Octagonal Glass cell: Technical drawing of our glass cell. All dimensions are given in millimeter.

A.3 Full Level Diagram

In Figure (A.3) we show the full level diagram of Dy consisting of 394 even and 346 odd partity states [65, 66].

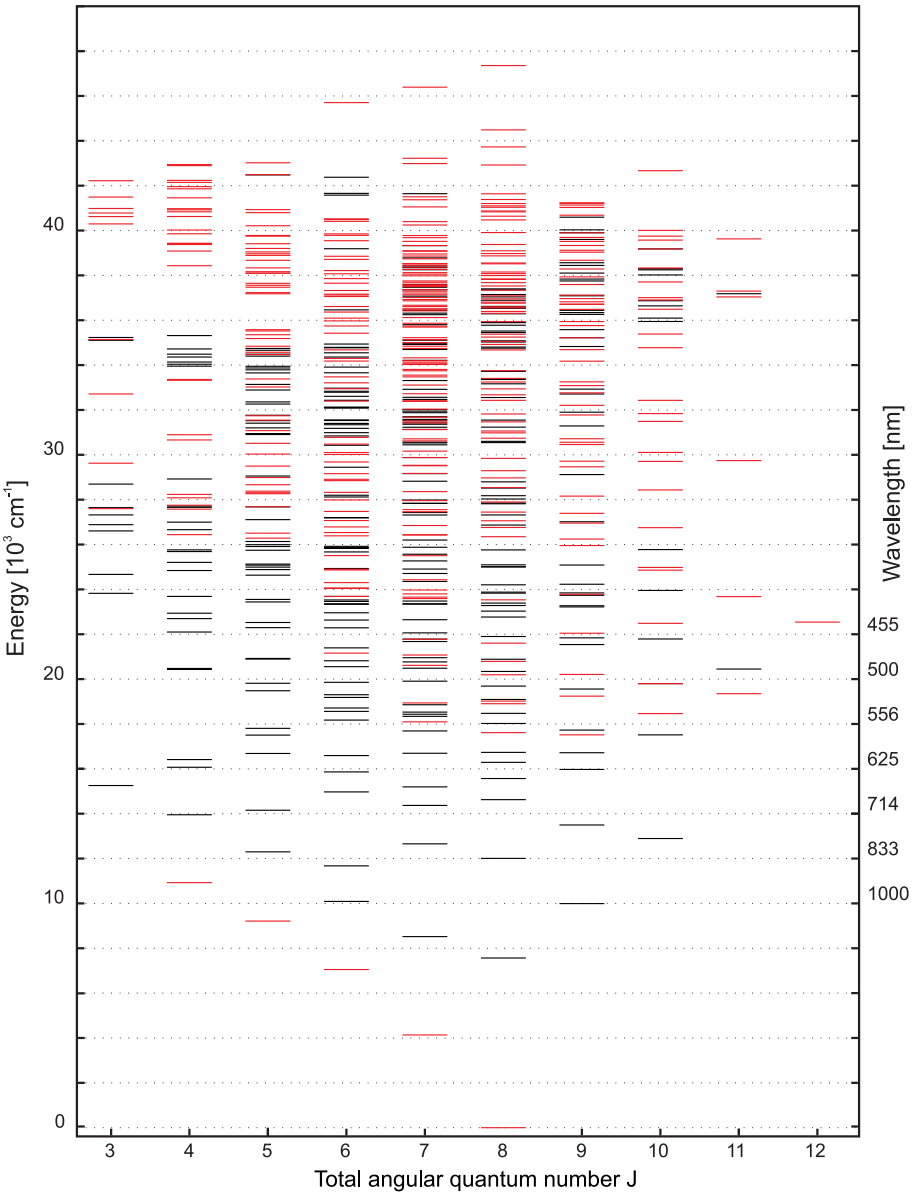

Fig. A.3, Full level diagramm of Dy: The levels are ordered by their total angular momentum quantum number J. States with even (odd) parity are shown in red (black).

References*

[1] K. B. Davis, M.-O. Mewes, M. R. Andrews, van Druten, N. J. D. S. Durfee, D. M. Kurn, and W. Ketterle: "*Bose-Einstein Condensation in a Gas of Sodium Atoms.*" Physical Review Letters **75**, 3969–3973 (1995)

[2] M. H. Anderson, J. R. Ensher, M. R. Matthews, C. E. Wieman, and E. A. Cornell: "*Observation of bose-einstein condensation in a dilute atomic vapor.*" Science **269**, 198–201 (1995)

[3] C. C. Bradley, C. A. Sackett, J. J. Tollett, and R. G. Hulet: "*Evidence of Bose-Einstein Condensation in an Atomic Gas with Attractive Interactions.*" Physical Review Letters **75**, 1687–1690 (1995)

[4] C. C. Bradley, C. A. Sackett, J. J. Tollett, and R. G. Hulet: "*Evidence of Bose-Einstein Condensation in an Atomic Gas with Attractive Interactions [Phys. Rev. Lett. 75, 1687 (1995)].*" Physical Review Letters **79**, 1170 (1997)

[5] D. G. Fried, T. C. Killian, L. Willmann, D. Landhuis, S. C. Moss, D. Kleppner, and T. J. Greytak: "*Bose-Einstein Condensation of Atomic Hydrogen.*" Physical Review Letters **81**, 3811–3814 (1998)

[6] A. Robert, O. Sirjean, A. Browaeys, J. Poupard, S. Nowak, D. Boiron, C. I. Westbrook, and A. Aspect: "*A Bose-Einstein condensate of metastable atoms.*" Science **292**, 461–464 (2001)

[7] G. Modugno, G. Ferrari, G. Roati, R. J. Brecha, A. Simoni, and M. Inguscio: "*Bose-Einstein condensation of potassium atoms by sympathetic cooling.*" Science **294**, 1320–1322 (2001)

[8] T. Weber, J. Herbig, M. Mark, H.-C. Nägerl, and R. Grimm: "*Bose-Einstein condensation of cesium.*" Science **299**, 232–235 (2003)

[9] Y. Takasu, K. Maki, K. Komori, T. Takano, K. Honda, M. Kumakura, T. Yabuzaki, and Y. Takahashi: "*Spin-Singlet Bose-Einstein Condensation of Two-Electron Atoms.*" Physical Review Letters **91**, 040404 (2003)

[10] A. Griesmaier, J. Werner, S. Hensler, J. Stuhler, and T. Pfau: "*Bose-Einstein Condensation of Chromium.*" Physical Review Letters **94**, 160401 (2005)

[11] S. Kraft, F. Vogt, O. Appel, F. Riehle, and U. Sterr: "*Bose-Einstein Condensation of Alkaline Earth Atoms: Ca_{40}.*" Physical Review Letters **103**, 130401 (2009)

[12] S. Stellmer, M. K. Tey, B. Huang, R. Grimm, and F. Schreck: "*Bose-Einstein Condensation of Strontium.*" Physical Review Letters **103**, 200401 (2009)

[13] M. Lu, N. Burdick, S. Youn, and B. Lev: "*Strongly Dipolar Bose-Einstein Condensate of Dysprosium.*" Physical Review Letters **107**, 190401 (2011)

*Most references are linked to the internet (pdf-version): The authors' names to the digital object identifier (doi) and the journal name to the URL-adress.

[14] K. Aikawa, A. Frisch, M. Mark, S. Baier, A. Rietzler, R. Grimm, and F. Ferlaino: "*Bose-Einstein Condensation of Erbium.*" Physical Review Letters **108**, 210401 (2012)

[15] W. Ketterle, D. S. Durfee, and D. M. Stamper-Kurn: "Making, probing and understanding Bose-Einstein condensates." in: *Proceedings of the International School of Physics Enrico Fermi, Course CXL: Bose-Einstein condensation in atomic gases.* (IOS Press, Amsterdam, 1999)

[16] B. DeMarco, and D. S. Jin: "*Onset of Fermi Degeneracy in a Trapped Atomic Gas.*" Science **285**, 1703–1706 (1999)

[17] F. Schreck, L. Khaykovich, K. L. Corwin, G. Ferrari, T. Bourdel, J. Cubizolles, and C. Salomon: "*Quasipure Bose-Einstein Condensate Immersed in a Fermi Sea.*" Physical Review Letters **87**, 080403 (2001)

[18] A. G. Truscott, K. E. Strecker, W. I. McAlexander, G. B. Partridge, and R. G. Hulet: "*Observation of Fermi pressure in a gas of trapped atoms.*" Science **291**, 2570–2572 (2001)

[19] J. M. McNamara, T. Jeltes, A. S. Tychkov, W. Hogervorst, and W. Vassen: "*Degenerate Bose-Fermi Mixture of Metastable Atoms.*" Physical Review Letters **97**, 080404 (2006)

[20] M. K. Tey, S. Stellmer, R. Grimm, and F. Schreck: "*Double-degenerate Bose-Fermi mixture of strontium.*" Physical Review A **82**, 011608(R) (2010)

[21] S. Sugawa, K. Inaba, S. Taie, R. Yamazaki, M. Yamashita, and Y. Takahashi: "*Interaction and filling-induced quantum phases of dual Mott insulators of bosons and fermions.*" Nature Physics **7**, 642–648 (2011)

[22] M. Lu, N. Burdick, and B. Lev: "*Quantum Degenerate Dipolar Fermi Gas.*" Physical Review Letters **108**, 215301 (2012)

[23] K. Aikawa, A. Frisch, M. Mark, S. Baier, R. Grimm, and F. Ferlaino: "*Reaching Fermi Degeneracy via Universal Dipolar Scattering.*" Physical Review Letters **112**, 010404 (2014)

[24] B. Naylor, A. Reigue, E. Maréchal, O. Gorceix, B. Laburthe-Tolra, and L. Vernac: "*Chromium dipolar Fermi sea.*" Physical Review A **91**, 011603(R) (2015)

[25] W. Ketterle, and M. W. Zwierlein: "Making, probing and understanding ultracold Fermi gases." in: *Proceedings of the International School of Physics Enrico Fermi, Course CLXIV: Ultracold Fermi Gases.* (IOS Press, Amsterdam, 2008)

[26] I. Bloch, J. Dalibard, and W. Zwerger: "*Many-body physics with ultracold gases.*" Reviews of Modern Physics **80**, 885–964 (2008)

[27] R. Grimm: "*Ultracold Fermi gases in the BEC-BCS crossover: a review from the Innsbruck perspective.*" arXiv:cond-mat/0703091v1 (2007)

[28] M. Greiner, O. Mandel, T. Esslinger, T. W. Hänsch, and I. Bloch: "*Quantum phase transition from a superfluid to a Mott insulator in a gas of ultracold atoms.*" Nature **415**, 39–44 (2002)

[29] W. S. Bakr, A. Peng, M. E. Tai, R. Ma, J. Simon, J. I. Gillen, S. Fölling, L. Pollet, and M. Greiner: "*Probing the superfluid-to-Mott insulator transition at the single-atom level.*" Science **329**, 547–550 (2010)

[30] J. F. Sherson, C. Weitenberg, M. Endres, M. Cheneau, I. Bloch, and S. Kuhr: "*Single-atom-resolved fluorescence imaging of an atomic Mott insulator.*" Nature **467**, 68–72 (2010)

[31] J. Stuhler, A. Griesmaier, T. Koch, M. Fattori, and T. Pfau: "*Magnetostriction in a degenerate quantum gas.*" Journal of Magnetism and Magnetic Materials **316**, 429–432 (2007)

[32] T. Lahaye, J. Metz, B. Fröhlich, T. Koch, M. Meister, A. Griesmaier, T. Pfau, H. Saito, Y. Kawaguchi, and M. Ueda: "*d-Wave Collapse and Explosion of a Dipolar Bose-Einstein Condensate.*" Physical Review Letters **101**, 080401 (2008)

[33] A. Griesmaier, J. Stuhler, T. Koch, M. Fattori, T. Pfau, and S. Giovanazzi: "*Comparing Contact and Dipolar Interactions in a Bose-Einstein Condensate.*" Physical Review Letters **97**, 250402 (2006)

[34] T. Lahaye, T. Koch, B. Fröhlich, M. Fattori, J. Metz, A. Griesmaier, S. Giovanazzi, and T. Pfau: "*Strong dipolar effects in a quantum ferrofluid.*" Nature **448**, 672–675 (2007)

[35] T. Takekoshi, L. Reichsöllner, A. Schindewolf, J. M. Hutson, Le Sueur, C. Ruth, O. Dulieu, F. Ferlaino, R. Grimm, and H.-C. Nägerl: "*Ultracold Dense Samples of Dipolar RbCs Molecules in the Rovibrational and Hyperfine Ground State.*" Physical Review Letters **113**, 205301 (2014)

[36] P. K. Molony, P. D. Gregory, Z. Ji, B. Lu, M. P. Köppinger, Le Sueur, C. Ruth, C. L. Blackley, J. M. Hutson, and S. L. Cornish: "*Creation of Ultracold Rb87Cs133 Molecules in the Rovibrational Ground State.*" Physical Review Letters **113**, 255301 (2014)

[37] J. W. Park, S. A. Will, and M. W. Zwierlein: "*Ultracold Dipolar Gas of Fermionic Na23K40 Molecules in Their Absolute Ground State.*" Physical Review Letters **114**, 205302 (2015)

[38] G. Pupillo, A. Micheli, M. Boninsegni, I. Lesanovsky, and P. Zoller: "*Strongly Correlated Gases of Rydberg-Dressed Atoms: Quantum and Classical Dynamics.*" Physical Review Letters **104**, 223002 (2010)

[39] T. Lahaye, C. Menotti, L. Santos, M. Lewenstein, and T. Pfau: "*The physics of dipolar bosonic quantum gases.*" Reports on Progress in Physics **72**, 126401 (2009)

[40] O. Dutta, and P. Meystre: "*Ground-state structure and stability of dipolar condensates in anisotropic traps.*" Physical Review A **75**, 053604 (2007)

[41] S. Ronen, D. C. E. Bortolotti, and J. L. Bohn: "*Radial and Angular Rotons in Trapped Dipolar Gases.*" Phys. Rev. Lett. **98**, 030406 (2007)

[42] H. P. Büchler, E. Demler, M. Lukin, A. Micheli, N. Prokof'ev, G. Pupillo, and P. Zoller: "*Strongly Correlated 2D Quantum Phases with Cold Polar Molecules: Controlling the Shape of the Interaction Potential.*" Physical Review Letters **98**, 060404 (2007)

[43] K. Góral, L. Santos, and M. Lewenstein: "*Quantum Phases of Dipolar Bosons in Optical Lattices.*" Physical Review Letters **88**, 170406 (2002)

[44] A. Bühler, and H. P. Büchler: "*Supersolid phase in atomic gases with magnetic dipole interaction.*" Physical Review A **84**, 023607 (2011)

[45] Y. Tang, A. Sykes, N. Q. Burdick, J. L. Bohn, and B. L. Lev: "*s -wave scattering lengths of the strongly dipolar bosons Dy162 and Dy164.*" Physical Review A **92**, 022703 (2015)

[46] S. Müller, J. Billy, E. Henn, H. Kadau, A. Griesmaier, M. Jona-Lasinio, L. Santos, and T. Pfau: "*Stability of a dipolar Bose-Einstein condensate in a one-dimensional lattice.*" Physical Review A **84**, 053601 (2011)

[47] B. Pasquiou, G. Bismut, E. Maréchal, P. Pedri, L. Vernac, O. Gorceix, and B. Laburthe-Tolra: "*Spin Relaxation and Band Excitation of a Dipolar Bose-Einstein Condensate in 2D Optical Lattices.*" Physical Review Letters **106**, 015301 (2011)

[48] K.-K. Ni, S. Ospelkaus, M. H. G. d. Miranda, A. Pe'er, B. Neyenhuis, J. J. Zirbel, S. Kotochigova, P. S. Julienne, D. S. Jin, and J. Ye: "*A High Phase-Space-Density Gas of Polar Molecules.*" Science **322**, 231–235 (2008)

[49] S. Ospelkaus, K.-K. Ni, D. Wang, de Miranda, M H G, B. Neyenhuis, G. Quéméner, P. S. Julienne, J. L. Bohn, D. S. Jin, and J. Ye: "*Quantum-state controlled chemical reactions of ultracold potassium-rubidium molecules.*" Science **327**, 853–857 (2010)

[50] T. Maier, H. Kadau, M. Schmitt, A. Griesmaier, and T. Pfau: "*Narrow-line magneto-optical trap for dysprosium atoms.*" Optics Letters **39**, 3138 (2014)

[51] T. Maier, H. Kadau, M. Schmitt, M. Wenzel, I. Ferrier-Barbut, T. Pfau, A. Frisch, S. Baier, K. Aikawa, L. Chomaz, M. J. Mark, F. Ferlaino, C. Makrides, E. Tiesinga, A. Petrov, and S. Kotochigova: "*Emergence of chaotic scattering in ultracold Er and Dy.*" arXiv:cond-mat/1506.05221v1 (2015)

[52] T. Maier, I. Ferrier-Barbut, H. Kadau, M. Schmitt, M. Wenzel, C. Wink, T. Pfau, K. Jachymski, and P. S. Julienne: "*Broad Feshbach resonances in collisions of ultracold Dysprosium atoms.*" arXiv:cond-mat/1506.01875v1 (2015)

[53] J. R. d. Laeter, J. K. Böhlke, P. d. Bièvre, H. Hidaka, H. S. Peiser, K. J. R. Rosman, and P. D. P. Taylor: "*Atomic weights of the elements. Review 2000 (IUPAC Technical Report).*" Pure and Applied Chemistry **75**, 683–800 (2003)

[54] J. Emsley: "*Nature's building blocks: An A-Z guide to the elements.*" (Oxford University Press, Oxford, 2003)

[55] D. Brown, B.-M. Ma, and Z. Chen: "*Developments in the processing and properties of NdFeb-type permanent magnets.*" Journal of Magnetism and Magnetic Materials **248**, 432–440 (2002)

[56] W. M. Haynes: "*CRC handbook of chemistry and physics, 2010-2011: A ready-reference book of chemical and physical data.*" (Taylor & Francis, London, 2010)

[57] G. K. Woodgate: "*Elementary atomic structure.*" serie: Oxford science publications. (Clarendon, Oxford, 1980)

[58] J. Ferch, W. Dankwort, and H. Gebauer: "*Hyperfine structure investigations in DyI with the atomic beam magnetic resonance method.*" Physics Letters A **49**, 287–288 (1974)

[59] N. Leefer, A. Cingöz, and D. Budker: "*Measurement of hyperfine structure and isotope shifts in the Dy 421 nm transition.*" Optics Letters **34**, 2548 (2009)

[60] W. Hogervorst, G. J. Zaal, J. Bouma, and J. Blok: "*Isotope shifts and hyperfine structure of natural dysprosium.*" Physics Letters A **65**, 220–222 (1978)

[61] M. Schmitt, E. A. L. Henn, J. Billy, H. Kadau, T. Maier, A. Griesmaier, and T. Pfau: "*Spectroscopy of a narrow-line optical pumping transition in atomic dysprosium.*" Optics Letters **38**, 637 (2013)

[62] M. Lu, S. Youn, and B. Lev: "*Spectroscopy of a narrow-line laser-cooling transition in atomic dysprosium.*" Physical Review A **83**, 012510 (2011)

[63] H. Haken, and H. C. Wolf: "*Atom- und Quantenphysik: Einführung in die experimentellen und theoretischen Grundlagen.*" serie: Springer-Lehrbuch. (Springer, Berlin, 2003)

[64] B. Judd, and I. Lindgren: "*Theory of Zeeman Effect in the Ground Multiplets of Rare-Earth Atoms.*" Physical Review **122**, 1802–1812 (1961)

[65] W.-C. Martin, R. Zalubas, and L. Hagan: "*Atomic Energy Levels - The Rare Earth Elements.*" NSRDS-NBS **60**, 261–279 (1978)

[66] G. Nave, and U. Griesmann: "*New Energy Levels and Classifications of Spectral Lines from Neutral and Singly-Ionized Dysprosium (Dy I and Dy II).*" Physica Scripta **62**, 463–473 (2000)

[67] J. McClelland, and J. Hanssen: "*Laser Cooling without Repumping: A Magneto-Optical Trap for Erbium Atoms.*" Physical Review Letters **96**, 143005 (2006)

[68] N. A. Leefer, A. Cingöz, D. Budker, S. J. Ferrell, V. V. Yashchuk, A. Lapierre, A.-T. Nguyen, S. K. Lamoreaux, and J. R. Torgerson: "*Variation of the Fine-Structure Constant and Laser Cooling of Atomic Dysprosium.*" arXiv:atom-ph/0811.3992v2 (2008)

[69] M. Lu, S. H. Youn, and B. L. Lev: "*Trapping Ultracold Dysprosium: A Highly Magnetic Gas for Dipolar Physics.*" Physical Review Letters **104**, 063001 (2010)

[70] M. Gustavsson, H. Lundberg, L. Nilsson, and S. Svanberg: "*Lifetime measurements for excited states of rare-earth atoms using pulse modulation of a cw dye-laser beam.*" Journal of the Optical Society of America **69**, 984 (1979)

[71] A. Frisch, K. Aikawa, M. Mark, A. Rietzler, J. Schindler, E. Zupani č, R. Grimm, and F. Ferlaino: "*Narrow-line magneto-optical trap for erbium.*" Phys. Rev. A **85**, 051401 (2012)

[72] T. Kuwamoto, K. Honda, Y. Takahashi, and T. Yabuzaki: "*Magneto-optical trapping of Yb atoms using an intercombination transition.*" Physical Review A **60**, R745–R748 (1999)

[73] M. Fattori, T. Koch, S. Goetz, A. Griesmaier, S. Hensler, J. Stuhler, and T. Pfau: "*Demagnetization cooling of a gas.*" Nature Physics **2**, 765–768 (2006)

[74] W.-G. Jin, T. Wakui, T. Endo, H. Uematsu, T. Minowa, and H. Katsuragawa: "*Specific Mass Shift in Gd I and Dy I.*" Journal of the Physics Society Japan **70**, 2316–2320 (2001)

[75] S. Müller: "*Stability and collapse dynamics of dipolar Bose-Einstein condensates in one-dimensional optical lattices.*" (PhD thesis, Stuttgart, 2013)

[76] L. D. Landau, and E. M. Lifshits: "*Quantum mechanics: Non-relativistic theory.*" serie: Course of theoretical physics. (Butterworth-Heinemann, Oxford, 1991)

[77] J. Dalibard: "Collisional dynamics of ultra-cold atomic gases." in: *Proceedings of the International School of Physics Enrico Fermi, Course CXL: Bose-Einstein condensation in gases.* (IOS Press, Amsterdam, 1999)

[78] J. Weiner, V. S. Bagnato, S. Zilio, and P. S. Julienne: "*Experiments and theory in cold and ultracold collisions.*" Reviews of Modern Physics **71**, 1–85 (1999)

[79] C. Pethick, and H. Smith: "*Bose-Einstein condensation in dilute gases.*" (Cambridge University Press, Cambridge, 2008)

[80] C. Chin, R. Grimm, P. Julienne, and E. Tiesinga: "*Feshbach resonances in ultracold gases.*" Reviews of Modern Physics **82**, 1225–1286 (2010)

[81] B. DeMarco, J. L. Bohn, J. P. Burke, M. Holland, and D. S. Jin: "*Measurement of p -Wave Threshold Law Using Evaporatively Cooled Fermionic Atoms.*" Physical Review Letters **82**, 4208–4211 (1999)

[82] S. Kotochigova, and A. Petrov: "*Anisotropy in the interaction of ultracold dysprosium.*" Physical Chemistry Chemical Physics **13**, 19165 (2011)

[83] G. Astrakharchik, and Y. Lozovik: "*Super-Tonks-Girardeau regime in trapped one-dimensional dipolar gases.*" Physical Review A **77**, 013404 (2008)

[84] A. Frisch: "*Dipolar quantum gases of erbium.*" (PhD thesis, Innsbruck, 2014)

[85] J. L. Bohn, M. Cavagnero, and C. Ticknor: "*Quasi-universal dipolar scattering in cold and ultracold gases.*" New Journal of Physics **11**, 055039 (2009)

[86] M. Baranov: "*Theoretical progress in many-body physics with ultracold dipolar gases.*" Physics Reports **464**, 71–111 (2008)

[87] C. Ticknor: "*Collisional Control of Ground State Polar Molecules and Universal Dipolar Scattering.*" Physical Review Letters **100**, 133202 (2008)

[88] S. Yi, and L. You: "*Trapped atomic condensates with anisotropic interactions.*" Physical Review A **61**, 041604 (2000)

[89] S. Yi, and L. You: "*Trapped condensates of atoms with dipole interactions.*" Physical Review A **63**, 053607 (2001)

[90] V. Hnizdo: "*Generalized second-order partial derivatives of 1/ r.*" European Journal of Physics **32**, 287–297 (2011)

[91] S. Ronen, D. C. E. Bortolotti, D. Blume, and J. L. Bohn: "*Dipolar Bose-Einstein condensates with dipole-dependent scattering length.*" Phys. Rev. A **74**, 033611 (2006)

[92] J. Metz: "*Collapse of dipolar Bose-Einstein condensates for different trap geometries.*" (PhD thesis, Stuttgart, 2010)

[93] H. Feshbach: "*Unified theory of nuclear reactions.*" Annals of Physics **5**, 357–390 (1958)

[94] U. Fano: "*Effects of Configuration Interaction on Intensities and Phase Shifts.*" Physical Review **124**, 1866–1878 (1961)

[95] W. Zwerger: "*The BCS-BEC crossover and the unitary Fermi gas.*" serie: Lecture notes in physics. (Springer, Heidelberg, 2012)

[96] F. Ferlaino, A. Zenesini, M. Berninger, B. Huang, H.-C. Nägerl, and R. Grimm: "*Efimov Resonances in Ultracold Quantum Gases.*" Few-Body Systems **51**, 113–133 (2011)

[97] J. G. Danzl, E. Haller, M. Gustavsson, M. J. Mark, R. Hart, N. Bouloufa, O. Dulieu, H. Ritsch, and H.-C. Nägerl: "*Quantum gas of deeply bound ground state molecules.*" Science **321**, 1062–1066 (2008)

[98] J. Stuhler, A. Griesmaier, T. Koch, M. Fattori, T. Pfau, S. Giovanazzi, P. Pedri, and L. Santos: "*Observation of Dipole-Dipole Interaction in a Degenerate Quantum Gas.*" Physical Review Letters **95**, 150406 (2005)

[99] H. Feshbach: "*Unified Theory of Nuclear Reactions.*" Reviews of Modern Physics **36**, 1076–1078 (1964)

[100] M. Marinescu, and L. You: "*Controlling Atom-Atom Interaction at Ultralow Temperatures by dc Electric Fields.*" Physical Review Letters **81**, 4596–4599 (1998)

[101] S. Inouye, M. R. Andrews, J. Stenger, H.-J. Miesner, D. M. Stamper-Kurn, and W. Ketterle: "*Observation of Feshbach resonances in a Bose-Einstein condensate.*" Nature **392**, 151–154 (1998)

[102] A. J. Moerdijk, B. J. Verhaar, and A. Axelsson: "*Resonances in ultracold collisions of Li6 , Li7 , and Na23.*" Physical Review A **51**, 4852–4861 (1995)

[103] B. Gao: "*General form of the quantum-defect theory for $-1/r^{\alpha}$ type of potentials with $\alpha > 2$.*" Physical Review A **78**, 012702 (2008)

[104] J. Werner, A. Griesmaier, S. Hensler, J. Stuhler, and T. Pfau: "*Observation of Feshbach Resonances in an Ultracold Gas of Cr.*" Physical Review Letters **94**, 183201 (2005)

[105] A. Petrov, E. Tiesinga, and S. Kotochigova: "*Anisotropy-Induced Feshbach Resonances in a Quantum Dipolar Gas of Highly Magnetic Atoms.*" Physical Review Letters **109**, 103002 (2012)

[106] S. Kotochigova: "*Controlling interactions between highly magnetic atoms with Feshbach resonances.*" Reports on progress in physics. Physical Society **77**, 093901 (2014)

[107] A. Frisch, M. Mark, K. Aikawa, F. Ferlaino, J. L. Bohn, C. Makrides, A. Petrov, and S. Kotochigova: "*Quantum chaos in ultracold collisions of gas-phase erbium atoms.*" Nature **507**, 475–479 (2014)

[108] F. Haake: "*Quantum signatures of chaos.*" serie: Springer series in synergetics. (Springer, Berlin, 2010)

[109] R. V. Jensen: "*Quantum chaos.*" Nature **355**, 311–318 (1992)

[110] D. Wintgen, and H. Friedrich: "*Classical and quantum-mechanical transition between regularity and irregularity in a Hamiltonian system.*" Physical Review A **35**, 1464–1466 (1987)

[111] G. Wunner: "*Gibt es Chaos in der Quantenmechanik?*" Physik Journal **45**, 139–145 (1989)

[112] E. Fermi, E. Amaldi, O. D'Agostino, F. Rasetti, and E. Segre: "*Artificial Radioactivity Produced by Neutron Bombardment.*" Proceedings of the Royal Society A: Mathematical, Physical and Engineering Sciences **146**, 483–500 (1934)

[113] W. M. Wilson, E. G. Bilpuch, and G. E. Mitchell: "*Applications of statistical tests to proton resonances in 45Sc and 49V.*" Nuclear Physics A **245**, 285–305 (1975)

[114] E. P. Wigner: "*On a Class of Analytic Functions from the Quantum Theory of Collisions.*" The Annals of Mathematics **53**, 36 (1951)

[115] M. L. Mehta, and F. J. Dyson: "*Statistical Theory of the Energy Levels of Complex Systems. V.*" Journal of Mathematical Physics **4**, 713 (1963)

[116] T. Guhr, A. Müller–Groeling, and H. A. Weidenmüller: "*Random-matrix theories in quantum physics: common concepts.*" Physics Reports **299**, 189–425 (1998)

[117] K. Rajan, and L. F. Abbott: "*Eigenvalue Spectra of Random Matrices for Neural Networks.*" Physical Review Letters **97**, 188104 (2006)

[118] J. P. Bouchaud, and M. Potters: "*Financial applications of random matrix theory: A short review.*" arXiv:q-fin.ST/0910.1205v1 (2009)

[119] H. A. Weidenmüller, and G. E. Mitchell: "*Random matrices and chaos in nuclear physics: Nuclear structure.*" Reviews of Modern Physics **81**, 539–589 (2009)

[120] T. A. Brody: "*A statistical measure for the repulsion of energy levels.*" Lettere Al Nuovo Cimento Series 2 **7**, 482–484 (1973)

[121] H.-J. Stöckmann: "*Quantum chaos.*" (Cambridge University Press, Cambridge, 2006)

[122] O. Bohigas, M. J. Giannoni, and C. Schmit: "*Characterization of Chaotic Quantum Spectra and Universality of Level Fluctuation Laws.*" Physical Review Letters **52**, 1–4 (1984)

[123] O. Bohigas, and M.-J. Giannoni: "Chaotic motion and random matrix theories." in: *Mathematical and Computational Methods in Nuclear Physics.* serie: Lecture Notes in Physics. ed.: J.S. Dehesa, J.M.G. Gomez, and A. Polls. (Springer, 1984)

[124] M. C. Gutzwiller: "*Chaos in classical and quantum mechanics.*" serie: Interdisciplinary applied mathematics. (Springer-Verlag, New York, 1990)

[125] A. Einstein, and J. Grommer: "Allgemeine Relativitätstheorie und Bewegungsgesetz." in: *Albert Einstein: Akademie-Vorträge.* (Wiley-VCH Verlag, Weinheim, 2006)

[126] S. Bose: "*Plancks Gesetz und Lichtquantenhypothese.*" Zeitschrift für Physik **26**, 178–181 (1924)

[127] J. Klaers, J. Schmitt, F. Vewinger, and M. Weitz: "*Bose-Einstein condensation of photons in an optical microcavity.*" Nature **468**, 545–548 (2010)

[128] J. P. Eisenstein, and A. H. Macdonald: "*Bose-Einstein condensation of excitons in bilayer electron systems.*" Nature **432**, 691–694 (2004)

[129] R. Balili, V. Hartwell, D. Snoke, L. Pfeiffer, and K. West: "*Bose-Einstein condensation of microcavity polaritons in a trap.*" Science **316**, 1007–1010 (2007)

[130] J. Kasprzak, M. Richard, S. Kundermann, A. Baas, P. Jeambrun, Keeling, J M J, F. M. Marchetti, M. H. Szymańska, R. André, J. L. Staehli, V. Savona, P. B. Littlewood, B. Deveaud, and S. Le Dang: "*Bose-Einstein condensation of exciton polaritons.*" Nature **443**, 409–414 (2006)

[131] M. Greiner, C. A. Regal, and D. S. Jin: "*Emergence of a molecular Bose–Einstein condensate from a Fermi gas.*" Nature **426**, 537–540 (2003)

[132] S. Jochim, M. Bartenstein, A. Altmeyer, G. Hendl, S. Riedl, C. Chin, J. Hecker Denschlag, and R. Grimm: "*Bose-Einstein condensation of molecules.*" Science **302**, 2101–2103 (2003)

[133] M. W. Zwierlein, C. A. Stan, C. H. Schunck, S. M. F. Raupach, S. Gupta, Z. Hadzibabic, and W. Ketterle: "*Observation of Bose-Einstein Condensation of Molecules.*" Physical Review Letters **91**, 250401 (2003)

[134] K. Xu, T. Mukaiyama, J. R. Abo-Shaeer, J. K. Chin, D. E. Miller, and W. Ketterle: "*Formation of Quantum-Degenerate Sodium Molecules.*" Physical Review Letters **91**, 210402 (2003)

[135] E. A. Cornell, J. R. Ensher, and C. E. Wieman: "Experiments in dilute atomic Bose-Einstein condensation in Bose-Einstein Condensation in Atomic Gases." in: *Proceedings of the International School of Physics Enrico Fermi, Course CXL: Bose-Einstein condensation in gases.* (IOS Press, Amsterdam, 1999)

[136] L. P. Pitaevskii, and S. Stringari: "*Bose-Einstein condensation.*" serie: Oxford science publications. (Clarendon Press, Oxford, 2003)

[137] F. Dalfovo, S. Giorgini, L. P. Pitaevskii, and S. Stringari: "*Theory of Bose-Einstein condensation in trapped gases.*" Reviews of Modern Physics **71**, 463–512 (1999)

[138] D. O'Dell, S. Giovanazzi, and C. Eberlein: "*Exact Hydrodynamics of a Trapped Dipolar Bose-Einstein Condensate.*" Physical Review Letters **92**, 250401 (2004)

[139] C. Eberlein, S. Giovanazzi, and D. O'Dell: "*Exact solution of the Thomas-Fermi equation for a trapped Bose-Einstein condensate with dipole-dipole interactions.*" Physical Review A **71**, 033618 (2005)

[140] T. Koch, T. Lahaye, J. Metz, B. Fröhlich, A. Griesmaier, and T. Pfau: "*Stabilization of a purely dipolar quantum gas against collapse.*" Nature Physics **4**, 218–222 (2008)

[141] T. Koch: "*Enhancing the dipolar character of a Bose-Einstein condensate: From perturbative effects to a purely dipolar quantum gas.*" (PhD thesis, Stuttgart, 2008)

[142] V. M. Pérez-García, H. Michinel, J. I. Cirac, M. Lewenstein, and P. Zoller: "*Low Energy Excitations of a Bose-Einstein Condensate: A Time-Dependent Variational Analysis.*" Physical Review Letters **77**, 5320–5323 (1996)

[143] H. Kadau, M. Schmitt, M. Wenzel, C. Wink, T. Maier, I. Ferrier-Barbut, and T. Pfau: "*Observing the Rosensweig instability of a quantum ferrofluid.*" arXiv:cond-mat/1508.05007 (2015)

[144] M. Lu: "*Quantum Bose and Fermi Gases of Dysprosium: Production and Initial Study.*" (PhD thesis, Stanford, 2014)

[145] S. Youn, M. Lu, U. Ray, and B. Lev: "*Dysprosium magneto-optical traps.*" Physical Review A **82**, 043425 (2010)

[146] P. O. Schmidt, S. Hensler, J. Werner, T. Binhammer, A. Görlitz, and T. Pfau: "*Doppler cooling of an optically dense cloud of magnetically trapped atoms.*" Journal of the Optical Society of America B **20**, 960 (2003)

[147] S. Hensler, J. Werner, A. Griesmaier, P. Schmidt, A. Görlitz, T. Pfau, S. Giovanazzi, and K. Rzazewski: "*Dipolar relaxation in an ultra-cold gas of magnetically trapped chromium atoms.*" Applied Physics B: Lasers and Optics **77**, 765–772 (2003)

[148] M. D. Cowley, and R. E. Rosensweig: "*The interfacial stability of a ferromagnetic fluid.*" Journal of Fluid Mechanics **30**, 671–688 (1967)

[149] P. Weinmann: "*Setting up a high-resolution optical system for trapping and imaging ultracold chromium atoms.*" (Diploma thesis, Stuttgart, 2011)

[150] R. P. Drever, J. L. Hall, F. V. Kowalski, J. Hough, G. M. Ford, A. J. Munley, and H. Ward: "*Laser phase and frequency stabilization using an optical resonator.*" Applied Physics B Photophysics and Laser Chemistry **31**, 97–105 (1983)

[151] E. D. Black: "*An introduction to Pound–Drever–Hall laser frequency stabilization.*" American Journal of Physics **69**, 79 (2001)

[152] J. Werner: "*Kontinuierliches Laden einer Magnetfalle mit lasergekühlten Chromatomen.*" (Diploma thesis, Stuttgart, 2000)

[153] B. Docters: "*Ein Lasersystem zur Kühlung von Dysprosiumatomen.*" (Bachelor thesis, Stuttgart, 2013)

[154] T. W. Hansch, and B. Couillaud: "*Laser frequency stabilization by polarization spectroscopy of a reflecting reference cavity.*" Optics Communications **35**, 441–444 (1980)

[155] U. Schünemann, H. Engler, R. Grimm, M. Weidemüller, and M. Zielonkowski: "*Simple scheme for tunable frequency offset locking of two lasers.*" Review of Scientific Instruments **70**, 242 (1999)

[156] A. C. Wilson, C. Ospelkaus, A. P. VanDevender, J. A. Mlynek, K. R. Brown, D. Leibfried, and D. J. Wineland: "*A 750-mW, continuous-wave, solid-state laser source at 313 nm for cooling and manipulating trapped 9Be+ ions.*" Applied Physics B **105**, 741–748 (2011)

[157] M. Schmitt: "*High Resolution Laser Spectroscopy of Dysprosium.*" (Master thesis, Stuttgart, 2012)

[158] J. Alnis, A. Matveev, N. Kolachevsky, T. Udem, and T. W. Hänsch: "*Subhertz linewidth diode lasers by stabilization to vibrationally and thermally compensated ultralow-expansion glass Fabry-Pérot cavities.*" Physical Review A **77**, 053809 (2008)

[159] B. Fröhlich, T. Lahaye, B. Kaltenhäuser, H. Kübler, S. Müller, T. Koch, M. Fattori, and T. Pfau: "*Two-frequency acousto-optic modulator driver to improve the beam pointing stability during intensity ramps.*" The Review of scientific instruments **78**, 043101 (2007)

[160] A. Griesmaier: "*Aufbau einer kombinierten magneto-optischen Falle für Chrom und Rubidium.*" (Diploma thesis, Stuttgart, 2002)

[161] M.-O. Mewes, M. R. Andrews, van Druten, N. J. D. M. Kurn, D. S. Durfee, and W. Ketterle: "*Bose-Einstein Condensation in a Tightly Confining dc Magnetic Trap.*" Physical Review Letters **77**, 416–419 (1996)

[162] M. Wenzel: "*Aktive Magnetfeldkompensation für atomoptische Experimente.*" (Bachelor thesis, Stuttgart, 2012)

[163] C.-L. Hung, X. Zhang, N. Gemelke, and C. Chin: "*Accelerating evaporative cooling of atoms into Bose-Einstein condensation in optical traps.*" Physical Review A **78**, 011604(R) (2008)

[164] E. Hecht: "*Optics.*" (Addison-Wesley, Reading, 2002)

[165] U. S. Military: "*Military standard photograph lenses.*" MIL-STG **150**, A (1951)

[166] M. Wenzel: "*A dysprosium quantum gas in highly controllable optical traps.*" (Master thesis, Stuttgart, 2015)

[167] I. Reis: "*Hochauflösendes Abbildungssystem für ultrakalte Atome.*" (Bachelor thesis, Stuttgart, 2014)

[168] B. H. Billings, and D. E. Gray: "*American Institute of Physics handbook.*" serie: McGraw-Hill handbooks. (McGraw-Hill, New York, 1972)

[169] R. Chicireanu: "*STUDIES OF COLD CHROMIUM ATOMS IN MAGNETIC AND OPTICAL TRAPS: steps towards Bose-Einstein Condensation.*" (PhD thesis, Paris, 2008)

[170] C. J. Foot: "*Atomic physics.*" serie: Oxford master series in atomic, optical and laser physics. (Oxford University Press, Oxford, 2003)

[171] W. D. Phillips, J. V. Prodan, and H. J. Metcalf: "*Laser cooling and electromagnetic trapping of neutral atoms.*" Journal of the Optical Society of America B **2**, 1751 (1985)

[172] A. Charnukha: "*Zeeman slower for 52Cr atoms.*" (Diploma thesis, Stuttgart, 2008)

[173] H. J. Metcalf, and. P. Van der Straten: "*Laser cooling and trapping.*" serie: Graduate texts in contemporary physics. (Springer, New York, 1999)

[174] H. Katori, T. Ido, Y. Isoya, and M. Kuwata-Gonokami: "*Magneto-Optical Trapping and Cooling of Strontium Atoms down to the Photon Recoil Temperature.*" Physical Review Letters **82**, 1116–1119 (1999)

[175] A. Berglund, J. Hanssen, and J. McClelland: "*Narrow-Line Magneto-Optical Cooling and Trapping of Strongly Magnetic Atoms.*" Physical Review Letters **100**, 113002 (2008)

[176] T. H. Loftus, T. Ido, M. M. Boyd, A. D. Ludlow, and J. Ye: "*Narrow line cooling and momentum-space crystals.*" Physical Review A **70**, 063413 (2004)

[177] M. Prentiss, A. Cable, J. E. Bjorkholm, S. Chu, E. L. Raab, and D. E. Pritchard: "*Atomic-density-dependent losses in an optical trap.*" Optics Letters **13**, 452 (1988)

[178] R. Grimm, M. Weidemüller, and Y. B. Ovchinnikov: "*Optical dipole traps for neutral atoms.*" Advances in Atomic, Molecular and Optical Physics **42**, 95–170 (2000)

[179] M. Lepers, J.-F. Wyart, and O. Dulieu: "*Anisotropic optical trapping of ultracold erbium atoms.*" Physical Review A **89**, 022505 (2014)

[180] S. Baier: "*An optical dipole trap for Erbium with tunable geometry.*" (Master thesis, Innsbruck, 2012)

[181] J. Rührig, T. Bäuerle, A. Griesmaier, and T. Pfau: "*High efficiency demagnetization cooling by suppression of light-assisted collisions.*" Optics express **23**, 5596–5606 (2015)

[182] Y. Tang, N. Q. Burdick, K. Baumann, and B. L. Lev: "*Bose–Einstein condensation of 162 Dy and 160 Dy.*" New Journal of Physics **17**, 045006 (2015)

[183] C. C. Bradley, C. A. Sackett, and R. G. Hulet: "*Bose-Einstein Condensation of Lithium: Observation of Limited Condensate Number.*" Physical Review Letters **78**, 985–989 (1997)

[184] K. Baumann, N. Q. Burdick, M. Lu, and B. L. Lev: "*Observation of low-field Fano-Feshbach resonances in ultracold gases of dysprosium.*" Physical Review A **89**, 020701(R) (2014)

[185] V. Vuletić, A. J. Kerman, C. Chin, and S. Chu: "*Observation of Low-Field Feshbach Resonances in Collisions of Cesium Atoms.*" Physical Review Letters **82**, 1406–1409 (1999)

[186] M. Repp, R. Pires, J. Ulmanis, R. Heck, E. D. Kuhnle, M. Weidemüller, and E. Tiemann: "*Observation of interspecies 6 Li- 133 Cs Feshbach resonances.*" Physical Review A **87**, 010701(R) (2013)

[187] S.-K. Tung, C. Parker, J. Johansen, C. Chin, Y. Wang, and P. S. Julienne: "*Ultracold mixtures of atomic 6 Li and 133 Cs with tunable interactions.*" Physical Review A **87**, 010702(R) (2013)

[188] S. T. Thompson, E. Hodby, and C. E. Wieman: "*Ultracold Molecule Production via a Resonant Oscillating Magnetic Field.*" Physical Review Letters **95**, 190404 (2005)

[189] S. T. Thompson, E. Hodby, and C. E. Wieman: "*Spontaneous Dissociation of R85b Feshbach Molecules.*" Physical Review Letters **94**, 020401 (2005)

[190] M. Berninger, A. Zenesini, B. Huang, W. Harm, H.-C. Nägerl, F. Ferlaino, R. Grimm, P. S. Julienne, and J. M. Hutson: "*Feshbach resonances, weakly bound molecular states, and coupled-channel potentials for cesium at high magnetic fields.*" Physical Review A **87**, 032517 (2013)

[191] H.-W. Cho, D. J. McCarron, M. P. Köppinger, D. L. Jenkin, K. L. Butler, P. S. Julienne, C. L. Blackley, Le Sueur, C. Ruth, J. M. Hutson, and S. L. Cornish: "*Feshbach spectroscopy of an ultracold mixture of 85 Rb and 133 Cs.*" Physical Review A **87**, 010703(R) (2013)

[192] K. Jachymski, and P. S. Julienne: "*Analytical model of overlapping Feshbach resonances.*" Physical Review A **88**, 052701 (2013)

[193] Y. Wang, and P. S. Julienne: "*Universal van der Waals physics for three cold atoms near Feshbach resonances.*" Nature Physics **10**, 768–773 (2014)

[194] F. H. Mies, E. Tiesinga, and P. S. Julienne: "*Manipulation of Feshbach resonances in ultracold atomic collisions using time-dependent magnetic fields.*" Physical Review A **61**, 022721 (2000)

[195] N. Nygaard, B. I. Schneider, and P. S. Julienne: "*Two-channel R -matrix analysis of magnetic-field-induced Feshbach resonances.*" Physical Review A **73**, 042705 (2006)

[196] S. Jochim, M. Bartenstein, G. Hendl, J. H. Denschlag, R. Grimm, A. Mosk, and M. Weidemüller: "*Magnetic Field Control of Elastic Scattering in a Cold Gas of Fermionic Lithium Atoms.*" Physical Review Letters **89**, 273202 (2002)

[197] T. Kraemer, M. Mark, P. Waldburger, J. G. Danzl, C. Chin, B. Engeser, A. D. Lange, K. Pilch, A. Jaakkola, H. C. Nägerl, and R. Grimm: "*Evidence for Efimov quantum states in an ultracold gas of caesium atoms.*" Nature **440**, 315–318 (2006)

[198] M. Zaccanti, B. Deissler, C. D'Errico, M. Fattori, M. Jona-Lasinio, S. Müller, G. Roati, M. Inguscio, and G. Modugno: "*Observation of an Efimov spectrum in an atomic system.*" Nature Physics **5**, 586–591 (2009)

[199] B. S. Rem, A. T. Grier, I. Ferrier-Barbut, U. Eismann, T. Langen, N. Navon, L. Khaykovich, F. Werner, D. S. Petrov, F. Chevy, and C. Salomon: "*Lifetime of the Bose Gas with Resonant Interactions.*" Physical Review Letters **110**, 163202 (2013)

[200] U. Eismann, L. Khaykovich, S. Laurent, I. Ferrier-Barbut, B. S. Rem, A. T. Grier, M. Delehaye, F. Chevy, C. Salomon, L.-C. Ha, and C. Chin: "*Universal Loss Dynamics in a Unitary Bose Gas.*" arXiv:cond-mat/1505.04523v2 (2015)

[201] B. S. Rem: "*The Road to the Unitary Bose Gas.*" (PhD thesis, Paris, 2013)

[202] Y. Wang, J. P. D'Incao, and C. H. Greene: "*Efimov Effect for Three Interacting Bosonic Dipoles.*" Physical Review Letters **106**, 233201 (2011)

[203] A. Frisch, M. Mark, K. Aikawa, S. Baier, R. Grimm, A. Petrov, S. Kotochigova, G. Quéméner, M. Lepers, O. Dulieu, and F. Ferlaino: "*Ultracold polar molecules composed of strongly magnetic atoms.*" arXiv:cond-mat/1504.04578v1 (2015)

[204] R. Rosensweig: "*Ferrohydrodynamics.*" serie: Cambridge Monographs on Mechanics. (Cambridge University Press, Cambridge, 1985)

[205] J. V. I. Timonen, M. Latikka, L. Leibler, R. H. A. Ras, and O. Ikkala: "*Switchable Static and Dynamic Self-Assembly of Magnetic Droplets on Superhydrophobic Surfaces.*" Science **341**, 253–257 (2013)

[206] L. Santos, G. V. Shlyapnikov, and M. Lewenstein: "*Roton-Maxon Spectrum and Stability of Trapped Dipolar Bose-Einstein Condensates.*" Phys. Rev. Lett. **90**, 250403 (2003)

[207] S. Komineas, and N. R. Cooper: "*Vortex lattices in Bose-Einstein condensates with dipolar interactions beyond the weak-interaction limit.*" Phys. Rev. A **75**, 023623 (2007)

[208] A. F. Andreev, and I. M. Lifshitz: "*Quantum Theory of Defects in Crystals.*" Sov. Phys. JETP **29**, 1107–1113 (1969)

[209] G. V. Chester: "*Speculations on Bose-Einstein Condensation and Quantum Crystals.*" Phys. Rev. A **2**, 256–258 (1970)

[210] A. J. Leggett: "*Can a Solid Be "Superfluid"?*" Phys. Rev. Lett. **25**, 1543–1546 (1970)

[211] E. Kim, and M. H. W. Chan: "*Probable observation of a supersolid helium phase.*" Nature **427**, 225–227 (2004)

[212] D. Y. Kim, and M. H. W. Chan: "*Absence of Supersolidity in Solid Helium in Porous Vycor Glass.*" Phys. Rev. Lett. **109**, 155301 (2012)

[213] M. Abad, M. Guilleumas, R. Mayol, M. Pi, and D. M. Jezek: "*A dipolar self-induced bosonic Josephson junction.*" Europhysics Letters **94**, 10004 (2011)

[214] T. Lahaye, T. Pfau, and L. Santos: "*Mesoscopic Ensembles of Polar Bosons in Triple-Well Potentials.*" Physical Review Letters **104**, 170404 (2010)

[215] D. Peter, K. Pawłowski, T. Pfau, and K. Rzażewski: "*Mean-field description of dipolar bosons in triple-well potentials.*" Journal of Physics B: Atomic, Molecular and Optical Physics **45**, 225302 (2012)

[216] Y. Wang, J. P. D'Incao, and C. H. Greene: "*Universal Three-Body Physics for Fermionic Dipoles.*" Physical Review Letters **107**, 233201 (2011)

Danksagung

Abschließend möchte ich mich bei allen, die zum Gelingen dieser Arbeit beigetragen haben, recht herzlich bedanken.

Mein besonderer Dank gilt Tilman Pfau. Vielen Dank, dass Du mir die Möglichkeit gegeben hast, an diesem spannenden Thema zu forschen. Du hast auftretende Probleme nicht als Rückschritt, sondern als Herausforderung angesehen und uns dadurch motiviert, diese zu lösen. Ich hoffe, dass dieses neue Experiment Dir noch viele interessante physikalische Probleme und die dazugehörigen Lösungen bietet.

Bei Herrn Günter Wunner und Herrn Harald Giessen möchte ich mich für den Prüfungsvorsitz und den Mitbericht bedanken.

Das erste halbe Jahr meine Promotionszeit durfte ich mit dem letzten Cr-I Doktoranden Stefan Müller und den beiden Post-Docs Juliette Billy und Emanuel Henn gemeinsam am Cr Experiment arbeiten. Ihr habt mir sowohl die experimentellen als auch die theoretischen Grundlagen beigebracht. Vielen Dank dafür!

Besonders möchte ich mich bei Holger Kadau bedanken. Wir, die beiden ersten Düsis, hatten die große Aufgabe, ein neues Experiment mit dem für uns bis dato unbekannten Element Dysprosium zu planen und aufzubauen. Es war nicht immer einfach und wir mussten viele Rückschläge wegstecken, doch schließlich haben wir die Maschine gemeinsam zum Laufen bekommen.

Vielen herzlichen Dank auch an Matthias Schmitt und Matthias Wenzel. Ihr habt als Masterstudenten das Experiment mit aufgebaut und seid schnell ein wichtiger Teil des Teams geworden. Daher freut es mich besonders, dass Ihr als Doktoranden nun das Experiment übernommen habt. Ich wünsche Euch viel Erfolg und Durchhaltevermögen. Es hat mir sehr viel Spaß gemacht, mit Euch gemeinsam an diesem Experiment zu arbeiten.

Vielen Dank auch an die Bachelor-, Master- und Diplomstudenten Micha Schilling, Simon Ristok, Bernd Docters, Nicolas Zuber, Matthias Feldmaier, Michaela Nickel, Isabel Reis und Clarissa Wink. Durch Eure Arbeit habt ihr entscheidend zum Erfolg dieses Experimentes beigetragen.

Einen großen Dank auch an Igor Ferrier-Barbut. Im Dezember 2014 bist Du als Post-Doc an unser Experiment gekommen und hast Dich sehr schnell eingelebt. Mit Deinem großen physikalischen Wissen sowie deiner freundlichen und offenen Art hast du das Experiment in vielerlei Hinsicht vorangebracht. Ich wünsche Dir viel Erfolg für Deine weitere wissenschaftliche Karriere.

Vielen Dank an die Gruppenleiter Axel Griesmaier, Robert Löw, Sebastian Hofferberth und Harald Kübler. Für viele technische und physikalische Probleme hattet Ihr stets die passende Lösung parat.

Vielen Dank an alle PI5ler. Wir hatten eine tolle gemeinsame Zeit und ich werde oft an unsere lustigen Kaffeerunden, Metertage und Ausflüge zurückdenken.

Danke auch an Karin Otter, Astrid Buck, Oliver Nagel und Nadine Prellwitz für die große Unterstützung bei allen Verwaltungs- und Organisationsaufgaben sowie für die netten und aufmunternden Gespräche zwischendurch.

Ein besonderer Dank gilt meinen Eltern. Dank Eurer Unterstützung und der Gewissheit, dass Ihr immer für mich da seid, hatte ich die Freiheit und Möglichkeit, diesen spannenden Weg zu gehen. Vielen herzlichen Dank auch an meine ganze Familie und an alle Freunde für Euer Interesse an meinem Experiment und für die guten und aufmunternden Worte zwischendurch.

Zum Schluss ein riesiges Dankeschön an meine Freundin Susanne. Während der ganzen Zeit hast Du mich aufgemuntert, wenn es mal nicht so lief und hast Dich zusammen mit mir gefreut, wenn wir kleine Erfolge feiern konnten. Vielen herzlichen Dank für alles!